Thesis

Application of dynamic elastography to the mechanical characterization of viscoelastic soft media via torsional, longitudinal, and transverse shear waves

Jorge Torres Pérez

UNIVERSIDAD DE GRANADA

Application of dynamic elastography to the mechanical characterization of viscoelastic soft media via torsional, longitudinal, and transverse shear waves

Thesis report

by

Jorge Torres Pérez

A thesis submitted to University of Granada
in partial fulfillment of the requirements for the degree of
Doctor of Philosophy

ADVISOR:
Prof. Guillermo Rus Carlborg

PhD Program in Civil Engineering
Non-destructive Evaluation of Materials and Structures

Department of Structural Mechanics & Hydraulic Engineering
University of Granada (Spain)

September 2023

Editor: Universidad de Granada. Tesis Doctorales
Autor: Jorge Torres Pérez
ISBN: 978-84-1195-120-3
URI: https://hdl.handle.net/10481/88507

UNIVERSIDAD
DE GRANADA

Application of dynamic elastography to the mechanical characterization of viscoelastic soft media via torsional, longitudinal, and transverse shear waves.

Abstract

The field of biomedical engineering has gained importance in assessing soft tissue elasticity for diagnosing and monitoring diseases. Traditionally, clinicians have relied on manual palpation, which is subjective and qualitative. Dynamic elastography, a noninvasive medical imaging technique, measures the elasticity of various soft tissues by generating, detecting, and tracking shear waves (SWs). SWs are elastic waves whose velocity relates objectively and quantitatively to the mechanical properties of the medium. Over the years, SW methods have gained significant attention, as evidenced by the substantial increase in publications on SW elastography. The technique has shown promising diagnostic potential for fibrosis staging and tumor detection, among many others. Different imaging modalities, including ultrasound, magnetic resonance, and optical techniques, have been developed to probe tissue mechanical properties. One of the motivations for using dynamic elastography is the recognition that tissues exhibit viscoelastic behavior, where their mechanical response depends on time and excitation frequency. This aspect adds complexity to the diagnosis and highlights the need to extract dynamic properties for a more refined understanding of tissue functionality and structure. The primary objective of the thesis is to advance our understanding of the behavior of SWs and their interaction with different materials. More specifically, the thesis aims to address several questions, such as avoiding capture of complex propagation modes in thin media, leveraging simple rheological models for distinguishing mechanical states, applying dynamic elastography at different scales, studying the limiting frequency where SWs are no longer observed (cutoff), and investigating SW propagation in complex materials.

The interest in dynamic properties at different scales has led to propose several sources of excitation and imaging modalities. These proposals may involve modifications to the experimental setup, imaging techniques, or data analysis algorithms, aiming to enhance the accuracy, resolution, or practicality of the elastography approach. They provide insights into the elastic properties, attenuation, viscosity, or other relevant characteristics of the investigated media.

Through collaborations with different research groups, several elastography techniques adapted to specific applications are proposed in this thesis. As a compendium of three publications, the objectives are detailed according to each of them.

Firstly, this thesis aims to develop a specialized elastography technique called torsional shear wave elastography (TWE) for the cornea. The objective is to determine if TWE can effectively differentiate between different mechanical states of the cornea. The research plan includes designing appropriate components, investigating shear displacements in different planes, and assessing the feasibility of detecting changes in corneal properties after chemical treatment. The results show that a design of an elastography device adapted to corneal geometry is achieved, the mechanical changes after chemical treatment are satisfactorily detected, and in-plane measurements are shown to simplify the velocity analysis by avoiding complex guided modes.

Secondly, the complex behavior exhibited by soft tissues is due to its multiscale microstructure. Beginning to explore the relationship between properties at the microscale and how they are translated to the macroscale will expand the applicability of elastography. Another objective of the thesis is to explore the feasibility of micro-elastography, that is, a technique that quantifies these mechanical parameters at a micrometric scale. Longitudinal SWs are generated with a magnetic excitation at very high frequency (several kHz) on a hydrogel commonly used as culture medium, and a high-speed camera records the displacements. As results, ultrasonic SWs (>20 kHz) are observed in relatively stiff media. The KV model may predict the cutoff frequencies, which means that they depend on rheological parameters, and a high variability in the viscosity parameter when using a reduced dispersion curve is found.

Finally, the previous concepts developed in the micro-elastography of solids are applied to viscoelastic liquids using transverse SWs. The medium is defined as either liquid or solid depending on the ratio of the loss shear modulus to storage shear modulus, and the cutoff frequencies mark the detection limit of the experimental system. Mathematical expressions are developed to study the attenuation, and three-element rheological models can identify the transition frequencies. It is also emphasized the advantages

of SW propagation methods over traditional rheometry, as they enable exploration of higher frequencies and offer insights into complex fluids.

Overall, the thesis contributes to the advancement of dynamic elastography techniques and their potential applications in refining diagnostics, and improving our understanding of SW propagation in biological media. All of the results have been supported by rheological models, whose parameters have been interpreted with respect to the microstructure and their relationship with attenuation and frequency. However, the understanding of the relationship between microscale and macroscale mechanical properties remains limited, posing challenges in predicting mechanical behavior solely based on microstructure.

Resumen

El campo de la ingeniería biomédica ha cobrado importancia en la evaluación de la elasticidad de los tejidos blandos para el diagnóstico y seguimiento de enfermedades. Tradicionalmente, los médicos se han basado en la palpación manual, que es subjetiva y cualitativa. La elastografía dinámica, una técnica de imagen médica no invasiva, mide la elasticidad de diversos tejidos blandos mediante la generación, detección y seguimiento de ondas de cizalla (SWs). Las SWs son ondas elásticas cuya velocidad se relaciona objetiva y cuantitativamente con las propiedades mecánicas del medio. A lo largo de los años, los métodos de basados en SWs han sido objeto de gran atención, como demuestra el considerable aumento de las publicaciones sobre elastografía mediante SWs. La técnica ha mostrado un potencial diagnóstico prometedor para la estadificación de la fibrosis y la detección de tumores, entre muchos otros. Se han desarrollado distintas modalidades de obtención de imágenes, como ultrasonidos, resonancia magnética y técnicas ópticas, para sondear las propiedades mecánicas de los tejidos. Una de las motivaciones para utilizar la elastografía dinámica es el reconocimiento de que los tejidos presentan un comportamiento viscoelástico, en el que su respuesta mecánica depende del tiempo y de la frecuencia de excitación. Este aspecto añade complejidad al diagnóstico y subraya la necesidad de extraer propiedades dinámicas para una comprensión más refinada de la funcionalidad y estructura de los tejidos. El objetivo principal de la tesis es avanzar en nuestra comprensión del comportamiento de las SWs y su interacción con diferentes materiales. Más concretamente, la tesis pretende abordar varias cuestiones, como evitar la captura de modos de propagación complejos en medios delgados, aprovechar modelos reológicos sencillos para distinguir estados mecánicos, aplicar la elastografía dinámica a diferentes escalas, estudiar la frecuencia límite en la que las SWs dejan de observarse (cutoff) e investigar la propagación de las SWs en materiales complejos.

El interés por las propiedades dinámicas a diferentes escalas ha llevado a proponer varias fuentes de excitación y modalidades de obtención de imágenes. Estas propuestas pueden implicar modificaciones en la configuración experimental, las técnicas de obtención de imágenes o los algoritmos de análisis de datos, con el objetivo de mejorar la precisión, la resolución o la viabilidad del enfoque de la elastografía. Proporcionan información sobre las propiedades elásticas, la atenuación, la viscosidad u otras características relevantes de los medios investigados.

A través de colaboraciones con diferentes grupos de investigación, en esta tesis se proponen varias técnicas de elastografía adaptadas a aplicaciones específicas. Como compendio de tres publicaciones, se detallan los objetivos según cada una de ellas.

En primer lugar, esta tesis pretende desarrollar una técnica de elastografía especializada denominada elastografía de ondas de cizalla torsional (TWE) para la córnea. El objetivo es determinar si la TWE puede diferenciar eficazmente entre los distintos estados mecánicos de la córnea. El plan de investigación incluye el diseño de los componentes adecuados, la investigación de los desplazamientos de cizalla en diferentes planos y la evaluación de la viabilidad de la detección de cambios en las propiedades de la córnea tras un tratamiento químico. Los resultados muestran que se ha logrado diseñar un dispositivo de elastografía adaptado a la geometría de la córnea, que se detectan satisfactoriamente los cambios mecánicos tras el tratamiento químico, y que se demuestra que las mediciones en el plano simplifican el análisis de la velocidad al evitar modos guiados complejos.

En segundo lugar, el complejo comportamiento que exhiben los tejidos blandos se debe a su microestructura multiescala. Empezar a explorar la relación entre las propiedades a microescala y cómo se traducen a macroescala ampliará la aplicabilidad de la elastografía. Otro objetivo de la tesis es explorar la viabilidad de la microelastografía, es decir, una técnica que cuantifique estos parámetros mecánicos a escala micrométrica. Se generan SWs longitudinales con una excitación magnética a muy alta frecuencia (varios kHz) sobre un hidrogel comúnmente utilizado como medio de cultivo, y una cámara de alta velocidad registra los desplazamientos. Como resultado, se observan SWs ultrasónicas (>20 kHz) en medios relativamente rígidos. El modelo KV puede predecir las frecuencias de corte, lo que significa que depen-

den de parámetros reológicos, y se encuentra una alta variabilidad en el parámetro de viscosidad cuando se utiliza una curva de dispersión reducida.

Por último, los conceptos anteriores desarrollados en la microelastografía de sólidos se aplican a líquidos viscoelásticos utilizando SWs transversales. El medio se define como líquido o sólido en función de la relación entre el módulo de cizalla de pérdida y el módulo de cizalla de almacenamiento, y las frecuencias de corte marcan el límite de detección del sistema experimental. Se desarrollan expresiones matemáticas para estudiar la atenuación, y los modelos reológicos de tres elementos pueden identificar las frecuencias de transición. También se destacan las ventajas de los métodos de propagación SW sobre la reometría tradicional, ya que permiten explorar frecuencias más altas y ofrecen una visión de los fluidos complejos.

En general, la tesis contribuye al avance de las técnicas de elastografía dinámica y a sus aplicaciones potenciales para refinar los diagnósticos y mejorar nuestra comprensión de la propagación de SWs en medios biológicos. Todos los resultados se han apoyado en modelos reológicos, cuyos parámetros se han interpretado con respecto a la microestructura y su relación con la atenuación y la frecuencia. Sin embargo, la comprensión de la relación entre las propiedades mecánicas a microescala y a macroescala sigue siendo limitada, lo que plantea retos a la hora de predecir el comportamiento mecánico basándose únicamente en la microestructura.

Acknowledgements

First and foremost, I am immensely grateful to my academic supervisor, Prof. Guillermo Rus, for giving me the opportunity to join such a well-equipped laboratory and giving me the freedom to work, which enhanced my autonomy and passion to face different challenges. Thanks to him, all the publications presented during this period were funded by MCIN/AEI /10.13039/501100011033 grant number PRE2018-086085 (Co-funded by European Social Fund "Investing in your future").

I extend my gratitude to Prof. Juan Melchor, who was the one who introduced me to research back in 2015, who first always asks how it's going, and showed me how to organize and write scientifically.

My sincere appreciation goes to Prof. Rafael Muñoz for his infectious energy throughout any arduous journey, and his patience in explaining complex concepts.

I would also like to thank all my colleagues in the Ultrasonics Lab for the moments shared during and outside of work, which taught me the inherent joy that accompanies the pursuit of knowledge. I would especially like to mention Antonio Callejas, Inas Faris and Antonio Gomez, with whom I had enlightening discussions and could always count on. Also Manuel Hurtado, Rafael Marques, Hirad Shamimi (agha), and Jose Cortes, with whom I have shared many good times, intense days of work, and jokes. I cannot forget my desk neighbor, Beatriz Blanco, whose empathetic ear eased the burdens of the day.

It is impossible for me not to show my gratitude and admiration to my research stay supervisor at Lyon, Dr. Stefan Catheline, for his exceptional mentoring and his ability to interpret results. Likewise, it was very interesting to collaborate directly with Gabrielle Laloy-Borgna as she gave me an innovative view on physics.

I would like to express my deepest gratitude to the rest of individuals who have contributed to the successful completion of this doctoral journey, but also to those with whom I have not worked and who have made my days more bearable (Virgil, Omar, Camila, Alireza, Roberto, Alberto García, among many others). Although I may not mention all their names, their invaluable support and guidance have had a profound impact on my academic and personal growth.

Another thanks goes to my family and friends, who provided me with moments of constant joy during my free time. Weekends of non-stop laughing and doing activities and sports with Juan will be in my memory forever. Although they did not get to see me start, I am grateful for the support that my grandparents always gave me.

Lastly, I would like to express my heartfelt gratitude to her, 陈钰铃, whose support and understanding have been a constant source of strength in the end of this PhD. 你是我的日出和日落，是激励我的光。

Thank you.

Compendium of publications

This thesis is presented as a compendium of three publications. Each of them was prepared in collaboration with several co-authors associated with various international research centers. The author of this thesis is responsible for most of the development of each paper, including: data curation, formal analysis, methodology, and writing the original draft.

A. Torres, Jorge, et al. "Torsional wave elastography to assess the mechanical properties of the cornea." Scientific Reports 12.1 (2022): 8354.
https://doi.org/10.1038/s41598-022-12151-2
Quality indications:

- Impact Factor: 4.997
- Rank: 19/74 (JCR, Q1)

B. Torres, Jorge, et al. "Optical micro-elastography with magnetic excitation for high frequency rheological characterization of soft media." Ultrasonics 132 (2023): 107021.
https://doi.org/10.1016/j.ultras.2023.107021
Quality indications:

- Impact Factor: 4.062
- Rank: 6/32 (JCR, Q1)

C. Torres, Jorge, et al. "A phase transition approach to elucidate the propagation of shear waves in viscoelastic materials." Applied Physics Letters 122.22 (2023): 223702.
https://doi.org/10.1063/5.0150219
Quality indications:

- Impact Factor: 3.971
- Rank: 50/161 (JCR, Q2)

Contents

List of Figures

List of Tables

1 Introduction

In the biomedical field, elasticity has been used to report on the state of a soft tissue and to determine abnormal conditions. One of the most notable applications is staging fibrosis, where higher elasticity (stiffer medium) in the liver is related to a more advanced stage of the disease. On the other hand, when an area with different elasticity is detected within a soft tissue, it is often due to the presence of a tumor, which in the case of being stiffer may be cancerous. Thus, probing mechanical properties, and especially elasticity, has the potential to become a diagnostic tool. Traditionally, clinicians have made a rough estimate of tissue elasticity by manual palpation. The diagnosis can only be made in superficial tissues and with a subjective and qualitative character.

Medical imaging encompasses a set of techniques that seek to create images of the human body for the purpose of diagnosis or monitoring of diseases. Dynamic elastography is one of these techniques that allows the measurement of the elasticity of different soft tissues, such as organs, tendons, or muscles. The procedure is performed noninvasively and is also applicable to tissues that do not necessarily have to be on the surface. Furthermore, being operator independent, the measurement is objective and quantitative. Dynamic elastography is based on the generation, detection, and tracking of shear waves (SWs). It is a type of elastic wave whose velocity is related to the mechanical properties of the medium in which they propagate. Depending on the characteristics of the medium, there may be a direct relationship with elasticity or it may also depend on viscosity and geometry.

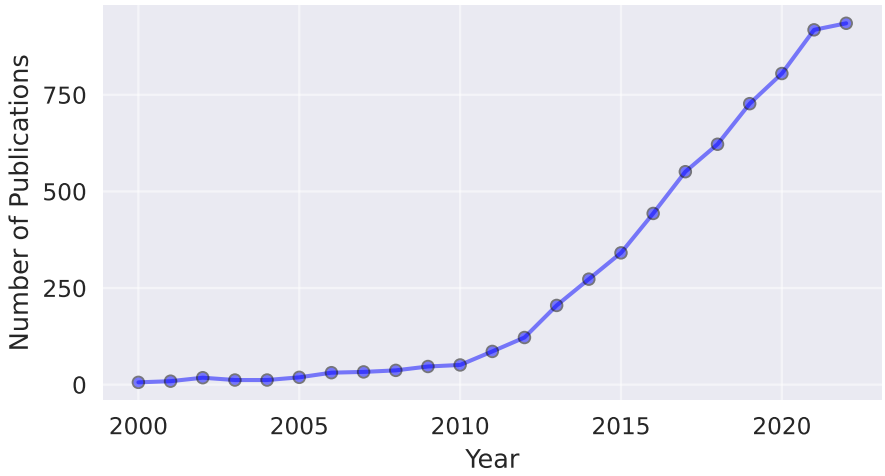

Figure 1.1. Number of publications in Web Of Science (2022) presenting the term "Shear Wave Elastography".

This field has continued to grow its interest since its conception, and in recent years the impact of SW methods has been more than remarkable. Figure 1.1 shows the publication records using Web Of Science with the term "Shear Wave Elastography" in their abstract. As we can see, the number of publications has increased tenfold in the last decade, with more than 6000 publications. In the early 2000s, the first proofs of concept for the detection of SW were carried out. Fast echography was used, an imaging technique

based on compression waves, and global values of the measured tissue elasticity were obtained. This was the birth of Ultrasound Elastography (USE). It was not until around 2005 that the first 2D maps of elasticity were produced, and consequently this technology expanded with its first clinical implementations.[1] Since then, different imaging modalities have been developed. Among them we can mention Magnetic Resonance Elastography (MRE), optical techniques such as Optical Coherence Elastography (OCE), and high-speed cameras. The common point of all techniques is the use of SWs to probe the mechanical properties of the medium to be analyzed.

1.1. Thesis Scope

One of the reasons for using dynamic elastography is that one cannot rely on elasticity alone, since tissues exhibit varying degrees of viscoelastic behavior.[2] In a viscoelastic tissue, the mechanical response depends on the time, and therefore on the excitation frequency. Extracting this type of dynamic properties refines the diagnosis by gaining insight into the functionality and structure of the tissue. This situation can raise several questions.

- Can we combine different modes of excitation with different imaging modalities and obtain results adapted to the medium?
- Can SWs be generated in such a way that complex propagation modes, such as guided waves, are not captured in thin media such as cornea or culture media?
- Despite the limitations of simple rheological models, can they provide sufficient information to distinguish mechanical states?
- It is feasible to apply dynamic elastography at the microscale and quantify viscoelastic parameters?
- Is it possible to study the frequency at which SWs are strongly attenuated (cutoff) and therefore no longer observable with current techniques?
- Can SWs propagate in viscoelastic liquids?

The measurement of mechanical properties in biological media holds significant importance for various applications. Specifically, early-stage diagnosis of certain pathologies is crucial for developing adapted clinical treatments. Currently, beyond the standard of linear elasticity, viscoelasticity is gaining momentum as a result of theoretical and technological developments in the biomedical field.[2],[3] At the same time, the feasibility of quantifying viscoelastic properties at the microscopic scale is beginning to mature.[4],[5] However, the relationship between micro-scale mechanical properties and the macro-scale properties derived from them remains poorly understood, hindering our ability to predict mechanical behavior based solely on microstructure. Consequently, it is intriguing to propose techniques that enable a better comprehension of mechanical properties that have been extensively studied at the macro level but scarcely explored at the micro level. Moreover, these properties elucidate the ability of culture media to facilitate cell migration and induce cell differentiation.[6] Similarly, SW propagation methods can overcome the technical limitations of traditional rheometry, and explore higher frequencies, rarely investigated in viscoelastic materials, such as complex fluids. Dynamic elastography could play a pivotal role in refining traditional diagnostics, in optimizing the efficiency of culture systems for regenerative medicine, and in better understanding the propagation of SW in various biological media.

1.2. Thesis Outline

As a compendium of three publications, the scope of this thesis is within the dynamic elastography field. The publications examine the viscoelastic properties of various media through the utilization of different SWs generation sources and imaging modalities. They focus on analyzing dispersion curves and try to provide a comprehensive interpretation of the obtained rheological parameters through fitting procedures. They have been included in this document in a homogeneous format although they have been published in different journals (see Scientific Articles).

The body of the thesis is divided into five chapters, the main details of which are listed below:

- Chapter 1. We begin by describing the scope and outlining the content of the thesis.

- Chapter 2. The objective of the thesis are presented divided according to the publications.
- Chapter 3. This chapter briefly presents the theoretical scientific background. A reminder of wave physics concepts useful for elastography, as well as the purpose, applicability, and evolution of dynamic elastography are given. The interest in measuring viscoelasticity and its feasibility on the micrometer scale is detailed.
- Chapter 4. This chapter briefly presents the methodological scientific background. It describes the basis of the techniques used, the displacement and velocity estimators, the preprocessing steps, and the characteristics of the analyzed media. Additionally, the study of viscoelasticity by means of rheological models is provided.
- Chapter 5. It is a discussion based on the results presented in the publications and some concluding remarks.

A graphical illustration of the dynamic elatography techniques applied, as well as the contributions of each publication, is shown in Figure 1.2.

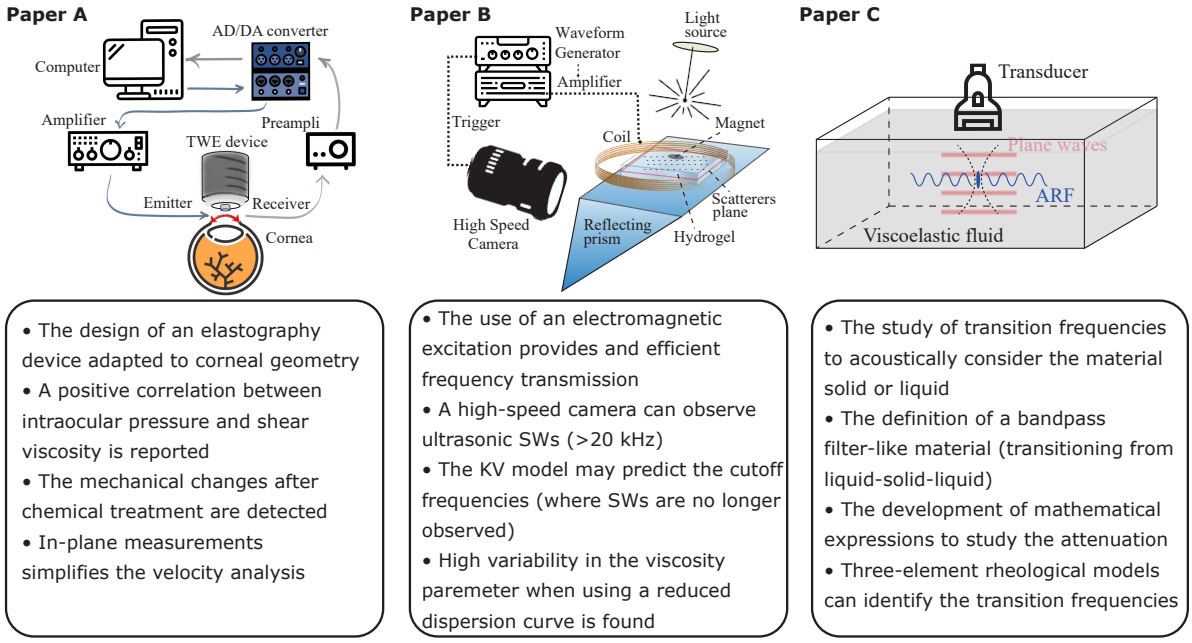

Figure 1.2. Graphical illustration of the applied dynamic elastography techniques with their respective experimental setups, and the main contributions of each paper.

Publications

In Paper A – *Torsional wave elastography to assess the mechanical properties of the cornea*: corneal mechanical changes preceding visible structural alterations have been of interest in clinical evaluation. This study proposed an adapted elastography technique, Torsional Wave Elastography (TWE), for the cornea. Ex vivo experiments were conducted on porcine corneal samples, including control and alkali burn treatment groups, and its viscoelasticity was estimated using a Kelvin-Voigt (KV) model. The results were compared between the control and treated groups, and the importance of studying the in-plane propagation was pointed out. A torsional wave transducer adapted to the geometry of the cornea was designed.

In Paper B – *Optical micro-elastography with magnetic excitation for high frequency rheological characterization of soft media*: the limited research on the propagation of SWs in elastography at high frequencies (>3 kHz) due to attenuation and technical constraints was addressed. Longitudinal SWs were generated at high frequencies (reaching ultrasonic SWs) and the high frequency limit was explored, where SWs were no longer observed (cutoff). It was shown that in order to infer accurate viscoelastic parameters, the KV

model required the full frequency range of the dispersion curve. For this application, wave generation was performed by magnetic excitation and imaging with a high-speed camera.

In Paper C – *A phase transition approach to elucidate the propagation of SWs in viscoelastic materials*: the study was focused on viscoelastic liquids where the traditional definition of a liquid becomes ambiguous. The study consisted of the dispersion and attenuation of transverse SWs using a rheological model-independent approach to also explore low and high cutoff frequencies. Three-element rheological models were required to accurately fit the experimental results. A standard Ultrasound Elastography methodology was followed.

2

Objectives

Throughout this thesis, various imaging modalities were employed, and new SW generation methods were proposed. The objective was to identify the most optimal form of SW propagation. For instance, by avoiding complex propagation modes like guided waves, the analysis was simplified, and the interpretation of results became more straightforward. Each experimental setup was adapted to the specificities and geometry of the biological medium under investigation, allowing for the study of different wave types interrogating the medium. These included torsional SWs in the cornea, longitudinal SWs in hydrogels utilized for cell culture, and transverse SW in viscoelastic liquids. The objectives of this thesis encompass alternative techniques in dynamic elastography, achieved either through innovative experimental setups or the approaches for extracting information about propagating waves.

Objective 1

Develop an elastography technique based on torsional SWs (TWE) adapted to the specificities of the cornea and determine its capability to differentiate between different mechanical states.

❶ Design an emitting disk that can generate torsional SWs and a piezoelectric sensor suitable for receiving the propagated waves, considering the curvature of the cornea.

❷ Investigate in-plane shear displacements (the plane perpendicular to the emitter axis) to eliminate the influence of guided waves.

❸ Assess the feasibility of the technique to detect changes in rheological properties by introducing structural modifications through chemical treatment.

Objective 2

Develop an optical micro-elastography (OME) technique capable of generating and tracking high-frequency SWs with sufficient spatial and temporal resolution, enabling viscoelastic analysis of soft media across an ultrawide frequency range.

❶ Devise a new wave generation method utilizing transient magnetic force to achieve high frequency SWs.

❷ Manufacture a transparent viscoelastic medium with an embedded magnetic element to observe high frequency displacements using a high-speed camera.

❸ Investigate the potential of the Kelvin-Voigt rheological model in explaining high cutoff frequencies (where SWs are no longer observed) and determining the errors in mechanical parameters based on the fitted frequency range.

Objective 3

Utilize a method based on transverse SWs to examine the frequency ranges in which a medium behaves as a classic solid (SW propagates) or a liquid (SW does not propagate) in viscoelastic liquids.

❶ Employ a rheological model-independent approach to calculate the storage and loss shear modulus by analyzing phase velocity and attenuation.

❷ Identify the region of minimal attenuation for the wave amplitude and determine the cutoff frequencies.

❸ Develop mathematical expressions for various rheological models to fit attenuation parameters.

3

Scientific Background: Theory

3.1. Wave propagation in soft media

The understanding of wave propagation in soft media is fundamental for the development of dynamic elastography techniques. It is crucial to characterize the properties of the medium through which the waves will propagate in order to accurately model the wave behavior. From there, expressions can be derived that establish relationships between the propagation velocity and mechanical properties such as elasticity. The governing equations that form the foundation of this analysis are briefly introduced here, with more comprehensive explanations available in established textbooks.[7]

Let us begin by considering an elastic, linear, isotropic, infinite, and homogeneous medium. In such a medium, the mechanical waves that can propagate exhibit wavelengths much larger than the interatomic distances. Consequently, the medium can be treated as a continuum, falling within the domain of continuum mechanics. By utilizing equations from mechanics that relate stress and strain, the deformation mode induced by an excitation can be determined, which corresponds to a specific type of wave within the medium. To fully describe the mechanical state of the system, it is necessary to define several relevant quantities in advance. The Einstein summation convention is employed, wherein repeated indices are understood to be implicitly summed over.

Displacement field. The displacement field is a vector field that is defined at each point in a material and at each instant in time. When deformation occurs as a result of an applied force, an element that was initially located at a position $\mathbf{x}$ (with respect to the origin) moves to a new position $\mathbf{x'}$. This defines the displacement vector $u(\mathbf{x}) = \mathbf{x'} - \mathbf{x}$. Note that the interest does not lie in the absolute displacement of individual elements, but rather on the relative displacements between different elements.

Deformation tensor. Assuming that the magnitude of the displacement field is small, the deformation tensor of order two is defined:

$$\varepsilon_{ij} = \frac{1}{2}\left(\frac{\partial u_i}{\partial x_j} + \frac{\partial u_j}{\partial x_i}\right) \tag{3.1}$$

The diagonal elements ($i = j$) characterize the relative length change in the direction of the analysis, due to longitudinal deformation. The other terms ($i \neq j$) represent the angle variation between two elements dx_i and dx_j, due to shear deformation.

Stress tensor. Stress represents the internal efforts that act when a material is deformed. The stress tensor of second order σ_{ij} completely describes the state of stress at a point inside a material and is defined as the force exerted F_{ij} across a surface described by its normal vector n_i:

$$F_{ij} = \sigma_{ij} \cdot n_i \tag{3.2}$$

Hooke's law. The relationship between these two tensors is established by the generalized Hooke's law:

$$\sigma_{ij} = C_{ijkl}\varepsilon_{kl} \tag{3.3}$$

The tensor of order four C_{ijkl} contains the elastic constants that define the mechanical behavior of the material. Using properties of tensor symmetry and assuming isotropy, the number of independent constants can be reduced to two:

$$C_{ijkl} = \lambda\delta_{ij}\delta_{kl} + \mu(\delta_{ik}\delta_{jl} + \delta_{il}\delta_{jk}) \tag{3.4}$$

where λ and μ are known as the Lamé constants and δ is the delta of Kronecker (when $i = j; \delta = 1$, while $i \neq j; \delta = 0$). The constitutive linear equation reduces to:

$$\sigma_{ij} = \lambda\delta_{ij}\varepsilon_{kk} + 2\mu\varepsilon_{ij} \tag{3.5}$$

Elastic wave propagation. Using the dynamic equilibrium law on an element of infinitesimal volume, whereby every external force is equal to mass by acceleration, it is obtained:

$$\rho\frac{\partial^2 u_i}{\partial^2 t} = \frac{\partial\sigma_{ij}}{\partial x_j} \tag{3.6}$$

ρ is the mass density of the material, and the right side represents the volume force due to internal efforts. It is considered that the system is not subject to any external force, and therefore the inertial force term mass is removed. Hooke's law is introduced next and Navier's equation is retrieved (in vectorial form):

$$\rho\frac{\partial^2\mathbf{u}}{\partial^2 t} = (\lambda + \mu)\boldsymbol{\nabla}(\boldsymbol{\nabla}\cdot\mathbf{u}) + \mu\boldsymbol{\nabla}^2\mathbf{u} \tag{3.7}$$

According to the Helmholtz theorem, we can decompose the displacement vector $\mathbf{u}$ as the sum of a curl-free component and a divergence-free component $\mathbf{u} = \mathbf{u}_L + \mathbf{u}_S$. By the definition of particle motion, $\mathbf{u}_L$ represents a longitudinal displacement, while $\mathbf{u}_S$ is a transverse displacement. This yields two D'Alembert equations that we can solve for each displacement component :

$$\rho\frac{\partial^2\mathbf{u}_L}{\partial^2 t} - (\lambda + \mu)\boldsymbol{\nabla}^2\mathbf{u}_L = 0 \quad \rightarrow \quad \frac{\partial^2\mathbf{u}_L}{\partial^2 t} - c_L^2\boldsymbol{\nabla}^2\mathbf{u}_L = 0 \quad \rightarrow \quad c_L = \sqrt{\frac{\lambda+\mu}{\rho}} \tag{3.8}$$

$$\rho\frac{\partial^2\mathbf{u}_S}{\partial^2 t} - \mu\boldsymbol{\nabla}^2\mathbf{u}_S = 0 \quad \rightarrow \quad \frac{\partial^2\mathbf{u}_S}{\partial^2 t} - c_S^2\boldsymbol{\nabla}^2\mathbf{u}_S = 0 \quad \rightarrow \quad c_S = \sqrt{\frac{\mu}{\rho}} \tag{3.9}$$

3.1.1. Compression and shear waves

The longitudinal compression wave velocity c_L describes a particle displacement that is parallel to the direction of wave propagation. The transverse SW velocity c_S describes a particle displacement that is perpendicular to the direction of wave propagation (see Figure 3.1). The existence of two uncoupled equations, c_L and c_S, shows that these two types of wave can coexist independently in a material.

In soft biological media longitudinal compression waves propagate much faster than SWs since $\lambda >> \mu$.[8] The constant λ does not have a direct physical interpretation; nevertheless, it is often associated with the bulk modulus $K = \lambda + \frac{2}{3}\mu$, which characterizes the response of a material to volume change under volumetric pressure. Since the compressibility of biological media tends to be similar to that of water, which has a significantly higher value compared to the μ provided by internal structures, a reasonable approximation is $K = \lambda$. The bulk modulus of water is approximately 2.2 GPa and assuming a density of $\rho = 1000\text{kg/m}^3$ we obtain a longitudinal compression wave velocity $c_L = 1480\text{m/s}$, which corresponds to the velocity of the sound in water.

The constant μ is generally called the shear modulus and represents the resistance to shear deformation. This modulus varies considerably among different biological tissues.[9] For example, the shear modulus of the liver can be around 5 kPa, while for muscle it can reach 20 kPa. These values lead to approximate shear wave velocities of c_S of 2.2 m/s and 4.5 m/s, respectively.

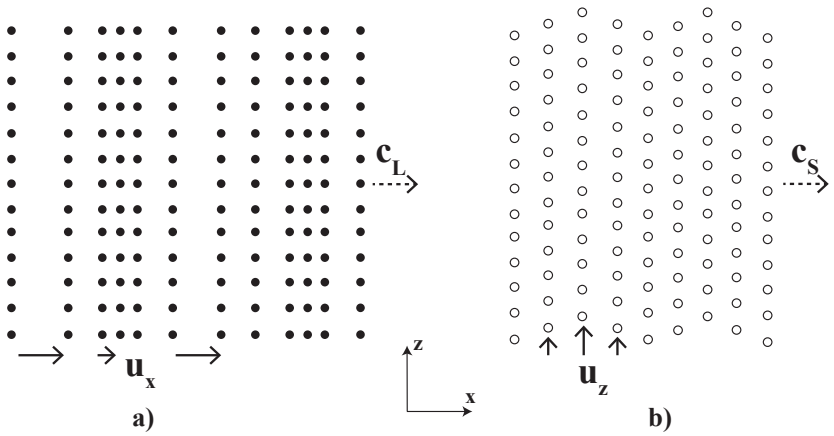

Figure 3.1. Classical compression (a) and shear (b) waves. Both propagation directions are horizontal, from left to right. In a) the particle displacement polarization is longitudinal (parallel), while in b) is transversal (perpendicular).

3.1.2. Dispersion relation

The information provided in Holm's book[10] discusses the SW equation, which assumes that the material layers experience shear motion without any significant change in volume, therefore the dilatational term is negligible $\nabla \cdot \mathbf{u} = 0$. In the case of a lossless medium:

$$\nabla^2 \mathbf{u}_s = \frac{1}{c_s^2} \ddot{\mathbf{u}}_s \tag{3.10}$$

To simplify the interpretation, the results are presented in 1D propagation in the right +x direction. By considering monochromatic plane waves, the solution of particle displacement in time at a single frequency is combined with the independent solution on space (free-field conditions):

$$u_z(x,t) = U_0 \cdot u_z(t) \cdot u_z(x) = U_0 e^{j(\omega t - kx)} \tag{3.11}$$

where U_0 is a real constant related to the maximum amplitude, j is the imaginary number, $\omega = 2\pi f$ is the angular frequency, and k is the wavenumber, with real-valued components. It's important to note that we are working with the lossless wave equation, which accounts for the real values of k. By inserting this solution into Equation 3.10, the dispersion relation can be derived, revealing the linear relationship between k and ω:

$$u_z\,(jk)^2 = \frac{1}{c_s^2} u_z\,(j\omega)^2 \tag{3.12}$$

$$k = \frac{\omega}{c_s} = \frac{2\pi}{\lambda} \tag{3.13}$$

3.1.3. Longitudinal shear waves

When a source of excitation is added as a transient term ($\mathbf{f}(r,t)$), the implications of Navier's equation (Equation 3.7) are extended.

$$(\lambda + \mu)\nabla(\nabla \cdot \mathbf{u}) + \mu \nabla^2 \mathbf{u} - \rho \frac{\partial^2 \mathbf{u}}{\partial^2 t} = \mathbf{f}(r,t) \tag{3.14}$$

In the near field, the distinction between displacement components based solely on being curl-free or divergence-free is no longer applicable, as there is a coupling of these terms.[11],[12] Although the two classic types of waves, compression and shear, can still be obtained, they can have any polarization. Longitudinal shear waves (LSWs) are a type of shear wave that travels at c_s with longitudinal polarization.

LSWs exhibit neither volumetric change nor particle velocity circulation during propagation, making them both curl- and divergence-free.

When a force is applied to the top of a material through a vertical vibrating source, the generated LSWs propagate along the depth direction (see Figure 3.2). This allows for the study of depth elasticity gradients by observing changes in wave velocity. An advantage of LSWs is that the imaging system can be aligned with the direction of propagation, facilitating the detection of displacements.

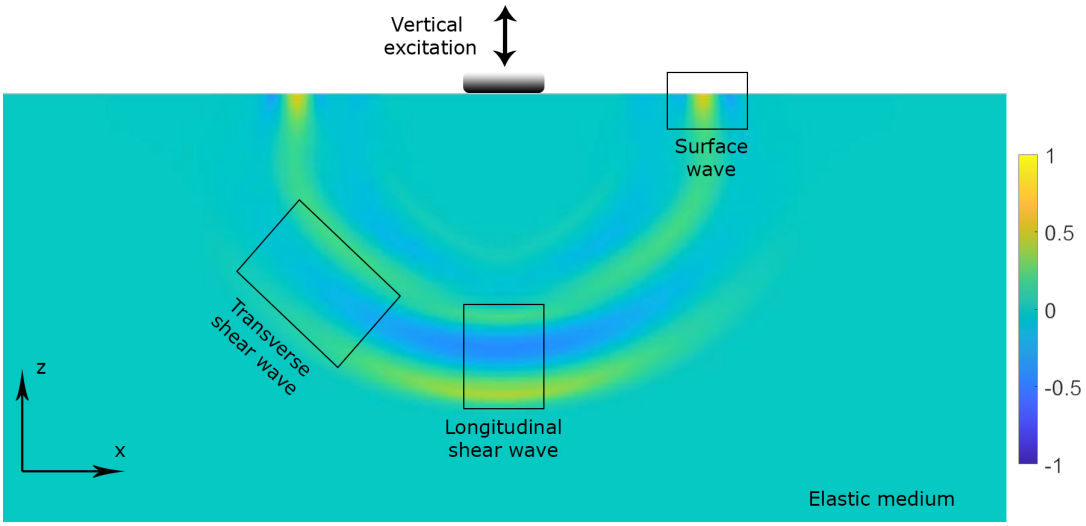

Figure 3.2. Numerical simulation on a semi-infinite elastic medium depicting different waves created after a vertical harmonic load applied on the surface. Different SWs are identified: waves traveling along the surface, transverse SWs, and longitudinal SWs.

3.1.4. Torsional waves

The concept of torsional waves was initially proposed by Reissner and Sagoci.[13] Torsional waves are SWs that propagate radially and in-depth through the medium, creating a pseudo-spherical propagation pattern. This laid the foundation for the development of a family of sensors based on the generation and reception of torsional shear waves in a solid medium.[14],[15] Torsional wave elastography (TWE) is an emerging technique that utilizes torsional waves for the viscoelastic characterization of several tissues.[16],[17] In TWE, torsional waves are generated using a rotational electromechanical actuator and then captured through a circumferentially aligned sensor (see Figure 3.3).

One of the advantages of torsional waves is its ability to isolate a pure shear wave, overcoming limitations associated with the separation of longitudinal and shear waves.[18] This is particularly beneficial when dealing with small organs like cornea or cervical tissue, where multiple reflections can occur.

The elastic propagation model of torsional waves is usually presented in cylindrical coordinates,[19] starting from Navier's equation (Equation 3.14). When axial symmetry is taken into account in the problem, certain simplifications are made. Firstly, the derivatives with respect to the angle θ ($\partial/\partial\theta = 0$) are neglected. Additionally, since torsional waves only involve rotational displacements, only displacements in the θ component are considered ($u_r = u_z = 0$). The remaining equations after simplifying the problem can be written as follows:

$$\rho \frac{\partial u_\theta^2}{\partial t^2} = \frac{\partial \sigma_{r\theta}}{\partial r} + \frac{2}{r}\sigma_{r\theta} + \frac{\partial u_{\theta z}}{\partial z} \tag{3.15}$$

$$\frac{\sigma_{r\theta}}{\partial t} = \mu \left[\frac{\partial v_\theta}{\partial r} - \frac{v_\theta}{r} \right]$$

$$\frac{\sigma_{\theta z}}{\partial t} = \mu \frac{\partial v_\theta}{\partial z}$$

where the variables (r, z, θ), follow the coordinate system shown in Figure 3.3, and v_θ is the time derivative of the displacement.

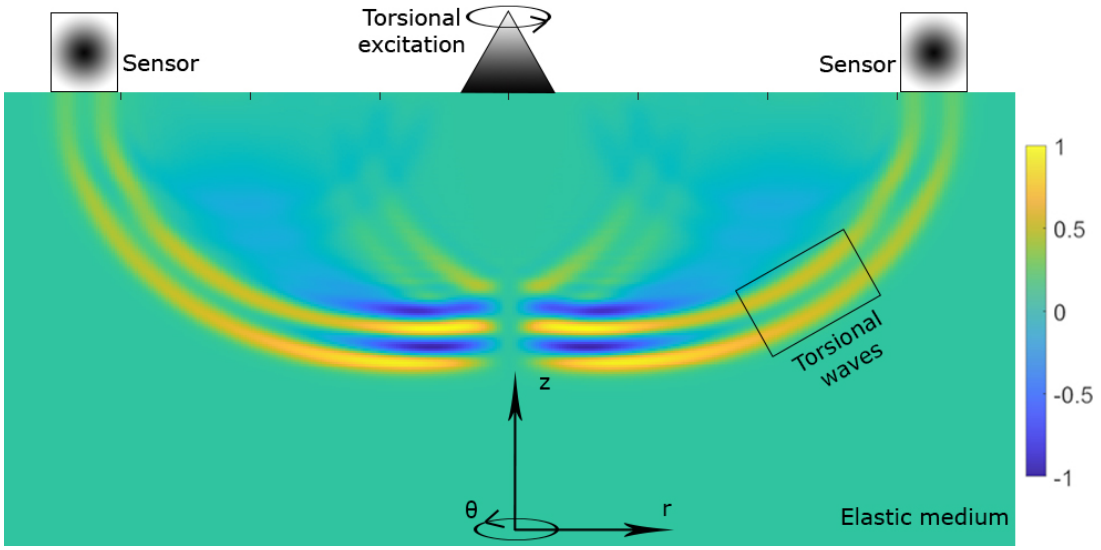

Figure 3.3. Numerical simulation on a semi-infinite elastic medium depicting torsional waves created after an harmonic rotational load applied on the top center and capturing sensors arranged symmetrically around the excitation axis.

3.2. Soft tissue viscoelasticity

Changes in tissue biomechanical properties have been extensively associated with physiological dysfunctions, representing structural alterations that disrupt the normal functionality of the tissue.[8],[20]–[22] The assessment of these changes holds the potential for early diagnosis and the development of more efficient and personalized treatments. The gold standard for mechanical characterization has traditionally been uniaxial tensile and compression tests. However, these tests are destructive in nature and make in-situ measurements challenging, especially in the case of delicate tissues that cannot maintain their functionality during testing.

Elasticity has been widely utilized as a biomarker. This is primarily due to the substantial differences in elasticity observed among different biological tissues, which are further altered in the presence of pathological conditions. As a result, high tissue contrast can be achieved.[8],[9],[23]

The first simplification commonly employed in modeling soft tissues is incompressibility, which arises from the high water content within the tissue. This property prevents significant changes in volume during deformation, they have a similar modulus of compressibility, and therefore $\lambda >> \mu$, leading to the consideration of a Poisson's ratio close to 0.5:

$$\nu = \frac{\lambda}{2(\lambda + \mu)} \approx 0.5 \tag{3.16}$$

The second simplification is isotropy, as accounting for tissue anisotropy poses challenges in formulating robust constitutive relationships. By assuming isotropy, researchers have been able to tackle more tractable problems, facilitating advancements in the understanding of the mechanical behavior of soft tissues.

$$\mu = \frac{E}{2(1 + \nu)} \approx \frac{E}{3} \tag{3.17}$$

E is the Young's modulus, and it describes how a material responds to an applied force or stress, indicating its resistance to deformation or stretching along the axis of the applied force. By measuring the SW velocity, E can also be obtained through $c_s = \sqrt{E/3\rho}$. Variations in μ or E are sufficient to detect changes, while λ has a negligible variation.[9] Figure 3.4 illustrates how the μ modulus extends over about eight orders of magnitude, while the K modulus has the same order of magnitude, similar to that of liquids such as water.

Equation 3.9, which directly relates SW velocity to the shear modulus, has been widely accepted as valid in numerous studies. However, it is important to note that the assumptions made to derive this equation are often not satisfied in the biomedical field. Various physical phenomena, including anisotropy and nonlinearity, among others, can significantly affect the validity of this expression. In our specific case, we are particularly interested in investigating the impact of viscoelasticity on the relationship between SWs and the shear modulus.

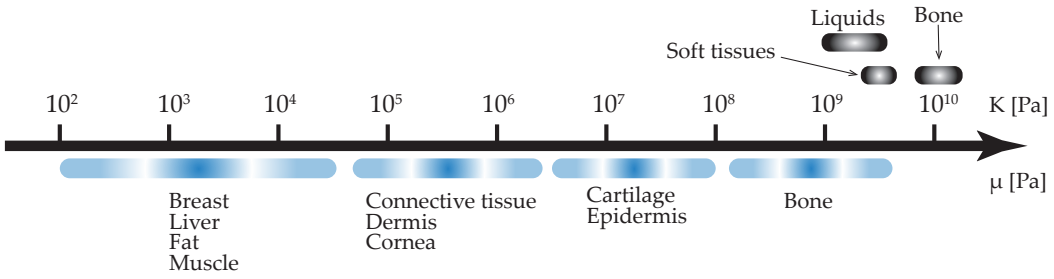

Figure 3.4. Approximate magnitudes of compression modulus K and shear modulus μ for different biological tissues.

Elasticity alone cannot provide a comprehensive understanding of organ pathologies and behaviors, necessitating the inclusion of additional parameters for improved characterization. Tissues exhibit viscoelastic behavior to varying degrees, and quantifying this behavior can provide more accurate diagnostic information.[2] This has been demonstrated in various organs such as the cornea,[24] breast tissue masses,[25] and hepatic tumor malignancy.[26]

Soft tissues exhibit both solid-like and fluid-like behavior. The solid-like behavior is characterized by elasticity, while the fluid-like behavior is represented by viscosity due to their high water content of over 70%.[8] Viscosity explains the delayed or hysteretic effect observed between stress and strain, as well as the tissue's ability to withstand deformation.[27] In a purely elastic medium, once the load causing stress is removed, the tissue returns to its original state. However, in a viscoelastic medium, if a constant strain is applied, a relaxation stress is observed, indicating the time-dependent response of the tissue. The complex modulus, denoted as G^*, provides a comprehensive measure of the material's resistance to deformation, given by the ratio of stress (τ) to shear strain (γ).[28],[29] In a purely elastic material, stress and strain are in phase, meaning they reach their maximum and minimum values simultaneously. In contrast, in a purely viscous material, stress and strain are 90° out of phase, with maximum stress occurring at the maximum shear strain rate.

Viscoelastic materials exhibit an intermediate behavior between pure elasticity and pure viscosity, resulting in a phase angle between the two states. This leads to the decomposition of the complex modulus into two components: the storage modulus (G') and the loss modulus (G''). In the complex plane, the complex modulus is represented as $G^* = G' + jG''$, where j is the imaginary unit.

The storage modulus (G') represents the elastic component, indicating the material's ability to store and recover energy during deformation. The loss modulus (G'') represents the viscous component, indicating the energy dissipation and irreversible deformation in the material. These moduli provide valuable information about the mechanical properties of the medium:

$$G^*(\omega) = G'(\omega) + jG''(\omega) = \rho \frac{\omega^2}{(k^*)^2} \tag{3.18}$$

where $\omega = 2\pi f$ is the angular frequency, with f the frequency, ρ the density, and k^* is the complex wavenumber.

One important parameter derived from the complex modulus is damping, quantified by the ratio G''/G'. Damping reflects the balance between the fluid-like and solid-like behavior of the material, indicating whether it tends to behave more like a fluid or a solid. Changes in damping can signify alterations in the viscoelastic nature of the material.

When studying the propagation of SWs, it is possible to perform both elasticity imaging and viscosity imaging, which provide information about the medium's elasticity and viscosity, respectively. These parameters are related to the velocity and attenuation of the SWs in the medium. The analysis begins with the Navier equation (Equation 3.7), which is an approximation based solely on physical assumptions. The presence of viscosity means that elastic waves are attenuated as a result of energy dissipation. Attenuation can be introduced as a damping term, and related to viscosity by means of a rheological model. Another option to include viscosity is to work in the frequency domain. Due to dissipation, G″ is no longer negligible. This term represents the viscous response, but it is not a viscosity parameter, that is why rheological models are needed to explain its relation to viscosity. After Fourier transformation into the frequency domain:

$$(\lambda^* + G^*)\boldsymbol{\nabla}(\boldsymbol{\nabla}\cdot\tilde{\mathbf{u}}) + G^*\boldsymbol{\nabla}^2\tilde{\mathbf{u}} + \rho\omega^2\tilde{\mathbf{u}} = 0 \tag{3.19}$$

where * indicate complex numbers, and $\tilde{\mathbf{u}}$ is the displacement in the frequency domain. The complex compression modulus $\lambda^* = \lambda' + j\lambda''$ represents the compression magnitudes in a similar manner as G*. In a pure elastic medium, $G^* = G'$ and $\lambda^* = \lambda'$, without a dissipation term. It is important to note that G* should not be confused with G′ or μ, as these parameters depend on the rheological model. In the case of purely elastic behavior, $G^* = G' = \mu$.[30]

If we consider the harmonic solution propagating in +x (1D) as a plane wave:

$$u(x,t) = U_0 e^{-j(k^* x - \omega t)} = U_0 e^{-j(k' x - \omega t) - k'' x} \tag{3.20}$$

Since all other variables are real positive defined, to introduce dissipation k* must be complex:

$$k^* = k' + jk'' = \frac{\omega}{\sqrt{G^*/\rho}} \tag{3.21}$$

where the dispersion relation is $k' = \frac{\omega}{c_{ph}}$, with c_{ph} the phase velocity, and the shear wave attenuation coefficient is $k'' = \alpha$ (m^{-1}). To estimate G*, which describes viscoelasticity by itself, independent experimental evaluation of c_{ph} and α from the displacement field is needed:

$$G'(\omega) = \rho\omega^2 \frac{k'^2 - k''^2}{(k'^2 + k''^2)^2} \tag{3.22}$$

$$G''(\omega) = -2\rho\omega^2 \frac{k'k''}{(k'^2 + k''^2)^2} \tag{3.23}$$

The variation of velocity with frequency in a viscoelastic medium commonly referred to as wave dispersion.[31] The dispersion phenomenon can be attributed to a combination of the poroelastic and microstructural properties that are governed by a complex fibrous multiscale in the medium.[32] The frequency variable has been employed for the estimation of viscoelasticity through phase velocity analysis.[33] However, it is essential to distinguish between the effects of guided waves and the influence of viscosity itself.[34]–[36] Additionally, it should be noted that dispersion can also arise from reflections occurring in media of comparable or lesser thickness.

3.2.1. Attenuation

In order to achieve a comprehensive rheological characterization of a material, including the determination of the storage modulus (G′) and the loss modulus (G″), it is necessary to estimate shear wave attenuation. Wave attenuation refers to the gradual decrease in the wave amplitude as it propagates through a medium with a certain frequency and over a certain distance. The variation of wave amplitude with distance can be ascribed mainly to both the geometrical spreading of wave energy and viscoelastic attenuation. The attenuation associated with viscosity can serve as a valuable biomarker. For instance, recently SWs have been observed in very low viscosity fluids,[37] so that the technique is being improved to evaluate media such as cysts.[38] Another example is when assessing the propagation of SWs in the liver, it enables accurate evaluation of the degree of fibrosis. However, it is important to consider that other

conditions such as inflammation or steatosis can also affect the velocity of these waves.[39] Viscoelasticity provides valuable information in such cases. One method to evaluate it includes SW dispersion, which involves measuring the linear slope of the phase velocity across a range of frequencies.[25],[33],[40],[41] Other method is SW attenuation, in which pathology adds or removes the viscous (lossy) component.[42],[43]

Several mechanisms contribute to the variation of wave amplitude with distance.

The observed attenuation can be attributed to energy absorption mechanisms. In the context of elastic wave propagation, energy is converted into heat, primarily due to the presence of inhomogeneities that are significantly smaller than the wavelength. In SW methods, the wavelength can be as small as 1 mm and the scale of cellular structures becomes crucial in energy absorption.

Scattering is another mechanism contributing to attenuation. Although the total energy remains conserved, it becomes scattered as a result of interactions with inhomogeneities, leading to a reduced amplitude of collected waves. Scattered waves lack coherence, and the energy becomes distributed across various phases, potentially causing dispersive effects. This behavior arises from the random distribution of scatterers within the medium. In medical ultrasound, scattering accounts for about 2-30% of attenuation at low frequencies.[44] Therefore, absorption is dominant, in the form of viscous losses.

Some of the quantities used to characterize attenuation are presented below.[10]

Attenuation per wavelength. It describes the attenuation per one wavelength of propagation.

$$\mathbf{A}(\omega) = \alpha(\omega)\lambda(\omega) = \frac{2\pi\alpha(\omega)c_{ph}(\omega)}{\omega} \tag{3.24}$$

Penetration depth. It defines the depth where the amplitude has fallen to a certain value. The damping term in the viscous equation is equaled to $e^{-\alpha x} = e^{-1} \approx 0.37$, and where this horizontal line cuts the envelope of the signal, $\delta_p(\omega)$ is obtained and normalized by λ.

$$\delta_p(\omega) = \frac{1}{\mathbf{A}(\omega)} \tag{3.25}$$

Log decrement. Logarithm of the ratio of two successive amplitudes in an exponentially decaying wave. In one λ, the wave decays $e^{\alpha\lambda}$.

$$\delta_{dec}(\omega) \approx \mathbf{A}(\omega) \tag{3.26}$$

Quality factor. It describes the energy loss per cycle, and its inverse Q^{-1} is an attenuation parameter, with higher values representing higher attenuation.

$$Q^{-1} \approx \frac{\mathbf{A}(\omega)}{\pi} \tag{3.27}$$

All of these quantities represent a common characteristic, which is attenuation (see Figure 3.5). The dependence $\mathbf{A}(\omega)$ on frequency implies that each frequency carries a different amount of energy. As a wave travels through a medium, changes in friction (relative motion) and viscosity cause a reduction in amplitude and lead to broadening of the wave's shape. Generally, high frequency components experience higher levels of attenuation and are more likely to be diminished. By plotting $\mathbf{A}(\omega)$ rather than just the attenuation, it becomes possible to identify frequency values at which waves are strongly attenuated, making them challenging to observe or causing them to cease propagation. These critical frequency values are referred to as frequency cutoffs.

The geometrical spreading mechanism accounts for the phenomenon where the energy of a wave becomes distributed over a larger area as it propagates. It is important to note that there is no loss of energy, but rather a decrease in energy density. Consequently, the intensity of the wave decreases as the distance from the source increases. It is important to address diffraction effects separately from the attenuation coefficient, as it is a distinct geometrical effect that requires correction.

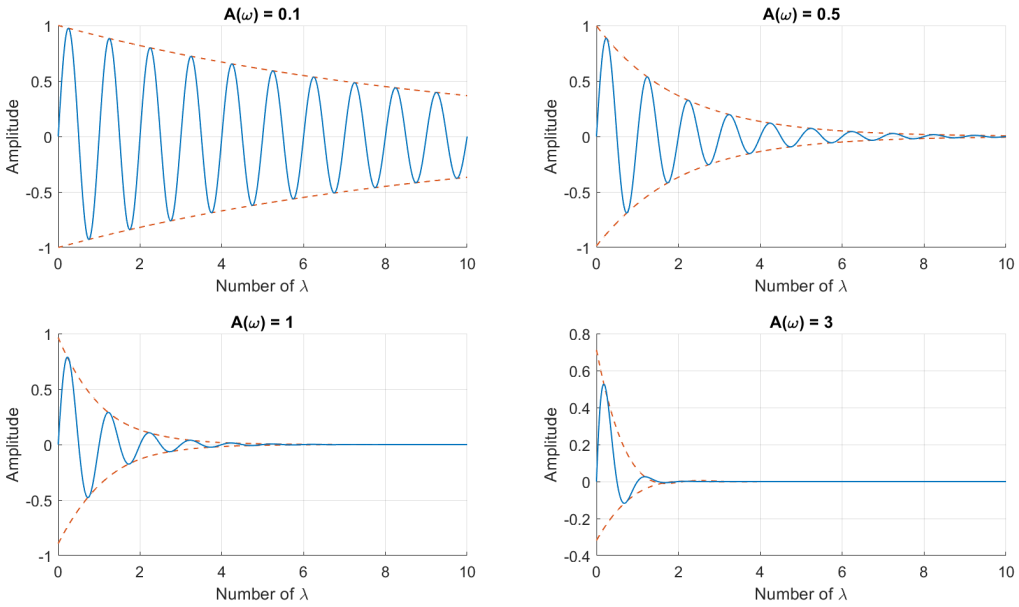

Figure 3.5. Effect of increasing $\mathbf{A}(\omega)$ on signals. Damped sinusoids are shown in where higher values of $\mathbf{A}(\omega)$ result in less oscillations until they are attenuated. When $\mathbf{A}(\omega) \approx 3$ there is barely 1 λ propagating.

Spherical wave solution. When the propagation exhibits spherical symmetry, as in the case of a point source, the problem becomes angle independent, and the governing wave equation transforms to:

$$\frac{1}{r^2}\frac{\partial}{\partial r}(r^2\frac{\partial u_s}{\partial r}) = \frac{1}{c_s^2}\frac{\partial^2 u_s}{\partial t^2} \tag{3.28}$$

where r is the distance from the source. By applying the Fourier transform its harmonic solution is obtained:

$$u(r,t) = \frac{U_0}{r}e^{j(\omega t - kr)} \tag{3.29}$$

where U_0 is a real constant.

Cylindrical wave solution. When the propagation exhibits cylindrical symmetry, as in the case of a line source, the problem becomes angle and height (z) independent, and the governing wave equation transforms to:

$$\frac{1}{r}\frac{\partial}{\partial r}(r\frac{\partial u_s}{\partial r}) = \frac{1}{c_s^2}\frac{\partial^2 u_s}{\partial t^2} \tag{3.30}$$

with a harmonic solution:

$$u(r,t) = \frac{U_0}{\sqrt{r}}e^{j(\omega t - kr)} \tag{3.31}$$

The solutions for spherical and cylindrical waves exhibit similarities to the solution for plane waves. However, there are distinct differences arising from the inclusion of attenuation factors $1/r$ and $1/\sqrt{r}$. These factors account for the spreading of energy over a larger area as the waves propagate away from the source. When waves are assumed to propagate in a spherical or cylindrical geometry, it is necessary to apply these correction factors to the displacement field. By doing so, the effect of geometric attenuation is appropriately considered, accounting for the spreading and diminishing of energy as the waves propagate through space. When the effects of wave diffraction are minimized, it is possible to focus on the evaluation of viscosity-related attenuation.[42] This approach has facilitated model-independent quantification of G*.[45] Furthermore, viscosity maps can be obtained without the need for specific geometric assumptions.[46]

3.3. Deviations from the elastic model

Various scoring systems have been proposed to facilitate clinical diagnosis using elastography.[47] However, maintaining a standardized approach proves challenging, as noted in the review article by Sigrist et al.[48] The characterization of shear modulus in the same tissue exhibits variability, partly due to differences in methodologies employed by commercial equipment and the presence of contrast mechanisms. These factors contribute to the impracticality of achieving complete standardization. Soft tissues are nonlinear viscoelastic, due to their mechanical properties that vary with deformation and strain rate.[49] Similarly, components in soft tissues exhibit inherent directional anisotropy, which arises primarily from the variations in the morphology of the crosslinked fiber network.[50] As a result, the stress experienced at a particular point within the tissue is influenced not only by the gradient of deformation but also by the orientation, connectivity, and distribution of its components.

These situations will not be detailed in depth but are introduced because of their relevance to the interpretation of results.

3.3.1. Anisotropy

The mechanical behavior of tissues varies depending on the direction of analysis. For instance, muscles consist of fibers that are oriented in different directions based on their specific functions. This inherent anisotropy in muscle structure leads to variations in mechanical properties, such as the velocity of SWs, depending on their polarization relative to the fiber orientation. As a result, direction-dependent mechanical models need to be established, reflecting the influence of tissue anisotropy on the propagation of mechanical waves.[51],[52] When ignored, the sensitivity of the technique can be reduced in direction-related pathologies.[53]

3.3.2. Nonlinearity

The interest of nonlinearity lies in the observation of different mechanical parameters in the presence of a pathology, which is related to changes in composition and structure.[54],[55] In collagenous tissues there is uncrimping and then straightening of the fibrils when they are stretched.[56] The linear viscoelastic regime is limited to strains less than 1%.[2] The linear viscoelastic models are only valid here, which is also where dynamic elastography works. Therefore, one of the origins of nonlinearity can be founded on the observation of nonlinear strain responses (high strains). Acoustoelasticity focuses on the influence of static preloads on wave propagation velocities. In this context, nonlinear coefficients are introduced and experimentally measured to model this phenomenon within a nonlinear framework.[57],[58] This assumes that measuring a tissue with a preload state influences the measured μ, which becomes what is called an apparent parameter.

The second origin of nonlinearity arises from nonlinear acoustics, which occurs when the effect of the propagating wave cannot be treated as a small perturbation. The considerable hyperelasticity observed in soft tissues, related to variations in the elastic modulus, can result in measurable shear wave harmonic generation.[59],[60]

3.3.3. Porosity

It is commonly assumed that the medium consists of a single-phase solid material. However, when this solid medium contains a network of interconnected blood vessels, it becomes a two-phase material. This is the case of organs like the liver, which can be regarded as a porous material or sponge filled with blood. Under dynamic excitation at low frequencies, an inflow or outflow of the fluid phase can be induced. These porosity effects are particularly noticeable at frequencies lower than 30 Hz, and they become dominant at 1–2 Hz.[61] The biphasic formulation is widely employed to describe fluid motion occurring within a solid.[62] This formulation involves the derivation of separate equilibrium equations for each phase,

and interaction forces are introduced. In the context of the poroelastic approach, the solid and fluid are considered as components of a homogeneous material. A fluid flow law is introduced to represent the ability of the fluid to permeate through the porous solid, thereby accounting for the fluid's behavior within the solid matrix. In its equilibrium equation a tissue porosity, the displacement field for the solid and fluid phase, as well as solid and fluid densities are introduced. Vena and Royston[63] detected two types of compression waves. The fast wave velocity increased with frequency until reaching a plateau. The slow wave presented a lot of attenuation due to the response lag between the solid and fluid parts, which would make it difficult to observe experimentally. Aichele et al.[64] they also detected two shear waves with distinct velocities. This scenario implies that the direct measurement of elasticity solely from the solid phase is challenging due to the influences of factors such as porosity and viscosity of the liquid phase.

3.3.4. Guided waves

The previous descriptions are based on the assumption of infinite media, where wave interactions with the surrounding geometry are negligible. However, in finite media, waves begin to interact with boundaries, which impose boundary conditions and give rise to additional types of waves beyond volume waves. There are numerous types of guided waves with specific names according to the polarization conditions, and associated with them an expression of velocity.[65] When waves propagate along a solid-air interface, they are known as Rayleigh waves. These waves have limited penetration depth (approximately 1 λ) and exhibit velocities similar to volume SWs. The velocity of surface or Rayleigh waves:[66]

$$c_R = c_s \frac{0.87 + 1.12\nu}{1 + \nu} \quad \rightarrow \quad \nu \approx 0.5 \quad \rightarrow \quad c_R \approx 0.95 \cdot c_s \tag{3.32}$$

with c_s the volume SW velocity.

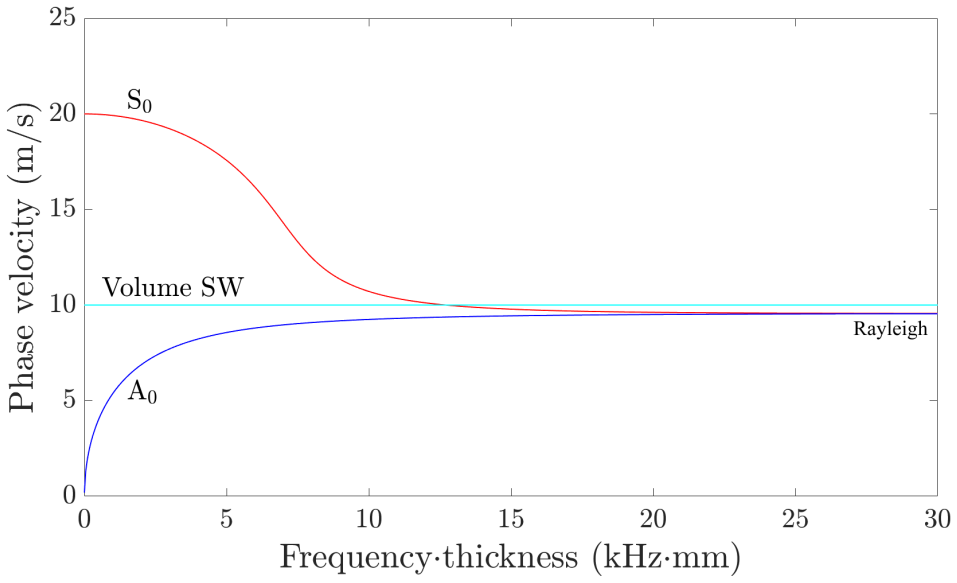

Figure 3.6. Dispersion curves of Lamb modes on a 1 mm soft solid plate. The phase velocity for each guided mode is presented as the product frequency and the thickness of the plate. The compression and shear velocity are $c_p = 1540\text{m/s}$ and $c_s = 10\text{m/s}$, respectively.

When the medium takes the form of a plate, with one dimension similar or smaller than λ, guided modes called Lamb waves are observed. Lamb waves propagate along the plate but experience constant reflections at the edges. This results in changes in polarization and complex propagation modes. In elastography, the most extensively studied Lamb wave modes are the first symmetric (S_0) and antisymmetric (A_0) modes (see Figure 3.6). The velocity of these modes depends on the relationship between the frequency and size of the medium. Moreover, they exhibit significant dispersion, even in elastic media. In the

case of volume shear waves, their dispersion is associated with the viscoelastic properties of the medium, making them ideal for characterization. Lamb waves behave differently at low frequencies, since A_0 tends to 0 while S_0 tends to a value higher than c_s. When the frequency–thickness product is increased, both tend to the Rayleigh velocity, and therefore the dispersion will no longer depend on the geometry. Hence, developing novel methods for generating and tracking SWs while considering the underlying geometry can significantly simplify the models utilized and the assumptions to be taken into account.

Several studies have attempted to model these waves to expand the potential of elastography in ophthalmology,[67],[68] arteries,[69],[70] tendons,[52],[71] or cardiology.[72],[73]

3.3.5. Validity of traditional assumptions

It is important to keep in mind the validity of some assumptions that are always taken as true.

Continuum. Structures such as blood vessels, membranes and other discontinuities may have wavelength dimensions in violation of this assumption.

Homogeneity. It is possible for properties to vary within an organ, which can occur due to physiological functions where the structure adapts to fulfill different roles or as a result of abnormalities such as tumors.

Incompressibility. While the wave equation remains independent of these variations, they do impact the relationship between velocity and mechanical properties.

Fluid content. The tissue is typically assumed to be a single-phase material, disregarding changes in water or fluid content and assuming no transport. However, in conditions such as edema, fluid accumulation occurs, which can affect μ. Studies have observed an increase in μ in muscles after physical exercise.[74]

3.4. Ultrasonic testing

Since the late 1940s, the material industry has been subject to quality standards to ensure optimal performance in challenging situations and specific environments, as well as to ensure longevity and reliability. Maintaining structural integrity and withstanding different types of loads are essential requirements for materials. Therefore, it is crucial to characterize their mechanical properties and detect defects without causing damage. Non-destructive testing comprises a set of non-invasive techniques that are cost-effective and provide information about the interior of a material without altering its integrity.

Over time, the presence of defects or changes in specific properties can cause the material to deviate from its expected behavior, leading to a pathological state. The impact of this state on performance can range from being within acceptable tolerance limits to potentially catastrophic failure. Detecting these deviations at an early stage is crucial for preventing short-term and long-term failures, as it allows for planned rehabilitation or intervention.

Among the various non-destructive testing techniques, ultrasonic inspection is widely used. Ultrasonic waves, which are mechanical waves with frequencies above the upper limit of human hearing (typically above 20 kHz), are employed in this technique. Ultrasonic inspection offers several advantages, including safety, non-ionizing properties, portability, and cost-effectiveness. It has proven to be effective in identifying pathologies based on mechanical and geometrical parameters, particularly in isotropic and homogeneous materials.

The applications of ultrasonic inspection include the detection of discontinuities, leaks, and corrosion, as well as thickness control and measurement.[75] Additionally, the technique enables the characterization of physical properties of materials by leveraging the known relationship between wave velocity and elastic modulus (Equation 3.8).

3.4.1. Ecography

When obtaining images of the human body's interior using a principle similar to echolocation, the technique is known as echography or ultrasound imaging. The physical principle underlying this technique is based on the concept of acoustic impedance ($Z = c \cdot \rho$), which can be understood as the ease with which sound waves propagate through a material. It is defined as the product of the wave propagation velocity c and the density of the material ρ. When ultrasound waves encounter an interface between two media with different acoustic impedances (Z), a portion of the wave energy is transmitted through the interface, while another portion is reflected back. This reflected wave is commonly referred to as an echo. By measuring the time it takes for the echo to return (known as time of flight) and knowing the wave velocity, information about distances can be obtained.

To create an ultrasound image, ultrasonic waves are generated and received by a transducer, which is typically made of piezoelectric materials. Piezoelectric materials exhibit electrical polarization when subjected to deformation and can deform proportionally to the applied electrical voltage. In a typical ultrasound probe, an array of 128 piezoelectric elements is arranged in a flat linear or curved configuration. The probe is placed in contact with the body near the target tissue. By applying alternating voltages to the piezoelectric elements at frequencies in the MHz range, they vibrate and generate ultrasonic waves that propagate into the body. These waves travel several centimeters before experiencing significant attenuation. As the waves encounter interfaces within the body, they are reflected back, and the mechanical energy is converted back into electrical voltage.

To reconstruct the received energy information for each piezoelectric element at each moment, beamforming algorithms are employed.[76] These algorithms help in forming the ultrasound image and provide details about the structural organization of the imaged area. The resulting image also exhibits echogenic contrast or echogenicity, which is represented by varying brightness levels for different points in the image. This brightness describes the intensity with which the waves are reflected from different scatterers and interfaces (see Figure 3.7). For instance, regions containing water will appear as completely black in the image. Increased echogenicity, observed as increased brightness, has also been utilized as a diagnostic tool, such as in detecting fatty liver conditions.[77]

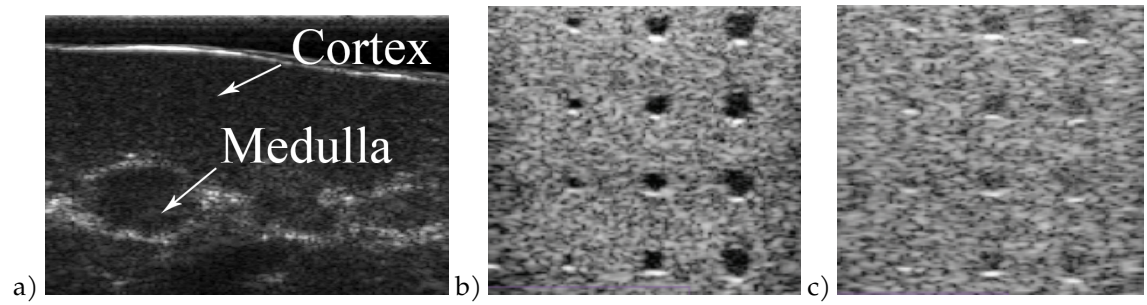

Figure 3.7. a) Kidney ecography in which the cortex and medulla are recognized. b) Focused ecography of a calibration phantom at 25 Hz. c) Ultrafast ecography using one plane wave on the same calibration phantom at 18 kHz.

In the past, the quality of ultrasound images has been improved by focusing the waves in a changing region, reconstructing them line by line, and then combining them to form the final image. However, this sequential acquisition process typically results in a low acquisition rate, usually less than 100 Hz, which is influenced by the imaging depth. To overcome aliasing effects and capture fast phenomena, ultrafast echography using plane waves has been developed.[78] With this technique, the entire field of view is illuminated by a single ultrasonic pulse, enabling acquisition rates of up to 20 kHz. However, the downside of this approach is that the acoustic energy is no longer localized in a specific region, leading to a degradation in image quality. This is illustrated in Figure 3.7b,c. To mitigate this loss of quality, an addition called angle compounding was proposed.[79] In this method several acquisitions are combined at different angles with respect to the transducer axis. An acquisition rate of several kHz is maintained and image quality is improved.

It is important to recognize that ultrasound is a compression wave, and its behavior is closely linked to the bulk modulus (K). While compression waves provide valuable information about tissue morphol-

ogy, they do not provide quantitative data on the mechanical properties of tissues. The bulk modulus K governs the propagation of compression waves, but it remains relatively consistent across different tissue types. Consequently, relying solely on echogenicity, which is based on changes in acoustic impedance, may not always be effective for diagnosing pathologies since such changes are not always present.

To address this limitation, more reliable and accurate imaging techniques, such as elastography, have emerged in the field of ultrasound testing. Elastography enables the assessment of tissue mechanical properties, which can be invaluable for diagnostic purposes.[8] This technique can be applied to study any deformable tissue, and ongoing advancements in technology are continually enhancing its capabilities. Elastography provides a diagnostic contrast by measuring the mechanical response of tissues, offering a more comprehensive understanding of tissue characteristics beyond what can be observed through echogenicity alone.

3.5. Dynamic elastography

For centuries, medical practitioners have relied on palpation, using their hands to assess tissue elasticity by applying slight pressure. This qualitative technique has been used to identify abnormalities or pathologies based on the perceived resistance of the tissue. However, palpation is a subjective practice and is limited to superficial tissues. The ability to quantitatively reproduce the clinician's palpation is known as stiffness, and elastography serves as a valuable diagnostic tool when palpation is utilized or intended to be used.

Dynamic elastography is a medical imaging modality that aims to probe and visualize the mechanical properties of soft tissues, including organs, muscles, and tendons, for diagnostic purposes. It combines an imaging principle, such as ultrasound (USE), Magnetic Resonance Imaging (MRI), or optical imaging, with one or more excitation sources that generate SWs in the tissue under investigation. This is why it is sometimes referred to as SW elastography (SWE). SW methods offer two significant advantages. Firstly, the local SW velocity can be estimated and related to various mechanical parameters. Secondly, the direct relationship between SW velocity and mechanical properties eliminates the need for complex stress distribution calculations. Various algorithms are available to reconstruct elasticity maps[48],[80] and, more recently, other properties such as viscosity,[46] using raw shear wave propagation data.

In contrast, static elastography, although widely used in detecting elasticity abnormalities in breast imaging, is being less favored. This is primarily due to challenges in transmitting stress to deep organs, the presence of artifacts, and the limited ability to report absolute deformation without knowledge of the applied stress.[81],[82]

3.5.1. The evolution of dynamic elastography

In the 1950s, Gierke et al.[83] conducted an analysis of SW propagation in soft tissues using optical methods. They discovered that SWs propagated at a significantly lower velocity compared to compression waves, which became a crucial characteristic for elastography development. Compression waves could track the displacement field generated by SWs, and the substantial velocity difference allowed for achieving high temporal resolution. In the 1980s, Krouskop et al.[84] materialized this concept by using a vibrator to generate SWs and an ultrasound pulse Doppler system to detect particle motion. They quantitatively estimated muscle elasticity based on the displacement amplitude at specific points. Parker et al.[85] made one of the initial attempts to create a qualitative 2D elasticity map.

In the late 1990s, Catheline et al.[86] demonstrated the feasibility of quantifying SW propagation velocity using a plane wave ultrasound system. They collected signals generated by a piston in contact with the medium using an ultrasonic transducer. To effectively capture a propagating front, the SW had to travel in the lateral direction. Furthermore, wave velocity was used to deduce mechanical properties in soft gels. At the same time, the first quantitative 2D elasticity maps were presented.[87] In parallel, Sarvazyan et al.[9] proposed a remote SW generation method called shear wave elasticity imaging (SWEI), which relied on the acoustic radiation force (ARF) of a focused ultrasound beam.[88] This technique produced transient SW pulses that propagated laterally from the focus point, and the front wave was tracked. The generated SW were broadband, and by retrieving different frequency components, viscoelastic parameters could be

derived.

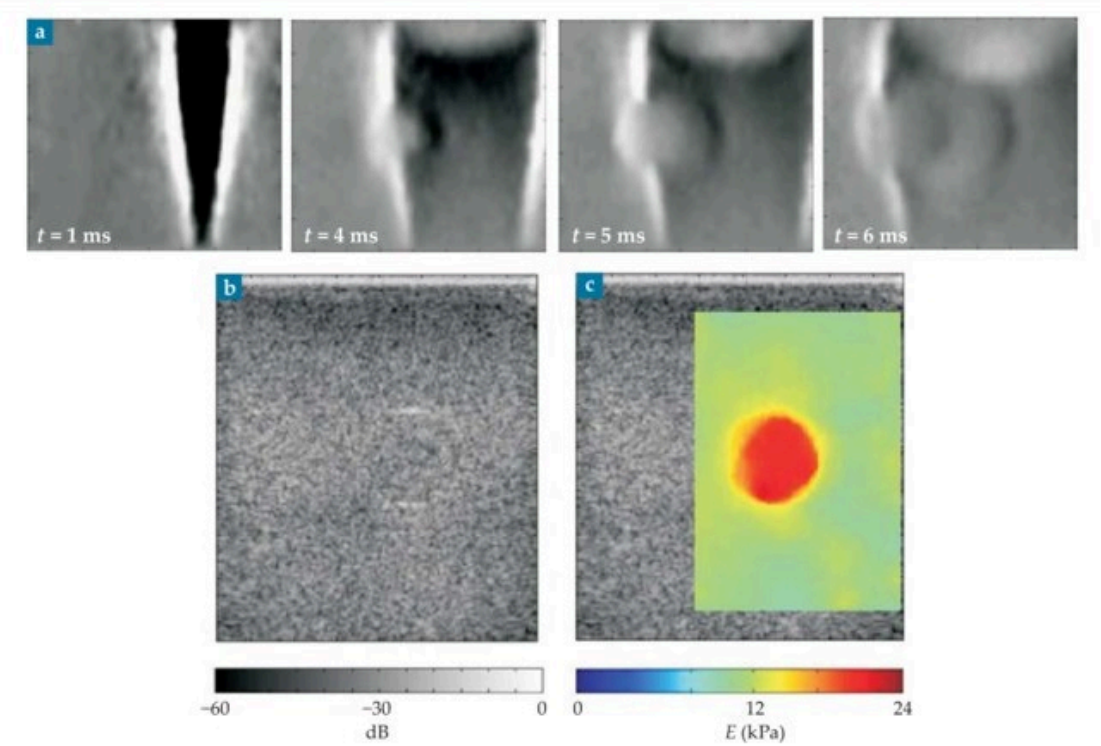

Figure 3.8. a) Snapshots of SW propagation after SSI excitation in a phantom. The wave is sensitive to the different mechanical properties of the inclusion. b) A conventional ecography image barely shows the boundaries of the inclusion. c) Elasticity map representing the Young's modulus and clearly identifying the inclusion. Adapted from.[89]

The first commercialization of dynamic elastography occurred in 2003 and was known as transient elastography due to the impulse nature of the generated SWs.[90] It involved performing a dynamic compression on the skin with a probe, followed immediately by ultrasound imaging along the axial center line. Transient elastography has been applied in the staging of liver fibrosis and breast imaging.[81],[91] By quantifying the group velocity of the SWs and assuming homogeneity and isotropy, the shear modulus can be estimated, providing a measure of global elasticity that is related to different pathological states. However, transient elastography has limitations, such as the lack of structural imaging for guidance and strong wave attenuation in obese patients, which may affect the reliability of the measurements.[91],[92]

The next advancement in elastography was the development of supersonic shear imaging (SSI).[93] SSI combined the impulse technique with ARF excitation. It used an ultrahigh-speed scanner and triggered multiple ARFs consecutively at different depths. Each ARF served as a source of SWs that constructively interfered, creating a quasi-plane propagation front. The same transducer generated the SWs and tracked tissue displacement. The reconstructed 2D elasticity maps from SSI could be superimposed on conventional ultrasound images, allowing for improved identification of the regions of interest (see Figure 3.8) .

Elastography techniques, including transient elastography and SSI, have primarily focused on evaluating elasticity through the Young's modulus ($E = 3\mu = 3\rho c_s^2$). While some studies have explored the viscoelastic properties of breast lesions,[41] muscles,[94] and the liver,[95] these approaches have not yet been validated in large cohorts. There is ongoing research to enhance the precision, resolution, and expand the applications of elastography measurements. The goal is to eventually replace biopsy, as elastography offers a noninvasive and safe alternative for examining soft tissues in vivo while preserving their functionality.[96] Biopsy involves risks such as bleeding, infection, and pain. Although elastography alone cannot currently diagnose the malignancy of a lesion, it can provide valuable information that helps reduce unnecessary biopsies.[97]

However, there are still challenges in USE. Significant variations have been observed in measurements from different research and clinical manufacturers, with biases mainly attributed to depth.[98] The stiffness of the interrogated areas also affects the signal-to-noise ratio (SNR), with stiffer areas yielding lower SNR.[99] SW dispersion due to viscosity can impact the group velocity and its relationship to the shear modulus. The inclusion of parameters such as viscosity and nonlinearity in clinical practice has been limited due to the different ways data are analyzed and presented. There is a lack of consensus and established protocols, including variations in frequency selection and different models of nonlinearity. Overcoming these challenges and establishing standardized approaches are necessary steps for further advancing elastography as a reliable and comprehensive diagnostic tool.[96] More specifically, it would be necessary to compare velocities calculated by different systems without transformations to other units, using the same parameters and equal frequencies for phase velocity.

3.5.2. Magnetic Resonance Elastography

In parallel to the advancements in USE, MRI-based elastography (MRE) emerged in the 1990s.[100] This technique utilizes low-frequency vibrations to induce displacements caused by propagating SWs. By employing phase-contrast-based MRI, the material properties of the tissue can be calculated. MRE has been primarily applied in the staging of liver fibrosis[101] and has shown promise in other applications such as brain imaging, where ultrasound may be limited (see Figure 3.9). It offers several advantages, including the ability to perform 3D scanning of the displacement field, providing highly detailed characterization, and excellent spatial sensitivity to capture displacements accurately.

However, MRE has some drawbacks compared to USE. It has longer scanning times and poorer temporal resolution, with acquisition rates typically in the range of a few hundred Hz.[102] Despite these limitations, it has seen significant research and development, leading to a comprehensive field of study. The details of these advancements and applications are beyond the scope of this response, as several review papers are available that cover these topics extensively.[103],[104]

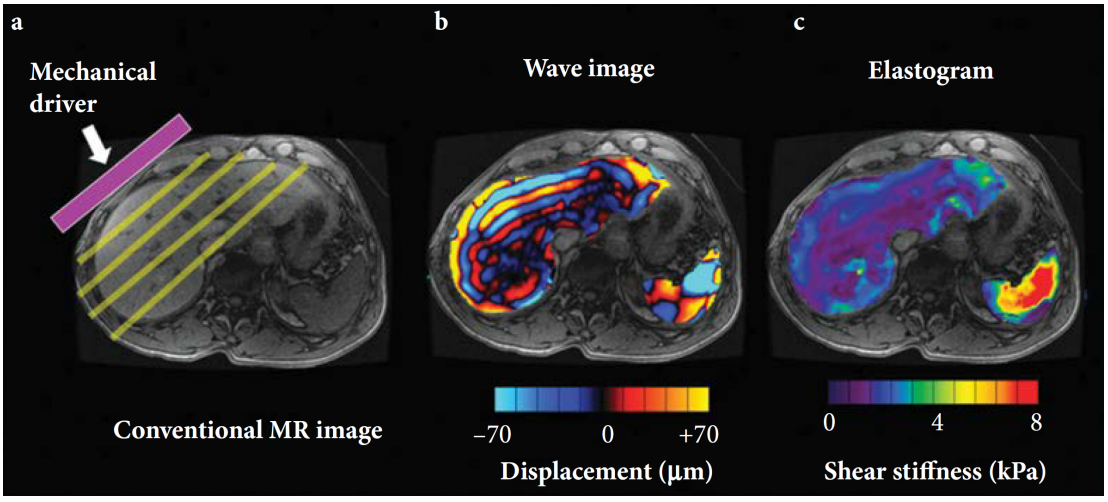

Figure 3.9. a) MRI of the brain. b) MRE results showing the transmitted SWs form the vibration source on the side its displacement amplitude. c) Elasticity map reconstructed from SW propagation. Adapted from[101]

3.5.3. Optical Coherence Elastography

Another method of dynamic elastography utilizes Optical Coherence Tomography (OCT) as the imaging modality.[105] OCT is based on optical contrast and provides structural imaging of tissues. In OCT-based elastography (OCE), displacement detection is achieved through optical interference between a reference beam and a reflected beam in the sample being measured. OCE offers micrometric spatial resolution (1-

10 μm) and nanometric displacement sensitivity, which are significant advantages compared to USE and MRE.[106] The acquisition rate in OCE can range from 10-200 kHz, enabling the imaging of micromechanical properties of the tissue.[107]

One limitation of OCE is its limited penetration depth, typically not exceeding 1–2 mm, and its susceptibility to surface and boundary effects.[108] OCE is also more sensitive to heterogeneities such as microvasculature, and the medium is no longer considered a continuum as it is in MRE or USE, where these features are averaged due to lower resolution.[109] OCE has demonstrated various propagation modes, including longitudinal and transverse SWs, Rayleigh waves, and Lamb waves, and efforts have been made to relate these modes to the microstructure of the tissue.[24],[110] Numerous methods of generating waves within the tissue and various acquisition protocols have been proposed in OCE. While a detailed discussion of the recent advances in this field is beyond the scope of this response, recent review articles provide comprehensive coverage of the topic.[107],[109]

The high resolution of OCE combined with the transparency of the eye have made OCE an interesting tool to focus on numerous studies (see Figure 3.10). The viscoelastic properties of the cornea have been studied ex vivo in pigs,[111] and the layered structure of the cornea has been observed for the first time through velocity maps.[112] In vivo human studies have also been performed.[113]

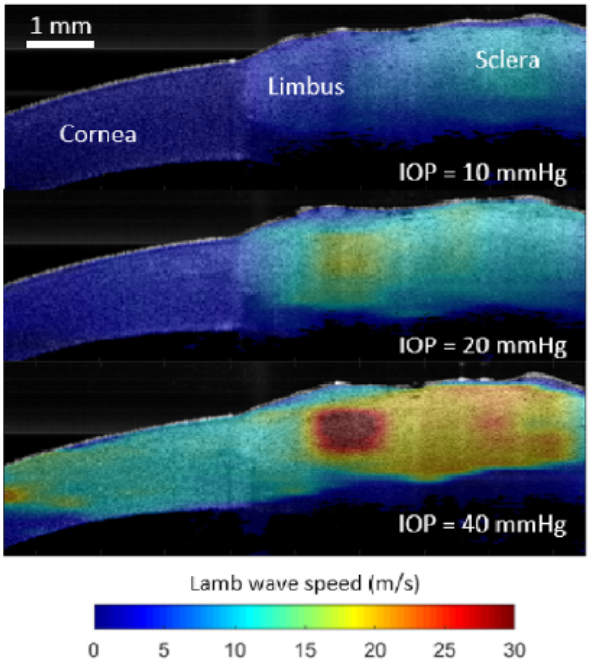

Figure 3.10. OCE results showing the SW velocity of the anterior porcine eye when the intraocular pressure (IOP) changes. Due to the thin geometry, the propagation mode is a Lamb wave. Adapted from[114]

3.5.4. Shear wave sources

There are numerous sources that can be used for SW generation. These include mechanical excitation by direct contact, acoustic, electromagnetic, or optical.[115]

Mechanical excitation. This is the simplest method where the vibration is transmitted by direct contact. The most common approach is through dynamic compression, in which a shaker in contact create a transient impulse or harmonic waves. Depending on the contact conditions, shear or compression waves can be generated that propagate, with a front that is usually not plane, with different properties.[80] This has been used with MRE[100] and OCE.[111],[116]–[118] One drawback of utilizing a shaker or a piezoelectric-connected element is that they depend on multiple parameters of the emitting device. Since the emission

is not easily controllable, it can act as a vibration filter, introducing uncertainties. Overcoming this challenge requires a robust analysis method that focuses on the captured response.

Acoustic excitation. The primary method used in this context involves the utilization of acoustic radiation force (ARF). ARF is a mechanism through which momentum is transferred between an acoustic wave and the medium. The medium in question should possess both absorbing and reflecting properties.[119] When the acoustic wave interacts with the medium, it creates a shearing effect, resulting in the displacement of its neighboring regions. This displacement then propagates laterally as SWs. A simplified expression considering only viscosity is commonly used to calculate the force magnitude[120] $F = \frac{2\alpha I}{c}$, with α the acoustic absorption, c the speed of sound, and I the temporal average intensity of the acoustic focus. However, it has been shown that using this expression can result in an lower order of magnitude force. This difference stems from the constitutive nonlinearity of the fluid, understood as a deviation from Hooke's law, which adds a parameter of nolinearity β.[121] The main advantage of this method is that the push can be focused within tissues, and stress can be generated locally. Being a relatively weak effect, the displacements generated are only a few microns, which helps the assumption of linearity. On the other hand, depending on the properties of the tissue, the SNR can worsen, due to a low magnitude of displacements, which would affect the reconstruction algorithms. Due to hardware and diagnostic limitations in tissues it is difficult to increase the intensity of the effect to avoid noisy results.[81]

Optical excitation. It is based on light absorption and scattering. In the photoacoustic effect, the tissue absorbs energy from optical beams, that is, light waves. Then there is thermal expansion that releases energy as acoustic waves. One of the approaches has been called photoacoustic viscoelasticity imaging.[122] One problem is that overabsorption can lead to phototoxicity and tissue damage.

Electromagnetic excitation. There are methods that rely on the Lorentz force phenomenon, where the application of current in a conductor within a magnetic field causes it to move and generate SWs, particularly at low frequencies (< 1 kHz). Ultrasound[123] and MRI[124] were used for imaging. Another proposed alternative involved the combination of the Lorentz force and surface contact by vibrating metal plates using an alternating magnetic field. This resulted in the generation of a bipolar front, which was attributed to the polarity change of the magnetic force acting on the plate.[125] It should be noted that in close proximity to the excitation source, these techniques may encounter challenges in accurately reconstructing displacements. This is primarily due to the constant interferences caused by the moving elements in the vicinity.

Magnetomotive ultrasound (MMUS) is a technique that involves the incorporation of magnetic nanoparticles into the medium under investigation. These nanoparticles are then displaced by a magnetic gradient, resulting in the generation of SWs that can be detected using US imaging. Typically, a tone burst is applied during the excitation process, and the magnetic force can be precisely controlled by determining the magnetic flux density in conjunction with its spatial gradient.[126]–[128] One notable advantage of MMUS is that the force exerted on the nanoparticles is modulated at twice the excitation frequency. This characteristic can be exploited if sufficient resolution is available to obtain a wide dispersion curve, providing valuable insights into the mechanical properties of the medium being examined.

3.6. Towards dynamic micro-elastography

In the biomedical field, the measurement of mechanical properties at the microscale holds significant importance. The mechanical properties of cells play a vital role in determining their function and behavior. By quantifying these properties, researchers can gain insight into the underlying mechanisms of different diseases and disorders, aiding in the development of novel treatments and therapies.[129] Similarly, microscale mechanical testing of biomaterials utilized in medical implants or regenerative medicine, contributes to enhancing the design and performance of such biomaterials, ultimately leading to improved medical interventions.

From a technical point of view, recent biomedical applications in ophthalmology, oncology, cell mechanics, and regenerative medicine are requiring submilliter-scale spatial resolution and temporal resolution of tens of kHz. Although the development of USE and MRE is making them popular clinical imaging

technologies, they have limited spatial or temporal resolutions. At their best setting, their spatial resolution can reach 200 μm, and their temporal resolution remains below 10 kHz, making it difficult to capture viscoelastic behavior in the microscale.[130],[131] To move in this direction, dynamic elastography methods are relying on the improvement of imaging modalities and new sources of SW generation. By enhancing the spatial and temporal resolution of these characteristics, it becomes possible to transition to smaller scales.

3.6.1. Mechanical properties at the microscale

At the microscale, tissue elasticity is primarily influenced by the cells and the extracellular matrix (ECM). Cells consist of various components, including the cell membrane, cytoplasm, and cytoskeleton. The cytoskeleton, in particular, provides mechanical stability and contributes to cell morphology. It plays a crucial role in determining the mechanical properties of cells and their response to external forces. It is important to note that tissue elasticity can vary depending on the specific context and scale of observation. For instance, in the case of malignant breast tumors, the surrounding tissue has been reported to feel stiffer compared to healthy tissue.[81] However, it has also been observed in certain cases that cancer cells themselves can be softer than healthy cells.[132] This discrepancy highlights the significance of the observation scale when considering tissue elasticity.

It has been observed that changes in the microstructure occur during tumor progression, resulting in stromal stiffening. This increased stiffness is associated with a higher risk of tumor development, including the formation of spheroids, as well as increased drug resistance.[133] Furthermore, it was found that cancer cells specifically invade an ECM with a controlled stiffness. This finding has important implications for targeted drug administration, as it allows for the delivery of drugs directly to cancer cells while minimizing the impact on healthy cells.[134]

The influence of the mechanical microenvironment on cell functioning and different behaviors is a subject of significant interest in current research.[135]–[137] The elasticity of the microenvironment plays a significant role in crucial processes such as cell division and apoptosis, as well as cell proliferation and drug sensitivity.[138] Additionally, precise control of mechanical properties is indeed crucial for regulating cell lineage,[135] and cell migration guided by elasticity, known as durotaxis.[139] There is evidence supporting the notion that cells have the ability to sense and respond to mechanical stimuli in their environment. This process is known as mechanosensing and is vital for maintaining proper cellular function and tissue homeostasis.

In order to study cell behavior and applications in regenerative medicine and tissue engineering within a controlled setting, developing an in vitro medium that mimics the mechanical properties of the native tissue where the cells reside, researchers can investigate the effectiveness of therapeutic methods. This culture media (scaffolds) can mimic the conditions and anatomical microenvironment found in biological tissues. Furthermore, the rheological properties of the scaffold used can influence the structure and organization of cells. By controlling these properties, such as viscosity and elasticity, it becomes possible to modulate cell morphology and behavior within the scaffold.[133] From an engineering perspective, there are many open questions about observed mechanics in these media.

To better replicate the mechanosensing effects that occur in vivo, it is essential to characterize scaffolds in vitro. This characterization helps to understand how changing scaffold properties, as observed in pathological environments, can impact cellular behavior. Hydrogels have gained widespread use in this regard due to their biocompatibility, composition, porosity, water content, and tunable properties.[140] To measure the mechanical properties of hydrogel scaffolds at the microscale, various methods have been proposed.[141] Most of these methods are quasistatic, meaning they control the deformation and/or the applied stress in accordance with Hooke's law. Quasistatic methods are commonly employed because they allow for controlled and precise measurement of mechanical properties.

Compression/Tensile Testing. In compression or tensile tests, controlled forces or displacements are applied to the scaffold, and the resulting stress-strain relationship is used to determine mechanical properties such as Young's modulus. It is widely used because of its methodological ease. Samples are prepared with a well-defined geometry and a linear stress-strain relationship is assumed.

Indentation Testing. Indentation tests involve applying a controlled force or displacement to the surface of the scaffold using a sharp probe or an indenter. The resulting indentation depth or force-displacement relationship can be used to calculate mechanical properties such as elastic modulus. As limitations it is difficult to obtain dynamic information and has adhesion problems in soft and hydrated media.

Atomic Force Microscopy (AFM). AFM utilizes a cantilever with a sharp tip to probe the surface of the scaffold, measuring the forces and displacements encountered. The data obtained can be used with different material models adapted to the experimental configuration to determine local mechanical properties, with high spatial resolution. To obtain a map, probing is done in different points of a delimited area. However, the generation of the mechanical image can take minutes.

Micropipette Aspiration. These methods involve applying a controlled force or suction to a small region of the scaffold using a micropipette or microneedle. The resulting deformation or pressure can be used to calculate mechanical properties. It can provide nonlinear characterization.

Static micro-elastography. It follows the same principles as conventional static elastography, i.e. it is fast, simple to apply and has a good spatial resolution. However, it provides qualitative results, since the stress distribution in the sample is unknown.[142]

In addition to the quasistatic methods mentioned earlier, there are other techniques that can be used to characterize the mechanical properties of scaffolds. These techniques, however, often have certain limitations and considerations that need to be taken into account. One such technique is nanoparticle labeling, known as Particle Tracking Microrheology (PTM).[143] This method involves attaching nanoparticles to the scaffold and tracking their movements to extract viscoelastic information. While PTM provides valuable data, it is limited to the positions of the labeled nanoparticles, which may not fully represent the overall mechanical properties of the scaffold. Tracking rheological methods, such as microrheology, reconstruct viscoelastic values but are limited to the positions of tracked particles.[144] Extrapolation is often required to obtain a comprehensive view of the mechanical properties. Other techniques utilize beads bound to the scaffold surface, which are then optically or magnetically excited, and their displacements are tracked (such as Magnetic Tweezers and Optical Tweezers). However, fitting the obtained data to viscoelastic models can be challenging and prone to variations, making standardization difficult.[145] These methods also involve an invasive exploration of the scaffold.

In general, many of these techniques have limitations. They often require long data acquisition times. When external forces are applied, the assumption of quasi-static strain can limit the accuracy of the measurements. Simplifications, such as assuming sample homogeneity and linearity, may disregard local features and stress distributions. Complex models and individual researcher preferences can lead to differing conclusions in the literature. Furthermore, fixing the specimen to a substrate introduces boundary conditions that must be considered during measurement and modeling.

3.6.2. Dynamic micro-elastography perspectives

Dynamic micro-elastography seeks to characterize mechanical properties at the microscale by means of propagating SWs. Several challenges need to be addressed to enable micro-elastography, including increasing signal-to-noise ratio, miniaturization, remote excitation characterization, integration/synchronization with imaging, and efficient transmission of mechanical waves in a confined medium with minimal mechanical loss.

One of the first studies in applying dynamic micro-elastography was that of Othman et al.[146] They employed a late-stage frog oocyte as the specimen, with a diameter of approximately 1.5 mm, and MRE as the imaging modality, with a spatial resolution of around 30 μm. A piezoelectric actuator was utilized to transmit vibrations through a small structure at its fundamental resonance frequency, which was measured to be around 585 Hz. This process amplified the amplitude of the vibrations to achieve a peak-to-peak displacement of up to 70 μm. The specimen was enclosed within an agarose gel. They estimated a nucleus elastic modulus of 0.3 kPa and observed a change in slope when the wave transitioned between different media. Direct contact techniques, like the one employed in this study, require higher amplitude

displacement to achieve higher frequencies. This is necessary due to the rapid attenuation of waves, which could introduce undesirable nonlinear effects and phase wrapping near the source.

In an effort to address the limitations encountered by other modalities, optical systems have emerged as highly versatile candidates. This field is called optical elastography, and has the potential for microscale probing of the mechanical properties, essential for fundamental research.[147] Significant advancements have been achieved using OCT techniques.[148] However, the emphasis of this discussion will be on the utilization of direct optics, particularly cameras, for various applications.

The study by Grasland-Mongrain et al.[149] presented an initial exploration of optical micro-elastography, specifically focusing on the evaluation of the elasticity of animal oocytes. They employed a micropipette in contact with the specimen, which vibrated at a frequency of 15 kHz to generate SWs inside the specimen. To track the propagation of these waves, a high-speed camera operating at 200.000 fps was connected to a microscope. This setup allowed for high spatial resolution in the order of a few microns and high temporal resolution in the range of a few milliseconds, enabling the creation of 2D maps, as shown in Figure 3.11. The study indicated the potential to investigate dynamic cellular processes with exceptional temporal detail. However, it is important to note certain limitations and assumptions in their approach. Firstly, the assumption of a homogeneous and elastic medium may not hold at such high frequencies, as the viscosity effect becomes significant. Additionally, considering the wavelength similar to the thickness of cell layers, the presence of guided waves should have been observed. Furthermore, the use of micropipettes in contact with the specimen introduced boundary conditions that were not taken into account.

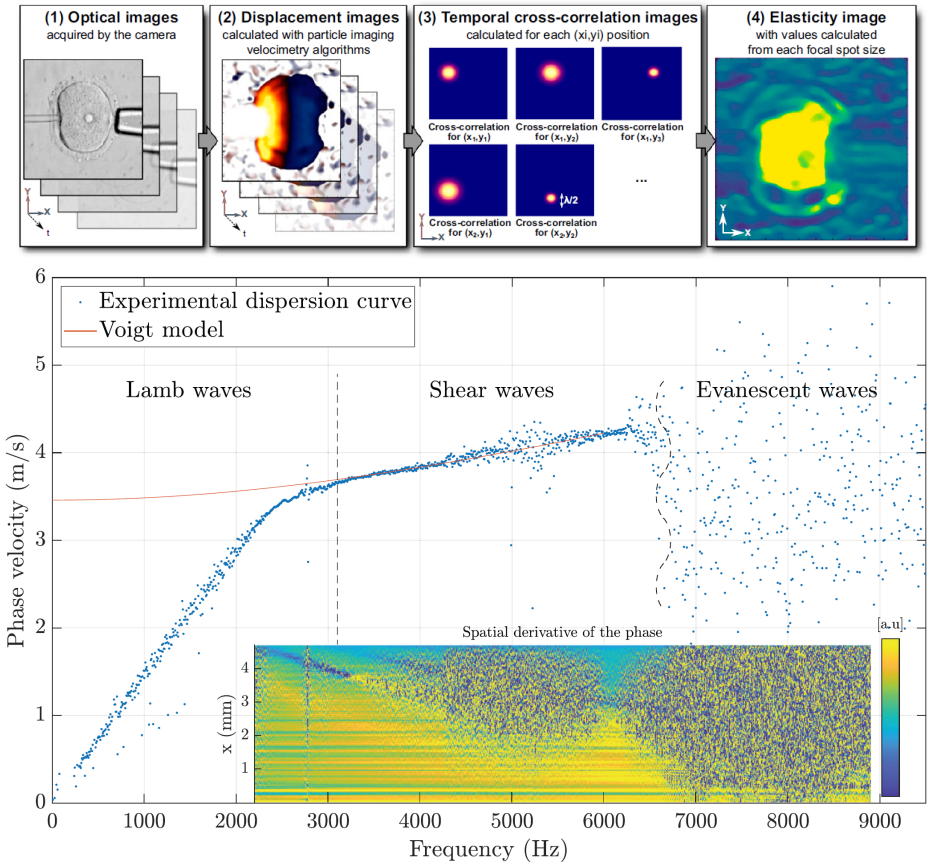

Figure 3.11. Top: optical micro-elastography on animal cell. With the optical images, the displacament is estimated using velocimetry algorithms, then through noise cross-correlation the velocity is calculated to finally create an elasticity map. Adapted from.[149] Bottom: dispersion curve on a 10% gelatin phantom showing three different type of waves. The cutoff frequency is identified as the beginning of evanescent waves. The bottom inset represents the spatial derivative of the phase as a function of propagation distance. Adapted from.[150]

In a subsequent study, the researchers made efforts to address the aforementioned issues by adopting a physical approach and employing controlled media.[150] A similar experimental setup was used, but with a plate connected to a vibrating piezoelectric in direct contact with the surface of gelatin phantoms. Viscoelastic properties were investigated across a broad frequency range spanning from 0.5 to 15 kHz using rheological models and the frequency limits of SW propagation were described (see Figure 3.11). They were even able to observe ultrasonic SWs (>20 kHz). However, the study encountered challenges related to the inconsistency of rheological fittings in samples with identical compositions. This inconsistency posed difficulties in establishing an accurate high-frequency cutoff experimentally. Additionally, the researchers were unable to verify whether the rheological model accurately fit the entire dispersion curve due to the detection of guided waves at the lower frequency range of the measurements. Another difficulty encountered by optical micro-elastography is comparing its results with standard rheology methods, due to the disparity in operating frequencies.

Another technique worth mentioning is Brillouin microscopy due to its nanometric spatial resolution. It utilizes the interaction between high-frequency pressure waves and light as its fundamental principle of operation.[151] In Brillouin microscopy, incident light interacts with acoustic phonons within the sample, resulting in a frequency shift in the outgoing light. This frequency shift is directly linked to the mechanical properties of the sample through the complex longitudinal modulus. The real part of the modulus provides information about the longitudinal elastic modulus, while the imaginary part is associated with the spectral width, enabling the determination of longitudinal viscosity.[152] These pressure waves are influenced by the bulk modulus of the medium, which, unfortunately, lacks the required sensitivity to detect structural changes adequately.

The advancement of optical modalities has significantly narrowed the spatial resolution gap between macroscopic techniques like USE/MRE and cellular-level techniques such as AFM.[153] This progress, coupled with high temporal resolution, which enables the tracking of rapid changes in mechanical properties, is becoming increasingly important in capturing dynamic properties like viscoelasticity.[2] Optical micro-elastography offers remarkable temporal resolution, surpassing many other techniques. However, it tends to have inferior spatial resolution compared to methods like AFM. To achieve a spatial resolution of 0.1 μm, one could explore the use of appropriate lenses. However, this would necessitate higher excitation frequencies, which can introduce challenges related to wave attenuation, requiring more accurate algorithms to compensate for these effects. Existing literature highlights that optical elastography has shown the most promising and impressive outcomes in superficial regions, such as the breast and cornea. This is attributed to the attenuation of surface SWs as they propagate deeper into the tissue.[4],[107]

By considering various factors such as imaging modality, as well as penetration depth, spatial and temporal resolution, and imaging speed (time to acquire an image), the different methods of elastography can be effectively classified. In Table 3.1 the performance metrics of different elastography techniques are summarized.[147] This allows researchers to select and employ the most appropriate elastography technique based on specific experimental requirements, thereby facilitating a comprehensive characterization of mechanical properties across different scales.

Table 3.1. Main characteristics of various elastography techniques. Ranges of values are presented as averages observed in the literature.

Technique	Spatial resolution	Temporal resolution	Imaging penetration	Imaging speed
Ultrasound Elastography	0.1–0.5 mm	1–20 kHz	4–5 cm	20 μs
Magnetic Resonance Elastography	1–3 mm	1–500 Hz	Complete	2-20 min
Optical Coherence Elastography	15–100 μm	10–200 kHz	0.5–3.0 mm	50 μs
Micro-elastography	10 –100 μm	1–200 kHz	0.1–20.0 mm	20 μs
AFM	1–100 nm	<1 Hz	Surface	1–30 min
Brillouin Microscopy	0.5-5.0 μm	MHz	0.1–3.0 mm	2–5 min

The future of microelastography lies in making it a more practical and automated technique while ensuring robust and accurate performance. By reducing user intervention, and improving data processing techniques, microelastography can become more accessible and efficient in various applications. In

particular, microelastography holds great potential in the fields of in vitro fertilization and medical implants and devices. In the fertilization field, the ability to assess the mechanical properties of oocytes and embryos can aid in the selection of viable candidates for successful implantation.[154] Furthermore, micro-elastography can play a crucial role in evaluating the integrity and functionality of medical implants and devices by monitoring their mechanical properties over time.[155] The combination of optical elastography techniques with US imaging offers a promising multimodal approach. By integrating the strengths of both modalities, such as high-resolution imaging and depth penetration of US and the ability to assess mechanical properties with optical elastography, a more comprehensive understanding of biological structure and functionality can be achieved. This integration enables complementary information acquisition at different length scales, enhancing our knowledge of tissue mechanics and enabling better diagnosis, monitoring, and treatment of various conditions.

4

Scientific Background: Methods

In this chapter, the information presented in the published papers on the methods used to analyze the propagation of SWs in viscoelastic media as well as the fabricated and used media is extended. Different algorithms have been implemented to reconstruct displacements, velocities, and attenuation mainly. Further details are provided on the rheological models used and the signal and image preprocessing.

4.1. Displacement reconstruction

Once the raw data has been obtained from the imaging modality used, the displacement field, i.e. the displacement between successive images or frames associated with each point, is calculated. For this purpose, it is necessary to reconstruct the SW propagation within the medium.

In ultrasound imaging, speckle refers to the granular appearance observed in ultrasound images, which arises from the interference of multiple backscatter signals with similar frequencies. The speckle pattern is created when the wavelength of the ultrasound is larger than the dimensions of individual scatterers within the medium. It is important to note that speckle patterns do not directly indicate the position of individual scatterers, but rather represent the random pattern generated by their interaction with the ultrasound wave. One of the first studies to take advantage of this phenomenon proposed speckle tracking.[86] It was assumed that the speckle patterns did not vary significantly from one frame to another, allowing for the determination of frame-to-frame motion. The similarity of speckle patterns from frame to frame relied on a sufficiently high frame rate. Cross-correlation algorithms were employed to estimate induced displacements and distinguish the nature of the propagated waves. Displacement estimation could be performed globally, providing a single value for the entire image, or locally, by tracking specific regions of interest.

While this description primarily focuses on ultrasound imaging, it is worth noting that other techniques, such as cameras also utilize speckle patterns for tracking the motion of particles within the medium. In the case of TWE, no speckle pattern is required since the receiver captures a 1D signal with no geometrical information.

Phase-shift and phase tracking algorithms were used in this thesis when using ultrasound imaging, while optical flow methods were applied in the case of the high speed camera.

4.1.1. Phase-shift algorithms

Ultrasound scanners provide RF data, comprising of reflected and scattered echoes that are detected at a high sampling rate by the transducer. Quadrature demodulation produces IQ data, which represents the low frequency version of the original data. This step effectively reduces the data transmission requirements.[156]

Displacement estimation methods, such as phase-shift algorithms, are employed to determine the motion of the imaged tissue. These algorithms are based on the relationship between flow velocity and Doppler frequency, which is the difference between the received and transmitted frequencies. One example of such an algorithm is the Loupas algorithm or 2D autocorrelator, which utilizes the IQ data to

calculate the phase shift between the reference and shifted signals.[157] This is achieved by measuring the average phase shift of the mean Doppler frequency and the mean RF frequency along each axial line, as shown in Equation 4.1.

$$u(t) = \frac{c}{4\pi f_c} \frac{\operatorname{atan}\left(\frac{\sum_{m=0}^{M-1}\sum_{n=0}^{N-2} Q(m,n)I(m,n+1) - I(m,n)Q(m,n+1)}{\sum_{m=0}^{M-1}\sum_{n=0}^{N-2} I(m,n)I(m,n+1) + Q(m,n)Q(m,n+1)}\right)}{1 + \operatorname{atan}\left(\frac{\sum_{m=0}^{M-2}\sum_{n=0}^{N-1} Q(m,n)I(m+1,n) - I(m,n)Q(m+1,n)}{\sum_{m=0}^{M-2}\sum_{n=0}^{N-1} I(m,n)I(m+1,n) + Q(m,n)Q(m+1,n)}\right)/2\pi} \tag{4.1}$$

For soft tissues c, the speed of sound, is normally set at 1540 m/s, and the center frequency of the RF signal f_c depends on the transducer used. The result is the average displacement in a selected axial range M (with typical values around 4) and ensemble length N (with typical values around 4).

4.1.2. Phase tracking

A similar analysis can be conducted by leveraging the fast performance in the frequency domain (Figure 4.1). This involves utilizing the IQ data and applying the Hilbert transform, which can be visualized as a 90º rotation of the Fourier Transform (FT). When the FT is applied to a signal, it yields a series of complex coefficients consisting of magnitude and phase components. The magnitude represents the energy concentration at specific frequencies, while the phase reflects the temporal distribution of energy (the structure).

In the case of US, displacements primarily occur in the vertical direction, which corresponds to the depth dimension (Z). The transformation is performed on each column and at each time point of the IQ matrix. The phase difference between consecutive time points at each spatial location gives rise to the displacement field,[158],[159] as described in Equation 4.2.

$$u(t) = \frac{c}{4\pi f_c}\left(S \circledast \arg\left[\mathcal{H}(t) \otimes \overline{\mathcal{H}(t+1)}\right]\right) \tag{4.2}$$

Here, $\mathcal{H}(t)$ and $\overline{\mathcal{H}(t+1)}$ represent the Hilbert transform and its conjugate, respectively. S is a smoothing filter with typical dimensions [21, 3], $\circledast$ denotes convolution, and $\otimes$ denotes the Hadamard product. c represents the speed of sound, while f_c denotes the center frequency.

One notable advantage of this method is its applicability to the lateral dimension (x-axis) for obtaining the displacement field in that direction. Additionally, this approach can be extended to images acquired from high-speed cameras.

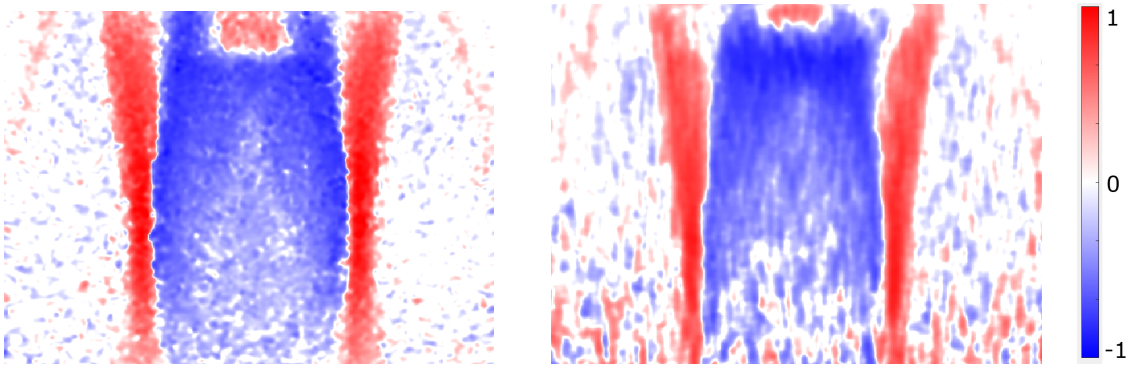

Figure 4.1. Reconstructed displacements in the vertical direction on a viscoelastic phantom using the Loupas algorithm (left) and the phase tracking method (right).

4.1.3. Optical Flow

Optical flow is the motion observed between two images due to actual movement of objects within the image, or the motion of the recording device. The objective is a displacement vector that describes the evolution of the target points. In a nutshell, it consists of taking pairs of sequential images and calculating a vector for each pixel that indicates the displacement from one image to that same pixel in the other image. Several assumptions must be taken into account: (1) the brightness (pixel intensity) of the tracked points should not change (or barely); (2) similar motion of surrounding pixels. Since this flow is calculated on video files, each image is called a frame. Two methods area mainly used for the estimation of displacement: correlation and Lucas-Kanade.

The Lucas-Kanade method is used for the estimation of displacements.[160] Starting with the initial frame and a point of interest or pixel, when moving to the next frame (having a sampling rate dt), and considering a displacement that can be divided into its horizontal dx and vertical dy components we get: $I(x, y, t) = I(x + dx, y + dy, t + dt)$. By using a Taylor series expansion up to the linear term and simplifying we get the Optical Flow equation:

$$f_x u + f_y v + f_t = 0 \tag{4.3}$$

where $f_x = \partial f/\partial x$ and $f_y = \partial f/\partial y$ are the spatial gradients of the image, $f_t = \partial f/\partial t$ is the time derivative (time gradient), and u and v are the unknowns, the components of the instantaneous velocity $u = \partial x/\partial t$ and $v = \partial y/\partial t$, which can be used to estimate motion.

The Lucas-Kanade method uses the information of neighboring pixels to calculate the displacement of a target pixel. By taking a square patch (3x3) around the target point, it is possible to find the gradients of the 9 points included. Each small ROI is a linear gradient, whose direction indicates the flow and whose magnitude refers to the intensity of change. The action of minimizing the discrepancy between the previous and current frame state is the basis of the algorithm, which is achieved by the least squares method. The solution of the problem is the desired displacement (pseudo-inverse method):

$$\begin{bmatrix} u \\ v \end{bmatrix} = \begin{bmatrix} \sum_i f_{x_i}{}^2 & \sum_i f_{x_i} f_{y_i} \\ \sum_i f_{x_i} f_{y_i} & \sum_i f_{y_i}{}^2 \end{bmatrix}^{-1} \begin{bmatrix} -\sum_i f_{x_i} f_{t_i} \\ -\sum_i f_{y_i} f_{t_i} \end{bmatrix} \tag{4.4}$$

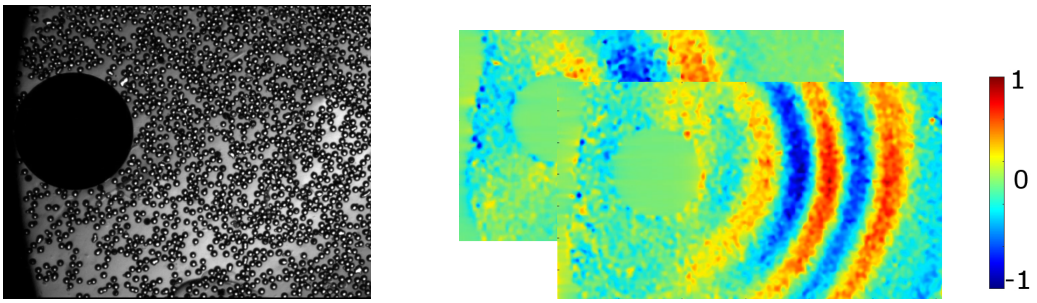

Figure 4.2. Using dense optical flow algorithms on a viscoelastic phantom. On the left the raw image is presented with optical speckles and black circle exciter, and on the right the displacements in the horizontal direction are satisfactorily reconstructed.

The Lucas-Kanade method computes optical flow only for sparse features. To obtain a displacement field, information is needed at all points of the frame, which is achieved by means of dense optical flow algorithms (Figure 4.2). The Farneback algorithm has been widely used.[161] The fundamental concept behind this method involves approximating the values of neighboring pixels using a polynomial function: $I(x) \approx x^T A x + b^T x + c$. Previously, in the Lucas-Kanade method, a linear approximation $I(x) = b^T x + c$ was employed, utilizing only the first-order Taylor's expansion. However, with this approach, the accuracy of the approximation is enhanced by considering second-order values. The key idea is to observe the discrepancies in the approximated polynomials caused by displacements of objects. Consequently, the objective is to calculate the displacement d in the equation $I_2(x) = I_1(x - d)$ using the polynomial approximation.

4.2. Data preprocessing in dynamic elastography

Depending on the imaging system employed, displacement (or velocity) information is obtained using different methods. In the case of ultrasound scanning, IQ demodulated data from raw RF data is processed using either Kasai's or Loupas's algorithms. Conversely, when an optical device such as high-speed cameras is utilized, the resulting frames exhibit the motion of a speckle pattern, and tracking this pattern allows retrieval of the desired particle displacement or velocity data. Various techniques can be employed for tracking, including optical flow, particle image velocimetry, or block matching. The accuracy and performance of these techniques are dependent on configuration parameters and theoretical assumptions.

The outcome is a dataset that includes a 3D matrix of displacement information, a sequence of images representing the temporal evolution of wave propagation (forming a wave propagation movie), conversion factors for translating the units of the imaging system (e.g., wavelengths or pixels) to length units (e.g., meters), and a time vector indicating the time between frame acquisitions (temporal resolution or frames per second).

With this dataset, a preprocessing sequence can be initiated.[156] Note that some of the following procedures are unique to US imaging, although extendable to high-speed camera imaging.

Preprocessing

Frame averaging. When US ultrafast imaging is utilized, lower resolution and random noise can occur due to all elements of the transducer working simultaneously, resulting in interferences and low energy reception. One approach to address this is to average several superframes with the same temporal start. Another option, which can be combined with the previous method, is the use of angular compounding.[79] This involves electronically tilting the emitting angle of the time planar waves by a few degrees instead of using all of them for imaging. By considering three angles, a third-order moving average filter (mean of three consecutive acquisitions) can be applied to generate averaged acquisitions with improved spatial accuracy. However, this comes at the expense of reducing the frame rate, as each new acquisition is now separated by three that have been averaged, effectively reducing the acquisition rate by three.

Reverberating frames. Acoustic phenomena such as ARF can introduce source-induced push excitation, leading to the generation of shear waves after medium relaxation. Transient elastography involves contact excitation through the vibration or motion of an element, resulting in the creation of SWs. Unrealistic amplitudes can be observed near the sources, which can cause diffraction effects and signal distortion, particularly in the case of ARF. One approach to mitigate this is to exclude lateral positions near the beamwidth, typically within a range of one wavelength.

Time filtering. It is important to ensure that the signal shape is preserved, as the timing information is crucial for velocity algorithms. Additionally, consideration should be given to selecting a frequency bandwidth that accurately reflects the properties under analysis. For addressing high frequency jitter, applying a low-pass filter (LPF) with a cutoff frequency of 1–2 kHz is usually sufficient, particularly for tissues or phantoms with relatively low speeds (< 3 m/s). If the DC component of the signal has a significant magnitude, it may alter the baseline of the signals, causing them to deviate from an average of zero. In such cases, a motion filter is necessary, especially if the imaging system or the medium experienced involuntary movement, such as ground vibrations. A high-pass filter (HPF) with a cutoff frequency of approximately 10 Hz can help address these issues. When applying filters, it is crucial to avoid distorting the phase information contained in the data. Hence, zero-phase filters are extensively used in the field of motion tracking.

Velocity limits. The minimum detectable velocity is determined by the ratio of the maximum lateral distance to the maximum time, expressed as $x_{max}/t_{max} = x_{max}/(N_f \cdot PRF)$., with N_f the number of acquisitions and PRF the frame or acquisition rate. The maximum detectable velocity corresponds to the Nyquist velocity, given by $v_{ny} = c^2/(8f_0 d_{max})$, where c is the speed of sound, f_0 is the central frequency used for tracking waves, and d_{max} is the depth of the ROI. It should be noted that increasing the PRF necessitates reducing d_{max} to maintain the same velocity limit.

Directional filtering. Many shear wave velocity estimation algorithms that operate in the time domain, particularly those based on velocity group estimators, rely on the assumption that a single wave is propagated from a single orthogonal source in a homogeneous medium. Under this assumption, no reflections or interference patterns are expected to appear in the time profiles. However, when waves encounter material interfaces, areas of low motion can be cancelled out due to destructive interference, leading to the decorrelation and distortion of the signals. This makes it challenging to accurately identify phase information peaks. Refraction effects within inclusions can exacerbate this problem. To address these issues, directional filters can be employed to separate propagating components and mitigate signal distortion. By applying such filters, we move closer to the single wave assumption, and since this is a linear operation, the results satisfy the equation of motion. Consequently, we can separately analyze the direct and reflected waves, thereby gaining a correct understanding of the results. This approach is particularly recommended when the excitation is transient, as it significantly improves the signal-to-noise ratio (SNR) (up to a twofold increase) and enhances contrast in the medium.[162] The following steps outline the procedure. First, a slice is taken along the depth to obtain lateral temporal images corresponding to the size of the depth. Next, a 2D discrete Fourier transform (DFT) is applied to each of these matrices to obtain the (f–k) representation, which describes the energy distribution of the signals in both the temporal and spatial frequency domains. Since we know that these magnitudes are related to the velocity through the equation $c = 2\pi f/k$, we can assume that positive velocities correspond to right-propagating waves, while negative velocities correspond to left-propagating waves. The k-space is divided into four quadrants with the origin at the center. The positive temporal frequency (f) increases towards the right, while the positive spatial frequency (k) increases towards the top. Consequently, velocities will be positive in the first and third quadrants and negative in the second and fourth quadrants. To analyze right-propagating waves, we apply a binary mask to remove the second and fourth quadrants. To ensure smooth transitions at the edges and minimize ringing artifacts, a Tukey window can be applied as an apodization function. The inverse 2D DFT is then used to retrieve the single wave. It is important to pay attention to the components close to the origin, as having a very low k value combined with an expected f value can lead to unrealistically high velocities. To address this issue, a circular mask can be placed around the origin with a radius determined based on the estimated undesired k values.[163] It has been observed that modifying the energy distribution in the frequency domain can introduce phase distortion, which may bias the results. While the impact on velocity estimations is generally not significant unless the modification is substantial, it becomes more pronounced in attenuation estimations. Similarly, when windowing is applied to reduce noise by assuming signal periodicity during the Fourier transform, it can alter the shape or shift the times, leading to a significant bias in the results. This issue is particularly critical when the data is located near the beginning or end of the signal.[42]

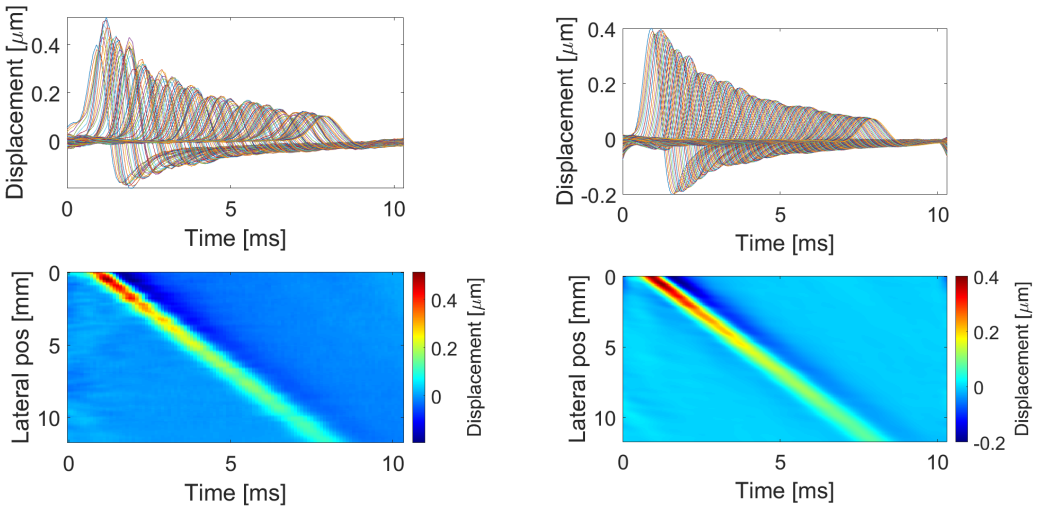

Figure 4.3. Preprocessed propagating wave on a viscoelastic phantom after SSI excitation with an ultrahigh-speed ultrasound scanner. Left: raw reconstructed displacements with no preprocessing. Right: reconstructed displacements after the application of smoothing, directional filter, time filter, depth averaging, and time upsampling.

Additional considerations. To obtain robust results and reduce computation time, it is advisable to average the time profiles of displacement or velocity over depth. This assumes that a plane wave is propagating, and therefore, the contribution from each depth line will be similar, allowing noise reduction through averaging. The depth of field (DOF) corresponds to the length of the data being used. To maximize the quality of results, it is recommended to position the ROI at the focal depth (push position in depth) and ensure that its DOF is approximately $8F^2\lambda$, where F is the F-number. To remove salt and pepper noise in the images, a median filter is suggested, where each pixel is replaced with the median value of its 3x3 neighborhood pixels. When the nature of the noise is unclear and it is expected to affect the results, smoothing functions that preserve phase information are recommended. Finally, increasing temporal resolution (time upsampling) can enhance the visualization of peak times. This can be achieved by increasing the PRF, resulting in an expanded time vector that allows for more accurate differentiation between temporal profiles.

Figure 4.3 illustrates the quality improvement after the application of different signal preprocessing.

4.3. Wave velocity and attenuation reconstruction

After preprocessing, an optimized dataset is obtained, which will undergo further processing to obtain mechanical parameters related to wave propagation in the studied medium. To fully characterize the viscoelasticity of the medium, independent experimental evaluation of c_{ph} and α from the displacement or velocity field is needed.

First of all, it is necessary to clarify the difference between two fundamental velocities in wave propagation that describe different aspects of wave behavior. Group velocity (c_g) refers to the velocity at which the overall envelope or group of wave energy propagates, related to a broadband SW pulse. It represents the velocity at which the peak or envelope of a wave packet, composed of multiple individual waves, moves through a medium. The group velocity can be different from the phase velocity, especially in dispersive media where different frequency components of a wave have different velocities. In dispersive media, the group velocity can be slower or faster than the phase velocity, depending on the frequency content of the wave.[164] On the other hand, phase velocity (c_{ph}) refers to the velocity at which an individual wave component or wavefront propagates. It represents the velocity at which the phase of the wave, which characterizes its position within a single oscillation cycle, travels through space.

4.3.1. Group velocity

The initial technique employed in clinical elastography involved the utilization of time-of-flight (TOF) algorithms to calculate c_g from particle displacement or velocity.[41],[165] One approach is to conduct multiple cross-correlations along a line (moving average) and reconstruct a 2D map.[41],[166] An alternative method involves obtaining a global value tracking the motion of multiple points.[165] This approach initially identifies the arrival time of shear waves at each propagation distance, through the time-to-peak (TTP) feature, and subsequently conducts a linear regression relating TTP to propagating distance to determine c_g (Figure 4.4).

Despite their robustness, it is important to note that the methods mentioned are limited in their applicability to elastic, homogeneous, isotropic, and linear tissues. In the presence of viscosity, these methods may not provide accurate results.[167] This limitation has become apparent in the diagnosis of breast cancer and the staging of liver fibrosis, where the observed specificity is lower than expected. This has been attributed to the presence of confounding factors, such as the development of new structures like highly vascularized areas in tumors or increased fat content in fibrosis.[168],[169] These factors can introduce inaccuracies in the measurements through viscosity, with the risk of misdiagnosing patients. This is particularly concerning as lower velocities may be obtained when they should be higher, reflecting the progression of the pathology.

Methods based on TTP or correlation are particularly sensitive to the wave shape, as they rely on accurately identifying the peaks. In the presence of inclusions or interfaces, the analysis window may include a combination of displacements, and reflections can distort the quasi-plane wave shape, introducing additional noise. Moreover, if the interface is not planar but rather spherical or cylindrical, out-of-plane

displacements can interfere with the peaks and alter their shape, leading to temporal shifts or the introduction of new frequency components. Utilizing particle velocity for calculating the c_g results in a dataset with higher frequency content, as shown in the following expression in the frequency domain, $\tilde{v}(\omega) = j\omega\,\tilde{u}(\omega)$. The peaks of the velocity, which represent the maximum slope of the displacement, occur earlier in time compared to the displacement itself. Consequently, they are less likely to be affected by shape changes caused by reflections or boundary interference effects. However, velocity measurements tend to be more susceptible to noise compared to other techniques.[170] A recommended approach is to combine TTP on the particle velocity data with directional filtering.[170] Selecting the size of the ROI should involve a tradeoff between the excitation wavelength and spatial resolution. It is important to note that using higher wavelengths can lead to increased errors. This compromise on spatial resolution reduces it to approximately one wavelength to ensure reliable characterization.[171]

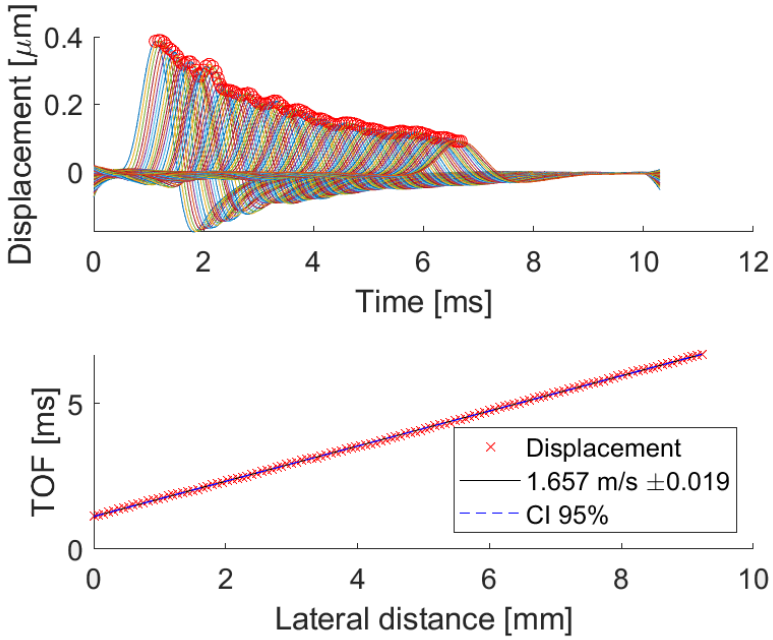

Figure 4.4. Top: TTP detection on the temporal profiles particle displacement data at different propagation distances (lateral dimension). Bottom: TOF vs propagation distance to calculate group velocity.

4.3.2. Phase velocity and attenuation

One method to estimate the phase velocity and attenuation is the phase gradient approach.[172] In the previous chapter, it was shown that in a viscoelastic, linear isotropic medium, the harmonic solution for a plane shear wave propagating in 1D (x) can be expressed as a product of time-dependent and spatial-dependent factors:

$$u(x,t)_{plane} = U_0(e^{j\omega t})(e^{-\alpha x}e^{-j\omega\frac{x}{c_{ph}}}) \tag{4.5}$$

To obtain the time frequency response we apply the FT:

$$\tilde{U}(x,\omega)_{plane} = \tilde{U}_0(\omega)e^{-\alpha x}e^{-j\omega\frac{x}{c_{ph}}} \tag{4.6}$$

where ω is the angular frequency, and $\tilde{U}_0$ is the frequency domain part of the maximum amplitude U_0.

By extracting the phase as a function of propagation distance (x) from the previous expression, the phase velocity can be determined. Notably, the phase expression takes the form of a straight line, and

thus, the slope of this line corresponds to $k' = \frac{\omega}{c_{ph}}$:

$$\text{Phase}(\tilde{U}(x,\omega)_{plane}) = \frac{\omega}{c_{ph}}x \tag{4.7}$$

Subsequently, by considering the logarithm of the amplitude of this response as a function of propagation distance (x), the only unknown parameter remaining is the attenuation. Once again, α can be represented as the negative slope of a straight line:

$$\text{Ln}|\tilde{U}(x,\omega)_{plane}| = \text{Ln}|\tilde{U}_0(\omega)| - \alpha x \tag{4.8}$$

Figure 4.5 illustrates the result of this algorithm.

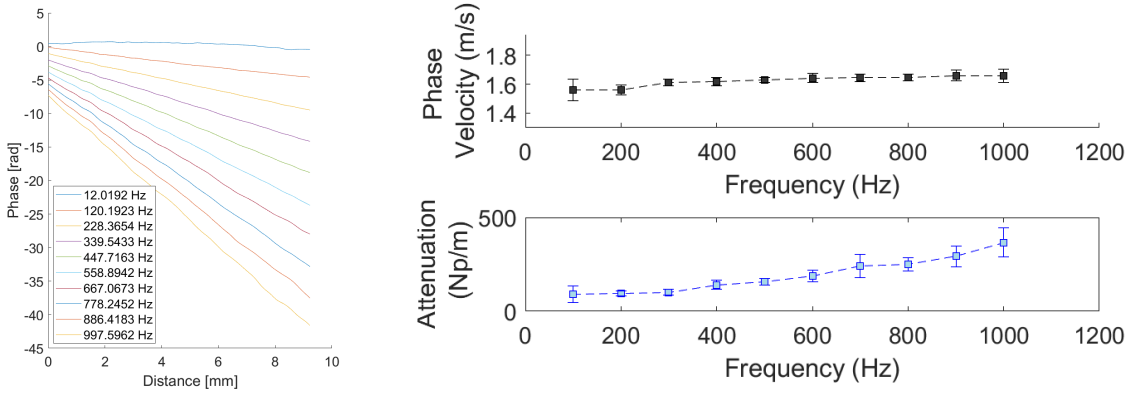

Figure 4.5. Left: phase as a function of propagating distance. Right: phase velocity and attenuation coming from the phase and amplitude using the the phase gradient approach.

However, when SWs propagate with a cylindrical front, there is a dissipation of energy as the radial distance (r) from the axial excitation line increases. As a consequence, the amplitude of the SWs gradually decreases as it propagates radially outward. These cylindrical waves are modeled as:[7]

$$u(r,t)_{cyl} = U_0 \frac{j}{4} H_0^1(k^* r) e^{-j\omega t} \tag{4.9}$$

H_0^1 is the Hankel function, whose asymptotic behavior when $|k^* r| >> 0$ is:

$$u(x,t)_{cyl} \approx U_0 \frac{j}{4} \sqrt{\frac{2}{\pi x(\frac{\omega}{c_{ph}} + j\alpha)}} e^{\alpha x} e^{j(\frac{\omega}{c_{ph}}x + \pi/4)} e^{-j\omega t} \approx A \frac{1}{\sqrt{x}} e^{\alpha x} e^{j(\frac{\omega}{c_{ph}}x + \pi/4)} e^{-j\omega t} \tag{4.10}$$

In cylindrical coordinates the radial distance would be the variable to use, but since the analysis are performed in a 2D plane it will be x, the lateral distance, because radial symmetry is assumed. Considering that A is a constant, the difference between cylindrical and plane SW propagation is in the amplitude only. By applying the same logic as with plane SWs, experimentally measuring the amplitude and phase of the frequency response as a function of propagating distance allows to characterize the medium:

$$\tilde{U}(x,\omega)_{cyl} = \tilde{U}_0(\omega) \frac{e^{-\alpha x}}{\sqrt{x}} e^{j(\frac{\omega_0}{c}x - \theta_0)} \tag{4.11}$$

$$\text{Phase}(\tilde{U}(x,\omega)_{cyl}) = \frac{\omega}{c_{ph}}x - \theta_0 \tag{4.12}$$

$$\text{Ln}|\tilde{U}(x,\omega)_{cyl}| = \text{Ln}|\tilde{U}_0(\omega)| - \alpha x - \frac{1}{2}\text{Ln}(x) \tag{4.13}$$

θ_0 is the phase at the excitation origin, which can be arbitrary. The new term in the amplitude accounts for the diffraction due to cylindrical waves. These two factors only add constant offsets.

In the case of spherical waves, a remarkable characteristic is their total radial symmetry, where the wavefronts propagate uniformly in all directions. The amplitude of the wave, however, diminishes more rapidly in every direction as a function of radial distance. These spherical waves are modeled as:[7]

$$u(r,t)_{sph} = U_0 h_0^1(k^* r) e^{-j\omega t} \tag{4.14}$$

h_0^1 is the Bessel function of the first kind, also called spherical Bessel function, whose asymptotic behavior when $|k^* r| >> 0$ is:

$$u(x,t)_{sph} \approx U_0 \frac{1}{jx(\frac{\omega}{c_{ph}} + j\alpha)} e^{-\alpha x} e^{j\frac{\omega}{c_{ph}}x} e^{-j\omega t} \approx A\frac{1}{x} e^{-\alpha x} e^{j\frac{\omega}{c_{ph}}x} e^{-j\omega t} \tag{4.15}$$

Considering that A is a constant, the difference between spherical and plane SW propagation is in the amplitude only. Again x represents both the radial and lateral dimension (in 2D) and experimentally measuring the amplitude and phase of the frequency response as a function of propagating distance all the parameters can be calculated:

$$\tilde{U}(x,\omega)_{sph} = \tilde{U}_0(\omega)\frac{e^{-\alpha x}}{x} e^{j(\frac{\omega}{c_{ph}}x - \theta_0)} \tag{4.16}$$

$$\text{Phase}(\tilde{U}(x,\omega)_{sph}) = \frac{\omega}{c_{ph}}x - \theta_0 \tag{4.17}$$

$$\text{Ln}|\tilde{U}(x,\omega)_{sph}| = \text{Ln}|\tilde{U}_0(\omega)| - \alpha x - \text{Ln}(x) \tag{4.18}$$

θ_0 is the phase at the excitation origin, which can be arbitrary. The new term in the amplitude accounts for the diffraction due to spherical waves. These two factors only add constant offsets.

With these two parameters (c_{ph}, α) the complex shear modulus can be obtained using Equation 3.22 and Equation 3.23.

The considerations previously presented for the calculation of group velocity using particle velocity can also be assumed to apply to phase velocity calculations. When rewriting the equations for plane SWs, only a constant offset is added, therefore, the same principles and methodologies can be applied to determine the phase velocity using the $\tilde{V}$ velocity field.

$$\text{Phase}(\tilde{V}(x,\omega) = \text{Phase}(\tilde{V}(x,\omega) - \pi/2 \tag{4.19}$$

$$\text{Ln}|\tilde{V}(x,\omega)| = |\tilde{U}(x,\omega)| + \text{Ln}(\omega) \tag{4.20}$$

As in any SW propagation situation, it is important to acknowledge that near-field variations and a high decaying rate can exist as the distance from the source increases. These variations can introduce aberrations and potentially bias the fitting model used for data analysis. However, in the intermediate points of SW propagation, where the wave is fully formed, better performance and more accurate results are expected. To account for these considerations, it becomes valuable to explore different combinations of starting and ending positions within the ROI. By evaluating the results obtained from these different combinations and employing a metric such as R^2 and setting a 0.9 or 0.95 threshold, the quality of the fitting and the reliability of our results are assesed.[173]

It is common practice to fit rheological models to the phase velocity at various frequencies while neglecting the attenuation parameter. Although this approach is particularly useful in vivo due to the presence of high levels of noise in the recorded data, there is an attractive alternative method that does not rely on a specific rheological model. This alternative method involves applying a two-dimensional Fourier

transform (2D FT) to the displacement (or velocity) $u(x,t)$ as a function of time and distance. This results in a representation in the (f, k) space, where f represents the frequency domain and k represents the wavenumber domain $\tilde{u}(f,k)$. The phase velocity can be determined by examining the location of the maximum magnitude in the (f, k) space (see Figure 4.6):[69]

$$c_{ph} = \frac{f}{k} \tag{4.21}$$

The attenuation can be determined by examining the shape of the maximum magnitude in the (f, k) space, which is proportional to the Full Width at Half Maximum (FWHM) of the wavenumber associated with each frequency:[42]

$$\alpha = \frac{FWHM \cdot \pi}{\sqrt{3}} \tag{4.22}$$

Note that any geometrical corrections should be applied to this expression.

Using this pair of values for each frequency (c_{ph}, α), the storage G′ and loss modulus G″ can be reconstructed considering the complex wavenumber:

$$G^* = G' + iG'' = \rho \left(\frac{\omega}{\omega / c_{ph} + i\alpha} \right)^2 \tag{4.23}$$

One of the primary advantages of this method is its ability to function as a directional filter. It selectively identifies specific energy locations in the (f, k) space, allowing for differentiation between waves propagating in opposite directions. This feature is particularly useful in distinguishing reflections from the direct wave.

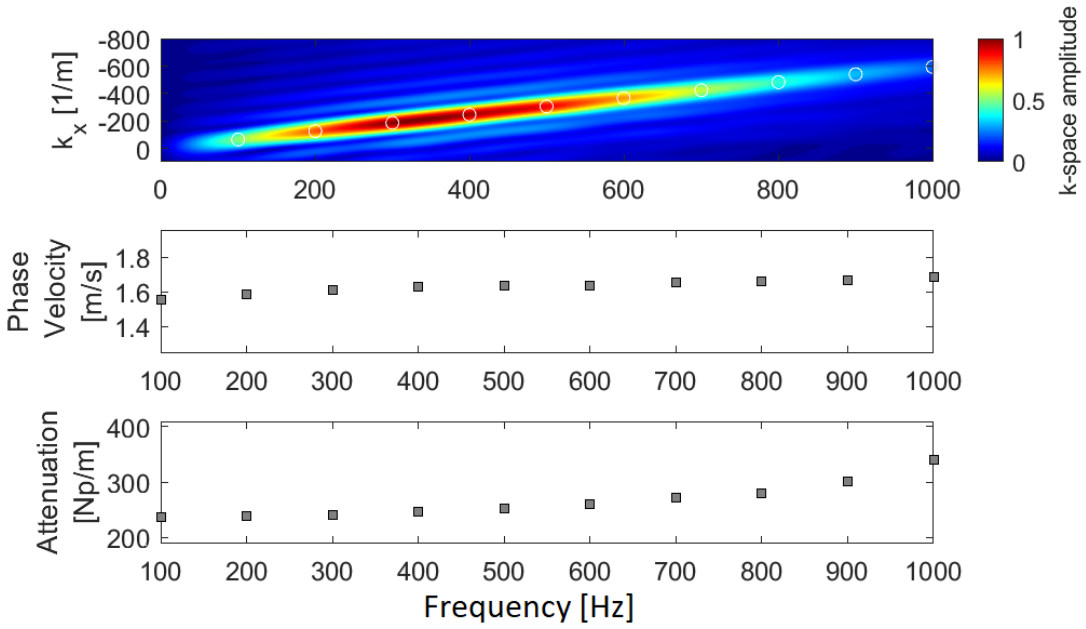

Figure 4.6. The 2D FT method uses the (f,k) space (top) to determine the main propagation mode by identifying pairs of wavenumber k and frequency f associated with the maximum amplitude values. The phase velocity was obtained as $c_{ph} = f/k$ (middle), and the attenuation was proportional to the Full Width at Half Maximum (FWHM) of the wavenumber signals associated with each frequency (bottom).

4.3.3. Time Of Flight in TWE

A Time of Flight (TOF) algorithm is employed to estimate the phase velocity using the TWE device. The emitter can generate torsional waves at several frequencies of excitation, and as the wave propagates

through the medium, the piezoelectric sensor captures the time signals. However, these signals are susceptible to corruption from electronic and mechanical crosstalk originating from the components of the device itself.

To accurately estimate the signals start (TOF), the FT is performed and a quarter period of the frequency with the highest energy is subtracted from the first peak of the signal.[17] Additionally, a calibration factor called internal delay is subtracted from this time. This internal delay accounts for the influence of crosstalk on the measured signals. This workflow is illustrated in Figure 4.7, Finally, knowing the distance emitter–sensor, the phase velocity associated to the frequency of the signal response is calculated $c_{ph} = \frac{\text{distance}}{\text{TOF}-\text{delay}}$.

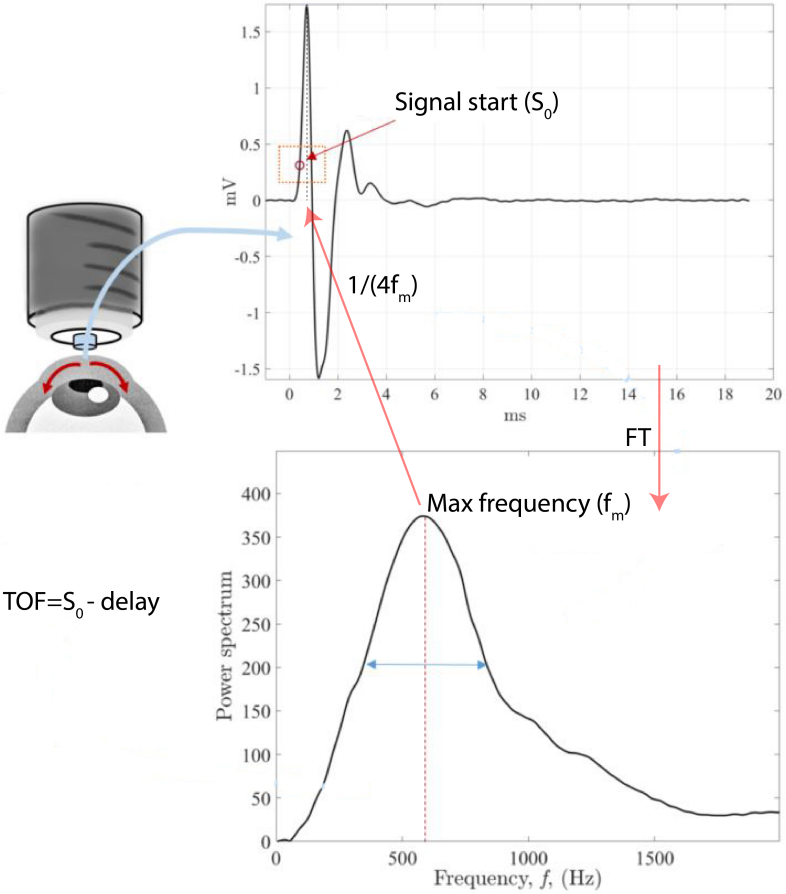

Figure 4.7. Workflow to calculate the TOF using the TWE device associated to each excitation frequency. TOF is equal to the estimated signal start S_0 and subtracting the internal delay of the device.

4.4. Rheological modeling

From a mechanical perspective, rheology seeks to explain the behavior of materials that exhibit properties of both solids and liquids. These materials, known as viscoelastic solids, behave as classical solids under the application of stress, even if it is small, but do not exhibit perfectly reversible deformation. Similarly, there are fluids that can deform indefinitely, but upon the removal of the applied stress, they show a small recovery of deformation. These fluids are referred to as viscoelastic liquids. The key to understanding their behavior lies in studying the relationship between forces and deformations over time, which is why rheology focuses on flow.[174]

A shear deformation is characterized by the relative slip between particles or layers within a material. For instance, consider an experiment involving a Hookean solid placed between two plates. The upper plate induces shear motion through rotation, while the lower plate remains static. The shear strain

γ represents the relationship between the horizontal displacement of the layers and the height from the reference. This material can be described by the shear elasticity parameter μ, which represents a purely elastic behavior $\tau = \mu\gamma$, where the shear stress τ can be calculated. In contrast, introducing a Newtonian fluid between the plates, τ will depend on the shear strain rate, which describes how fast the deformation occurs. The shear viscosity η succinctly captures this phenomenon, as it quantitatively measures the internal friction associated with damping and the loss of kinetic energy. The constitutive equation for this material represents a purely viscous behavior $\tau = \eta\frac{\partial\gamma}{\partial t}$.

In materials such as soft tissues, stress can induce deformations ranging from molecular rearrangements on a small scale to observable macroscale changes, accompanied by viscoelastic flow. Phenomenologically, this behavior is modeled using combinations of spring and dashpot elements. The spring element instantly stretches proportionally to the applied load and maintains this deformation as long as the load persists. Upon removal of the load, the spring returns to its initial state following the same path. This behavior resembles that of a Hookean solid. On the other hand, the dashpot element, immersed in a Newtonian fluid, responds based on the rate of deformation. In this case, upon load removal, there is no recovery. Rheological models such as the Kelvin-Voigt (KV) and Maxwell (Mx) models are commonly employed to describe the viscoelastic properties of tissues[2],[175] (Figure 4.8).

Kelvin-Voigt. KV is the most widely used model in the literature to describe biological media.[31],[95],[176] The spring and dashpot elements are arranged in parallel, and the stress-strain relationship in the time-domain:

$$\tau = \mu_{kv}\gamma + \eta_{kv}\frac{\partial\gamma}{\partial t} \tag{4.24}$$

In this representation, both the spring and dashpot elements function simultaneously as they undergo the same deformation. Initially, the dashpot acts as a filter, gradually transferring the stress to the spring. This arrangement provides a simplified depiction of a viscoelastic solid. When a static stress is applied, the solid undergoes a finite deformation and resists the applied stress, ultimately reaching a state of mechanical equilibrium.

This expression in the frequency domain:

$$\tau = \mu_{kv}\gamma + \eta_{kv}j\omega\gamma \tag{4.25}$$

is used to calculate G′ and G″, the real and imaginary parts of the ratio $\frac{\tau}{\gamma}$:

$$G'(\omega) = \mathrm{Re}\left(\frac{\tau}{\gamma}\right) = \mu_{kv} \quad \text{and} \quad G''(\omega) = \mathrm{Im}\left(\frac{\tau}{\gamma}\right) = \omega\eta_{kv} \tag{4.26}$$

G′ is frequency-independent, meaning that the elasticity of the material remains unaffected by changes in the frequency of the propagating wave. On the other hand, G″ exhibits a linear dependence on frequency, where the attenuation term is directly influenced by the frequency.

Next, by employing the fundamental principle of dynamics, expressed as $\rho\frac{\partial^2\gamma}{dt^2} = \frac{\partial^2\tau}{\partial x^2}$ (ρ being the density of the material) the wave vector expression can be derived as a function of the frequency and the rheological parameters.

$$k^2 = \frac{\rho\omega^2}{\mu_{kv} + j\omega\eta_{kv}} \tag{4.27}$$

Finally, from the real and imaginary wave vector parts the wave velocity and attenuation for shear waves are obtained, respectively.

Wave velocity:

$$c_{ph}(\omega) = \frac{\omega}{\mathrm{Re}(k)} = \sqrt{\frac{2(\mu_{kv}^2 + \omega^2\eta_{kv}^2)}{\rho(\mu_{kv} + \sqrt{\mu_{kv}^2 + \omega^2\eta_{kv}^2})}} \tag{4.28}$$

Attenuation:

$$\alpha_s(\omega) = \mathrm{Im}(k) = \sqrt{\frac{\rho\omega^2(\sqrt{\mu_{kv}^2 + \omega^2\eta_{kv}^2} - \mu_{kv})}{2(\mu_{kv}^2 + \omega^2\eta_{kv}^2)}} \tag{4.29}$$

Attenuation per wavelength:

$$\mathrm{A}(\omega) = \lambda\alpha = 2\pi \mathrm{Re}(\mathrm{k})\alpha = 2\pi\sqrt{\frac{\sqrt{\mathrm{x}^2+\omega^2}-\mathrm{x}}{\sqrt{\mathrm{x}^2+\omega^2}+\mathrm{x}}} \quad \text{with} \quad \mathrm{x} = \frac{\mu_{\mathrm{kv}}}{\eta_{\mathrm{kv}}} \tag{4.30}$$

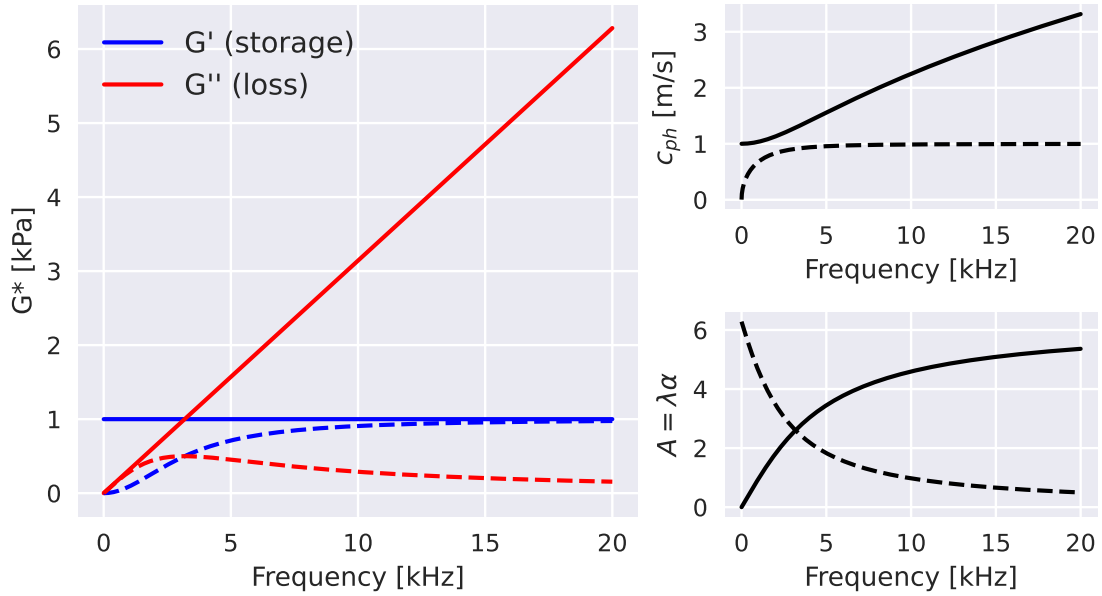

Figure 4.8. Complex shear modulus G*, phase velocity c_{ph}, and attenuation per wavelength **A** for the KV model (continuous line –), and the Mx model (dash line - -). Model's parameters: μ=1 kPa, and η=0.05 Pa · s.

This type of model tends to produce smoothed results by interpolating any gaps between the different bandwidths used. Additionally, it also smooths out any values that deviate from the expected trend in the medium. These deviations can arise from the selection of the ROI or the reconstruction algorithm employed in the analysis.

It is common practice to fit this model to a limited range of frequencies in the lower part of the spectrum, often without considering its response at higher frequencies. However, it is important to note that the model's behavior at higher frequencies can have a significant impact on the conclusions drawn from the analysis.[177]

Maxwell model. The Mx model has been used to characterize highly fluid-like media such as brain,[178] liver,[179] or blood clot.[180] In the Maxwell model, the elements are arranged in series, resulting in a stress-strain relationship in the time-domain:

$$\tau + \frac{\eta_M}{\mu_M}\frac{\partial\tau}{dt} = \eta_M\frac{\partial\gamma}{dt} \tag{4.31}$$

The spring element exhibits an immediate, constant, and reversible response. Its behavior is unaffected by the presence of the dashpot element, allowing for a rapid response. On the other hand, the dashpot responds by pulling at a constant rate of deformation. After a certain period of time, it begins to contribute to the overall behavior, representing a viscoelastic liquid. The derivation of parameters can proceed following the same procedure as described previously. The stress-strain relationship in the frequency-domain:

$$\tau + \frac{\eta_M}{\mu_M} j\omega\tau = \eta_M j\omega\gamma \tag{4.32}$$

The G* expression:

$$G'(\omega) = \frac{\mu_M\eta_M^2\omega^2}{\mu_M^2+\omega^2\eta_M^2} \quad \text{and} \quad G''(\omega) = \frac{\mu_M\eta_M^2\omega^2}{\mu_M^2+\omega^2\eta_M^2} \tag{4.33}$$

G′ is proportional to ω^2 at low frequencies, and then it reaches a plateau due to the spring at high frequencies. The increase is faster than the loss modulus. G″ is proportional to frequency ω in the low frequencies, then at high frequencies it becomes inversely proportional to ω^2.

The wave vector expression:

$$k^2 = \frac{\rho\omega^2}{\mu_M} - j\frac{\rho\omega}{\eta_M} \tag{4.34}$$

The wave velocity:

$$c_{ph}(\omega) = \frac{\omega}{Re(k)} = \sqrt{\frac{2\mu_M}{\rho\left(1+\sqrt{1+\left(\frac{\mu_M}{\omega\eta_M}\right)^2}\right)}} \tag{4.35}$$

The attenuation:

$$\alpha_s(\omega) = Im(k) = \sqrt{\frac{\rho\omega^2}{2\mu_M}\left(-1+\sqrt{1+\left(\frac{\mu_M}{\eta_M\omega}\right)^2}\right)} \tag{4.36}$$

The attenuation per wavelength:

$$A(\omega) = 2\pi\sqrt{\frac{\sqrt{x^2+\omega^2}-\omega}{\sqrt{x^2+\omega^2}+\omega}} \quad \text{with} \quad x = \frac{\mu_M}{\eta_M} \tag{4.37}$$

This approach for deriving these acoustic parameters has been published in our paper.[181] Generally, it is recognized that at short time scales, the elastic component governs the behavior, while at longer time scales, there is a dominant viscous flow. However, it is important to acknowledge that the complexity of biological media, including their morphology and composition, can significantly modify the viscoelastic flow, making it challenging to capture accurately using simple models such as the Mx and KV models.[29] Despite their limitations, these models have been widely employed in the literature and have provided valuable physical interpretations for their parameters. Furthermore, the relationship between G′ and G″ can be utilized in simple models. When these moduli are measured as a function of frequency, their crossover point indicates a transition between solid-like and fluid-like behavior. Specifically, it corresponds to a shift from a solid-like (elastic) behavior where G′ > G″ to a fluid-like (viscous) behavior where G″ > G′. In this latter regime, the material's solid behavior cannot adequately respond to the imposed vibrations, and the fluid behavior becomes dominant.

Three-element models. The previous models, which incorporate a single relaxation time ($\tau = \eta/\mu$), oversimplify the complex nature of tissues, which are composed of multiple structures spanning different spatial scales. Each of these structures corresponds to different relaxation times, highlighting the multiscale character of tissues. To account for this, three-element models introduce an additional relaxation time by incorporating a new element into the existing configurations[182] (Figure 4.9).

For instance, the standard linear solid model (also known as the Zener model) incorporates relaxation and delay by adding a spring in series with the KV representation, or a spring in parallel with the Mx representation. These configurations enable the material to fully recover when the load is removed, as the added spring exerts a restorative force on the dashpot, resulting in reversible deformation and defining a solid-like behavior.[4]

On the other hand, the standard linear liquid model involves placing a dashpot in series with the Jeffreys representation of the KV model, or in parallel with the Mx model (the Extended Maxwell model). In this configuration, the material only partially recovers after the load is removed, as the added dashpot does not return to its original position. This defines a viscoelastic liquid behavior.[37]

Fractional models. Simple rheological models are advantageous in that they can be physically interpreted by understanding the behavior of their constituents, enabling comparisons between different me-

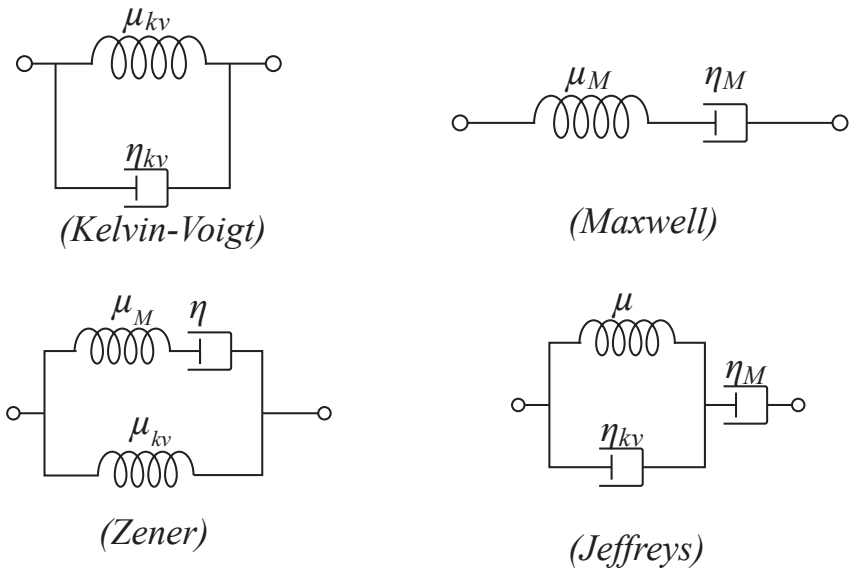

Figure 4.9. Schemes of rheological models.

dia. Viscoelastic behavior, observed when data are collected over a wide range of frequencies, exhibits multiple relaxation times, characteristic of a multiscale medium. This variation of wave amplitude with frequency in biological media usually follows a power law, i.e., linear on a log–log scale:

$$\alpha(\omega) = a_0|\omega|^y \tag{4.38}$$

where a_0 and y are constants, with $0 \leq y \leq 2$. When $y = 1$ the attenuation is proportional to the frequency. The characterization of the power law attenuation in SWs has been used for tissue classification.[183]

Fractional derivative models effectively capture this behavior in a concise manner, although their physical interpretation is not always straightforward.[29],[177]

4.5. Investigated media

Each publication within this thesis focuses on investigating the propagation of SWs in diverse media using innovative dynamic elastography techniques or novel methods of analyzing specific parameters. In this section, the interest in characterizing the selected media as well as its manufacturing process is further extended. Torsional SWs were used in the cornea; longitudinal SWs were used in polyacrylamide hydrogels; and transverse SWs were used in viscoelastic liquids.

4.5.1. Cornea

The cornea is a transparent tissue that allows the passage of light into the eyeball. It plays a crucial role in focusing the incoming light onto the retina, thanks to its high refractive power. This power is achieved by maintaining a constant intraocular pressure (IOP) of approximately 15–20 mmHg within the eyeball, giving the cornea its rounded and smooth shape. Consequently, the cornea needs to possess both flexibility to deform in response to these conditions and durability to withstand them over an extended period. The study of corneal biomechanics provides valuable insights into its physiology, as well as potential dysfunctions or pathologies.

The cornea consists of multiple layers, with the stroma comprising about 90% of its thickness and being primarily responsible for its mechanical integrity (see Figure 4.10). Collagen fibers within the stroma are arranged in lamellae, which are thin layers running from the periphery (limbus) to the center (also

Table 4.1. Summary of the main techniques used for characterize corneal biomechanics, indicating the measured property and the primary drawbacks for each one.

Technique	Property	Drawbacks	References
Extensiometry	Tensile E	Destructive, imposed boundary conditions	[188]
Inflation testing	Tensile E	Destructive	[187]
Shear rheometry	In-plane μ	Destructive	[189]
AFM	Individual (fiber) E	Ex-vivo, very sensitive	[190]
Ocular Response Analyzer	Empirical parameters	No spatial resolution, limited interpretation of output data	[191]
Corvis ST	Empirical parameters	No spatial resolution, limited interpretation of output data	[192]
Brillouin microscopy	K (bulk) modulus	Difficult to obtain mechanical contrast	[151]
Phase-decorrelation OCT	Diffusion coefficient	Unclear measured property (probably viscosity)	[193]
USE	Out-of-plane μ	Complex propagation modes	[67]
OCE	Out-of-plane μ	Very sensitive	[194]

known as the limbus-to-limbus direction) of the cornea. These lamellae are quasi-parallel to the corneal surface and exhibit varying relative angles, forming a complex interwoven network of fibers. In the central part of the cornea, lamellae run along the superior-inferior axis, while near the limbus, they adopt a circular path, forming a ring-like structure. This intricate microarchitecture is vital for maintaining corneal transparency.[184]

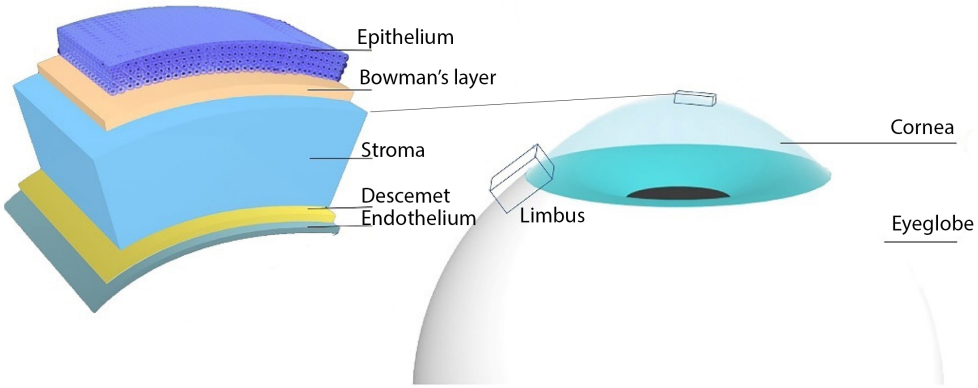

Figure 4.10. Simple anatomical structure of the eyegloble and main layers composing the cornea. Adapted from.[185]

The cornea, as a complex biocomposite, exhibits distinct characteristics that differentiate it from a simple elastic medium. It possesses viscoelastic properties, resulting from the dissipation of energy during deformation. This dissipation is attributed to the friction between the collagen fibrils and the proteoglycan matrix that holds the lamellae together.[186] Furthermore, the cornea demonstrates nonlinearity in its stress-strain response. The arrangement of collagen fibers within the cornea initially presents a wavy configuration, allowing for easy extensibility and flexibility in response to IOP. However, when these fibers align with the deformation, their stiffness increases.[187] Another notable feature is the cornea's anisotropy, which is characterized by the overlapping and interweaving of lamellae throughout its structure. This unique arrangement provides resistance against forces originating from the posterior segment, such as IOP. In contrast, the cornea exhibits weak resistance to in-plane shear forces, such as rubbing.[68] This weakness in resistance is associated with potential ectatic disorders like keratoconus.[186]

Given the complexity of the cornea, various techniques have been proposed to enhance our understanding of its biomechanical properties. These techniques offer the ability to measure different properties, often at different scales, resulting in a wide range of reported results. A summary of these techniques can be found in Table 4.1.

4.5.2. Hydrogel (Polyacrylamide)

Hydrogels are widely utilized in tissue engineering and elastography, both as tissue-mimicking phantoms and as materials for regenerative medicine. These gels offer adjustable mechanical properties that closely resemble those of soft tissues, making them ideal for simulating biological environments. Physical gels, such as agar or gelatin, are commonly used in research due to their simple fabrication process involving a heating-cooling cycle. These gels can be easily prepared by most researchers and offer accessibility and ease of implementation. In contrast, chemical gels like polyacrylamide (PAM) are created through polymerization reactions, providing a broader range of available chemical reactions for tuning mechanical parameters and achieving complex geometries.[195] To investigate the propagation of longitudinal SWs, PAM hydrogels were chosen due to their popularity when studying cell-substrate mechanical interactions, whose interest was explained in Section 3.6.1.

Acrylamide serves as the monomer, which interacts with bis-acrylamide (MBAM), acting as a crosslinking agent to create a stable network structure. An acrylamide solution is typically employed, with an acrylamide to bis-acrylamide ratio of 19:1 and a mass concentration of 40% (w/v). This solution can be adjusted by dilution with distilled water to achieve the desired concentration. Higher concentrations of acrylamide result in a firmer gel matrix. To initiate the polymerization reaction, redox agents such as ammonium persulfate (APS) and N,N,N′,N′-tetramethylethylenediamine (TEMED) are utilized. The APS concentration is typically 10% (w/v). The resulting product is polyacrylamide, a polymerized form of acrylamide that is considered non-toxic.[196]

To visualize propagating waves within the gel medium, scattering particles or elements that respond to mechanical excitation are incorporated. In the case of relatively homogeneous media like polyacrylamide, visualizing the waves can be challenging. To address this, scattering particles smaller than the wavelength of the wave are commonly used. Examples include graphite powder or TiO_2 particles. However, it's important to note that incorporating a high concentration of particles may render the solution opaque, making it difficult to visualize the wave using direct optical methods such as high-speed cameras.

The concentration of each component in the gel formulation plays a critical role in determining the mechanical properties of the gel, similar to how the microstructure of soft tissues governs their mechanical behavior. The synthesis of polyacrylamide involves an exothermic reaction, resulting in temperatures of 40–50ºC. It is worth noting that the mechanical properties of the gel are temperature-dependent.[197] Employing a forced cooling process during polymerization has been observed to yield a more transparent gel phantom at approximately 25ºC.[198]

Table 4.2 presents the concentrations of ingredients commonly used for high-intensity focused ultrasound (HIFU) dosimetry studies.

Table 4.2. Concentrations of ingredients used to manufacture PAM by application. HIFU: high-intensity focused ultrasound. NS: Not Specified.

Acrylamide solution %	APS %	TEMED %	Scattering particles %	Application	Reference
5-6 (w/v)	0.2 (w/v)	0.1 (v/v)	Graphite: 2 (w/v)	USE	[195]
30 (v/v)	0.84 (w/v)	0.05 (v/v)	Glass beads: 0.002 (w/v)	HIFU	[198]
8 (w/w)	0.01 (w/w)	NS	-	Mechanosensing	[199]
2-20 (w/v)	0.06 (w/v)	NS	TiO_2: 30 (w/v)	USE	[200]
7 (w/v)	10 (w/v)	NS	-	HIFU	[197]
24.8 (v/v)	0.5 (v/v)	0.2 (v/v)	-	HIFU	[201]
25.71 (v/v)	0.64 (v/v)	0.39 (v/v)	-	HIFU	[202]

4.5.3. Viscoelastic liquids

A viscoelastic liquid is a type of fluid that exhibits both viscous and elastic behavior when subjected to deformation. This means that the liquid can flow and deform like a solid, depending on the conditions

and the time scale of the deformation. In a viscoelastic liquid, the deformation response is characterized by an elastic component, which causes it to resist deformation and return to its original shape once the deformation is removed, and a viscous component, which resists shear and dissipates energy as the liquid flows.[174] Examples of viscoelastic liquids include polymer solutions, low concentration gels, and certain biological fluids such as blood and mucus.

The flow behavior of polymeric liquids is determined by their chemical composition. Polymers are macromolecules composed of repeating chemical structural units that are interconnected to form the macromolecule. The molecular weight of a macromolecule is proportional to the molecular weight of its structural units and their number. In general, higher molecular weight or more ordered structures result in longer relaxation times for polymers. Thermal movements cause rearrangements of the interconnections between structural units, leading to various relaxation times based on the number of changes. These relaxation times impart memory to the material, contributing to its elastic behavior, although it is not perfect since polymeric fluids are not chemically cross-linked.

Xanthan gum (XG) is a polysaccharide produced through the fermentation of the Xanthomonas campestris bacteria. It consists of monosaccharide units that covalently bond to form polymeric chains of carbohydrates. XG is water-soluble and acts as a viscosity-enhancing polymer. It has a high molecular weight and good water solubility.[203] It can be dissolved in an aqueous solution, either cold or hot. Its viscoelastic and fluid properties are attributed to the ability of XG macromolecules to form intra- and intermolecular hydrogen bonding. When the shear rate increases, these bonds are gradually disrupted and aligned with the flow direction, resulting in shear thinning behavior. Hydrogen bonds form and break during fluid motion, and this dynamic behavior dominates the intermolecular forces, influencing viscosity.[204] These types of bonds are easily disrupted, particularly compared to covalent bonds. The elasticity of XG comes from the three-dimensional polymeric network (molecular chains) that imparts a gel-like structure. A high viscosity measurement indicates that the intermolecular forces can impede flow more effectively.

XG finds applications in various industries, including pharmaceuticals, oil, and the food industry. More recently, due to its biocompatibility, it is being explored for use in tissue engineering and as a hydrogel.[205] It acts as a thickening agent and stabilizer, preventing the separation of mixed materials and enabling the suspension of solid particles. Typically, XG is used in concentrations below 1%. The rheology of XG is commonly studied in the low-frequency range.[206]

The investigation of SW propagation in this type of medium has received limited attention in the field of elastography. Due to the specific mechanical properties and excitation characteristics, a portion of the energy associated with wave propagation is lost. This energy loss is attributed to the absorption of acoustic energy and the presence of viscosity, which generate pressure gradients and deform the medium. In liquids, these effects result in internal flow and deformation of molecular chains. The viscous penetration length represents the distance over which viscous forces exert a significant effect, causing the wave amplitude to decay by a certain value. Beyond this length, no further momentum (inertial forces) can be transmitted.

$$\delta = \sqrt{\frac{2\eta}{\omega\rho}} \tag{4.39}$$

where δ is the viscous penetration length, η is the dynamic viscosity of the medium, ω is the angular frequency of the shear wave, and ρ is the density of the medium.

A diffusion equation can represent a viscous wave in a viscoelastic fluid.[10] By omitting the spring term on the KV viscoelastic wave equation, and integrating with respect to time:

$$\boldsymbol{\nabla}^2 \mathrm{u} - \frac{\rho}{\eta}\frac{\partial \mathbf{u}}{\partial \mathrm{t}} = 0 \tag{4.40}$$

The attenuation and phase velocity terms:

$$\alpha = \sqrt{\frac{\rho\omega}{2\eta}} \qquad \mathrm{c_{ph}} = \sqrt{\frac{2\eta\omega}{\rho}} \tag{4.41}$$

By inserting this magnitudes into the attenuation per wavelength expression (Equation 3.24), $\mathbf{A}(\omega) = 2\pi$, meaning that the amplitude of the wave could be measurable only around 0.16λ penetration depth. That is why is considered a non propagating solution.

5

Concluding Remarks

This chapter provides a concise summary of the key conclusions derived from each paper, along with a brief discussion highlighting their respective contributions. The fulfillment of the proposed objectives are reviewed (along with the proposed tasks), and the research questions posed in the introduction are addressed.

Objective 1: Develop an elastography technique based on torsional SWs (TWE) adapted to the specificities of the cornea and determine its capability to differentiate between different mechanical states.

In Paper A, the diagnostic capabilities of the TWE technique in assessing the mechanical properties of the cornea were demonstrated. The design of the piezoelectric sensor and the generation of torsional waves by means of an electromechanical actuator made it possible to work with a device adapted to the curvature of the cornea (*Task 1*). By measuring displacements in the propagation plane perpendicular to the emitter axis, the influence of guided waves in the corneal thickness was effectively eliminated (*Task 2*). The TWE technique provided a direct and accurate assessment of the corneal viscoelasticity, reducing the need for complex wave models and provided a fast reconstruction method with minimal post-processing. The results showed that as deformation increased, the elastic modulus of the cornea also increased, highlighting the ability of TWE to capture changes in rheological properties. Importantly, the study revealed that measurements performed on collagen lamellae planes (in-plane) provided valuable insights into corneal viscoelasticity, distinct from USE and OCE techniques that measured out-of-plane propagation. The findings were consistent with previous studies, demonstrating the potential of TWE in evaluating the mechanical properties of the cornea. Furthermore, the study investigated the effects of alkali burn on corneal viscoelasticity and observed alterations in shear elasticity and viscosity parameters. The results indicated that TWE could detect changes in the cornea resulting from chemical treatment, suggesting its potential for assessing corneal health conditions (*Task 3*). The viscosity parameter increased in the treated group, indicating a greater loss of energy and enhanced viscous damping. The corneal thickness also increased in response to the chemical treatment. The study also explored the correlation between SW speed and intraocular pressure (IOP). The findings revealed a positive correlation between wave speed and IOP, indicating the influence of tissue stress on mechanical properties. Additionally, shear viscosity showed a positive correlation with IOP, suggesting alterations in the viscous proteoglycans and shear interactions with the extracellular matrix under varying stress conditions.

While the study presented promising results, it is important to acknowledge certain limitations. The method may have missed focal abnormalities due to the absence of a 2D imaging component. Considerations such as stress distribution generated by IOP and physiologic conditions should be incorporated to address potential bias. Future studies could focus on integrating TWE into conventional examination procedures and exploring the feasibility of contactless measurements. Further investigations could also incorporate anisotropy and nonlinearity into the analysis, considering the anisotropic nature of the cornea. The use of axisymmetric propagation and sectorized rings could provide information in multiple directions simultaneously, enabling the assessment of regional heterogeneity in corneal mechanical properties.

Objective 2: Develop an optical micro-elastography (OME) technique capable of generating and tracking high-frequency SWs with sufficient spatial and temporal resolution, enabling viscoelastic analysis of soft media across an ultrawide frequency range.

In Paper B, the feasibility of using Optical Micro-Elastography (OME) to obtain reliable viscoelastic analysis over a wide frequency range was demonstrated. A high frequency excitation technique to achieve micrometer resolutions and prevent guided wave propagation was employed. A magnetically based excitation method without direct mechanical contact was proposed, allowing for efficient transmission of the excitation frequency to the medium displacement (*Task 1*). Unlike previous studies, higher frequencies (>3 kHz) were achieved by vibrating a magnet embedded in the investigated medium, which enabled the generation of SWs. A chirp-type signal for excitation ensured a continuous dispersion curve and higher signal-to-noise ratio. The study demonstrated that by starting the excitation at 5 kHz, a balance could be achieved to avoid guided waves caused by large wavelengths. Sufficient information was obtained to reconstruct the velocity at frequencies lower than the excitation, starting at 3 kHz. By replacing the magnet with a metal plate (aluminum), it was observed a reduction in the magnetic force, indicating that the permanent magnetic field provided the necessary force to observe displacements in the medium. A high-speed camera was used to capture small displacements in a polyacrylamide (PAM) transparent hydrogel (*Task 2*).

Tests on bilayer samples revealed that only the imaging system's resolution limited the accuracy of displacement field reconstruction. The impact of window size and propagation distances on velocity estimations were discussed, which affected the final resolution and led to blurred and irregular transitions. The observed waves were confirmed to be longitudinal SWs, and their group velocity was measured. Factors such as high attenuation and inhomogeneous particle distribution could influence the shape of the dispersion curve. The study showed that the dispersive behavior of shear waves measured with OME was not sensitive to the geometrical conditions of the medium. The (f, k) space analysis indicated a single dominant propagation mode, ruling out the presence of other modes. Several arguments to confirm that the observed shear waves were volume shear waves and not Rayleigh waves or waveguide effects were provided.

The KV model, a simple rheological model based on single relaxation processes, was found to accurately describe the hydrogel materials studied, and the cutoff frequencies obtained from OME were consistent with the relaxation times of the materials. However, fitting the reduced dispersion curve to the KV model presented challenges, with high variability in estimated rheological parameters. A wider frequency bandwidth dispersion curve improved the modeling of the response from quasi-static to cutoff frequencies. The calculated cutoff frequencies depended solely on the rheological parameters and indicated the point beyond which the material did not have time to relax and vibrate at the excitation frequency (*Task 3*).

The proposed OME technique has potential applications in regenerative medicine and studying cell-substrate mechanical interactions. It offers a wide range of viscoelastic properties for media like PAM hydrogels, facilitating monitoring without disrupting cells.

Objective 3: Utilize a method based on transverse SWs to examine the frequency ranges in which a medium behaves as a classic solid (SW propagates) or a liquid (SW does not propagate) in viscoelastic liquids.

In Paper C, viscoelastic liquids, which exhibit complex rheological behavior, have been studied using SW propagation methods. Unlike Newtonian fluids, viscoelastic liquids can support SW propagation due to their internal structures. The experimental evaluation of these liquids has traditionally been limited to low frequencies using conventional rheometers. To overcome these limitations, SW propagation methods have been employed to reach higher frequencies. Various studies have successfully detected SWs in viscoelastic liquids using optical, ultrasonic, or mechanical methods. These studies have provided insights into the mechanical properties and flow processes of these liquids. Here it was investigated the frequency ranges at which a medium transitions between a classic solid and liquid state using dynamic elastography. An aqueous solution of xanthan gum (XG), a polysaccharide with viscoelastic properties, was chosen as the medium. The phase velocity and attenuation of the shear waves were derived using Fourier transform methods. The storage modulus (G') and loss modulus (G'') were reconstructed based on the phase velocity and attenuation using a rheological model-independent approach (*Task 1*). The experimental results showed that the shear wave propagation in the XG solution exhibited a dispersive behavior, similar to other viscoelastic fluids. Cutoff frequencies were identified, indicating the frequency limits beyond which shear wave propagation ceased. The XG solution exhibited liquid-like behavior at low frequencies, where the dissipating term dominated, and solid-like behavior at intermediate frequencies, where the storage term dominated. At higher frequencies, the shear waves were strongly attenuated, and the

XG solution behaved like a liquid again, therefore resembling a bandpass filter (*Task 2*). The comparison between α and λ offered an advantageous method that is independent of a specific rheological model or the type of wave propagation. It provided valuable information regarding the number of λ that can be observed before they attenuate to the noise level.

Four rheological models were proposed to explain the observed behavior. Their expressions were derived to study mainly the attenuation property, and their parameters were estimated using a fitting algorithm (*Task 3*). The three-element Jeffreys model was able to accurately fit the entire frequency range and identify the region of minimal attenuation for the wave amplitude. The study of shear waves within biological viscoelastic liquids is a promising tool for evaluating their mechanical properties.

This thesis began by highlighting the growth in the number of papers addressing "Shear Wave Elastography" over the past two decades. Several of these papers have presented new imaging modalities and experimental setups whose potential may have a significant impact on clinical practice, particularly in the field of diagnosis. Elastography, for instance, extends beyond morphology and direct observation evaluation, as commonly observed in ultrasound and X-rays. It primarily utilizes shear modulus or SW velocity to provide valuable information. These parameters prove highly advantageous in diagnosing tumors or fibrosis, effectively replacing the subjective and limited palpation techniques employed by clinicians, as well as mitigating the discomfort and unpredictability associated with biopsies. The exploration of new parameters and analysis approaches further enhances the versatility of this technique, reinforcing its appeal and potential utility.

Each of the papers included has investigated a distinct medium, and all of them have examined the propagation of SWs and derive viscoelastic properties using rheological models.

The findings presented in Paper B on the importance of having a wide dispersion curve enable us to revisit the outcomes achieved in the context of the cornea (Paper A). It is worth noting that using the TWE technique, the rheological model was only fitted to a limited number of data points in a reduced dispersion curve. Consequently, there is a potential for overestimating the shear viscosity parameter, which could partially account for the disparities observed in comparison to other methods documented in the existing literature. The generation of a wide bandwidth displacement field offers numerous opportunities for robust characterization and refined diagnostics.

As evident throughout Paper B and Paper C, dynamic elastography can be employed at various scales. Consequently, diverse excitation frequencies can be employed, prompting an exploration of wave dispersion for each specific application. In situations where the medium exhibits characteristics that are neither purely elastic nor homogeneous, and further, where wave propagation may be guided, the velocity of the waves becomes frequency-dependent. It becomes interesting to understand the nature of the propagated wave, establish its correlation with velocity and viscoelasticity, and account for and correct any significant geometrical effects that may be present. A shared objective among these studies was to avoid relying on guided waves, either by inducing in-plane deformation or by increasing the frequency. However, the latter approach posed the challenge of attenuation, as the waves propagated over shorter distances. By establishing a relationship between λ and the dimensions of the medium, as well as by analyzing dispersion curves, it becomes possible to discern the type of wave propagation occurring within a given frequency range. This can help differentiate between volume propagation and guided wave propagation. The selection of an appropriate frequency for elastography should adhere to certain criteria that depend on the specific medium and application at hand. In the context of imaging, the Nyquist criterion serves as a guideline for determining the maximum capturable frequency, while the minimum capturable frequency is determined by the imaging time. When it comes to excitation, working with volume SWs simplifies the estimation of their relationship with mechanical properties.

The utilization of micro-elastography requires the application of very high frequency SWs, which have received limited investigation within the domain of elastography. Gaining a comprehensive understanding of their characteristics and limitations using existing technology is a compelling area of research, particularly within controlled media. By studying characteristics such as dispersion and attenuation of SWs at high frequencies, it becomes possible to predict and/or determine the optimal working range. The determination of a cutoff frequency, beyond which SWs were no longer observed, not only characterized

the experimental setup's capabilities but also defined the frequency range suitable for micro-elastography. The utilization of ultrasonic SWs proves to be a promising approach for applications involving relatively stiff media, such as the cornea, skin layers, or scaffolds, among others. However, it is important to note that there is a cutoff frequency beyond which λ becomes limited, preventing an indefinite increase in frequency. In Paper B, the maximum frequency of SW propagation in a medium designed for cell culture were experimentally investigated. Additionally, the relationship between these frequencies and the utility of simple rheological models, such as KV, was explored, demonstrating the feasibility of making a reasonable approximation to this propagation limit. Similarly, this concept was applied to media that are rarely studied in elastography, such as viscoelastic liquids, which allowed to revisit rheology on these media. Delving deeper into these types of studies allows for a better understanding of the physico-chemical relationship with the mechanical parameters. The relationship between λ and the constituents of the medium is crucial for achieving a proper characterization. Exploring the evolution of viscoelastic parameters in relation to the concentration and treatments applied to the investigated media is an important area for further investigation. Despite attempts to address this issue, decoupling the contributions and providing a physical interpretation for each component or structure remains challenging.

Part I

Scientific Articles

A

Torsional wave elastography to assess the mechanical properties of the cornea

Jorge Torres, Inas Faris, Antonio Callejas, Felisa Reyes-Ortega, Juan Melchor, Miguel Gonzalez-Andrades, Guillermo Rus

Published in: Torres, Jorge, et al. "Torsional wave elastography to assess the mechanical properties of the cornea." Scientific Reports 12.1 (2022): 8354.

Quality indications:

- Impact Factor: 4.997
- Rank: 19/74 (JCR, Q1)

DOI: https://doi.org/10.1038/s41598-022-12151-2

Scientific Reports 12.1 (2022): 8354.
https://doi.org/10.1038/s41598-022-12151-2

Torsional wave elastography to assess the mechanical properties of the cornea

Jorge Torres[1,2], Inas Faris[1,2]*, Antonio Callejas[1,2], Felisa Reyes-Ortega[3], Juan Melchor[2,4,5], Miguel Gonzalez-Andrades[3], Guillermo Rus[1,2,4]

Abstract
Corneal mechanical changes are believed to occur before any visible structural alterations observed during routine clinical evaluation. This study proposed developing an elastography technique based on torsional waves (TWE) adapted to the specificities of the cornea. By measuring the displacements in the propagation plane perpendicular to the axis of the emitter, the effect of guided waves in plate-like media was proven negligible. Ex vivo experiments were carried out on porcine corneal samples considering a group of control and one group of alkali burn treatment (NH_4OH) that modified the mechanical properties. Phase speed was recovered as a function of intraocular pressure (IOP), and a Kelvin-Voigt rheological model was fitted to the dispersion curves to estimate viscoelastic parameters. A comparison with uniaxial tensile testing with thin-walled assumptions was also performed. Both shear elasticity and viscosity correlated positively with IOP, being the elasticity lower and the viscosity higher for the treated group. The viscoelastic parameters ranged from 21.33 to 63.17 kPa, and from 2.82 to 5.30 Pa·s, for shear elasticity and viscosity, respectively. As far as the authors know, no other investigations have studied this mechanical plane under low strain ratios, typical of dynamic elastography in corneal tissue. TWE reflected mechanical properties changes after treatment, showing a high potential for clinical diagnosis due to its rapid performance time and paving the way for future in vivo studies.

[1] *Ultrasonics Lab (TEP-959), Department of Structural Mechanics, University of Granada, Granada, Spain*
[2] *Biomechanics Group (TEC-12), Instituto de Investigación Biosanitaria, ibs.GRANADA, Granada, Spain*
[3] *Department of Ophthalmology, Maimonides Biomedical Research Institute of Cordoba (IMIBIC), Reina Sofia University Hospital, University of Cordoba, Cordoba, Spain*
[4] *Excellence Research Unit "ModelingNature" (MNat), Universidad de Granada, Granada, Spain*
[5] *Department of Statistics and Operations Research, University of Granada, Granada, Spain*
***Corresponding author**: inas@ugr.es

Contents

1. Introduction

The mechanical state of the cornea is assumed to be defined almost exclusively by the stroma.[1] The rest of the layers that comprise this tissue are believed to have indirect contributions, as in the case of the endothelium, which deturgesces the cornea to maintain adequate functionality.[2] The main component to which mechanical stability is attributed is collagen, whose fibers are packed and arranged, forming stacked oriented lamellae[3] (Figure 1a). Significant changes in the organization of this layer may lead to corneal disorders, including progressive and generalized weakening of the cornea, corneal opacity, and subsequent vision loss.[4] Among those, chemical eye burns, keratoconus and other ectatic disorders[5,6] emerge as a priority because of their incidence, severity, and impact on the patient´s quality of life. More than 70% of chemical burns in the eye are accidents that occur at work and 84% of them are due to alkali chemicals.[7] These high pH chemical reactants show a high penetration that can cause severe injury to external organs and tissues like the cornea.[8] They can even penetrate the anterior chamber damaging the lens, the ciliary body, and the trabecular meshwork, causing

cataract and secondary glaucoma in severe cases. The damage caused depends on the exposure time to the chemical, showing different grades of severity.[9]

From a physiological perspective, the primary function of the cornea, together with the lens, is to redirect light to the retina. Whereas the lens can change its geometry to improve focus on objects near it, the cornea has a fixed focus.[10] This means that pathologies or alterations in the cornea that manifest themselves as changes at the microstructure level directly affect its refractive capacity, primarily by modifying optical power and transparency.[11] It is believed that early diagnosis of these states could be achieved by evaluating constitutive mechanical properties, since changes in these properties occur before any of the macroscopically visible structural changes observed during routine clinical evaluation.[12,13] In addition, as a viscoelastic tissue, the relevance of viscosity has been evidenced in recent studies, which adds to the scene an important contrasting parameter.[14,15] Mechanical differences between physiological and pathophysiological conditions are expected to be sufficiently relevant to be included in the diagnosis and design of treatments adapted to each patient, whose evolution could be monitored and even predicted.[16] Therefore, effective visual care might be supported by reliable quantitative mechanical techniques.

Current capabilities from state-of-the-art are focusing on the direct quantification of mechanical properties considering different principles since a multiscale approach has not yet been sufficiently developed, where changes in the microstructure are used to explain macroscale properties. The most widespread in vivo method is designed to quantify IOP by noncontact tonometry.[17] Its working principle is based on the difference in pressure between applanation events, providing two indices of viscosity and elasticity; however, its predictive power has not been well demonstrated, since the estimation combines geometric and mechanic variables.[18] It is also known that tonometry implies high displacements for a correct measurement, which leads to a nonlinear regime that is being ignored.[19] Using the main idea of passive elastography, ocular pulse elastography was recently proposed.[20] Ocular pulsation was simulated at a typical heart rate in ex vivo eye globes, and high-frequency displacement tracking was performed. As the authors discussed, speckle tracking over consecutive frames was highly affected by several involuntary eye motions, introducing noise artifacts during postprocessing. In other techniques based on static elastography,[21] a relative strain field caused by an unknown stress field could not be considered a reliable quantitative biomechanical evaluation. Encouraged by promising results in other soft tissues, several studies applied remote palpation by acoustic radiation force to obtain 2D elasticity maps.[22–26] Polarized shear waves were induced within the field of view of the transducer and then displacements or velocities were tracked at a high frame rate as the waves propagated. These approaches provided valuable information, mainly due to a fine resolution (>15 kHz), generating high sensitivity images at the nearly micrometric level. Still, for the time being, it is difficult to reengineer a clinical setup for its in vivo implementation. Scanning time could take tens of seconds or even minutes, and the characterization and application of the high energy acoustic radiation force remain elusive, especially due to the thin corneal geometry, where complex wave patterns governed by guided waves could bias the results.[27] Lastly, optical coherence elastography (OCE) stands as the most prolific technique in terms of publications.[28,29] OCE main advantages were the microscale resolution of the images together with the microscale sensitivity in motion detection and the noncontact approach. This has prompted the development of material models that consider the complex propagation of guided waves, also including physiological conditions.[30] Even so, it was not exempted from limitations depending on the imaging modality, such as long acquisition imaging times, from several seconds to minutes, repeated stimulation that could lead to bias due to relaxation effects in the tissue, a very precise positioning where a slight motion could cause image artifacts, and a low frame rate in 2D imaging.[31,32]

Recently, the concept of torsional waves applied to elastography was introduced.[33] Preliminary work was carried out in the field of obstetrics to explore the feasibility of in vivo implementation.[34] Here we proposed developing an elastography method based on torsional waves (TWE) adapted to the specificities of the cornea. An emitting disk contacted the outermost layer and generated shear (torsional) waves that propagated axisymmetrically in depth and radially. A piezoelectric sensor adapted to the curvature of the cornea collected travelling waves through the specimen, which were used to derive biomechanical-related properties.A distinctive feature of this technique was that we obtained information about in-plane shear deformation in the cornea, therefore, the influence of guided waves, likely present in out-of-plane propagation, was found to be negligible. Measurements were performed on ex vivo porcine corneas, considering two groups, one control group and an alkali burn group that modified the mechanical properties of the cornea. After that, the corneal buttons were excised for a tensile test to compare the trends of the estimated results. Both techniques provided responses in the same mechanical plane (Figure 1). The experimental results showed evidence that this technique could discern different mechanical states and paved the way for supporting current in vivo techniques, given its methodological simplicity and fast parameter reconstruction.

2. Methods

2.1 Ex vivo Alkali Burn Corneal Model

Porcine corneal samples were obtained from a local abattoir and enucleated immediately postmortem, then placed in phosphate buffered saline solution (PBS, pH 7.4) solution until testing to prevent moisture loss. The buffer solution was prepared using di-Sodium Hydrogen Phosphate anhydrous (Reag. Ph. Eur. 99%), Potassium di-Hydrogen Phosphate (Reag. Ph. Eur. 99% purity) and Sodium Chloride (USP, BP, Ph. Eur.

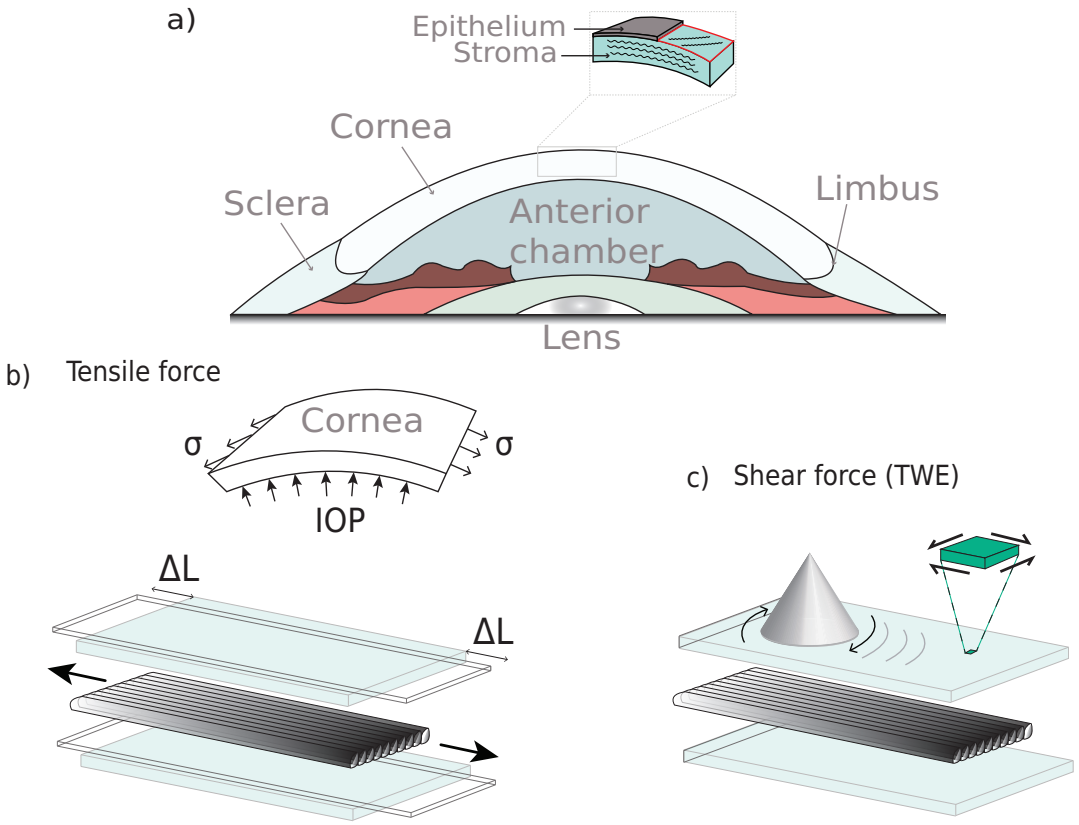

Figure 1. Sample description and applied loads: a) Sagittal superior plane of the eye, where the stroma and stacked collagen lamellae are depicted. b) In the upper part, it can be seen how the IOP creates circumferential stresses on the cornea, conferring a state of preload and therefore of nonlinearity that affects wave propagation. The mechanical response to a tensile load is shown at the bottom. c) The torsional wave emitting disk generates a mechanical response to the shear-type stimulus on the anterior surface of the cornea, which is in the same plane as the stretching produced by the tensile test.

JP 99%) from Panreac AppliChem. To produce changes in mechanical properties, a treatment solution associated with alkali burns that modified the structure of the stroma was selected taking into account the most frequent chemical reactants in house or industrial cleaning products.[35] Ammonium hydroxide 3 mM (NH_4OH at 10% v/v) was used at a similar concentration as usual fertilizers and the double concentration found in cleaning products.[36] Ammonium hydroxide solution (EMSURE ACS, Reag. Ph Eur 28-30%) was purchased from Merck. Treatment solutions were prepared in MilliQ water. All reactants were used as received without further purification. No treatment was applied to the control group, only washing for 1 minute in PBS.

A total of 16 samples were tested within the first ten hours after excision. They were classified considering the treatment and exposure time (Figure 2), resulting in 2 groups with 8 samples in each of them: control and NH_4OH for 5 minutes. Treatment was applied to the entire eye globe by immersion in 50 mL of the respective solution during the established exposure time. The treated samples were then washed in PBS, and the epithelium was mechanically removed using a spatula. Visually, we can observe that the damaged cornea leads to the opacity of the stroma. All corneal samples were used for a subsequent examination with TWE and tensile test.

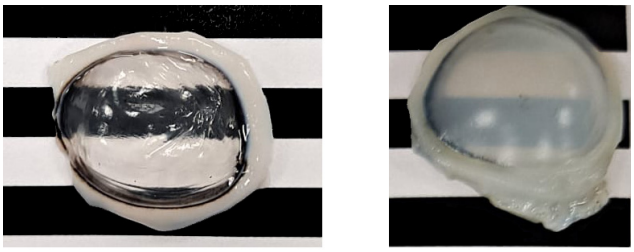

Figure 2. Porcine corneal samples from the control and treated groups. The background pattern evidenced structural changes that ammonium hydroxide (NH_4OH) causes.

2.2 Torsional Wave Elastography

An elastography device with a matching design was proposed, where the excitation and sensor parts were assembled. The excitation generated torsional waves in the specimen by direct contact. These were shear waves that propagate axisymmetrically within the cornea's surface, transmitting an oscillatory rotation through a cone-shaped disk (4 mm base) that was

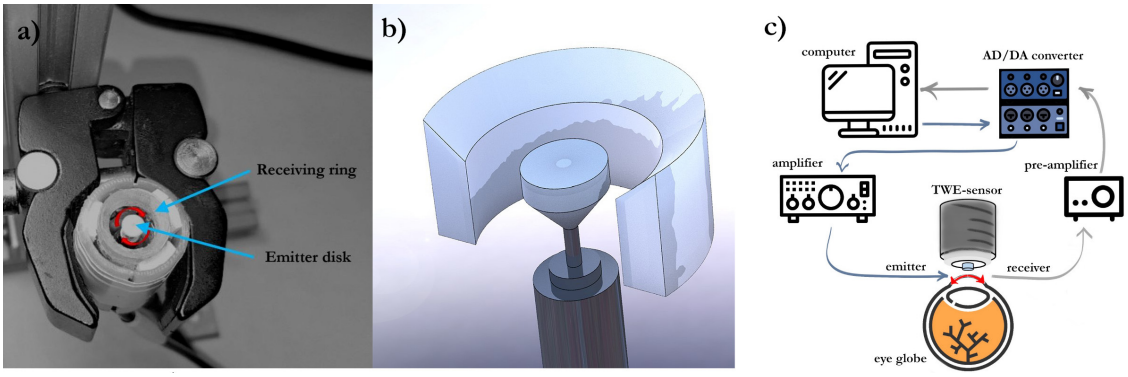

Figure 3. Torsional Wave Elastography (TWE): a) the final assembly with the contact components marked and the attenuator elements visible in white on the contour of the device; b) rendered isometric view where the curvature of the contact ring is visible; c) experimental setup for corneal tissue characterization using TWE.

driven by an electromechanical actuator. Two parallel rings formed the sensor, with four slots in each inner face, where four ceramic piezoelectric elements (PZT-5) working in shear mode were connected with a conductive resin.[33] This configuration minimized the recording of unwanted compressional waves.[37,38]

The dimensions and geometry of the contacting receiving ring were selected to match the samples.[39] The external and internal diameters were 13 mm and 9.6 mm, respectively, with an internal curvature that covered the corneal shape completely. This set was assembled in a casing with mechanical attenuators that also centered the emitting disk relative to the receiving ring (Figure 3a,b). All components were 3D printed using a biocompatible photopolymer resin (MED610, Stratasys Inc., Eden Prairie, MN, USA) except for the casing that was printed in PLA (polylactic acid).

A multichannel AD/DA converter with 24 bits and a 192 kHz sampling rate was used to generate and record the received signals. In principle, this sampling frequency increased the maximum wave speed limit sensitivity compared to ultrasound elastography modalities. The digital to analog converter outputs a single sinusoidal pulse of 500, 600, 700, 800, 900, and 1000 Hz, the six frequencies used in this study, connected to a sound amplifier (100 W) that transmitted a load of 25V peak-to-peak to the emitter. Immediately after that, the recording step started and a preamplifier captured the receiver's electrical signal (40 dB gain), to reach the AD converter; this setup is illustrated in Figure 3c. During this transition, no interfering effect between steps was observed. A 5 kHz low-pass filter was applied to the received signal to eliminate the high-frequency jitter. To reduce random noise, the resulting signal consisted of an average of 16 signals, acquired at 200 ms time intervals, for a total measurement time of 3.2 seconds. Prior to measuring the sample, a calibration signal was taken to counterbalance crosstalk effects. Finally, a dedicated algorithm was used to calculate the phase shear wave speed. The cornea behaves as a dispersive medium, therefore its mechanical response depends on the excitation frequency. By leveraging this fact, the time-of-flight was computed for each excitation by subtracting a quarter of the period, corresponding to the frequency of the highest energy in the response, from the first peak. Speed was retrieved by considering the distance traveled and this time. Note that medium curvature has been shown to be irrelevant for speed calculation.[40] All elements were computer controlled using high speed communication ports and a Matlab environment (R2018b, The MathWorks Inc., Natick, MA, USA).

The entire porcine eyeball was placed in a custom-made holder and the cornea was oriented side up. The device covered the cornea with gentle pressure, a fixed force of 500mN, and all samples were measured three times by repositioning for averaging. The eyeball was cannulated with a needle near the limbus to access the anterior chamber. This needle was connected to a saline infusion reservoir, which was used to modulate IOP by adjusting its height. Measurements were performed at pathophysiologically relevant controlled pressures of 5, 10, 15, 20, 25, and 30 mmHg, waiting 2 minutes for IOP stabilization.

Preliminary safety considerations were examined. In this modality, no cavitation-related problems were expected. Induced displacements were measured with an ultrafast ultrasound scanner (Vantage 256, Verasonics Inc., Redmond, WA, USA) that tracked the wave propagation with plane waves at a rate of 25 kHz, placing a 18.5 MHz transducer in a plane perpendicular to the axis of the emitter in the same setup previously described. The displacement peaked in the control group at around 2 µm, thus a linear regime was assumed. In a recent study with a similar configuration,[34] the maximum acoustic intensity of TWE was estimated at 5.3 mW/cm^2, well below the spatial peak temporal-average intensity limit of 17 mW/cm^2 set by the FDA for ophthalmic applications.[41]

To characterize the viscoelasticity of the tissue given the dispersion curve, a rheological model is the most straightforward approach. The diligent task of identifying the best model is currently under discussion in the scientific community. The Kelvin-Voigt model (KV) was chosen in this work due to its widespread use in the literature and the low range of frequencies.[28] This model is composed of two elements

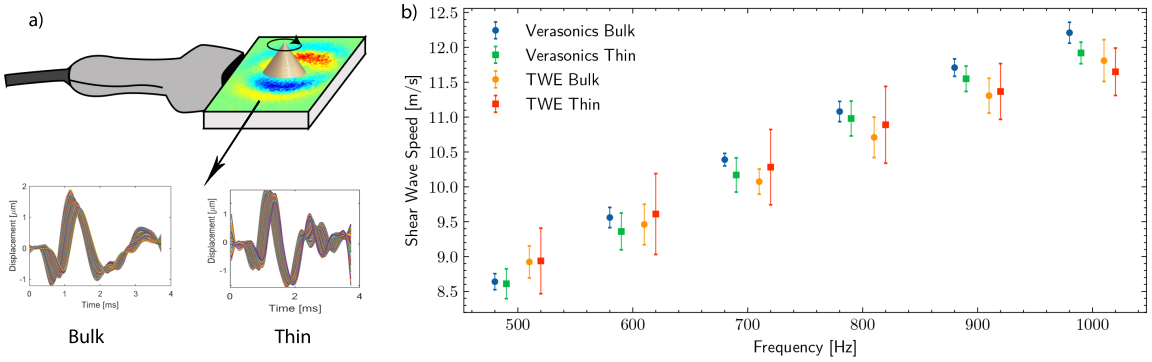

Figure 4. Exploring the torsional wave propagation under different geometries: a) Shear wave imaging was performed on the horizontal plane of both thin and bulk polyacrylamide phantoms. The time profile of the displacements was similar for both geometries. b) Comparison plot of TWE (Torsional Wave Elastography) and verasonics (shear wave imaging) results. Verasonics validates both the values obtained and the negligible effect of guided waves. Results are displayed as mean ± standard deviation.

that connect the physical interpretation with the experimental values. Shear elasticity and viscosity were obtained by fitting the dispersion curve using a nonlinear least squares (BFGS) method.

2.3 Torsional Wave Dispersion In Confined Media

The configuration of the TWE device was optimized to emit and receive displacements in the same plane of the emitter axis, which in the anterior surface of the cornea corresponds to the lamellae plane or the in-plane mechanical response, see Figure 1c. To study the effects introduced by confined geometries on the propagation plane perpendicular to the axis of the emitter (axysimmetrical propagation), two prismatic phantoms were manufactured. Isotropic viscoelastic polyacrylamide phantoms (PAAm) have been manufactured with 50% concentration following the recipe of Kumar et al.[42] This material provided a surface similar to the cornea, ideal for our contact approach, and reached speeds in the range of the corneal tissue. The phantoms were made with different thicknesses, thin ones of 1.2mm mimicking, a typical thickness of a porcine cornea, and bulk ones of 15mm thickness. The phantoms were measured three times with TWE at constant pressure to average, and an ultrasound gel was placed underneath to simulate aqueous humor.

For the purpose of validation, the induced displacements were measured with the previously described configuration of the Verasonics research equipment. The L22-14v transducer was used to receive torsional waves generated by an emitter identical to the one encapsulated in our torsion wave probe. The phase speed was retrieved with the classical method of computing the phase from the Fourier transform and fitting a linear model to the propagation distance at each frequency.

2.4 Tensile Test Setup

As a reference to TWE, uniaxial tensile tests were conducted to obtain the shear wave speed of porcine corneas in the two studied groups. The device used was ElectroForce 3200 Series (TA Instruments, EEUU). The setup consisted of two clamps with specific surface roughness to avoid sample slippage. The lower clamp was attached to a load cell whose maximum capacity was 22 N, with a resolution of 0.001 N.

After corneal button extraction, all samples were cut into vertical strips in the nasotemporal direction to avoid orientation dependency and without the sclera. The samples were gripped by two shoulders and the main deformation occurred in the central cross section (gauge section). The dimensions of the samples (length, width, and thickness) were measured using an electronic caliper. The average thickness was 1.32 ± 0.0608 mm and 1.87 ± 0.1277 mm for the control and NH_4OH groups, respectively.

The samples were preconditioned with one load/unload sequence at 1 N to reach a stage of stable behavior.[43] Then the tissues underwent another load/unload quasi-static uniaxial sequence at a rate of 0.05 N/s up to a limit force of 2 N. The test was performed by moving the lower clamp through an extended stroke accessory. The corneal samples were kept continuously hydrated by spraying them with PBS to prevent severe alteration of the mechanical properties during the experiment. To obtain the complete stress-strain curve, the stress was obtained by dividing the force measured in each increment of displacement by the initial section in the most unfavorable area, and the deformation by dividing the displacement by the initial length between the clamps. This initial length was set when the sample was stretched under a load of 0.01 N. The thickness of the samples was considered constant throughout the test (Figure 5).

Following the nonlinear behavior of the stress-strain curve, we approximated the stress state caused by the internal applied pressure during TWE measurements for a valid comparison. The curve was analyzed in six regions corresponding to the stress associated with each of the previously imposed IOPs in the cornea. This circumferential stress (see Figure 1 b), under the thin-walled hypothesis, was calculated according to the following equation,

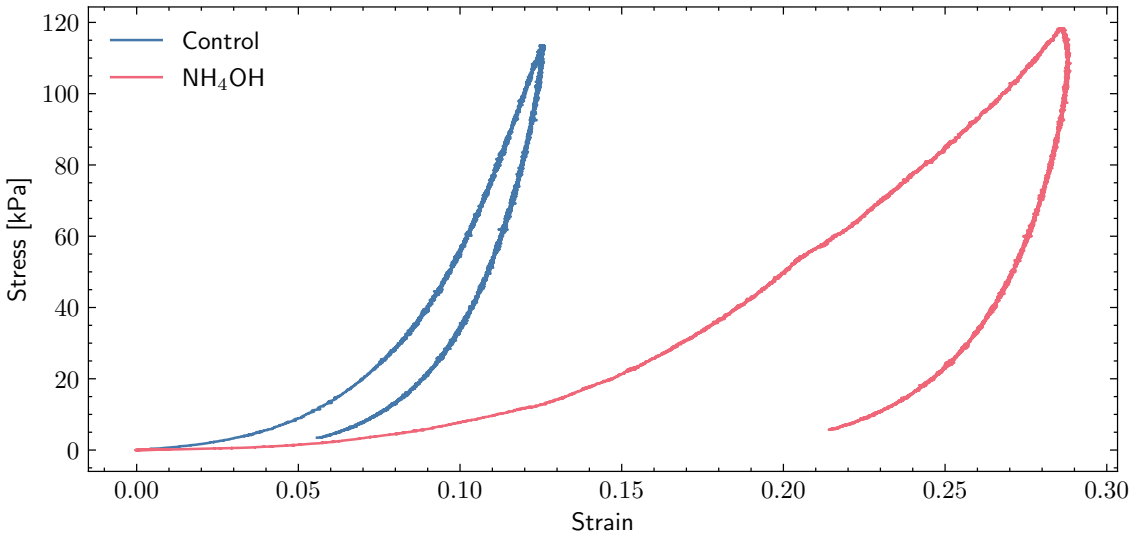

Figure 5. Typical load/unload curves for control and NH_4OH samples. Hysteresis is more pronounced after chemical treatment. The limit force was 2 N.

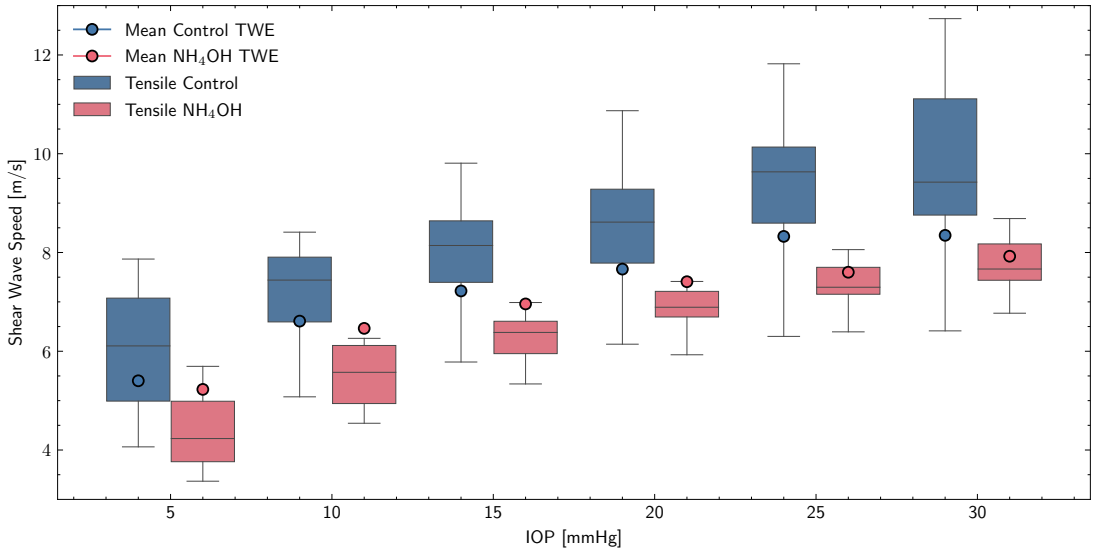

Figure 6. Comparison of shear wave speed from uniaxial tensile tests and TWE (Torsional Wave Elastography) results for each intraocular pressure (IOP). The boxplot of the tensile tests shows the same trend as the mean shear wave speed of TWE (blue points - control samples, red points - NH_4OH samples).

$$\sigma = \frac{P \cdot r}{2 \cdot e} \tag{1}$$

where P was the internal pressure, r the mean corneal radius (8.45 mm),,[44] and e the average cornea thickness. To determine the Young's modulus, a searching algorithm was implemented in Matlab to identify the strain region that corresponded to the circumferential stress for each IOP. Then with assumptions of incompressibility, linearity, and isotropy, the shear wave speed was retrieved.

3. Results

3.1 Dispersion Analysis With Material Thickness

Figure 4 a shows similar displacement in time profiles for both geometries: thin and thick polyacrylamide phantoms, with the difference of some ripples at the end of the thin phantom that were not relevant for analysis. Figure 4b displays a dispersion curve for a range of excitation frequencies 500-1000Hz for

both methods and geometries. We noticed that Verasonics, as the gold standard, validated our proposed device and that the confined geometries did not affect our wave propagation analysis. The effect of guided waves, if present under this excitation, was neglected in this measurement plane.

3.2 Tensile Tests At Low Strains

Figure 5 shows the representative cyclic behavior of the studied groups, where the maximum stress value, relative to 2 N, marks the starting point of the unloading phase.

By observing Figure 5, the control group (blue line) has a steeper slope with respect to the treated group (red line). Despite the 2 N limit, different stresses were reached in each sample due to different cross sections. The circumferential stresses ranged from 8.71 to 13.27 kPa for both groups, and the corresponding strain ranges in the curve were 4-6% for control, and 11-13% for NH_4OH. Additionally, it can be observed how the enclosed area (hysteresis) varies in each cycle, increasing in the case of the treated sample compared to the control sample.

Figure 6 shows a comparison of the shear wave speed of the uniaxial tensile test and TWE for both groups (control and NH_4OH samples) and for each IOP. TWE results are displayed as the mean of all frequencies to verify that both techniques follow the same trend. We observed that strain varied nonlinearly with IOP and shear wave speed increased as well for both techniques. Furthermore, the values of the treated group were lower than those of the control sample.

3.3 Corneal Viscoelastic Characterization by TWE

Figure 7 displays a summary of the dispersion curves obtained by TWE for each group under different IOPs. The speed of the shear wave increased with frequency and IOP for both the control and NH_4 OH groups, showing lower values for the treated group. It can also be seen in all results figures that the increase in IOP accentuates the differences between the groups studied.

As a dispersive medium, the cornea showed that different excitation frequencies affected the final estimation, with higher speed related to higher frequencies. Figure 8 shows the Kelvin Voigt (KV) fitted values of the dispersion curves of both control and NH_4OH groups for each IOP value. Shear elasticity increased with IOP in both groups, being higher in the control group. The viscosity was higher in the treated groups; this agreed with the results shown in Figure 6.

4. Discussion

4.1 Plane Of Measurement And Propagation

In this study, the diagnostic capabilities of TWE were reported on a geometry as specific as that of the cornea. Figure 4 reveals that when displacements were measured in the propagation plane perpendicular to the axis of the emitter, there were no differences in speeds at different thicknesses. This meant that by measuring the direct wave, the results were not affected by guided waves in the corneal thickness. The use of the torsional wave technique reduced assumptions of complex wave models. When soft tissue is deformed at low ratios, typical of dynamic elastography, collagen bends easily and offers little resistance; the response is taken over by other stromal components and interlamellar forces.[45] As the deformation increases, the collagen fibers begin to align with the load, inducing greater stress and thus higher elastic modulus. These strain ranges ($>$20%) are those shown in various studies (see Figure 6 in Pitre et al.[40]), resulting in values in the MPa range. For our part, we leveraged the resolution of the load cell and the 10kHz data acquisition rate of the software to generate curves with sufficient resolution in the strain range 1-10% to obtain results in kPa magnitudes. This allowed a direct comparison with tensile tests and a consistent mechanical validation of the proposed technique (Figure 6). We noticed that with our methodology, the tensile results were similar to TWE, so that the geometrical constraints imposed, such as clamping and loss of curvature had minimal effect at such low strains. However, the determination of circumferential stress due to IOP needs to be carefully interpreted, since we assumed the cornea to be spherical and its thickness to be uniform.

It is important to emphasize that all measurements were performed on collagen lamellae planes (in-plane), unlike the ultrasound and OCE techniques[40] presented in the literature, which measured out-of-plane propagation. Studies that considered that guided waves were created within the corneal tissue concluded that the use of Lamb wave models was necessary to provide a more accurate description of the viscoelasticity of the cornea.[24,46] We observed that their results were below 10 kPa, which was supposed to reflect the out-of-plane (interlamelar shearing) shear modulus. When no Lamb wave model was considered, several studies reported a shear modulus between 40 and 80 kPa.[14,23,25,47,48] Our results of shear elasticity ranged from 21.33 to 63.17 kPa for the cornea in the lamellae plane (in-plane). Assuming homogeneity and isotropy, these values were consistent with the previous ones, even though to our knowledge, none of them have evaluated a rheological model in this propagation plane. Although different planes of mechanical behavior have been studied, it would be interesting to elucidate which of them could be more sensitive to pathological-related changes.

This evidences that our current knowledge of the role of viscoelasticity in corneal health status is limited. The procedures presented in the literature are still in the research phase, besides obtaining a dispersion curve is a complex analysis of the signal that consumes considerable time and is not integrated into clinical equipment focused on optics. In the specific case of Verasonics, which is research-only equipment, the FDA has not authorized them for clinical in vivo application. The proposed TWE technique presented values as an average of global mechanical properties that translated into a fast reconstruction method, with hardly any postprocessing. The Kelvin-Voigt parameters reconstruction took around 3 seconds *in situ*. A significant advantage was the low energy deposited in the medium compared to ARF-based techniques.

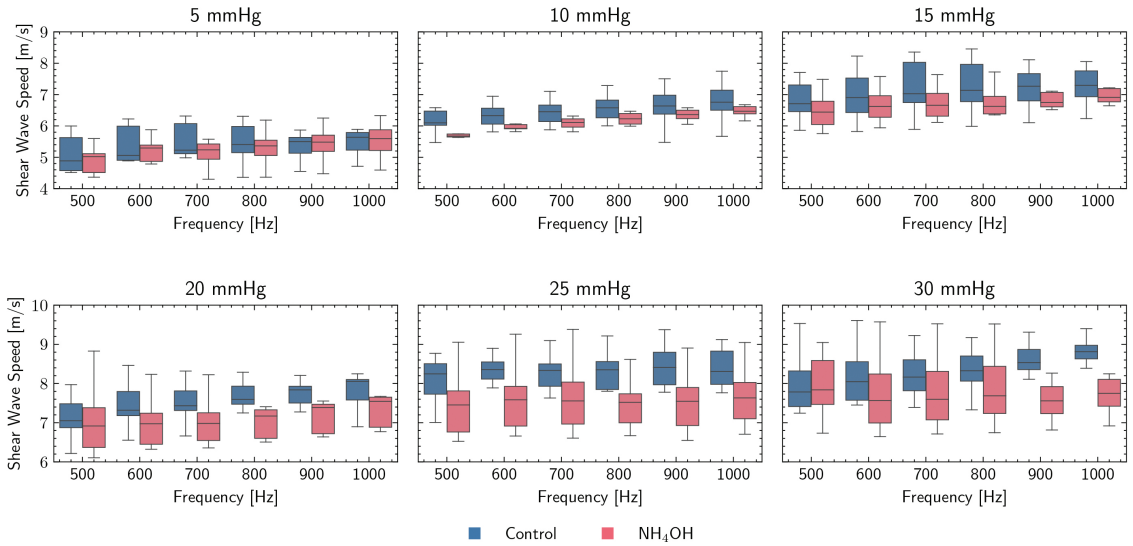

Figure 7. Torsional Wave Elastography (TWE) results: box plots of TWE dispersion curves differentiating each group. Two increasing trends are observed, the first with increasing frequency, and the second with increasing intraocular pressure (IOP). Ammonium hydroxide (NH_4OH) group exhibits lower values than the control group.

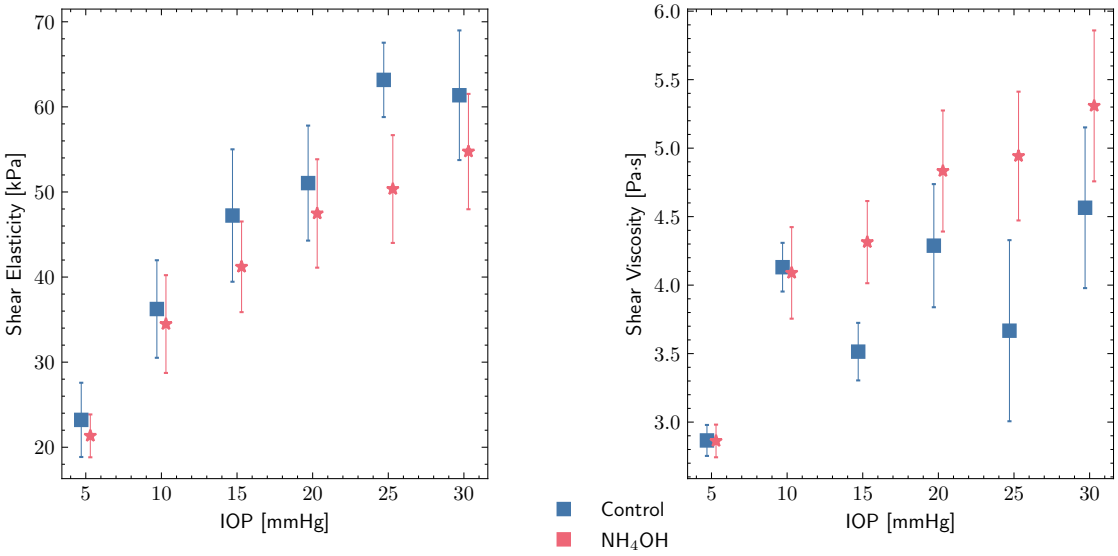

Figure 8. Viscoelastic parameters for *ex vivo* porcine corneal samples using Kelvin Voigt (KV) model on elastography results. Shear elasticity and viscosity are displayed for Ammonium hydroxide (NH_4OH) and control groups under different intraocular pressures (IOP). The results are displayed as mean ± standard deviation.

Here we have used six frequencies, observing a lower variability at higher frequencies. This flexibility in choosing the excitation frequency within the limits of the tissue response could be used to improve the SNR or explore the potential for attenuation and dispersion in specific ranges. Unlike other techniques, where a map was reconstructed, no analysis artifacts were detected or included, such as diffraction or guided waves.

4.2 Alkali Burn Corneal Model Effects On Viscoelasticity

Several studies have tried to shed some light on the potential of viscoelastic biomarkers by associating corneal hysteresis with viscosity in air puff applanation experiments, since they observed lower hysteresis values in patients with keratoconus, post LASIK, and Fuch's dystrophy.[49] In the literature, there is a lack of corneal shear viscosity values under the same configuration for comparative purposes. Shear viscosity or viscosity

parameter was mainly reported after using OCE, with values below 1 Pa·s,[14,15,46,50] whereas this study reported a range of 2.82 to 5.30 Pa·s. The increasing viscosity was expected since it was directly related to the increasing shear wave speed inherent to the KV model. In this measurement plane, the dispersive effects could be attributed to the viscosity of the tissue and not to the guiding of waves as previously discussed.

The variability of results was a consequence of the different timescales and lengthscales of each technique, wave models, and experimental conditions, reaching ambiguous conclusions. In this study, a simple Kelvin-Voigt model was used. The application of this model was subject to the assumption that the medium was macroscopically homogeneous, isotropic, and linear, besides no guided waves were generated.

Both shear elasticity and viscosity were altered after chemical treatment. In the alkali burn group (NH_4OH), the speeds and elasticity parameters were lower than in the control group. This loss was attributed to the disruption of lamellae, interweaving and collagen cross-linking in a comparable manner to keratoconus.[51] As for shear viscosity we believed that the high values were due to the highly unusual thickness of the corneas, since we could not found any other study with such values. Besides, we used ultrasonography and confirmed these thicknesses. As opposed to elasticity, the viscosity was higher for the treated group, which agreed with its hysteresis curve in Figure 5, representing a greater loss of energy, meaning that its viscous damping was more pronounced. Its reaction to the chemical treatment was to increase the corneal thickness in about 30%, probably in response to an inflammatory process. Another factor essential during *ex vivo* experiments, which we controlled, was hydration. It is known to be a confounding factor due to corneal dehydration, resulting in tissue thinning.[2,52] Since the epithelium was removed, water could easily penetrate the tissue and swell it.

4.3 Correlation Of Shear Elasticity And Shear Wave Speed With IOP

The effect on wave speed and viscoelasticity due to varying tissue stress state was studied by using different IOPs.[53] As in other investigations,[24,54] we found a positive correlation with speed and elasticity. As IOP increased, the variability of the measurements increased. Noteworthy are the results for an IOP of 30 mmHg, whose values did not differ much from those of 25 mmHg. This is believed to be due to complex wave propagation in which linear models are no longer valid.[55] Very recently, differences have been reported when IOP was considered during OCE measurements, suggesting that changes in mechanical properties and IOP were independent and could reveal different health states.[30] However, Ramier et al.[47] found no correlation between these magnitudes, possibly due to a convenient distribution of stress in the human cornea *in vivo*. Interestingly, shear viscosity was positively correlated with IOP. We hypothesized that IOP-induced stress compressed the stroma, compacting all its components.[56] This derived in an alteration of the viscous proteoglycans and shear interactions with the extracellular matrix.

4.4 Limitations and future studies

Some limitations of the current method need to be detailed. We likely missed focal abnormalities, since no 2D image was obtained. Boundary conditions like the stress distribution generated by IOP conferred a preloaded state, which could be modified because of the direct contact, The physiologic conditions surrounding biomechanical quantification should be included to correct for possible bias. IOP could be measured with tonometry, whose magnitude will define the calculated mechanical parameters. Thus, TWE has the potential to be integrated into conventional examination procedures to achieve a more direct interpretation of the experimental parameters, but several points need to be studied further. Although direct corneal contact is necessary, it is not an unfamiliar methodology with routine protocols such as tonometry or corneal pachymetry, where topical anesthetic is instilled. Recent studies have shown that this approach is feasible,[46] and that contact could be made through lenses.[57] Besides, a stable localized excitation was achieved in this modality, and by changing the diameter of the emitting disk, a shorter temporal response with increased exploitable frequency bandwidth would be expected. To further reduce contact, the receiving ring could be substituted by a small sector. To be on the side of safety, the effect of the pressure exerted when measuring will be studied in the future, both to assure an efficient propagation of torsional waves, confirming that local induced stresses do not severely affect wave propagation, and to avoid patient discomfort. The effect of sensor pressure and friction will be monitored to avoid epithelial disruption. On the other hand, this applied pressure could become an opportunity to obtain nonlinear elasticity parameters, as in acoustoelasticity, whose relevance could be substantial.[35,45] Since it is difficult for patients to maintain a fixed position or avoid involuntary movements, the short times required to take measurements are an additional benefit that helps reduce motion artifacts. Some studies have shown that the cornea is an anisotropic tissue.[23,30,40] Future studies of TWE could incorporate anisotropy and nonlinearity into the analysis and interpretation of the measurements. Additionally, one can take advantage of the axisymmetric propagation of TWE together with a sectorized ring to obtain information in several directions at the same time as a means of assessing any regional heterogeneity in cornea mechanical properties.

Acknowledgements

This research was funded by Ministerio de Educación, Cultura y Deporte grant numbers DPI2017-83859-R, DPI2014-51870-R, UNGR15-CE-3664 and EQC2018-004508-P; Ministerio de Sanidad, Servicios Sociales e Igualdad grant numbers DTS15/00093 and PI16/00339; Instituto de Salud Carlos III y Fondos Feder; Junta de Andalucía grant numbers PI-0107-2017, PIN-0030- 2017 and IE2017-5537; MCIN/AEI /10.13039/501100011033 grant number PRE2018-086085

(Co-funded by European Social Fund “Investing in your future”); Consejería de economía, conocimiento, empresas y universidad and European Regional Development Fund (ERDF) SOMM17/6109/UGR, B-TEP-026- IE2017-5537 and P18-RT-1653.

Author contributions statement

G.R., M.G.A., J.T. and I.H.F. contributed to the research design. J.T., I.H.F., A.C. and F.R.O. conducted the experiments. J.T., I.H.F. and J.M. analysed the results. J.T., I.H.F., A.C. and F.R.O contributed to manuscript preparation. All authors reviewed the manuscript.

Additional information

Competing interests: J.M., A.C., J.T. and G.R. are partners of Innitius, a company developing clinical diagnostic sensors; they have not received funding from the company for the submitted work.

References

[1] Brecken J. Blackburn, Michael W. Jenkins, Andrew M. Rollins, and William J. Dupps. A review of structural and biomechanical changes in the cornea in aging, disease, and photochemical crosslinking, 2019.

[2] Manmohan Singh, Zhaolong Han, Jiasong Li, Srilatha Vantipalli, Salavat R. Aglyamov, Michael D. Twa, and Kirill V. Larin. Quantifying the effects of hydration on corneal stiffness with noncontact optical coherence elastography. *J. Cataract Refract. Surg.*, 44(8):1023–1031, aug 2018.

[3] Steven J. Petsche, Dimitri Chernyak, Jaime Martiz, Marc E. Levenston, and Peter M. Pinsky. Depth-dependent transverse shear properties of the human corneal stroma. *Investig. Ophthalmol. Vis. Sci.*, 53(2):873–880, feb 2012.

[4] Antti J. Tuori, Ismo Virtanen, Esko Aine, R. Kalluri, J. H. Miner, and Hannu M. Uusitalo. The immunohistochemical composition of corneal basement membrane in keratoconus. *Curr. Eye Res.*, 16(8):792–801, 1997.

[5] Perry S. Binder. Ectasia after laser in situ keratomileusis. *J. Cataract Refract. Surg.*, 29(12):2419–2429, dec 2003.

[6] Keith M. Meek, Stephen J. Tuft, Yifei Huang, Paulvinder S. Gill, Sally Hayes, Richard H. Newton, and Anthony J. Bron. Changes in collagen orientation and distribution in keratoconus corneas. *Investig. Ophthalmol. Vis. Sci.*, 46(6):1948–1956, jun 2005.

[7] Mukhtar Bizrah, Ammar Yusuf, and Sajjad Ahmad. An update on chemical eye burns, sep 2019.

[8] Medi Eslani, Alireza Baradaran-Rafii, Asadolah Movahedan, and Ali R. Djalilian. The ocular surface chemical burns, 2014.

[9] Parul Singh, Manoj Tyagi, Yogesh Kumar, K. Gupta, and P. Sharma. Ocular chemical injuries and their management, 2013.

[10] Miguel Gonzalez-Andrades, Pablo Argüeso, and Ilene Gipson. Corneal anatomy. In *Corneal Regeneration*, pages 3–12. Springer, 2019.

[11] Keith M. Meek and Carlo Knupp. Corneal structure and transparency, nov 2015.

[12] AbhijitSinha Roy, Rohit Shetty, and MathewKurian Kummelil. Keratoconus: A biomechanical perspective on loss of corneal stiffness. *Indian J. Ophthalmol.*, 61(8):392, aug 2013.

[13] Riccardo Vinciguerra, Renato Ambrósio, Cynthia J. Roberts, Claudio Azzolini, and Paolo Vinciguerra. Biomechanical characterization of subclinical keratoconus without topographic or tomographic abnormalities. *J. Refract. Surg.*, 33(6):399–407, jun 2017.

[14] Zhaolong Han, Jiasong Li, Manmohan Singh, Chen Wu, Chih hao Liu, Raksha Raghunathan, Salavat R. Aglyamov, Srilatha Vantipalli, Michael D. Twa, and Kirill V. Larin. Optical coherence elastography assessment of corneal viscoelasticity with a modified Rayleigh-Lamb wave model. *J. Mech. Behav. Biomed. Mater.*, 66:87–94, feb 2017.

[15] Antoine Ramier, Behrouz Tavakol, and Seok-Hyun Yun. Measuring mechanical wave speed, dispersion, and viscoelastic modulus of the cornea using optical coherence elastography. *Opt. Express*, 27(12):16635, jun 2019.

[16] Charles N. J. McGhee, Bia Z. Kim, and Peter J. Wilson. Contemporary Treatment Paradigms in Keratoconus. *Cornea*, 34(Supplement 10):S16–S23, oct 2015.

[17] Sunil Shah, Mohammed Laiquzzaman, Rajan Bhojwani, Sanjay Mantry, and Ian Cunliffe. Assessment of the biomechanical properties of the cornea with the ocular response analyzer in normal and keratoconic eyes. *Investig. Ophthalmol. Vis. Sci.*, 48(7):3026–3031, jul 2007.

[18] Vinicius S. De Stefano and William J. Dupps. Biomechanical Diagnostics of the Cornea. *Int. Ophthalmol. Clin.*, 57(3):75–86, 2017.

[19] Roland Kempf, Yuichi Kurita, Yoshichika Iida, Makoto Kaneko, Hiromu K. Mishima, Hidetoshi Tsukamoto, and Eiichiro Sugimoto. Understanding eye deformation in noncontact tonometry. In *Annu. Int. Conf. IEEE Eng. Med. Biol. - Proc.*, pages 5428–5431, 2006.

[20] Keyton Clayson, Elias Pavlatos, Xueliang Pan, Thomas Sandwisch, Yanhui Ma, and Jun Liu. Ocular pulse elastography: Imaging corneal biomechanical responses to simulated ocular pulse using ultrasound. *Transl. Vis. Sci. Technol.*, 9(1):5–5, jan 2020.

[21] Kyle W. Hollman, Stanislav Y. Emelianov, Jason H. Neiss, Gagik Jotyan, Gregory J.R. Spooner, Tibor Juhasz, Ron M. Kurtz, and Matthew O’Donnell. Strain imaging of corneal

tissue with an ultrasound elasticity microscope. *Cornea*, 21(1):68–73, 2002.

[22] Pei-Yu Chen, Cho-Chiang Shih, Wei-Chen Lin, Teng Ma, Qifa Zhou, K. Shung, and Chih-Chung Huang. High-Resolution Shear Wave Imaging of the Human Cornea Using a Dual-Element Transducer. *Sensors*, 18(12):4244, dec 2018.

[23] Thu Mai Nguyen, Jean Francois Aubry, Mathias Fink, Jeremy Bercoff, and Mickael Tanter. In vivo evidence of porcine cornea anisotropy using supersonic shear wave imaging. *Investig. Ophthalmol. Vis. Sci.*, 55(11):7545–7552, nov 2014.

[24] Xuejun Qian, Teng Ma, Cho Chiang Shih, Martin Heur, Jun Zhang, Koping Kirk Shung, Rohit Varma, Mark S. Humayun, and Qifa Zhou. Ultrasonic Microelastography to Assess Biomechanical Properties of the Cornea. *IEEE Trans. Biomed. Eng.*, 66(3):647–655, mar 2019.

[25] M. Tanter, D. Touboul, Jean Luc Gennisson, Jeremy Bercoff, and Mathias Fink. High-resolution quantitative imaging of cornea elasticity using supersonic shear imaging. *IEEE Trans. Med. Imaging*, 28(12):1881–1893, dec 2009.

[26] David Touboul, Jean Luc Gennisson, Thu Mai Nguyen, Antoine Robinet, Cynthia J. Roberts, Mickael Tanter, and Nicolas Grenier. Supersonic shear wave elastography for the in vivo evaluation of transepithelial corneal collagen cross- linking. *Investig. Ophthalmol. Vis. Sci.*, 55(3):1976–1984, mar 2014.

[27] Mathieu Couade, Mathieu Pernot, Claire Prada, Emmanuel Messas, Joseph Emmerich, Patrick Bruneval, Aline Criton, Mathias Fink, and Mickael Tanter. Quantitative Assessment of Arterial Wall Biomechanical Properties Using Shear Wave Imaging. *Ultrasound Med. Biol.*, 36(10):1662–1676, oct 2010.

[28] Mitchell A. Kirby, Ivan Pelivanov, Shaozhen Song, Łukasz Ambrozinski, Soon Joon Yoon, Liang Gao, David Li, Tueng T. Shen, Ruikang K. Wang, and Matthew O'Donnell. Optical coherence elastography in ophthalmology. *J. Biomed. Opt.*, 22(12):1, dec 2017.

[29] Vladimir Y. Zaitsev, Alexander L. Matveyev, Lev A. Matveev, Alexander A. Sovetsky, Matt S. Hepburn, Alireza Mowla, and Brendan F. Kennedy. Strain and elasticity imaging in compression optical coherence elastography: The two-decade perspective and recent advances. *J. Biophotonics*, page e202000257, nov 2020.

[30] Michael G Sun, Taeyoon Son, Joseph Crutison, Victor Guaiquil, Shujun Lin, Lara Nammari, Dieter Klatt, Xincheng Yao, Mark I Rosenblatt, and Thomas J Royston. Optical coherence elastography for assessing the influence of intraocular pressure on elastic wave dispersion in the cornea. *Journal of the Mechanical Behavior of Biomedical Materials*, 128:105100, 2022.

[31] Matt S. Hepburn, Philip Wijesinghe, Lixin Chin, and Brendan F. Kennedy. Analysis of spatial resolution in phase-sensitive compression optical coherence elastography. *Biomed. Opt. Express*, 10(3):1496, mar 2019.

[32] Shaozhen Song, Wei Wei, Bao Yu Hsieh, Ivan Pelivanov, Tueng T. Shen, Matthew O'Donnell, and Ruikang K. Wang. Strategies to improve phase-stability of ultrafast swept source optical coherence tomography for single shot imaging of transient mechanical waves at 16 kHz frame rate. *Appl. Phys. Lett.*, 108(19):191104, may 2016.

[33] Antonio Callejas, Antonio Gomez, Juan Melchor, Miguel Riveiro, Paloma Massó, Jorge Torres, Modesto López-López, and Guillermo Rus. Performance Study of a Torsional Wave Sensor and Cervical Tissue Characterization. *Sensors*, 17(9):2078, sep 2017.

[34] Paloma Massó, Antonio Callejas, Juan Melchor, Francisca S. Molina, and Guillermo Rus. In Vivo Measurement of Cervical Elasticity on Pregnant Women by Torsional Wave Technique: A Preliminary Study. *Sensors*, 19(15):3249, jul 2019.

[35] A. Ashofteh Yazdi, J. Melchor, J. Torres, I. Faris, A. Callejas, M. Gonzalez-Andrades, and G. Rus. Characterization of non-linear mechanical behavior of the cornea. *Sci. Rep.*, 10(1):11549, dec 2020.

[36] Marion J. Fedoruk, Rod Bronstein, and Brent D. Kerger. Ammonia exposure and hazard assessment for selected household cleaning product uses. *J. Expo. Anal. Environ. Epidemiol.*, 15(6):534–544, nov 2005.

[37] Juan Melchor and Guillermo Rus. Torsional ultrasonic transducer computational design optimization. *Ultrasonics*, 54(7):1950–1962, 2014.

[38] Juan Melchor, Rafael Muñoz, and Guillermo Rus. Torsional Ultrasound Sensor Optimization for Soft Tissue Characterization. *Sensors*, 17(6):1402, jun 2017.

[39] Jens Heichel, Frank Wilhelm, Kathleen S Kunert, and Thomas Hammer. Topographic Findings of the Porcine Cornea. *Med. hypothesis, Discov. Innov. Ophthalmol. J.*, 5(4):125–131, 2016.

[40] John J. Pitre, Mitchell A. Kirby, David S. Li, Tueng T. Shen, Ruikang K. Wang, Matthew O'Donnell, and Ivan Pelivanov. Nearly-incompressible transverse isotropy (NITI) of cornea elasticity: model and experiments with acoustic micro-tapping OCE. *Sci. Reports 2020 101*, 10(1):1–14, jul 2020.

[41] Thomas R. Nelson, J. Brian Fowlkes, Jacques S. Abramowicz, and Charles C. Church. Ultrasound biosafety considerations for the practicing sonographer and sonologist, feb 2009.

[42] Kishore Kumar, Maneesha E. Andrews, V. Jayashankar, Ashok K. Mishra, and S. Suresh. Measurement of viscoelastic properties of polyacrylamide-based tissue-mimicking phantoms for ultrasound elastography applications. *IEEE Transactions on Instrumentation and Measurement*, 59(5):1224–1232, 2010.

[43] JunJie Wang, XiaoYu Liu, FangJun Bao, Bernardo T. Lopes, LiZhen Wang, Ashkan Eliasy, Ahmed Abass, and Ahmed Elsheikh. Review of ex-vivo characterisation of corneal biomechanics. *Med. Nov. Technol. Devices*, 11:100074, sep 2021.

[44] Irene Sanchez, Raul Martin, Fernando Ussa, and Ivan Fernandez-Bueno. The parameters of the porcine eyeball. *Graefe's Archive for Clinical and Experimental Ophthalmology*, 249(4):475–482, 2011.

[45] Guillermo Rus, Inas H. Faris, Jorge Torres, Antonio Callejas, and Juan Melchor. Why Are Viscosity and Nonlinearity Bound to Make an Impact in Clinical Elastographic Diagnosis? *Sensors*, 20(8):2379, apr 2020.

[46] Chien Chang Weng, Pei Yu Chen, Dean Chou, Cho Chiang Shih, and Chih Chung Huang. High Frequency Ultrasound Elastography for Estimating the Viscoelastic Properties of the Cornea Using Lamb Wave Model. *IEEE Trans. Biomed. Eng.*, 2020.

[47] Antoine Ramier, Amira M. Eltony, Yi Tong Chen, Fatima Clouser, Judith S. Birkenfeld, Amy Watts, and Seok Hyun Yun. In vivo measurement of shear modulus of the human cornea using optical coherence elastography. *Sci. Rep.*, 10(1):1–10, dec 2020.

[48] Stephen R Sloan, Yousuf M Khalifa, and Mark R Buckley. The location-and depth-dependent mechanical response of the human cornea under shear loading. *Investigative ophthalmology & visual science*, 55(12):7919–7924, 2014.

[49] Nery Garcia-Porta, Paulo Fernandes, Antonio Queiros, Jose Salgado-Borges, Manuel Parafita-Mato, and Jose Manuel González-Méijome. Corneal Biomechanical Properties in Different Ocular Conditions and New Measurement Techniques. *ISRN Ophthalmol.*, 2014:1–19, mar 2014.

[50] Zi Jin, Yuheng Zhou, Meixiao Shen, Yuanyuan Wang, Fan Lu, and Dexi Zhu. Assessment of corneal viscoelasticity using elastic wave optical coherence elastography. *J. Biophotonics*, 13(1):e201960074, jan 2020.

[51] Giuliano Scarcelli, Sebastien Besner, Roberto Pineda, Patricia Kalout, and Seok Hyun Yun. In vivo biomechanical mapping of normal and keratoconus corneas. *JAMA ophthalmology*, 133(4):480–482, 2015.

[52] Hamed Hatami-Marbini and Ebitimi Etebu. Hydration dependent biomechanical properties of the corneal stroma. *Exp. Eye Res.*, 116:47–54, nov 2013.

[53] Daniel V. Litwiller, Sung J. Lee, Arunark Kolipaka, Yogesh K. Mariappan, Kevin J. Glaser, Jose S. Pulido, and Richard L. Ehman. MR elastography of the ex vivo bovine globe. *J. Magn. Reson. Imaging*, 32(1):44–51, jun 2010.

[54] Boran Zhou, Arthur J. Sit, and Xiaoming Zhang. Noninvasive measurement of wave speed of porcine cornea in ex vivo porcine eyes for various intraocular pressures. *Ultrasonics*, 81:86–92, nov 2017.

[55] Kevin Anderson, Ahmed El-Sheikh, and Timothy Newson. Application of structural analysis to the mechanical behaviour of the cornea. *Journal of the Royal Society Interface*, 1(1):3–15, 2004.

[56] R Carmona, Víctor Carriel, R Ghinea, Elena González-Andrades, Miguel González-Andrades, and AM Ionescu. Generación y caracterización de un modelo lesional corneal ex vivo para su uso en ingeniería tisular. *Actualidad Médica*, (797).

[57] Vinicius Silbiger De Stefano, Matthew R Ford, Ibrahim Seven, Brent Hughes, and William J Dupps. In-vivo assessment of corneal biomechanics using optical coherence elastography. *Investigative Ophthalmology & Visual Science*, 58(8):4325–4325, 2017.

B

Optical micro-elastography with magnetic excitation for high frequency rheological characterization of soft media

Jorge Torres, Antonio Callejas, Antonio Gomez, Guillermo Rus

Published in: Torres, Jorge, et al. "Optical micro-elastography with magnetic excitation for high frequency rheological characterization of soft media." Ultrasonics 132 (2023): 107021.

Quality indications:

- Impact Factor: 4.062
- Rank: 6/32 (JCR, Q1)

DOI: https://doi.org/10.1016/j.ultras.2023.107021

Ultrasonics 132 (2023): 107021
https://doi.org/10.1016/j.ultras.2023.107021

Optical micro-elastography with magnetic excitation for high frequency rheological characterization of soft media

Jorge Torres[1,2]*, Antonio Callejas[1,2], Antonio Gomez[3], Guillermo Rus[1,2,4]

Abstract
The propagation of shear waves in elastography at high frequency (>3 kHz) in viscoelastic media has not been extensively studied due to the high attenuation and technical limitations of current techniques. An optical micro-elastography (OME) technique using magnetic excitation for generating and tracking high frequency shear waves with enough spatial and temporal resolution was proposed. Ultrasonics shear waves (above 20 kHz) were generated and observed in polyacrylamide samples. A cutoff frequency, from where the waves no longer propagate, was observed to vary depending on the mechanical properties of the samples. The ability of the Kelvin–Voigt (KV) model to explain the high cutoff frequency was investigated. Two alternative measurement techniques, Dynamic Mechanical Analysis (DMA) and Shear Wave Elastography (SWE), were used to complete the whole frequency range of the velocity dispersion curve while avoid capturing guided waves in the low frequency range (<3 kHz). The combination of the three measurement techniques provided rheology information from quasi-static to ultrasonic frequency range. A key observation was that the full frequency range of the dispersion curve was necessary if one wanted to infer accurate physical parameters from the rheological model. By comparing the low frequency range with the high frequency range, the relative errors for the viscosity parameter could reach 60 % and they could be higher with higher dispersive behavior. The high cutoff frequency may be predicted in materials that follow a KV model over their entire measurable frequency range. The mechanical characterization of cell culture media could benefit from the proposed OME technique.

Keywords
Optical elastography; Magnetism; High frequency; Rheological modeling; Kelvin–Voigt model

[1] *Ultrasonics Lab (TEP-959), Department of Structural Mechanics, University of Granada, Granada, Spain*
[2] *Biomechanics Group (TEC-12), Instituto de Investigación Biosanitaria, ibs.GRANADA, Granada, Spain*
[3] *Department of Mechanical Engineering, University College London, London WC1E 6BT, UK*
[4] *Excellence Research Unit "ModelingNature" (MNat), Universidad de Granada, Granada, Spain*
***Corresponding author**: geresez@ugr.es*

Contents

1. Introduction

Micro-elastography is a subcategory of dynamic elastography that was born to map the mechanical parameters at the microscopic scale.[1,2] This technique has been proposed as a bridge for mechanical characterization between the organ scale, where diseases are studied at an advanced stage, and the subcellular scale, where the earliest stage of diseases has been observed.[3–5] The micrometer scale of micro-elastography imposes challenging requirements that imply the need for a very fine spatial resolution. The resolution limit of the captured image stems from the capabilities of the detection system, and

high speed cameras are presented as good candidates.[6] The resolution of elastography, that is, when displacements are reconstructed or velocities are estimated, has been shown to be not limited by the shear wavelength (λ) of the excitation, but by the algorithms used.[7,8] However, the minimum λ of the propagated shear wave also plays a role in the accuracy of the final result. The relationship between λ and the characteristics of the propagating medium will dictate the mechanical model to use and the assumptions to be made for the analysis. When the wavelength approaches the dimensions of the medium or the thickness of a layer, propagation is conditioned by geometry, which requires guided wave models to avoid erroneous velocity estimations.[9] Diffraction and reflection as a result of the presence of inclusions or boundaries may also generate biased velocity values and artifacts.[10]

In addition, viscoelastic media are described by a complex shear modulus that is time dependent. This means that shear wave velocity is frequency dependent, and shear wave attenuation increases with frequency.[11] Viscoelastic characterization at the clinical stage is providing novel and meaningful insights into the diagnosis of pathologies and disorders.[12–14] The most widespread and direct methodology for viscoelastic characterization consists of fitting the dispersion curve (frequency-dependent response) to a rheological model. KV is one of the most widely used models due to the straightforward physical interpretation of its parameters and simplicity.[15] To achieve an optimal mechanical contrast using viscoelastic properties, reaching higher frequencies will allow to reconstruct more realistic values with a lower error.[16] Increasing the excitation frequency might result in observable volume shear waves even in submillimeter thickness layers, although the exponentially increasing attenuation over distance may result in only a few observable wavelengths before the amplitude is too low to detect it. A very recent study has shown that with a suitable setup, high frequency (>3 kHz) shear waves can be observed in phantoms and that the KV model might predict the frequency from where the waves no longer propagate (the cutoff frequency).[17]

Currently, the most widespread elastography modalities are based on ultrasound[18] and magnetic resonance.[19] In this context, most studies have focused only on the macroscale elasticity with simplified boundary conditions and linear elastic assumptions, examining large field of views at moderate resolutions. Acoustic Radiation Force (ARF)-based elastography techniques have been widely used due to their real-time results and their ability to perform in vivo studies effectively.[20] But the tissue response to the impulse excitation of ARF does not contain high frequency components, generally below 1 kHz. With this, λ usually ranges from a few to tens of millimeters depending on the propagation velocity.[2,21] In addition, the maximum acquisition rate is generally limited to 20 kHz, and its spatial resolution is proportional to the ultrasound beamwidth, reaching hundreds of microns. In the case of magnetic resonance elastography, the resolution drops to several millimeters and the acquisition rate drops to a few hundred Hz.[22] These technical limitations have precluded the adoption of these techniques at the microscale. Early works using high speed cameras have reported significant insights into shear wave propagation at high frequencies at the microscale. In a first study, a piezoelectric transducer vibrating at 15 kHz was used for exciting an animal cell of 100 μm diameter.[23] As a proof of concept, the authors did not consider viscoelasticity and the effect of guided waves was ignored. In a second study, they attempted to address the above problems from a physical perspective using controlled media.[17] Viscoelascity was studied using a KV model. They created shear waves over a wide frequency range from 0.5 to 15 kHz. However, they observed inconsistent values in the KV fittings in samples with the same composition, which made it difficult to experimentally establish an accurate high frequency cutoff. Likewise, they were not able to check that the KV model fit correctly over the entire dispersion curve as they registered guided waves at the low frequency end of the measured range.

These previous studies have shown that for a micro-elastography study, an efficient method for remotely generating shear waves at high frequencies with enough amplitude away from the source, and an imaging system with sufficient acquisition rate to capture the propagation is essential. Controlling how the medium is stimulated at that scale facilitates and enhances the analysis of wave propagation. We proposed to go one step further to solve the above mentioned problems. First, a new measurement technique, called optical micro-elastography (OME), was proposed and validated. It involved a new form of wave generation that could reach high frequency using a vibrating magnetic disk embedded in a transparent medium that was excited by a transient magnetic force. A high speed camera with high resolution tracked the propagation and the displacement fields were reconstructed using optical flow algorithms. The OME technique covered from 3 kHz to the cutoff frequency. Alternative measurement techniques were also proposed to avoid capturing guided waves in the low frequency range and complete the spectrum. Dynamic Mechanical Analysis (DMA), was used to provide frequency information from 0.1 to 150 Hz. The samples were subjected to a sinusoidal strain waveform at varying frequencies in a compression machine, and the complex shear modulus was obtained. Shear Wave Elastography (SWE) covered the typical range of soft tissues, from 200 Hz to 3 kHz. Secondly, by investigating the potential of the KV model to explain the high cutoff frequency and the agreement of the rheological behavior of soft media at different frequency ranges. The paper is organized as follows: the physical origin of the disk vibration from the magnetic force is explained; then the experimental setups for a wide frequency characterization are described, including DMA, SWE, and the proposed OME technique; after that, the OME technique is validated against simulations; finally, the phase velocity curves and the rheological behavior are presented, along with the estimation of the cutoff frequencies. The results are analyzed in the discussion.

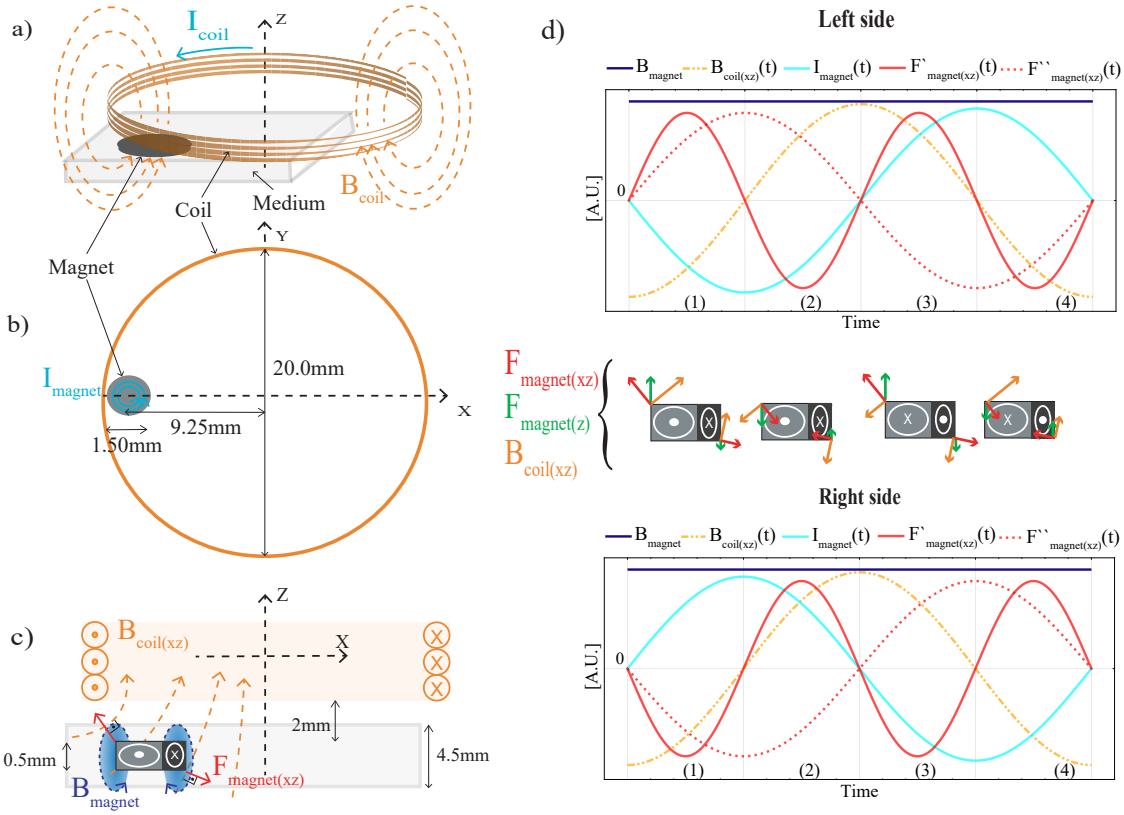

Figure 1. Generation of a transient magnetic force after applying a sinusoidal input voltage. a) The disk-shaped neodymium magnet receives the magnetic field of the air-cored coil. b) The magnet is placed in a diameter coinciding with the X-axis and close to the edge of the coil. c) The eddy current generated in the magnet $I_{\text{magnet}}(t)$ interacts with the magnetic field of the coil $B_{\text{coil(xz)}}$ and its own magnetic field B_{magnet}, thus producing a Lorentz force $F_{\text{magnet(xz)}}$ perpendicular to both fields. The position of the magnet causes the forces in the XZ plane to be non-symmetrical. The equilibrium point is displaced and dominated by the side closer to the coil. d) The fields on each side of the magnet present inverted trends, creating a pair of forces and causing the disk-shaped magnet to vibrate in a seesaw-like manner. The different gray shades distinguish the opposite polarity of the eddy current inside the magnet. Each time interval (1 to 4) represents the directional behavior of B_{magnet} (purple line), $B_{\text{coil(xz)}}(t)$ (orange line), $I_{\text{magnet}}(t)$ (cyan line), $F'_{\text{magnet(xz)}}(t)$ and $F''_{\text{magnet(xz)}}(t)$ (red lines) after the harmonic excitation.

2. Theory

2.1 Magnetic force on the neodymium disk magnet

Shear wave generation was achieved by applying a transient magnetic force to a disk-shaped neodymium magnet confined in a soft medium (Fig.1a). The medium was considered diamagnetic. The magnet was placed in a fixed horizontal position below a circular air core coil and aligned with the X-axis diameter (Fig.1b). The coil was driven with a sinusoidal time-varying voltage load $V_{\text{coil}}(t)$ that resulted in a current $I_{\text{coil}}(t)$ through the inductor, 90º out of phase with respect to the voltage (Eq. 1).

$$\begin{aligned} V_{\text{coil}}(t) &= V_{\text{c}} sin(2\pi f_0 t) \\ I_{\text{coil}}(t) &= -I_{\text{c}} cos(2\pi f_0 t) \end{aligned} \tag{1}$$

By Ampère's law, a magnetic vector field $B_{\text{coil}}(\mathbf{r},t)$ was produced around the coil that was proportional to the total current density $J_{\text{coil}}(\mathbf{r},t)$, the coil cross section S and the vacuum permeability μ_0 (Eq. 2). $B_{\text{c}}(\mathbf{r})$ indicates the maximum time amplitude of $B_{\text{coil}}(\mathbf{r},t)$, where $\mathbf{r}$ is the distance vector.

$$\begin{aligned} \oint B_{\text{coil}}(\mathbf{r},t) \cdot dl &= \mu_0 \iint J_{\text{coil}}(\mathbf{r},t) \cdot dS \\ B_{\text{coil}}(\mathbf{r},t) &= -B_{\text{c}}(\mathbf{r}) cos(2\pi f_0 t) \end{aligned} \tag{2}$$

$B_{\text{coil}}(\mathbf{r},t)$ also induced an eddy current $J_{\text{magnet}}(\mathbf{r},t)$ on the disk magnet by Faraday's law (Eq. 3), with σ the electrical conductivity of the magnet. Due to its thin geometry (0.5 mm), $J_{\text{magnet}}(\mathbf{r},t)$ was assumed to be constant along the thickness of the magnet with its flow concentric (Fig. 1c). $I_{\text{m}}(\mathbf{r})$ indicates the maximum time amplitude of $I_{\text{magnet}}(\mathbf{r},t)$.

$$\begin{aligned} \oint J_{\text{magnet}}(\mathbf{r},t) \cdot dl &= -\sigma \iint \frac{\partial B_{\text{coil}}(\mathbf{r},t)}{\partial t} \cdot dS \\ I_{\text{magnet}}(\mathbf{r},t) &= -I_{\text{m}}(\mathbf{r}) sin(2\pi f_0 t) \end{aligned} \tag{3}$$

Ultimately, the combination of these phenomena gave rise to the Lorentz force acting on the magnet (Eq. 4), with V the volume of the magnet. The eddy current $J_{\text{magnet}}(\mathbf{r},t)$ in the magnet interacted with the magnetic field of the coil

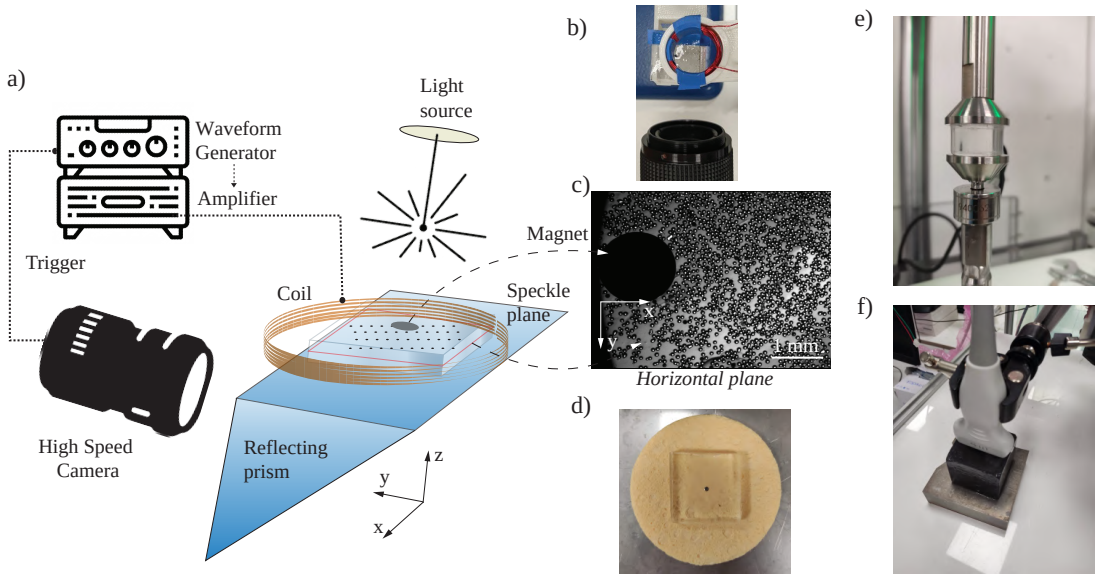

Figure 2. Experimental setups for mechanical characterization. a) The medium is placed on a reflecting prism in contact with its larger surface allowing horizontal positioning of the high-speed camera. b) A picture taken from the position of the light source. The light is also reflected in the prism to directly reach the camera lens. c) Image captured by the camera of the speckle plane (XY). The disk-shaped magnet is displayed in total black. d) Transparent sample fabricated for the OME test. e) DMA frequency sweep test with cylindrical sample. f) SWE experiment with cubic sample.

$B_{\text{coil}}(\mathbf{r},t)$ creating a force perpendicular to both fields. Since the neodymium magnet had permeability close to air, its magnetic field $B_{\text{magnet}}(\mathbf{r})$ was static and could not be altered by the magnitude of the transient fields used, allowing one to neglect the effect of this current on the magnet itself. Assuming that both materials were magnetically linear, their fields could be added and the force value enhanced. Two force components were considered. $F'_{\text{magnet}}(\mathbf{r},t)$ was generated from $B_{\text{coil}}(\mathbf{r},t)$, and would be able to develop twice the frequency of the introduced transient magnetic field, while $F''_{\text{magnet}}(\mathbf{r},t)$ was generated from $B_{\text{magnet}}(\mathbf{r})$, with the same frequency as the input excitation (Eq. 4).

$$F_{\text{magnet}}(\mathbf{r},t) = \iiint J_{\text{magnet}}(\mathbf{r},t) \times (B_{\text{coil}}(\mathbf{r},t) + B_{\text{magnet}}(\mathbf{r}))dv$$

$$F_{\text{magnet}}(\mathbf{r},t) = \underbrace{\frac{I_{\text{m}}(\mathbf{r})B_{\text{c}}(\mathbf{r})}{2} sin(2\pi(2f_0)t)}_{F'_{\text{magnet}}(\mathbf{r},t)} + \underbrace{I_{\text{m}}(\mathbf{r})B_{\text{magnet}}(\mathbf{r})sin(2\pi(f_0)t)}_{F''_{\text{magnet}}(\mathbf{r},t)} \tag{4}$$

An alternative expression of the force, in terms of the magnetic flux density, can be derived by using Ampère's law in its vectorial form (Eq. 5).[24] Considering only the effect on the z axis and being C a constant depending on magnetic parameters and the volume of the magnet, we concluded that the force was proportional to the spatial gradient of B_{coil}. This expression was used to find the optimal location of the magnet in the z axis. As shown in the results section, the spatial gradient was higher just outside the coil. That was why the magnet and the medium were placed just outside, as observed in Fig. 1c.

$$F_{\text{magnet}}(z,t) = C\left(B_{\text{coil}}(z,t)\frac{\partial B_{\text{coil}}(z,t)}{\partial z} + B_{\text{magnet}}(z,t)\frac{\partial B_{\text{coil}}(z,t)}{\partial z}\right) \tag{5}$$

These equations explain how it was possible to get the magnet to act as a shaker and generate shear waves. The magnitude in each direction of the $B_{\text{coil}}(\mathbf{r},t)$ field depended on the position. When the magnet was near the edge of the coil, the dominant component was $B_{\text{coil(x)}}$ with a moderate contribution of $B_{\text{coil(z)}}$, as shown in Fig. 1c. These components coupled with $I_{\text{magnet(y)}}$ to generate $F_{\text{magnet(xz)}}$ (Fig. 1d). Due to the rapid change in polarity of the magnetic field and the opposite directions of current within the magnet, a pair of forces was generated, thus simulating a simple lever motion. However, the pivot point was closer to the right end because the force was not perfectly symmetric and its magnitude was greater closer to the coil. This is shown in Fig. 1d with larger circles indicating a higher eddy current on the magnet. This decompensation could try to move the magnet in the XY plane, but since it was confined, this motion was constrained. The rest of the force components had a very low magnitude. If the magnet were aligned with the Z-axis shown in Fig. 1, most of the $B_{\text{coil}}(\mathbf{r},t)$ flux lines that would pass through the magnet would be vertical ($B_{\text{coil(z)}}$) and therefore the value of $F_{\text{magnet(z)}}$ would be significantly reduced.

3. Methods

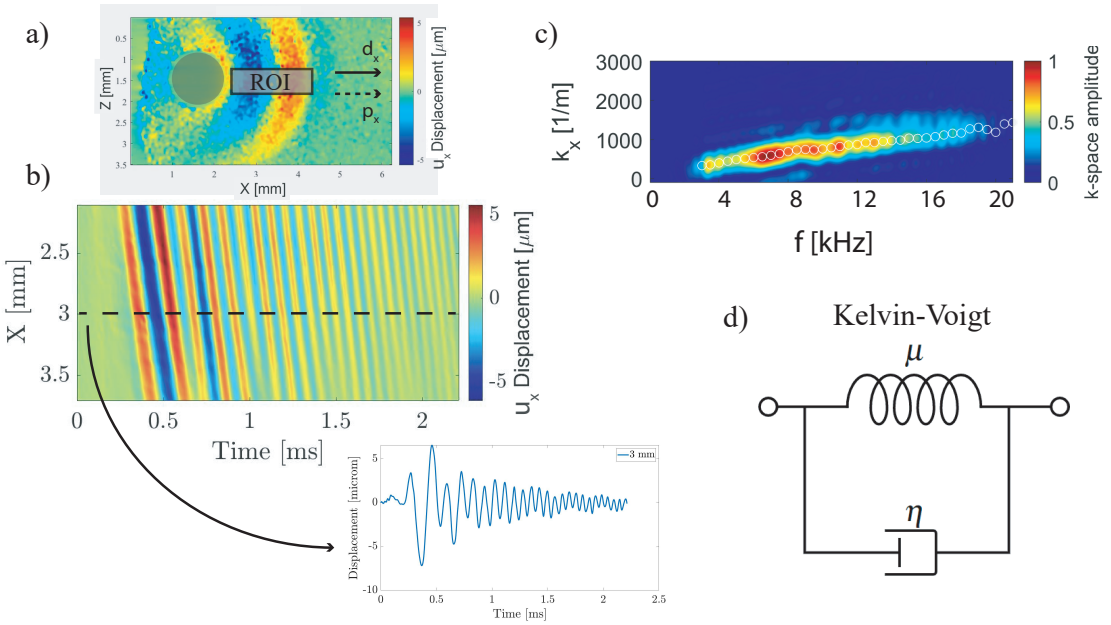

Figure 3. High frequency data reconstruction of longitudinal waves in a 40 % PAM sample. a) Displacement map estimated using a dense optical flow algorithm. The propagation direction d_x and the particle polarization p_x was parallel. b) Spatiotemporal displacement profiles of the horizontal component (u_x) averaged in depth taking the Region of Interest (ROI) indicated. The graph below displays the temporal displacement profile at 3 mm. c) 2D Fourier transform of the displacement profiles with highest energy points detected for each frequency. d) Kelvin-Voigt rheological model scheme that was used for viscoelastic characterization.

3.1 Experimental setups for a wide frequency characterization

The remote transient magnetic force produced by the coil induced the generation of high frequency shear waves by a disk-shaped magnet, as explained in Section 2. The permanent magnet was made of neodymium (NdFeB-45) with 1.5 mm of diameter and 0.5 mm of thickness. The circular coil was made of copper with a wire diameter of 0.5 mm, 75 turns, inner diameter of 20.0 mm, and 12.5 mm of height. This resulted in a very low inductance of 0.1 mH. Low inductances are an advantage because more current will be induced in the coil at the same voltage. The chosen excitation was a linear frequency sweep (chirp) from 5 to 22 kHz, coming from a waveform generator (33500B Series, Keysight, California, USA) that after power amplification (7224, AE Techron, Indiana, USA) reached 200 Vpp. The magnetic field B_{coil} at different frequencies was characterized experimentally by using Faraday's law of induction with a pickup coil, made with 10 turns and 10 mm diameter. This second coil captured the electromotive force at different positions along the Z axis of the main coil.

A high-speed camera (FastCam SA-Z, Photron, Japan) was the core of the imaging section. It had installed a 12x zoom lens (Navitar, New York, USA) from which we acquire 640x360 images with 10x10 μm^2 pixel resolution at a frame rate of 80 kHz. This ensured compliance with the Nyquist criterion. The camera lens was aimed at a 45º reflecting prism that held the medium and allowed us to study the horizontal plane of propagation (Fig. 2b). A fiber-coupled halogen light source (OSL2, Thorlabs, Inc., New Jersey, USA) with a collimation attachment provided adequate stable continuous lighting. The camera sent a trigger to the waveform generator to ensure synchronization. All elements were placed in independent structures to avoid unwanted vibrations (see Fig. 2).

The camera tests provided data to reconstruct the dispersion curve in the high-frequency range. To cover the low frequency range of the dispersion curve, we used a Verasonics research system (Vantage 256, Verasonics Inc., Redmond, WA, USA) to perform Shear Wave Elastography (SWE).[25] To remotely produce shear waves, an ARF push of 1000 cycles[26] was applied to the medium with an L11-5v linear probe (Fig. 2f). The central frequency was 7.6 MHz. The focal distance was set at 25 mm. Immediately after, ultrafast imaging was performed using plane waves with an acquisition rate of 12.5 kHz. To remove the effect of random noise, 10 consecutive frames were averaged.

Finally, a DMA experiment on an ElectroForce 3200 (TA Instruments, EEUU) device completed the lower end of the frequency spectrum. A cylindrical sample was placed between two planar plates. The lower plate was attached to a load cell whose maximum capacity was 22 N, with a resolution of 0.001 N (Fig. 2e). Frequency sweep tests were conducted to obtain the complex modulus of the samples. The displacement was controlled by moving the upper plate. Before starting the measurements, to ensure an even contact, a ramp load was applied until 1 N was reached. Oscillatory compression loads with stepped values from 0.1 to 150 Hz with a dynamic amplitude of 0.05 mm were carried out. The software performed a

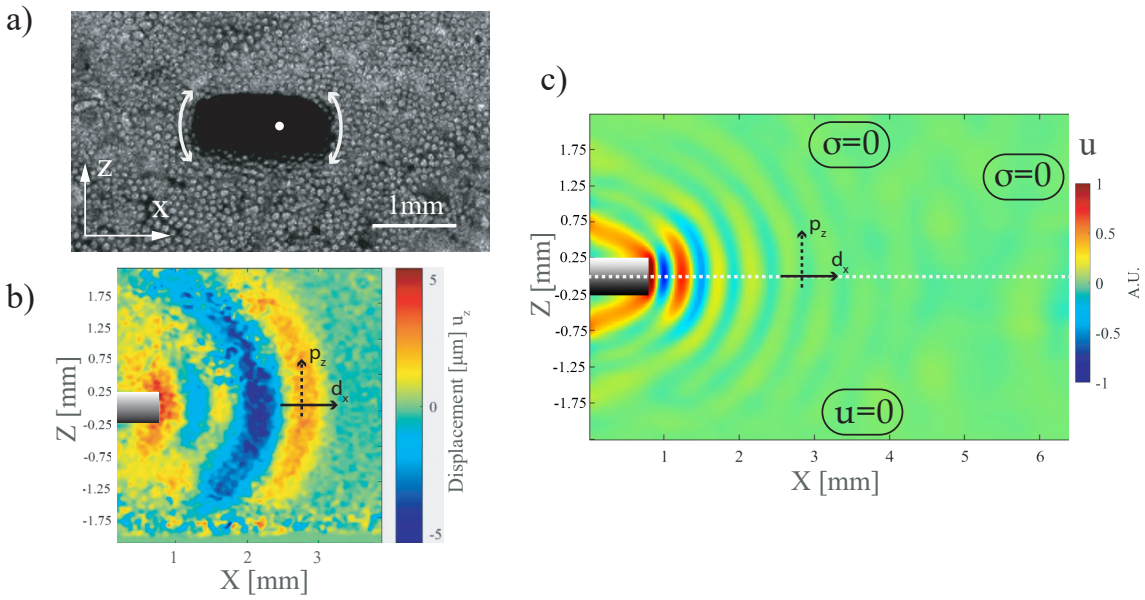

Figure 4. a) Lateral view (XZ) showing the transient alternating magnet motion. The magnet is fixed on the white point due to the alternating magnetic forces. b) Reconstructed experimental vertical displacements (u_z) showing consecutive wavefronts at 0.6 ms after the beginning of magnet motion in the lateral plane of propagation (XZ). c) Geometry and map of the vertical particle displacements (u_z) of the right side of the simulation model (FDTD) at 0.6 ms after the beginning of magnet motion. $\sigma = 0$ indicates free border, while $u = 0$ indicates fixed border. The particle displacement p_z was perpendicular to the propagation direction d_x.

Fourier analysis to obtain the real and imaginary components of the complex modulus, the storage and the loss modulus, respectively. The acquisition rate was 10 kHz.

3.2 Sample preparation

For each measurement technique, DMA, SWE, and OME, hydrogel samples with a different geometry were fabricated. The hydrogel was manufactured with polyacrylamide (PAM), a polymerized material with two useful properties. First, varying the concentration of PAM allowed tuning the viscoelastic properties. Second, the medium was completely transparent, which was necessary for light to pass through and allow visualization by the camera. A previous recipe mimicking the acoustic properties of biological tissues was adapted to manufacture PAM with these requirements.[27,28] Acrylamide-bis solution (19:1 bis ratio, 40% solution, OmniPur) was reconstituted by mixing with distilled water and glycerol 10% (v/v) in a conical tube. We considered three different concentrations of PAM to have a variety of mechanical responses, namely 20%, 30% and 40% (v/v). To initialize the polymerization of PAM, Ammonium Persulfate (APS 98%, Sigma Aldrich), 0.5% (v/v) of 10% (w/v) was added and mixed until homogenization. N,N,N',N'-Tetramethylethylenediamine (TEMED 99%, ReagentPlus) was added 0.2% (v/v) as a catalyst to accelerate gel polymerization. All materials were supplied by Merck (Merck KGaA, Darmstadt, Germany).

For a successful visualization of the shear waves, the addition of optical speckles using particles smaller than the wavelength was required. Glass beads with diameter of 75 μm (Model 59200U, Supelco) were added to form a single plane within the sample to ensure high image contrast and to avoid the observation of out-of-plane displacements. The procedure had a duration of 40-60 seconds and was conducted as follows. A first layer of PAM mixture was poured into a rectangular mold shortly after TEMED was added. During the polymerization process, it was observed that as the medium solidified, a thin liquid layer formed on top of it. At this point, glass beads were placed, forming a homogeneous distribution on the surface, after passing through a 100 μm mesh sieve. Then the neodymium disk was placed on the same plane. Finally, the second layer of PAM was poured and began to diffuse into the first layer. The molecules in the two layers began to interact, causing the layers to merge. The images taken by the camera (Fig. 2c and d) show that both the particles and the disk were on the same plane. Similarly, a homogeneous propagating wavefront during displacement reconstruction confirmed that the layers were merged. The resulting medium had a 20x20 mm^2 surface and a thickness of 4.5 mm. 3 samples were made for each PAM concentration.

To study the combined spatial resolution of the imaging and excitation systems for high frequency waves, bilayer samples were fabricated. They were composed of two vertically divided layers with different PAM concentration. The left layer had a 40 % concentration of PAM, while the right layer had a 20 % concentration. The procedure was similar to that explained above. In this case, each layer was subdivided into two parts for each concentration, which eventually merged. The neodimyum disk was placed in the 40% part.

The samples used for the SWE control experiment fol-

lowed the same fabrication procedure. The cubic mold used had dimensions of 50x50x50 mm^3 to avoid reflections or guided waves in our analysis. It consisted of a single layer with graphite powder (Pressol Schmiergerate GmbH, Germany) for acoustical scattering instead of glass beads. For the DMA experiment, the cylindrical mold had 20 mm of diameter and 12 mm of height. No scattering particles were required. Magnets were not embedded in the sample for DMA and SWE (see Fig. 2e,f).

3.3 Displacement and phase velocity reconstruction

To obtain a dispersion curve that provided a consistent wide frequency characterization, the results of the three techniques used, DMA, SWE, and OME, were combined to obtain values from the quasi-static range to the cutoff frequency.

The camera was only able to capture the displacements of the particles on the horizontal plane (XY). However, the alternating motion of each side of the magnet took place in a perpendicular plane (see Fig. 4a). This motion sheared the surrounding medium and the diffracted transverse shear waves coming primarily from the borders of the magnet disk created a new propagation front due to the displacement component in the horizontal direction (u_x).[29] This led to the generation of longitudinal shear waves in the speckle plane that the camera could detect as a sequence of frames that formed a wave propagation movie.

A dense optical flow algorithm was used to estimate 2D displacement maps.[30] Ideally, each pixel in the frame was assigned a displacement value. However, the spatial resolution was reduced in favor of a more robust and smoother result. The size of the pixel neighborhood was 5, which worsened the spatial resolution from 10x10 to 50x50 μm^2. A spatial Gaussian filter of size 10 pixels was also applied, for noise reduction and better detection of fast motion. Note that this filter did not change the spatial resolution. Only the lateral propagating component was considered, corresponding to the X-axis (see Fig.3a). Before velocity estimation, a region of interest (ROI) to the right of the emitting disk was taken. The ROI dimensions were 2 mm in the lateral dimension, and 0.5 mm in the depth dimension, aligned with the center of the disk. To reduce random noise and computation time, displacement time profiles were averaged over ROI depth (Z-axis), and time upsampled by cubic interpolation (see Fig. 3b). For the bilayer samples we also applied a spatial directional filter to keep only the forward propagation direction.[10]

In the SWE part, the Verasonics system provided the beamformed IQ data with which particle motion can be estimated using the Loupas correlation algorithm.[31] An ROI of dimensions 10x10 mm^2 was taken to the right of the push. The same pre-processing as with OME was used here.

The dispersion curve can be obtained with the 2D Fourier transform. The reconstructed spatiotemporal data was converted to the frequency do, also called the (f,k) space (Fig.3c). The highest energy propagation mode was identified by finding the pairs of wavenumber k (spatial frequency) and frequency f (temporal frequency) related to the peak values of the (f,k) space amplitude. No amplitude mask was used to explore the maximum frequency information. The shear wave phase velocity for each frequency was obtained directly as $c_s = f/k$.[32] The characterization of the viscoelastic properties of the medium was carried out by fitting the theoretical expression of the shear wave phase velocity $c_s(\omega)$ according to the KV model (fig.3d) to the experimental dispersion curve.[33] To obtain the shear elasticity μ and viscosity η the BFGS nonlinear minimization method was used. It is an iterative algorithm used for unconstrained optimization problems. It uses an approximation of the Hessian matrix to update the search direction at each iteration.[34] The phase velocity was also calculated from DMA data, replacing the storage and loss moduli in the KV expression.[33]

Finally, the potential of the KV model to explain the high cutoff frequency was investigated. According to Holm,[35] in the low frequency regime ($\omega\tau < 1$) elasticity dominates over viscosity and waves propagate, being $\tau = \eta/\mu$ the relaxation time, and ω the angular frequency. As the frequency increases, the viscous term ($\omega\eta$) gets closer to the elasticity term (μ) and waves are strongly attenuated, and the physical phenomenom approaches to the solution of a diffusion equation. Setting the observable propagation limit in $\omega\tau = 1$, the theoretical cutoff frequency is calculated as $f_c = \frac{1}{2\pi\tau}$.

3.4 FDTD model

A 2D finite difference time domain (FDTD) model was used to validate the velocity estimated from the propagation of longitudinal shear waves created from the vibration of the magnet disk. The mechanical wave propagation problem was solved numerically based on previous work of the group[36,37] using the Matlab programming environment (R2018b, The MathWorks Inc., Natick, MA, USA). The governing equations, namely dynamic equilibrium, kinematic, and constitutive, were implemented considering a KV viscoelastic model.

A 3D model would be required since the excitation and the mechanical response were distributed perpendicularly to each other. However, this would entail a high difficulty in reproducing the excitation coming from the magnetic field, as well as several diffraction artifacts near the borders, which would be out of the scope of the study. To simplify this complexity and reduce computational load, a 2D numerical study was performed in the lateral plane (XZ), focusing on the midplane. The geometry consisted of a 2D rectangular medium with an embedded rectangular magnet element located in its center. The model considered a staggered grid for spatial discretization of the variables. Free boundary conditions were established for all edges of the propagation medium, with the exception of the bottom edge that was fixed (Fig. 4c). The neodymium magnet was modeled as a solid elastic material. The excitation was an angular displacement that was prescribed in the right corner of the magnet. The real excitation could not be fully reconstructed by looking at the lateral plane with the camera. This was due to the fact that the light

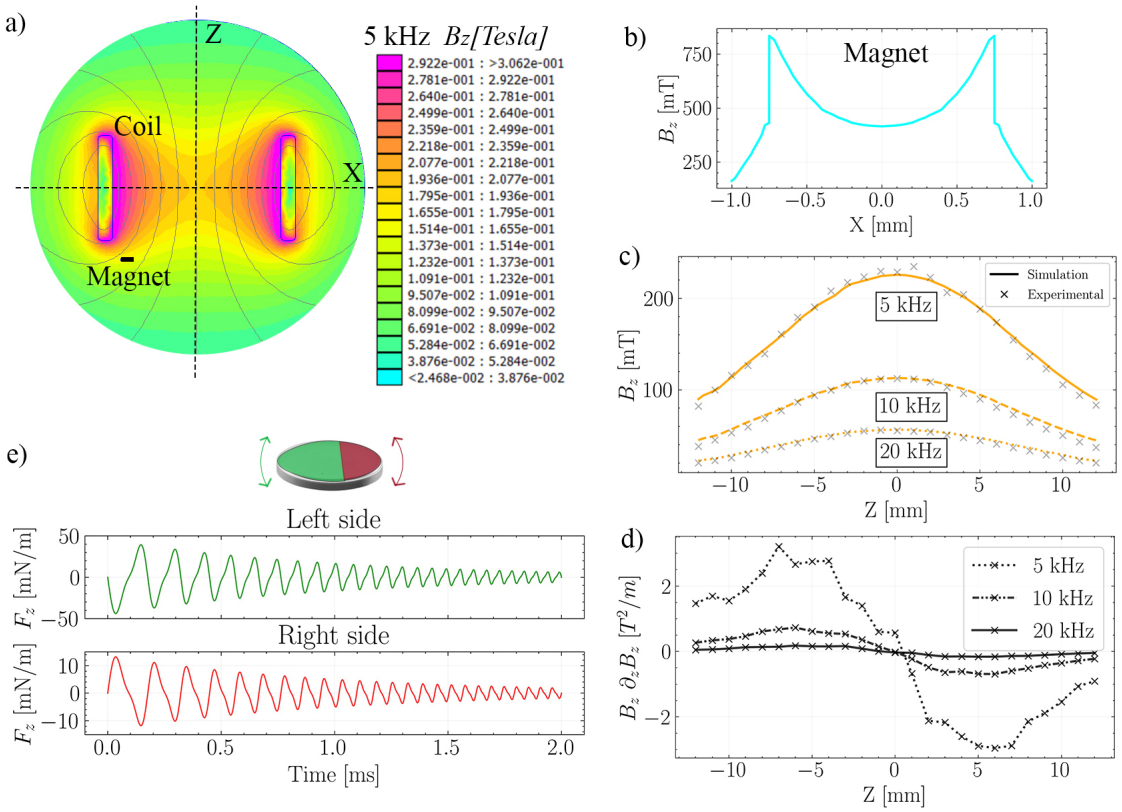

Figure 5. Magnetic simulation results. a) Magnetic flux density generated by the coil at 5 kHz. b) Static magnetic field of the neodymium magnet that is added to the field coil. c) B_z measured experimentally along the central vertical axis Z with the simulated values. d) Spatial gradient in the z axis of the coil magnetic field. e) Time evolution of the Z component of the Lorentz force on the upper face of the magnet.

had to pass through 20 mm of material. Therefore, we used as excitation the output signal of the generator scaled by the initial rotation of the magnet, which was observable. Also, the magnet was fixed at a point to the right of its vertical median plane because of the non-symmetrical magnetic field (see Fig. 4a). The distance was obtained from magnetic simulations (see Fig. 5e).

The material properties of the medium were inferred from the fitting of the KV parameters with the OME results, shown in Table 2. The compressional modulus K was estimated assuming $K = c_p^2\rho$,[38] where $c_p = 1540$ m/s is the speed of sound and $\rho = 1000$ kg/m^3 the density of PAM.[27] The volumetric viscosity parameter η^v was neglected. Notice that this simplification would overestimate the absolute amplitude in the simulations compared with the and high speed camera observations. However, since the objective of the simulations was to validate the experimentally estimated velocity values, the absolute amplitude information was not relevant. The dimensions and parameters of the discretization model are summarized in Table 1. To obtain the phase velocity, the same reconstruction algorithm described in subsection 3.3 was applied. The horizontal component of the displacement u_x was taken, which theoretically should have the same velocity as the longitudinal shear waves captured by the camera (white midline in Fig. 4c).

Fig. 4b shows the experimental displacement reconstruction in the lateral plane (XZ) of a 40% PAM sample. When the magnet disk sheared the medium, the vertical displacement component u_z created transverse shear waves in this plane. The amplitude of these shear waves was similar to that of the longitudinal shear waves, but due to low light conditions and poor image quality, the result was noisier compared to the XY plane. Still, a comparison with the displacements of the simulations showed that there was a qualitative agreement between them. The observations confirmed that the magnet vibrated as a simple lever, which was in agreement with the expected behavior foreseen in Section 2.

Table 1. Values of the parameters for all the cases simulated by using the FDTD model.

Parameter	Description	Value
xS	Horizontal dimension of the domain	20 mm
zS	Vertical dimension of the domain	4.5 mm
Δx	r spatial step	20 μm
Δz	z spatial step	20 μm
Δt	time interval	5e-9 s
t_T	total time of simulation	2.5 ms

4. Results

4.1 Magnetic field and force optimization

Magnetic characterization was performed using the Finite Element Method Magnetics (FEMM v4.2) software.[39] An axisymmetric problem was defined with the geometry and material properties previously described. At 5 kHz, with an input voltage of 200 V, the current was 60 A. The magnetic flux density peaked at 0.31 T where the X-axis intersected the coil (Fig. 5a). Near the top surface of the magnet B_z was 0.14 T. The permanent magnetic field of the magnet reached a maximum of around 800 mT at its edges (Fig. 5b). In Fig. 5c the measurements taken by the pickup coil of B_z along the Z axis validated the simulation results. As described in the theory section (Eq. 5) the magnetic force in the z axis is proportional to its spatial gradient. Thus, the magnet was placed near the edge of the coil where the magnetic force was maximum (Fig. 5d). The time behavior of the Lorentz force showed some deviation from the generator output because of the double frequency term that the coil added (see Fig. 5e). The inductive impedance increased with frequency, which meant that a lower current developed. Therefore, the magnitude of F_z attenuated over time as the excitation chirp changed frequency. The attenuation factor was proportional to the recorded displacement. To find the position on the magnet where F_z changed direction, we searched for the sign change of J_{magnet}, assuming a constant value in its thickness. It was found approximately 1 mm from the left side (the edge closest to the coil, the green part). This distance was used in the wave simulations.

4.2 OME results and experimental dispersion curves combining with DMA and SWE

The dispersion curves in the high frequency range (HF >3 kHz) obtained by OME are presented for each PAM concentration in Fig. 6a. The frequency information started around 3 kHz up to the estimated high cutoff frequency. This upper limit was observed at the point where information about the highest energy propagation mode in the (f,k) space was no longer available. It was noticed that as the PAM concentration of the sample increased, the recovered velocity information reached higher frequencies. For 40% the response reached a frequency of 20.2 kHz, for 30% it is up to 15.3 kHz, and for 20% up to 9.8 kHz. Therefore, ultrasonic shear waves were generated and captured. The phase velocities coming from the simulation displacement data (FDTD) are also displayed. They are mostly superimposing on the OME data. This proved that in a KV medium, the magnet lever motion was capable of generating longitudinal shear waves in the observed frequency range. It was also emphasized that, since the velocities were of a few m/s, they belonged to shear waves. The right inset in Fig. 6a displays the exploitable frequency content of each PAM concentration. It can be seen that the frequency information is comparable to the cut-off obtained with the phase velocity. In the case of 40%, the energy is spread over a wider frequency range, which may cause the wavy shape and the jumps seen in the phase velocity.

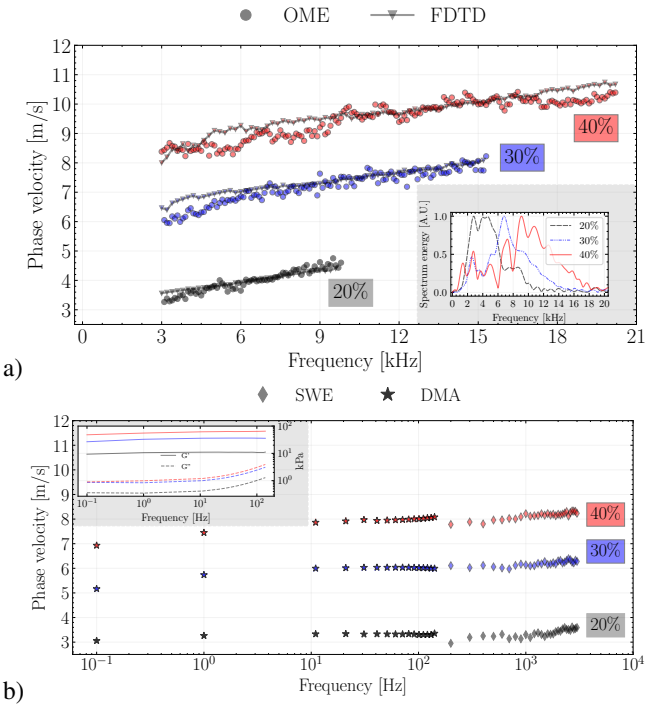

Figure 6. Experimental dispersion curves. a) The high frequency phase velocity values estimated from optical micro-elastography (OME) and simulations (FDTD). The right inset displays the energy frequency content for each concentration of PAM. b) The low frequency phase velocity values estimated from Dynamic Mechanical Analysis (DMA) and Shear Wave Elastography (SWE). The frequency axis is represented in log scale. The inset represents the storage G' and loss G'' moduli on a log-log scale.

The low frequency range (LF <3 kHz) was the combination of DMA and SWE (Fig. 6b). For SWE the frequency information started at 200 Hz and ended at 3 kHz for the 20% concentration, in the case of 30% it went up to 3.8 kHz and for 40% up to 4.5 kHz. For all of them, 3 kHz was established as their upper limit for a consistent comparison. In this range, a higher concentration of PAM implied a more noticeable dispersion response. The DMA values ranged from 0.1 to 150 Hz with phase velocities in line with those of SWE. The frequency axis in Fig. 6b is represented in log scale. Furthermore, storage G' and loss modulus G'' are shown in a log-log scale in the upper inset. In this frequency range G' is one order of magnitude higher than G''. All techniques provided consistent values with each other without significant jumps between them.

4.3 Rheological behavior and cutoff frequencies

Table 2 shows the KV fitted parameters for each frequency range, including the whole frequency range as WF = LF + HF. For the study of the goodness of fit, the mean absolute error (MAE) was chosen, with smaller values representing a better fit. A wider frequency range implied a poorer fitting. The shear elasticity μ parameters were similar in all ranges, espe-

cially for lower values. The shear viscosity η parameters were significantly different between the low frequency range and the high frequency range. Furthermore, to better observe these behaviors, the KV models are represented for each frequency range in Fig. 7. The lines are extrapolated to cover the entire frequency range. In the low frequency range, η was higher for higher concentrations, implying that the high frequency range behavior could not be captured. On the contrary, the high frequency range η was able to satisfactorily capture the low frequency range behavior.

In Table 3, the KV parameters are used to explore the cutoff frequencies. First, we calculate on the left side the values of the frequency regime ($\omega\tau$) considering the upper frequency limits and the relaxation times estimated from the experimental results. It can be seen that in the low frequency range, $\omega\tau$ is in all cases less than 1, while in the other ranges it is around 1. On the right side, high cutoff frequencies are calculated assuming $\omega\tau = 1$. Given the overestimation of the viscous parameter in the low frequency range, the cutoff frequency was underestimated. In the other ranges, a fair approximation was obtained with respect to the limits that were reached when calculating the phase velocity.

4.4 Spatial analysis of the mode of wave propagation

The series of sequential snapshots in Fig. 8a show that the longitudinal shear waves captured have a spherical front due to the circular geometry of the magnet. We analyzed the propagated waves to confirm that they did not form part of complex modes of guided propagation. The tested samples had a thickness larger (4.5 mm) than the maximum λ. The same applies to the SWE measurements, where the maximum λ was around 20 mm in the 40 % PAM, and the sample thickness was 50 mm. As displayed in Fig. 8a, the minimum wavelength is 0.517 mm for the 40% PAM, 0.502 mm for the 30% PAM, and 0.451 mmm for the 20% PAM, in OME measurements. This can in fact be verified in the snapshots shown in the same figure.

To verify that the previous minimum λ did not limit the resolution of the system, wave propagation at high frequencies from a hard to a soft medium was explored. In the bilayer sample (shown in Fig. 8b) the straight transition plane has a constant length of 0.3 mm. When the wave traveled through this plane, there was an abrupt alteration in its front due to a change in mechanical properties. To see that change, the spatial gradient of the displacement in the same direction of propagation was calculated and plotted in the right hand side image. The length of the lateral distance of the gradient (marked between the white lines) was approximately 0.3 mm, decreasing slightly as the frequency increases.

5. Discussion

In this study, OME was presented as a feasible technique for obtaining a reliable viscoelastic analysis over an ultrawide frequency range. To achieve micrometer resolutions and avoid guided wave propagation, a high frequency excitation was used, and the detecting capabilities of the imaging system were enhanced.

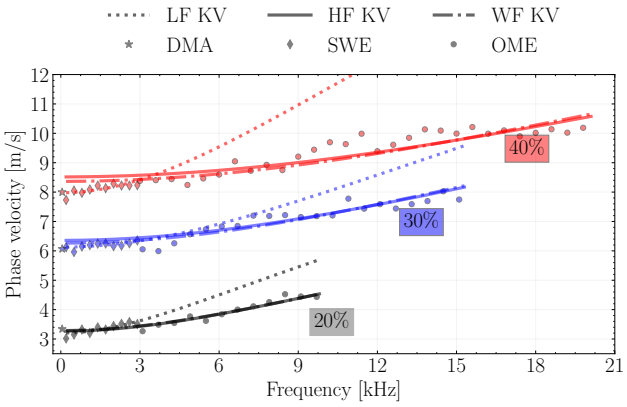

Figure 7. KV fitting to experimental data in different frequency ranges. The low frequency range (LF) corresponds to DMA+SWE, while the high frequency range (HF) corresponds to OME. The whole frequency range is the combination of the previous ranges (WF=LF+HF). Fewer experimental points are plotted for the sake of clarity.

A magnetically based excitation without direct mechanical contact was proposed. This method of excitation provided high-efficiency transmission between the input excitation frequency and the medium displacement. This remote generation of shear waves by means of the Lorentz force has already been explored.[40,41] In contrast to these previous studies, where the waves generated had a low frequency response (<1 kHz), here the motion of the magnet allowed it to reach higher frequency (> 3 kHz). A chirp-type signal provided a uniform magnitude throughout the frequency sweep, which was convenient for achieving a continuous dispersion curve, as well as a higher SNR than an impulse.[42] When the magnet began to vibrate, it first had to overcome the inertia of the medium that was holding it. At high frequency, the inductance of the coil reduces the current developed in the coil, which directly affects the magnetic force. Therefore, to beat the inertia, a continuous frequency sweep starting at lower frequencies guaranteed to observe wave displacements beyond 20 kHz. When excitation started at low frequencies (<3 kHz), the magnet vibration was slow and had a large amplitude, and high frequencies could not be developed. To achieve balance and avoid guided waves due to large λ, the input signal started at 5 kHz. Even so, enough information was obtained to reconstruct the velocity at frequencies lower than the excitation, starting at 3 kHz. This was because in the transition from standing to moving, lower frequency components were generated. The shape of the wavefront can be changed with the geometry of the embedded magnet. In our case, a circular geometry facilitated the study of the excitation force as a result of the assumptions made about the eddy current. By replacing the magnet by a metal plate, such as aluminum, the maximum magnetic force was reduced by 85 %, and we did not observe any motion or propagating wave. This meant that the permanent magnetic

Table 2. KV model parameters (shear elasticity and viscosity) fitted to each PAM concentration and frequency range. Data presented as mean ± standard deviation. LF: low frequency, HF: high frequency, WF: whole frequency. MAE: Mean Absolute Error.

	LF			HF			WF		
PAM concentration (%)	μ (kPa)	η (Pa·s)	MAE (m/s)	μ (kPa)	η (Pa·s)	MAE (m/s)	μ (kPa)	η (Pa·s)	MAE (m/s)
40	63.62 ± 11.54	1.33 ± 0.21	0.07	72.52 ± 7.85	0.51 ± 0.12	0.25	69.94 ± 8.07	0.53 ± 0.06	0.25
30	37.52 ± 7.01	0.61 ± 0.18	0.07	40.40 ± 5.04	0.41 ± 0.12	0.17	39.21 ± 3.28	0.43 ± 0.07	0.16
20	10.26 ± 3.10	0.34 ± 0.04	0.06	10.68 ± 2.29	0.21 ± 0.09	0.09	10.81 ± 0.53	0.21 ± 0.02	0.09

Table 3. KV frequency regimes and prediction of high cutoff frequencies using $\omega\tau = 1$. LF: low frequency, HF: high frequency, WF: whole frequency. f_c: cutoff frequency.

	LF		HF		WF	
PAM concentration (%)	$\omega\tau$	$\omega\tau$=1 f_c [kHz]	$\omega\tau$	$\omega\tau$=1 f_c [kHz]	$\omega\tau$	$\omega\tau$=1 f_c [kHz]
40	0.59	7.6	0.89	22.6	0.96	21.0
30	0.38	9.8	0.97	15.7	1.05	14.5
20	0.62	4.8	1.21	8.0	1.19	8.2

field provided the force necessary to move the disk within the medium. To further increase this force, a magnet with a higher permanent field can be used, such as NdFeB-52, and the input current can be increased. Besides, strong magnetic fields are biologically harmless.[24]

Techniques using high speed cameras have found a niche application in gaining greater insight into the physics of wave propagation and some of its limits.[6,17] Its advantages are the high acquisition rate and spatial resolution, which allow small displacements to be captured in short times. By exploring the propagation in the immediate vicinity of the excitation area, it is possible to capture some wavelengths at high frequencies that attenuate quickly. To obtain an accurate displacement field, the algorithm used to calculate the dense optical flow presented a problem. If excitation frequencies lower than 3 kHz were used, the displacements would be greater than 10 μm. Due to the large amplitude of vibration of the magnet to generate this displacement, the sample was lifted off the base. This changed the illumination conditions, and the results were erroneous.

The tests on the bilayer samples proved that it was the resolution of the imaging system that limited the accuracy of the displacement field reconstruction. The minimum λ was 0.451 mm, and we could detect a transition of 0.3 mm. As discussed in,[7] the use of minimum windows or propagation distances for velocity estimations decreases the final resolution. Blurred and irregular transitions have been frequently observed.[2] The camera resolution can be increased by using a microscopic lens, which can provide a resolution of less than 1x1 μm. However, the generated displacement amplitude would have to be decreased to be captured in the field of view, which at high frequencies might mean no motion.

With this setup, waves traveling at the speed of shear waves (a few m/s) and with a longitudinal displacement were observed. Longitudinal shear waves have already been used in optical coherence elastography with satisfactory results.[43,44] To confirm the shear wave nature of these observed longitudinal waves, the group velocity was measured in the lateral plane shown in Fig. 4b. A value of 9.4 m/s was obtained for the 40% concentration sample, which was in the range of its dispersion curve. The geometrical diffraction due to the spherical front did not seem to affect the phase information in the frequency domain. We compared the velocity values with and without spherical front corrections, and the differences were all below 5%. The changes in the shape of the dispersion curve (Fig. 6a) at specific frequency intervals can be caused by various factors, such as high attenuation or inhomogeneous particle distribution. This meant that in the ROI chosen, the propagation front was not completely homogeneous. In the case of SWE, it was necessary to stir the graphite during curing to prevent it from settling at the bottom, while for OME in some cases there were gaps or a higher density of particles due to the fabricating process.

Several results were used to confirm that the dispersive behavior of the shear waves measured with OME was not sensitive to the geometrical conditions of the medium. First, the (f,k) space gave information on how the propagation was distributed spatially and temporally. Its magnitude revealed that only one propagation mode was captured. When there are other modes, additional information appears that deviates from the dominant mode.[32,42] In our case, we did not apply any amplitude mask, and consequently, the measurement data at some points had some apparent noise or artifact. Secondly, given the boundary conditions of the experiment, the potential lowest-order Lamb waves would propagate along the surface, known as Rayleigh waves. The simulation results in the lateral plane allowed one to see the ratio of amplitudes between the displacements at the midline of the medium and at the border. The energy near the edges was found to be four times lower than in the midline. In addition, the high attenuation together with the geometrical dispersion caused the possible effects of this surface wave on the dominant mode to be negligible. Third, the thickness of the samples (4.5 mm) was greater than the wavelength in the frequency range studied. In the worst case, for each PAM concentration (at 3 kHz), the wavelength was 2.7, 2.0, and 1.0 mm, for 1.0%, 0.5%, and 0.25%, respectively. These values decreased rapidly with frequency. Similarly, the values obtained by SWE consistently follow the dispersion curve toward low frequencies, and in this case the thickness of the samples (50 mm) was much greater than λ in the frequency range. With these arguments, the possibility that the captured mode was a Rayleigh wave was ruled out. Therefore, they were considered bulk shear waves whose frequency dependence was attributed to the material dispersion and not to the waveguide dispersion.

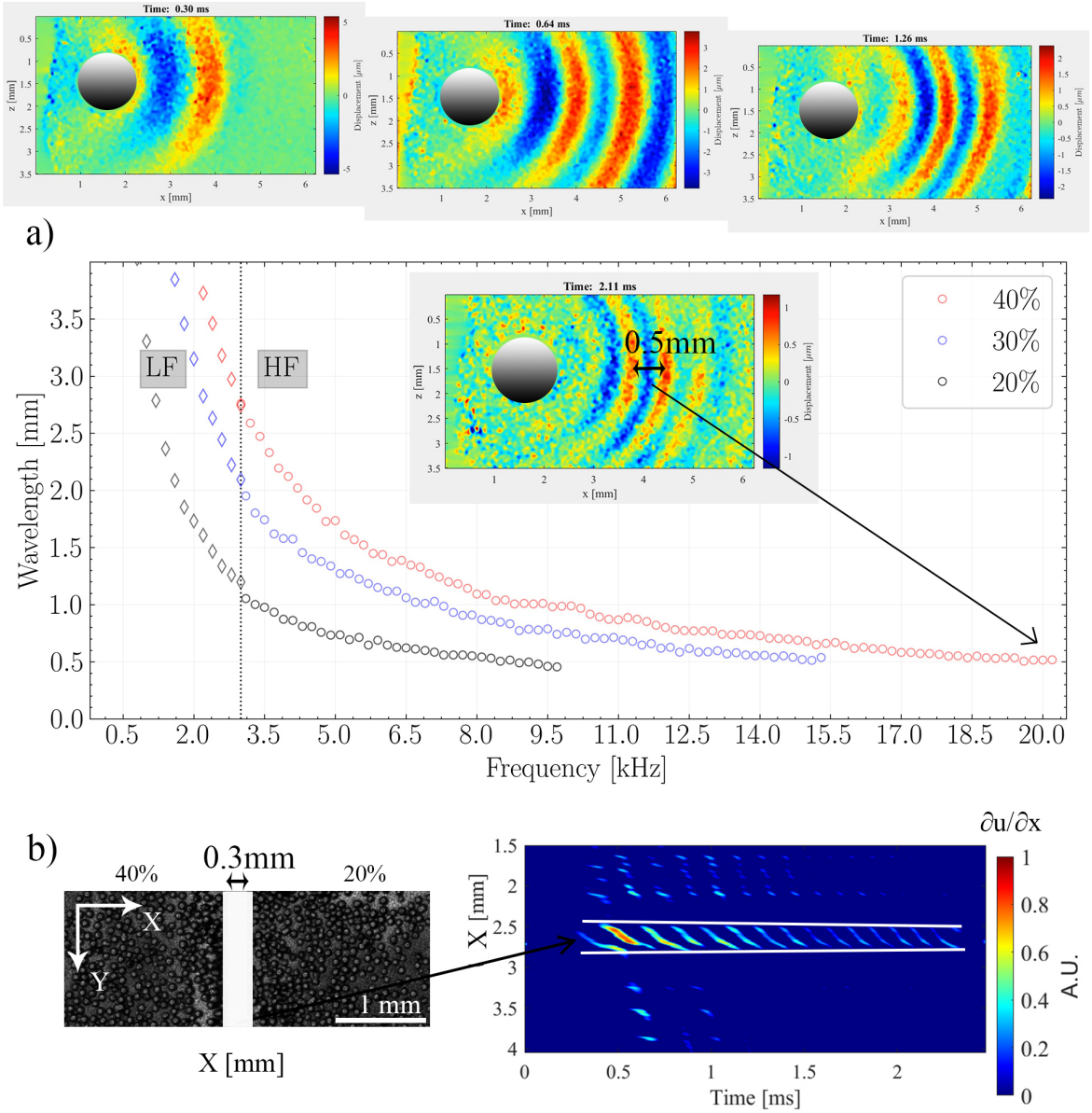

Figure 8. a) Sequential snapshots of the longitudinal shear wave propagating in the 40% PAM showing the horizontal component (X) of the particle displacement after optical flow reconstruction. The plot shows the decreasing wavelength as the excitation reached higher frequencies. b) Image of the transition between two concentrations (bilayer) and the spatial gradient of displacement when the wave propagated in the white rectangle (transition zone).

The manufactured PAM hydrogels are considered linear elastic materials,[45] and as such we had to add glycerol to increase the viscosity.[46] In the literature, this material had not been characterized at such high concentrations and, in any case, without ingredients that add viscosity. For the 20 % PAM, the shear modulus has been found between 8 and 12 kPa,[27,45] which is similar to our DMA results. The difference between values has been attributed to crosslinker concentration, polymerization temperature, and swelling equilibrium.[47] In our case, we used a 5 % crosslinker, reaching a maximum temperature reaction of 42 ºC, and we let the medium undisturbed for 30 minutes in water before measuring.

Some considerations that may limit the scalability of the proposed method include the need for transparency of the medium and the need for embedding the magnet and a sample to be measured. Although the OME technique can achieve a fine spatial resolution, it is not comparable to nanometric resolution techniques such as Atomic Force Microscopy (AFM) or Brillouin microscopy. However, this situation can be advantageous for some applications. Exploring the mechanical behavior of a material beyond the low frequency or quasi-static regimes, such as those provided by AFM, will allow

us to understand its response to a full range of dynamic mechanical stimuli. This is relevant, for example, in regenerative medicine. Measurement of the viscoelasticity of the culture substrate provides information on its ability to support cell migration and its potential to induce cell differentiation.[48] PAM hydrogels have been a popular choice for studying cell-substrate mechanical interactions.[49] On the one hand, this is due to the wide achievable range of mechanical properties by varying its concentration. Optimization of mechanical parameters increases the efficiency of culture systems. On the other hand, its total transparency facilitates visualization of cellular processes. With the OME technique, a wide spectrum of viscoelastic properties could be obtained from this type of media. By separating the plane in which measurements are taken from the plane in which the cells are seeded, the properties could be monitored over time without disrupting the cells. A confocal lens would provide at the same time an imaging system for mechanical characterization and an observing system for cellular reactions.

We demonstrated that techniques available for mechanical characterization, such as SWE and DMA, agreed well with OME's phase velocity. The rheological agreement was also studied according to the frequency range. Simple rheological models, such as the KV model, are based on single relaxation processes, which are not representative of many multiscale materials and biological structures.[50] Still, it has been shown in hydrogels, such as gelatin and agar,[17,51] and here in PAM, that they can be well described by this type of model. In the case of other models, such as Maxwell, its plateau behavior at high frequencies would not accurately describe the observed dispersive response. For more complex models, such as Zener, where an additional elastic term is added, the interpretation of multiple relaxation times is no longer straightforward.

A problem arose when taking a reduced dispersion curve to fit the KV model, since the estimated rheological parameters showed high variability. By comparing the low frequency range (<3 kHz) with the high frequency range (>3 kHz), for μ the relative errors were less than 10 %, but for η the errors reached 60 % and they can be higher with a higher dispersive behavior. By using a wide frequency bandwidth dispersion curve for the rheological parameter, the response from quasistatic to cutoff frequency was successfully modeled. Furthermore, to verify the robustness of the fittings, several initial guess values were randomly chosen. For μ between 1 and 100 kPa and for η between 0.05 and 2 Pa·s. All converged to the values shown with a variation of less than 5%.

The calculated cutoff frequencies shown in Table 3 only depended on the rheological parameters. This can be interpreted from another physical point of view. If the excitation frequency is higher than the relaxation time, the material does not have time to relax and respond, that is, to vibrate at that frequency. Therefore, the propagation energy at these frequencies is diffused. The differences between theory and experiments were mainly attributed to experimental setup and reconstruction algorithms. On the other hand, attenuation increases exponentially with distance. At one wavelength, the amplitude decreases by $e^{\alpha\lambda}$, with α the attenuation factor. The inverse of the attenuation per wavelength (A) measures the distance in number of wavelengths, when the amplitude decays close to the noise level. For low frequencies, the KV model approaches $A \approx \pi\omega\tau$.[35] If the limit is set to $\omega\tau = 1$, as observed in Table 3, then $A = \pi$, thus $A^{-1} = 0.318\lambda$. If the propagation distance is less than one third of a wavelength, no waves will propagate. This result was in line with the expression proposed by Laloy et al.[17]

6. Conclusions

The proposed micro-elastography technique was validated. A setup for generating and imaging high frequency shear waves with enough spatial and temporal resolution was configured. Few studies on elastography have reached such high frequencies and even fewer have observed ultrasonic shear waves in soft media. Tracking the displacements close to the excitation area with high resolution and without near-field effects was key to reaching the cutoff frequencies, since at such short propagation distances other methods are technically limited. The combination of the three measurement techniques provided rheology information over 6 orders of magnitude of frequencies. The study at different frequencies of a simple rheological model such as KV yielded interesting conclusions. There was no good agreement on the viscous parameter if the measurements were made at low frequencies (SWE range) and extrapolated to higher frequencies. A wide dispersion curve was necessary for the rheology to be well interpreted. This led us to hypothesize that in viscoelastic and homogeneous materials that follow a KV model over their entire measurable frequency range, the KV model was capable of predicting the high frequency cutoff. As a potential application, the mechanical characterization of tissue engineering scaffolds is envisioned.

Acknowledgements

The authors would like to thank R. Muñoz for illuminating discussions on magnetism.

This research was funded by Ministerio de Educación, Cultura y Deporte grant numbers DPI2017-83859-R, and EQC2018-004508-P; Ministerio de Ciencia e Innovación grant numbers PID2020-115372RB-I00, PYC20 RE 072 UGR; Ministerio de Sanidad, Servicios Sociales e Igualdad grant numbers DTS15/00093 and PI16/00339; Instituto de Salud Carlos III y Fondos Feder; Junta de Andalucía grant numbers PI-0107-2017, PIN-0030- 2017 and IE2017-5537; P21-00182 Consejería de Universidad, Investigación e Innovación de la Junta de Andalucía; MCIN/AEI 10.13039/501100011033 grant number PRE2018-086085 (Co-funded by European Social Fund "Investing in your future"); Consejería de economía, conocimiento, empresas y universidad and European Regional Development Fund (ERDF) SOMM17/6109/UGR, B-TEP-026- IE2017-5537 and P18-RT-1653.

Author contributions statement

Jorge Torres: Data curation, Formal analysis, Writing - original draft, Investigation, Methodology. Antonio Callejas: Software, Validation. Antonio Gomez: Validation, Writing - review & editing. Guillermo Rus: Supervision, Funding acquisition.

Additional information

Competing interests: The authors declare that they have no known competing financial interests or personal relationships that could have appeared to influence the work reported in this paper.

References

[1] Kelsey M. Kennedy, Lixin Chin, Robert A. McLaughlin, Bruce Latham, Christobel M. Saunders, David D. Sampson, and Brendan F. Kennedy. Quantitative micro-elastography: imaging of tissue elasticity using compression optical coherence elastography. *Sci. Reports 2015 51*, 5(1):1–12, oct 2015.

[2] Xuejun Qian, Teng Ma, Mingyue Yu, Xiaoyang Chen, K. Kirk Shung, and Qifa Zhou. Multi-functional Ultrasonic Micro-elastography Imaging System. *Sci. Reports 2017 71*, 7(1):1–11, apr 2017.

[3] Kristina Haase and Andrew E. Pelling. Investigating cell mechanics with atomic force microscopy. *J. R. Soc. Interface*, 12(104), mar 2015.

[4] Charlotte Alibert, Bruno Goud, and Jean Baptiste Manneville. Are cancer cells really softer than normal cells? *Biol. Cell*, 109(5):167–189, may 2017.

[5] Matt S. Hepburn, Matt S. Hepburn, Philip Wijesinghe, Philip Wijesinghe, Philip Wijesinghe, Luke G. Major, Jiayue Li, Jiayue Li, Jiayue Li, Alireza Mowla, Alireza Mowla, Chrissie Astell, Hyun Woo Park, Yongsung Hwang, Yongsung Hwang, Yu Suk Choi, Brendan F. Kennedy, Brendan F. Kennedy, and Brendan F. Kennedy. Three-dimensional imaging of cell and extracellular matrix elasticity using quantitative micro-elastography. *Biomed. Opt. Express, Vol. 11, Issue 2, pp. 867-884*, 11(2):867–884, feb 2020.

[6] Ali Zorgani, Tarek Abdul Ghafour, Maxime Lescanne, Stefan Catheline, and Aline Bel-Brunon. Optical elastography: tracking surface waves with digital image correlation. *Physics in Medicine & Biology*, 64(5):055007, 2019.

[7] C Zemzemi, A Zorgani, L Daunizeau, S Belabhar, R Souchon, and S Catheline. Super-resolution limit of shear-wave elastography. *EPL (Europhysics Letters)*, 129(3):34002, 2020.

[8] Mitchell A Kirby, Kanheng Zhou, John J Pitre, Liang Gao, David S Li, Ivan M Pelivanov, Shaozhen Song, Chunhui Li, Zhihong Huang, Tueng T Shen, et al. Spatial resolution in dynamic optical coherence elastography. *Journal of biomedical optics*, 24(9):096006, 2019.

[9] Guo Yang Li, Yang Zheng, Yu Xuan Jiang, Zhaoyi Zhang, and Yanping Cao. Guided wave elastography of layered soft tissues. *Acta Biomater.*, 84:293–304, jan 2019.

[10] Thomas Deffieux, Jean-Luc Gennisson, Jeremy Bercoff, and Mickael Tanter. On the effects of reflected waves in transient shear wave elastography. *IEEE transactions on ultrasonics, ferroelectrics, and frequency control*, 58(10):2032–2035, 2011.

[11] Naoki Sasaki. Viscoelastic Properties of Biological Materials. *Viscoelasticity - From Theory to Biol. Appl.*, nov 2012.

[12] Hongliang Li, Guillaume Flé, Manish Bhatt, Zhen Qu, Sajad Ghazavi, Ladan Yazdani, Guillaume Bosio, Iman Rafati, and Guy Cloutier. Viscoelasticity Imaging of Biological Tissues and Single Cells Using Shear Wave Propagation. *Front. Phys.*, 9:350, jun 2021.

[13] Kaiwen Zhang, Min Zhu, Evan Thomas, Sevan Hopyan, and Yu Sun. Existing and Potential Applications of Elastography for Measuring the Viscoelasticity of Biological Tissues In Vivo. *Front. Phys.*, 9:294, jun 2021.

[14] Guillermo Rus, Inas H. Faris, Jorge Torres, Antonio Callejas, and Juan Melchor. Why Are Viscosity and Nonlinearity Bound to Make an Impact in Clinical Elastographic Diagnosis? *Sensors 2020, Vol. 20, Page 2379*, 20(8):2379, apr 2020.

[15] Edwin L Carstensen and Kevin J Parker. Physical models of tissue in shear fields. *Ultrasound in medicine & biology*, 40(4):655–674, 2014.

[16] Piotr Kijanka and Matthew W Urban. Phase velocity estimation with expanded bandwidth in viscoelastic phantoms and tissues. *IEEE transactions on medical imaging*, 40(5):1352–1362, 2021.

[17] G. Laloy-Borgna, A. Zorgani, and S. Catheline. Microelastography: Toward ultrasonic shear waves in soft solids. *Appl. Phys. Lett.*, 118(11):113701, mar 2021.

[18] Rosa M.S. Sigrist, Joy Liau, Ahmed El Kaffas, Maria Cristina Chammas, and Juergen K. Willmann. Ultrasound elastography: Review of techniques and clinical applications. *Theranostics*, 7(5):1303–1329, 2017.

[19] Yogesh K Mariappan, Kevin J Glaser, and Richard L Ehman. Magnetic resonance elastography: a review. *Clinical anatomy*, 23(5):497–511, 2010.

[20] Armen Sarvazyan, Timothy J. Hall, Matthew W. Urban, Mostafa Fatemi, Salavat R. Aglyamov, and Brian S. Garra. An Overview of Elastography-An Emerging Branch of Medical Imaging. *Curr. Med. Imaging Rev.*, 7(4):255–282, nov 2011.

[21] Raffaella Righetti, Seshadri Srinivasan, and Jonathan Ophir. Lateral resolution in elastography. *Ultrasound Med. Biol.*, 29(5):695–704, may 2003.

[22] Sören J Backhaus, Georg Metschies, Marcus Billing, Jonas Schmidt-Rimpler, Johannes T Kowallick, Roman J Gertz, Tomas Lapinskas, Elisabeth Pieske-Kraigher, Burkert Pieske, Joachim Lotz, et al. Defining the optimal temporal and spatial resolution for cardiovascular magnetic resonance imaging feature tracking. *Journal of Cardiovascular Magnetic Resonance*, 23(1):1–12, 2021.

[23] Pol Grasland-Mongrain, Ali Zorgani, Shoma Nakagawa, Simon Bernard, Lia Gomes Paim, Greg Fitzharris, Stefan Catheline, and Guy Cloutier. Ultrafast imaging of cell elasticity with optical microelastography. *Proceedings of the National Academy of Sciences*, 115(5):861–866, 2018.

[24] John F Schenck. Safety of strong, static magnetic fields. *Journal of magnetic resonance imaging*, 12(1):2–19, 2000.

[25] Armen P Sarvazyan, Matthew W Urban, and James F Greenleaf. Acoustic waves in medical imaging and diagnostics. *Ultrasound in medicine & biology*, 39(7):1133–1146, 2013.

[26] Kathryn R Nightingale, Mark L Palmeri, Roger W Nightingale, and Gregg E Trahey. On the feasibility of remote palpation using acoustic radiation force. *The Journal of the Acoustical Society of America*, 110(1):625–634, 2001.

[27] Min Joo Choi, Sitaramanjaneya Reddy Guntur, Kang IL Lee, Dong Guk Paeng, and Andrew Coleman. A tissue mimicking polyacrylamide hydrogel phantom for visualizing thermal lesions generated by high intensity focused ultrasound. *Ultrasound in medicine & biology*, 39(3):439–448, 2013.

[28] Jean-Luc Gennisson, Alba Marcellan, Alexandre Dizeux, and Mickaël Tanter. Rheology over five orders of magnitude in model hydrogels: agreement between strain-controlled rheometry, transient elastography, and supersonic shear wave imaging. *IEEE transactions on ultrasonics, ferroelectrics, and frequency control*, 61(6):946–954, 2014.

[29] S Catheline and N Benech. Longitudinal shear wave and transverse dilatational wave in solids. *The Journal of the Acoustical Society of America*, 137(2):EL200–EL205, 2015.

[30] Gunnar Farnebäck. Two-Frame Motion Estimation Based on Polynomial Expansion. *Lect. Notes Comput. Sci. (including Subser. Lect. Notes Artif. Intell. Lect. Notes Bioinformatics)*, 2749:363–370, 2003.

[31] Thanasis Loupas, JT Powers, and Robert W Gill. An axial velocity estimator for ultrasound blood flow imaging, based on a full evaluation of the doppler equation by means of a two-dimensional autocorrelation approach. *IEEE transactions on ultrasonics, ferroelectrics, and frequency control*, 42(4):672–688, 1995.

[32] Miguel Bernal, Ivan Nenadic, Matthew W. Urban, and James F. Greenleaf. Material property estimation for tubes and arteries using ultrasound radiation force and analysis of propagating modes. *J. Acoust. Soc. Am.*, 129(3):1344, mar 2011.

[33] Alexander Ya Malkin and Avraam I Isayev. *Rheology: concepts, methods, and applications*. Elsevier, 2022.

[34] R_ Fletcher. Practical methods of optimization: Vol. 2: Constrained optimization. *JOHN WILEY & SONS, INC., ONE WILEY DR., SOMERSET, N. J. 08873, 1981, 224*, 1981.

[35] Sverre Holm. *Waves with power-law attenuation*. Springer, 2019.

[36] A Callejas, J Melchor, Inas H Faris, and G Rus. Viscoelastic model characterization of human cervical tissue by torsional waves. *Journal of the Mechanical Behavior of Biomedical Materials*, 115:104261, 2021.

[37] Antonio Callejas, Antonio Gomez, Inas H Faris, Juan Melchor, and Guillermo Rus. Kelvin–voigt parameters reconstruction of cervical tissue-mimicking phantoms using torsional wave elastography. *Sensors*, 19(15):3281, 2019.

[38] Jeffrey Bamber, David Cosgrove, Christoph F Dietrich, Jérémie Fromageau, Jörg Bojunga, Fabrizio Calliada, V Cantisani, J-M Correas, M D'onofrio, EE Drakonaki, et al. Efsumb guidelines and recommendations on the clinical use of ultrasound elastography. part 1: Basic principles and technology. *Ultraschall in der Medizin-European Journal of Ultrasound*, 34(02):169–184, 2013.

[39] David Meeker. Finite element method magnetics. *FEMM*, 4(32):162, 2010.

[40] Zhishen Sun, Bruno Giammarinaro, Alain Birer, Guoqiang Liu, and Stefan Catheline. Shear wave generation by remotely stimulating aluminum patches with a transient magnetic field and its preliminary application in elastography. *IEEE Transactions on Biomedical Engineering*, 68(7):2129–2139, 2020.

[41] Pol Grasland-Mongrain, Erika Miller-Jolicoeur, An Tang, Stefan Catheline, and Guy Cloutier. Contactless remote induction of shear waves in soft tissues using a transcranial magnetic stimulation device. *Physics in Medicine & Biology*, 61(6):2582, 2016.

[42] Antoine Ramier, Behrouz Tavakol, and Seok-Hyun Yun. Measuring mechanical wave speed, dispersion, and viscoelastic modulus of the cornea using optical coherence elastography. *Optics express*, 27(12):16635–16649, 2019.

[43] Jiang Zhu, Junxiao Yu, Yueqiao Qu, Youmin He, Yan Li, Qiang Yang, Tiancheng Huo, Xingdao He, and Zhongping Chen. Coaxial excitation longitudinal shear wave measurement for quantitative elasticity assessment using phase-resolved optical coherence elastography. *Optics letters*, 43(10):2388–2391, 2018.

[44] Fernando Zvietcovich, R Ge Gary, Humberto Mestre, Michael Giannetto, Maiken Nedergaard, Jannick P Rolland, and Kevin J Parker. Longitudinal shear waves for elastic characterization of tissues in optical coherence elastography. *Biomedical Optics Express*, 10(7):3699–3718, 2019.

[45] Aleksandra K Denisin and Beth L Pruitt. Tuning the range of polyacrylamide gel stiffness for mechanobiology applications. *ACS applied materials & interfaces*, 8(34):21893–21902, 2016.

[46] Ananya Sharma, Sai Geetha Marapureddy, Abhijit Paul, Sapna R Bisht, Manik Kakkar, Prachi Thareja, and Karla P Mercado-Shekhar. Characterizing viscoelastic polyvinyl alcohol phantoms for ultrasound elastography. *Ultrasound in Medicine & Biology*, 49(2):497–511, 2023.

[47] Vesna Damljanovic, B Christoffer Lagerholm, and Ken Jacobson. Bulk and micropatterned conjugation of extracellular matrix proteins to characterized polyacrylamide substrates for cell mechanotransduction assays. *Biotechniques*, 39(6):847–851, 2005.

[48] Adam J Engler, Florian Rehfeldt, Shamik Sen, and Dennis E Discher. Microtissue elasticity: measurements by atomic force microscopy and its influence on cell differentiation. *Methods in cell biology*, 83:521–545, 2007.

[49] Casey E Kandow, Penelope C Georges, Paul A Janmey, and Karen A Beningo. Polyacrylamide hydrogels for cell mechanics: steps toward optimization and alternative uses. *Methods in cell biology*, 83:29–46, 2007.

[50] KJ Parker, T Szabo, and S Holm. Towards a consensus on rheological models for elastography in soft tissues. *Physics in Medicine & Biology*, 64(21):215012, 2019.

[51] S Catheline, J-L Gennisson, G Delon, M Fink, R Sinkus, S Abouelkaram, and J Culioli. Measurement of viscoelastic properties of homogeneous soft solid using transient elastography: An inverse problem approach. *The Journal of the Acoustical Society of America*, 116(6):3734–3741, 2004.

C

A phase transition approach to elucidate the propagation of shear waves in viscoelastic materials

Jorge Torres, Gabrielle Laloy-Borgna, Guillermo Rus, Stefan Catheline

Published in: Torres, Jorge, et al. "A phase transition approach to elucidate the propagation of shear waves in viscoelastic materials." Applied Physics Letters 122.22 (2023): 223702.

Quality indications:

- Impact Factor: 3.971
- Rank: 50/161 (JCR, Q2)

DOI: https://doi.org/10.1063/5.0150219

Applied Physics Letters 122.22 (2023): 223702
https://doi.org/10.1063/5.0150219

A phase transition approach to elucidate the propagation of shear waves in viscoelastic materials

Jorge Torres[1,2], Gabrielle Laloy-Borgna[3]*, Guillermo Rus[1,2,4], Stefan Catheline[3]

Abstract
In the field of acoustics, a medium has traditionally been considered a liquid if shear waves cannot propagate. For more complex liquids, such as those containing polymer chains or surfactant aggregates, this definition begins to be unclear. By adopting a rheological model-independent approach, this work investigated by means of dynamic elastography the liquid-solid phase transitions in viscoelastic liquid media. When the storage shear modulus G' dominated the loss shear modulus G'', a minimal shear wave attenuation frequency region was defined and the medium was considered solid. When G'' dominated G', the shear waves were strongly attenuated and the medium was considered liquid. The investigated medium, an aqueous solution of xanthan gum, behaved as a bandpass filter with transition bands, showing liquid-solid-liquid behavior from low to high frequency. During these transitions bands, shear waves still propagated but highly attenuated. The limiting values where shear waves were no longer observed were identified as the low and high cutoff frequencies. Finally, the ability of various rheological models to predict the phase transition frequencies and describe the dispersion curves was tested. A three-element rheological model, the Jeffreys model, was required to accurately fit the experimental response of the medium at different concentrations over the entire frequency range. Shear wave propagation methods can overcome the technical limitations of traditional rheometry, and explore higher frequencies, rarely investigated in viscoelastic liquids.

[1] *Ultrasonics Lab (TEP-959), Department of Structural Mechanics, University of Granada, Granada, Spain*
[2] *Biomechanics Group (TEC-12), Instituto de Investigación Biosanitaria, ibs.GRANADA, Granada, Spain*
[3] *LabTAU, INSERM, Centre Léon Bérard, Université Lyon 1, Univ Lyon, F-69003 Lyon, France*
[4] *Excellence Research Unit "ModelingNature" (MNat), Universidad de Granada, Granada, Spain*
*__Corresponding author__: gabrielle.laloy-borgna@inserm.fr

Initially, a solid is defined as a medium in which shear waves can propagate, since its shear elasticity allows shear strain energy to be stored. In contrast, in a liquid with near-zero shear elasticity, shear wave propagation is often not observed. This is in part due to a small penetration depth, defined as the distance beyond which shear waves do not propagate anymore. This holds true for Newtonian fluids, which can be characterized by a single coefficient, the Newtonian viscosity, which defines the proportionality between the shear stress and the strain rate. In this case, the friction drag due to viscosity is the support mechanism for shear wave propagation at a distance smaller than half a wavelength. For its part, complex liquids, including those containing internal structures such as polymer chains or surfactant aggregates, exhibit viscoelastic behavior, which is more intricate than simple viscous behavior and can support shear waves. They are more commonly termed viscoelastic liquids, which means that they can flow or deform as solids depending on the length and time scales of the deformation.[1]

Understanding viscoelastic liquids mechanical properties is crucial in various fields such as materials science and biomedical engineering. Moreover, if a wide frequency range is covered, flow processes can be characterized and their application in different dynamic situations can be optimized.[1] Their experimental evaluation has been carried out mainly by oscillatory shear experiments with conventional rotational rheometers. They are usually limited to 15.92 Hz ($\backsim$ 100 rad/s), because instrumental inertial effects dominate at higher frequencies.[2]

To overcome the technical limitations of rheology methods, shear wave propagation methods are capable of reaching higher frequencies, rarely investigated in viscoelastic liquids. In the literature, optical, ultrasonic, or mechanical methods have been used to detect shear waves in micellar fluids,[3–5] partially coagulated blood,[6,7] or oil.[8] Gennisson et al.[6] monitored blood coagulation over time and detected the time from liquid to solid phase transition. Schmitt et al.[7] compared standard rheological models during blood coagulation at high frequencies (50-150 Hz). Amador et al.[3] described the varying viscoelastic properties of micellar fluid at different concentrations using ultrasound elastography. Gladden et al.[4] studied rheometry and shear wave propagation at a single frequency in a micellar fluid to conclude that the medium acted as a Newtonian fluid at very low frequencies. In the low frequency range studied by rheometry, the Maxwell (Mx) model accurately predicted the experimental data up to a frequency of

about 2 Hz with significant discrepancies beyond this value.

These studies have demonstrated the possibility of describing rheologically the propagation of shear waves in viscoelastic liquids, but several questions remain open about observed phenomena. In particular, in the same way that there are liquid-solid phase transitions in thermodynamics, this work consisted of studying by means of dynamic elastography, the frequency ranges for which a medium is regarded as a classic solid (G'>G") or liquid (G'<G"). At the same time, we studied the low and high frequency limits (cutoffs), where shear waves are no longer observed, to better understand shear wave propagation in viscoelastic liquids. Finally, as it has been observed that simple rheological models do not reproduce the experimental complex shear modulus at high rheometry frequencies,[9] the capacity of different rheological models to predict the phase transition frequencies was tested.

The chosen medium was an aqueous solution of xanthan gum (XG, E415 Le Meilleur du Chef, France), a polysaccharide produced by the fermentation of a bacteria. It is a water-soluble and viscosity enhancing ingredient that can create an internal polymeric structure[10] and thus a viscoelastic liquid. It has also been used very recently for tissue engineering and tissue-mimicking applications.[11] A volume of 1.2 liters of distilled water was heated to a temperature of 70ºC to ensure good mixing. Then, a mixture of XG with graphite was slowly added while magnetically stirring for 30 minutes. The concentrations (w/w) of XG used were 0.25, 0.5 and 1%, together with 0.1% graphite to provide acoustic scattering. A vacuum pump was used to remove the bubbles created by the stirring. The medium was finally poured into a recipient of dimensions 33x19x6cm^3 and covered for 18-24 hours until it reached room temperature.

The generation and tracking of shear waves was carried out using dynamic elastography with a Verasonics research system (Vantage 256, Verasonics Inc., Redmond, WA, USA) and an L11-5v linear probe (Fig. 1a). For a complete and efficient viscoelastic characterization, a multi-frequency excitation was required. A short-duration high-intensity ultrasound pulse was transmitted to the medium to generate shear waves. This acoustic radiation force (ARF) push impulse caused a wide bandwidth response.[12] The parameters for the ARF push were 1000 cycles, 7.6 MHz central frequency, and 25 mm focal distance. Immediately after, ultrafast imaging was performed using plane waves with a pulse repetition frequency (PRF) of 3 kHz. To remove the effect of random noise, 10 consecutive frames were averaged. The displacement field was reconstructed using a phase tracking algorithm,[13] which was applied on the Hilbert transform of the raw data. A rectangular Region Of Interest (ROI) of 8 mm lateral distance (x) was averaged over 5 mm depth (z) to obtain the displacement profile (Fig. 1b). The dimensions of the ROI were experimentally chosen to achieve the optimal spatial resolution for velocity and amplitude reconstruction. To avoid the clutter of the ARF push zone, the lateral position of the ROI started at 4 mm. Due to the geometric attenuation caused by the cylindrical front, the signal amplitude was adjusted by multiplying it by $\sqrt{r}$, with r the distance to the excitation plane.[14] Particle velocity data were obtained by time differentiating, which were less sensitive to low frequency motion. A spatial frequency limit was applied to suppress both compressional waves and out-of-plane shear waves with propagation velocities greater than 0.5 m/s by removing their k component in the (f,k) space.[15] A spatiotemporal representation of the velocity field $v_z(t,x)$ is presented in Fig. 1c. It can be seen how the impulse spreads out during its propagation, generating a dispersive wave. This confirms what has been observed in the literature,[3–5] in a medium that is, according to common sense, a liquid, since it flows on time scales of the order of a second, it is possible to observe propagating shear waves.

In order to detect the liquid-solid phase transition frequencies, a rheological model-independent approach was adopted. First, by applying a 2D Fourier transform method, the phase velocity and attenuation were derived.[14] The reconstructed spatiotemporal data $v_z(t,x)$ was transformed into the $\tilde{v}_z(f,k)$ space. The main propagation mode was determined by identifying pairs of wavenumber k and frequency f associated with the maximum amplitude values of the $\tilde{v}_z(f,k)$ space. The phase velocity was obtained as $c_{ph} = \omega/k$. The attenuation was proportional to the Full Width at Half Maximum (FWHM) of the wavenumber signals associated with each frequency,[14] as shown in Fig. 1f. It was calculated as $\alpha = \text{FWHM}\frac{\pi}{\sqrt{3}}$. Finally, using the pair (c_{ph}, α), the storage modulus G' and the loss modulus G'' were reconstructed with $G^* = G' + iG'' = \rho\left(\frac{\omega}{\omega/c_{ph}+i\alpha}\right)^2$. The cutoff frequencies were determined when there were abrupt changes (jumps) in the information of the main propagation mode, as shown in Fig. 1d. Alternatively, a 1D Fourier transform was performed on $v_z(t,x)$ and a study of the phase of the waves as a function of frequency and propagation distance is presented in Fig. 1e. When a wave propagates, the phase must be linear over a distance, so that a linear regression can be performed to obtain the associated k.[16,17] When the phase is noisy or oscillates, it cannot be attributed to a propagating wave. This was used to prove the reliability of the identified cutoffs observed in $\tilde{v}_z(f,k)$. After this, four rheological models (Kelvin-Voigt KV, Mx, Jeffreys, and Extended Maxwell) were proposed to explain the observed behavior. To estimate the parameters of the models, a nonlinear least squares method was applied using a trust-region algorithm implemented in Matlab (R2021b, The MathWorks Inc.) to fit the dispersion curve (c_{ph}). Then the fitted parameters were used to compute the response of the model for G', G''. This is a highly ill-posed inverse problem in the sense that small perturbations and experimental values propagate as high variability in the reconstructed parameters. To tackle this problem, the uncertainty was calculated as the gradient of the phase velocity with the frequency. Lastly, the inverse of uncertainty was used as a weight metric for the fitting function.[18] This dependency of the weights on the gradient is intuitive, since high gradients imply a deviation from the general trend of the dispersion curve, which are associated

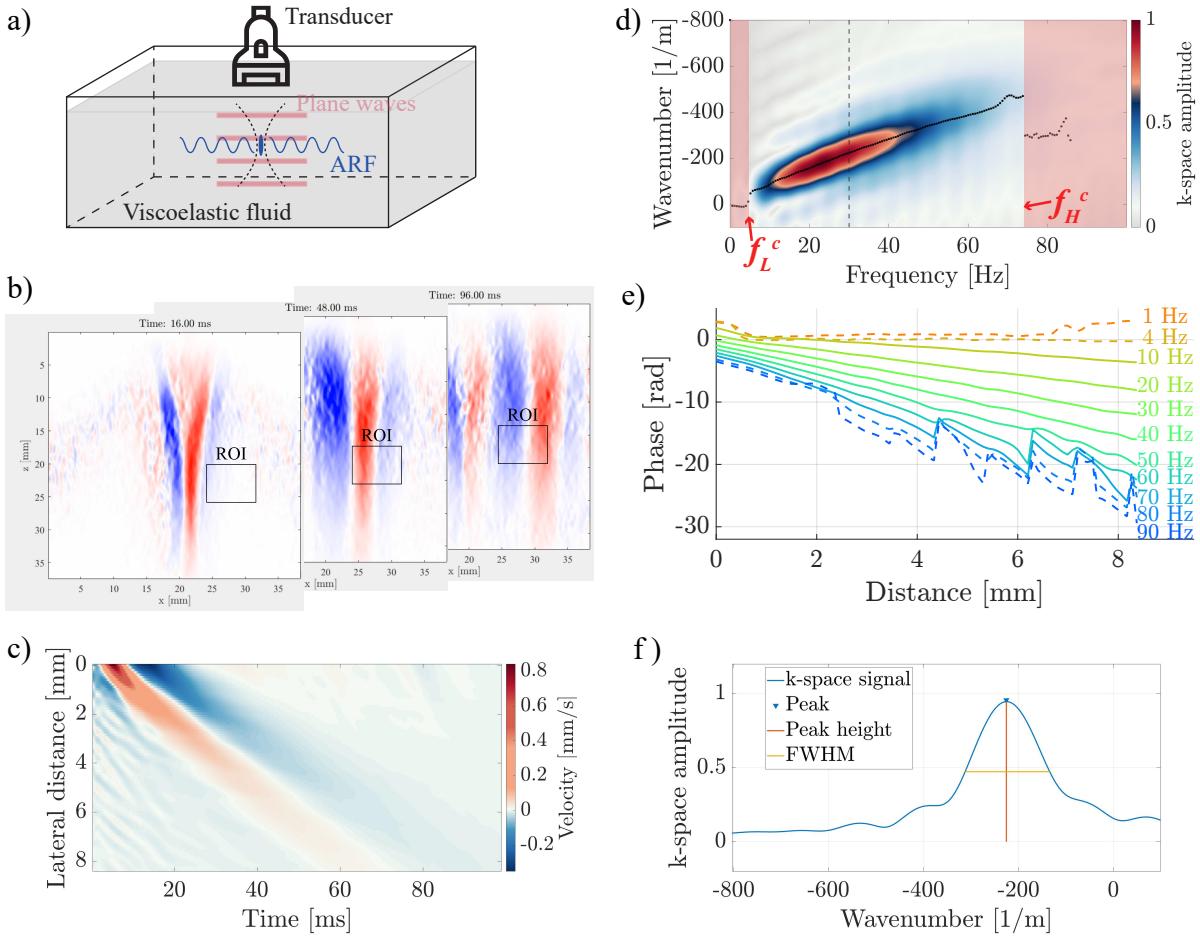

Figure 1. a) Experimental setup to capture shear waves on viscoelastic liquids with an Acoustic Radiation Force (ARF) excitation. b) Snapshots of the rightward propagating shear wave and the particle displacement at 16, 48 and 96 ms. The black rectangle marks the Region of Interest (ROI). c) Particle velocity map $v_z(t,x)$ for a 0.5% sample. d) $\tilde{v}_z(f,k)$ space showing the peaks (black points) that correspond to the phase velocity for each frequency. The low (f_L^c) and high frequency (f_H^c) limits are marked. e) Phase as a function of frequency and propagation distance showing similar limits as the $\tilde{v}_z(f,k)$ space. f) Calculation of the Full Width at Half Maximum (FWHM) at 30 Hz for attenuation estimation.

to the behavior at the frequency limits.

The experimental dispersive behavior of the phase velocity for a sample of 0.5% XG concentration is shown in Fig. 2a. The calculated values are between 0.1 and 0.2 m/s, which are similar to those reported for other viscoelastic fluids.[3,4] The detected cutoff frequencies are 5 Hz (f_L^c) and 73 Hz (f_H^c). Beyond these values, the phase velocity points deviate significantly from the represented propagation mode. This behavior can also be observed through Fig. 1e, where the phase of the waves is studied. The distance at which the phase is linear decreases as the frequency increases, and therefore the propagation distance also decreases. We see that at 70 Hz, the phase is linear up to about 4 mm, and then oscillates, which would correspond to non-propagating waves. As the frequency increases, the phase oscillates more and there is very little propagation distance, making it difficult to attribute it to propagating waves. At low frequencies (1 and 4 Hz), it is seen that the phase starts oscillating and then presents slopes that would not correspond to shear wave velocities in the medium. To confirm the low frequency cutoff, a longer acquisition time of 10 s, in comparison to the 200 ms in the normal acquisition, was used to meet the Nyquist criterion and to allow sufficient time to capture possible propagating shear waves down to 0.2 Hz, as represented by the green points in Fig. 2a. Characterization in terms of attenuation per wavelength **A** has been widely used in different domains[19] and is used here. The advantage is that it can provide a relative value that represents the frequency transition between propagating and nonpropagating waves. It is defined as $\mathbf{A} = \lambda/L_{att}$, with λ the wavelength, and L_{att} the attenuation length (the inverse of α). It is shown in the inset of Fig. 2a as a function of frequency. In the low frequency range, the long λ result in a very large **A**. In the middle range, both values balance each other and **A** decreases. In the high frequency

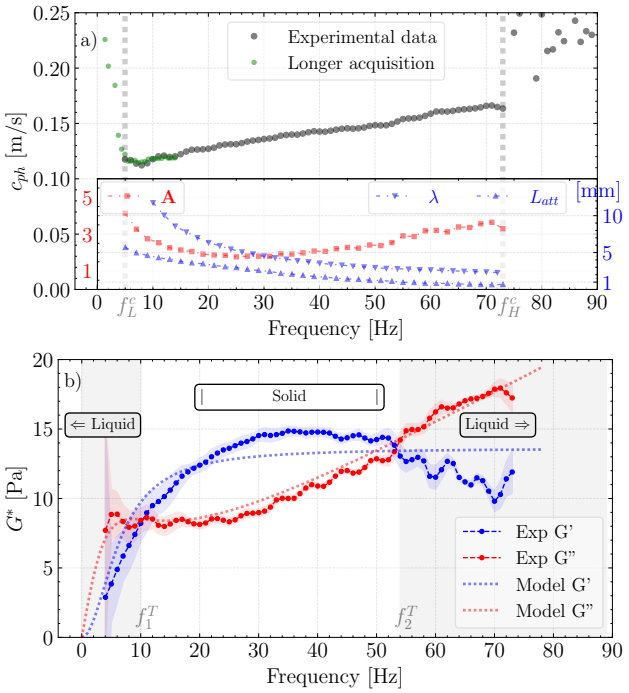

Figure 2. Experimental results for a 0.5% concentration sample. a) Phase velocity curve with vertical gray lines representing the setup detected cutoff frequencies. The inset shows the attenuation per wavelength **A**, and the attenuation parameters that compose it: wavelength and attenuation length, in color blue. b) Experimental storage G' and loss modulus G'' presenting solid-liquid phase transition zones. The Jeffreys model fitting is also represented. The error bands represent the uncertainty .

range, the attenuation increases compared to λ, resulting in a new increase in **A**.

Fig. 2b shows the behavior of G^*. For a frequency lower than 10 Hz (f_1^T, first transition frequency), G'' is higher than G', indicating that the dissipating term dominates over the storage term. Below this frequency, the relaxation time of the medium is faster than the vibration, and shear waves are strongly attenuated due to restoring forces. In rheological terms the medium is regarded as a liquid. The storage term G' then dominates up to a second crossover point around 55 Hz (f_2^T, second transition frequency), and the medium can be considered a solid between 10-55 Hz. Beyond this intermediate range, shear waves begin to become strongly attenuated again, and the medium is regarded as a liquid ($G'' > G'$). Above this f_2^T frequency, the solid-like behavior of the material cannot follow a vibration whose amplitude is rapidly decaying. It has been found that the adopted approach can detect both the cutoff frequencies and the liquid-solid phase transition frequencies. The reason why their values do not match can be explained by an analogy with electronic filters. A bandpass filter includes two stop bands, where the frequency content of the signals is eliminated, and a pass band, which defines the region of minimal attenuation for the signals. Between these zones there are transition bands, where the signals start to be strongly attenuated until they reach the stop band. Accordingly, the investigated medium behaves as a bandpass filter with transition bands. Therefore, the solid phase bandwidth (10-55 Hz) defines the region of minimal attenuation for the wave amplitude. In turn, the bandwidth between cutoff frequencies (5-73 Hz) defines the region of experimental detection threshold.

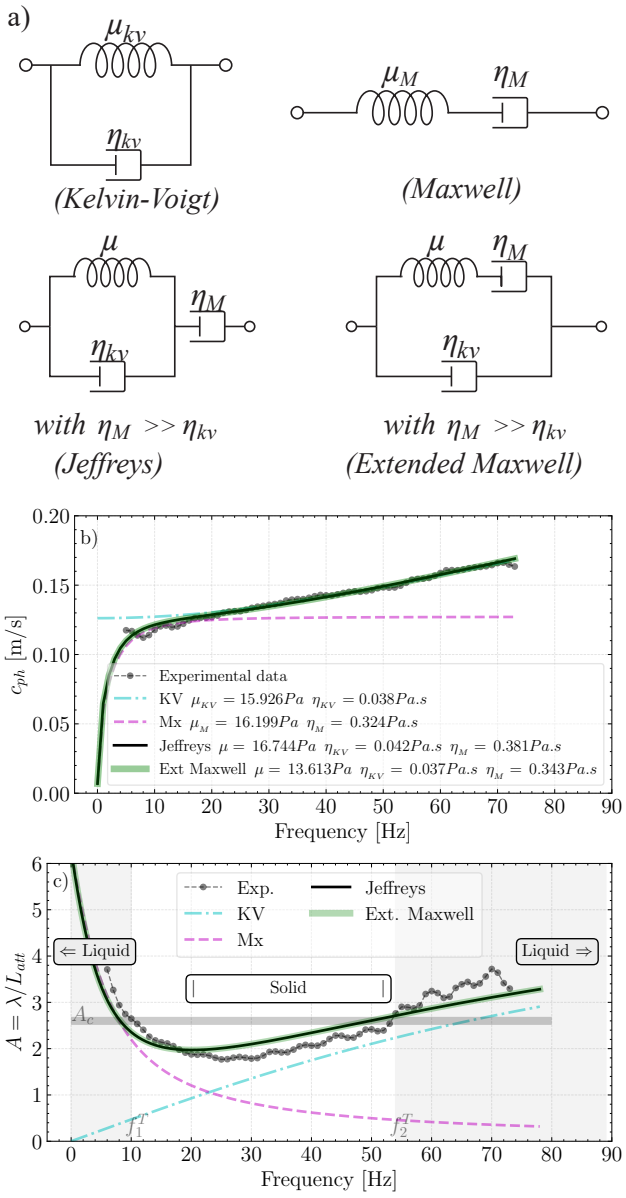

Figure 3. Experimental results and rheology models comparison for a 0.5% concentration sample. a) Scheme of the studied rheological models. b) Phase velocity curve with rheological parameters. c) Attenuation per wavelength **A** and solid-liquid phase transition zones.

The response of the four proposed rheological models shown in Fig. 3a is compared with the experimental data. The subindices of the rheological parameters are associated with KV or Mx. The KV model is frequently used to explain solid-like behaviors.[17] In Fig. 3b, this model appears to be compatible almost throughout the entire range, but there

are significant discrepancies at frequencies below 20 Hz. The elastic parameter is $\mu_{kv} = 15.926$ Pa and the viscous parameter is $\eta_{kv} = 0.038$ Pa·s. These values are plausible according to measurements in similar media.[5] For its part, the Mx model often describes liquids. Observing the dispersive behavior of the medium and knowing that the Mx model tends to plateau at high frequencies, the fitting is performed only up to 20 Hz. This model is found to adequately reproduce the values at low frequencies. The fit parameters are $\mu_M = 16.199$ Pa and $\eta_M = 0.324$ Pa·s.

Fig. 3c illustrates attenuation through $\mathbf{A}$ and allows to explain in terms of filters the behavior of each model. The same transition frequencies f_1^T and f_2^T previously reported are plotted. For KV the attenuation starts from 0 and increases faster than the wavelength decreases. The medium behaves as a solid-like KV only at frequencies higher than 30 Hz, with a high frequency transition f_2^T beyond which shear waves are strongly attenuated. Therefore, KV represents a medium that acts as a low-pass filter. In contrast, at low frequencies, the KV model is not suitable for a flowing medium. Mx exhibits a behavior opposite to that of KV. At low frequencies, large wavelengths result in high $\mathbf{A}$ values that are rapidly decreasing. The viscous component G'' dominates the propagation, and the model and experiment agree well only up to 10 Hz. Thus, the medium behaves like a liquid Mx with a low frequency transition f_1^T. Mx represents a medium that act as a high-pass filter, going from the liquid to the solid phase. These frequencies intersect at $\mathbf{A}_c \approx 2.6$. Because attenuation increases exponentially with distance, at one wavelength, the amplitude decreases by $e^{\alpha\lambda}$. The inverse of $\mathbf{A}$ measures the distance in number of wavelengths, when the amplitude decays close to a noise level value. Therefore $\mathbf{A_c}^{-1} = 0.385\lambda$, that is, if the propagation distance is less than 1/26 of the wavelength, the amplitude of the waves eventually becomes too small to be detected experimentally. This threshold is in line with previous works, where a $\mathbf{A}_c = 3$ indicated the critical attenuation per wavelength.[16]

Because simple rheological models cannot reproduce the behavior over the entire frequency spectrum, a three-element model is proposed. The extended Maxwell model has already been used in viscoelastic fluid rheometry to capture the experimental complex shear modulus.[3,20] This model consists in connecting a dashpot in parallel with a Mx model. It can also be obtained by connecting a dashpot in series with a KV, which is the Jeffreys model,[21] also called standard linear liquid model. This pair of conjugate approaches for the same model follow the same constitutive equation but with different coefficients.[22] The Jeffreys approach is adopted because it allows for a more intuitive physical explanation according to the observed results. The constitutive equations and expressions for the mechanical parameters are described in the Supplementary Material file.

The behavior of this model can be deduced from its scheme (see Fig. 3a). At low frequencies, the stress term associated with the viscosity η_{kv} in the expression $\eta_{kv}\omega\gamma$ can be considered negligible compared to the stress exerted by the spring in $\mu\gamma$ and by the dashpot η_{kv}, because the viscosity η_{kv} is much lower than η_M. Thus, the impact of the low-frequency viscosity damper η_{kv} on the overall behavior of the system can be ignored, and the three-element model can be approximated as a Mx model, consisting of a series connection of an elastic component with modulus μ and a viscous component with viscosity η_M. On the other hand, at high frequencies, the factor $\eta_M\omega$ is much larger than μ and $\eta_{kv}\omega$ for finite strain values. As a result, the deformation of the viscous damper with viscosity η_M is negligible compared to the deformation of the KV model in series with it. Since the total deformation is the sum of these two deformation terms, the three-element Jeffreys model can be approximated as a KV model at high frequency.

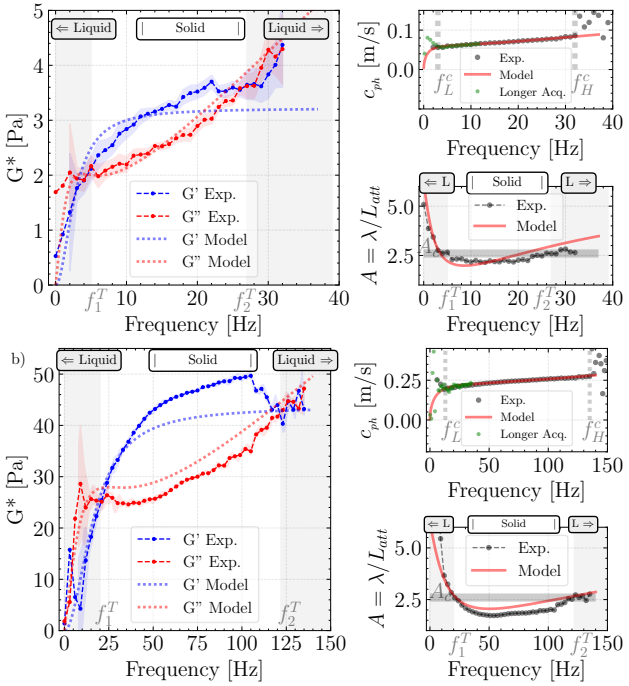

Figure 4. Experimental and Jeffreys model results for the complex modulus G^*, phase velocity, and attenuation per wavelength $\mathbf{A}$, with detected cutoff and phase transition frequencies. a) XG concentration of 0.25%. b) XG concentration of 1%. The error bands represent the uncertainty.

The agreement of the previously presented model with the experimental measurements is shown in Fig. 3 (black lines). The rheological parameters obtained with this fitting are $\mu = 16.744$ Pa, $\eta_{kv} = 0.042$ Pa·s, and $\eta_M = 0.381$ Pa·s, which are in line with the parameters of the simplest models. As before, these parameters are used to calculate $\mathbf{A}$ and (G', G''). The Extended Maxwell model (green line in Fig. 3) is perfectly superimposed on all the Jeffreys model curves, verifying that they represent the same system but with different parameters, as seen in the dispersion curve. It is observed that the theoretical curves predicted by the Jeffreys and Extended Maxwell models can accurately describe the experimental

measurements.

Table 1. Rheological parameters and determination coefficients estimated for the Jeffreys model from the nonlinear least squares method for aqueous solutions of different concentrations of Xanthan gum.

XG Concentration (%)	μ [Pa]	η_{kv} [Pa·s]	η_M [Pa·s]	R^2
0.25	3.970	0.023	0.211	0.923
0.5	16.744	0.042	0.381	0.913
1	54.659	0.057	0.475	0.862

To gain a deeper insight into these rheological parameters, one of the approaches explored is to change the concentration of XG in the medium and study the resulting changes, as presented in Fig. 4. The cutoff frequencies (f_L^c–f_H^c) are 3–32 Hz and 13–135 Hz, for 0.25% and 1% concentrations, respectively. The liquid-solid phase transition frequencies (f_1^T–f_2^T) are 5–27 Hz and 20–122 Hz, for 0.25% and 1% concentrations, respectively. In the liquid phases ($G'' > G'$), the experimental data diverge from the model, showing a higher uncertainty error band. This is attributed to both strong attenuation and the presence of evanescent waves that cause noisy reconstruction. Evanescent waves have already been observed in soft gels at high frequencies.[16] They have a rapidly decaying amplitude and no transport of energy.[19] In both samples, $\mathbf{A}_c$ is approximately 2.6 as well. This implies that when $\mathbf{A}$ is greater than this threshold value, waves at these frequencies start to be difficult to observe. In the solid phase ($G' > G''$) it is observed that experimental G' deviates from the model as the frequency increases. On the one hand, these differences are due to the fact that the fit is performed only on c_{ph} and small errors are amplified when transforming into G^*. On the other hand, as a complex liquid with different concentrations, some deviations are expected in the elastic part. Qualitatively, the 0.25% concentration looks like a stabilized fluid emulsion, the 0.5% one is a firm emulsion, and the 1% one starts to approach a gel. Complete solid-like behavior was observed for concentrations higher than 1%.[10] Even so, it can be seen that the Jeffreys model curves demonstrate a strong level of agreement with the experimental measurements over the entire frequency range. This confirms that the model is able to reproduce the bandpass filter behavior of this type of media. The values presented in Table 1 are the rheological parameters and determination coefficients R^2 estimated for the three samples used. R^2 is computed by comparing the variability (sum of squares) of the estimation errors with the variability of the original values. They are in good agreement with micellar fluids of similar properties that resemble the properties of actual biological samples like mucus,[3,20] where they obtained μ=37 Pa and η_M=0.33 Pa·s. All parameters increase with concentration, in a pseudolinear fashion for viscosity and following a power-law for elasticity.

To estimate the shear wave propagation frequency limits, we have based ourselves on two criteria: the information in the frequency domain of the waves and, the relationship between wavelength and attenuation, which describes the number of oscillations that we can observe. When the lateral distance (x) of the ROI was decreased, the cutoff frequency could increase, as shown in Fig. 1e, where it is seen that the phase remains linear in small propagation distances. But in this case the attenuation was difficult to reconstruct because the spatial resolution decreased and the FWHM associated to a plausible attenuation value could not be estimated. When the lateral distance (x) of the ROI increased, the cutoff decreased, because in this case, the phase was not linear at longer distances, which would not correspond to a propagating wave. In the low frequency range, λ is in an order of magnitude not much larger than the dimensions of the ROI, and as discussed in Zemzemi et al.[23] this should not be a limitation to estimate mechanical parameters. In the high frequency range, it is observed that as the concentrations increase, so does the frequency limit. Thus, if we assume that the experimental setup had a constant $\mathbf{A}$,[16] the frequency range of detection threshold was defined.

Some limitations of the current study include the evaluation of the effect of chemical factors such as solvent pH, salinity, etc., which are known to affect the mechanical response[24] but are outside the scope of the study. Also, the fitting of parameters, especially for the three-element models, is a delicate process due to the sensitivity and unicity of the inverse problem. However, from a practical perspective that is focused on finding coherent parameters, and by judging from the consistency between different XG concentration samples, it is reasonable to claim that the probability that the algorithm returned a wrong range of values is negligible. Considering that the maximum amplitude observed is about 2 μm the strain is assumed to be less than 1%.[25] With this low strain amplitude, typical of dynamic elastography, it can be assured that the material is in the linear viscoelastic regime. If a higher strain amplitude were used, the Jeffreys model would not be able to capture the response of XG due to its shear thinning.[26]

The aqueous solution of XG can be perceived as a network of polymer chains entangled within a Newtonian fluid, specifically water.[10] A higher density of these associations at higher concentrations creates a stronger network. At the same time, the entanglements of polymer chains increase the resistance to internal flow and thus the viscosity. Hydrogen bonding can also occur between polymer chains and solvent molecules, and consequently, the strength of these interactions can significantly influence the physical and chemical properties of the material.[24] Although it would be intriguing to relate the estimated rheological parameters in Table 1 to this internal structure, at this point it is difficult to give a convincing interpretation. In a simplified way, we postulate that the polymer chains exhibit the characteristics of a KV solid. This rheological system is placed in series with a dashpot, to represent that the medium is embedded in a Newtonian fluid, which is the Jeffreys model.

The viscoelastic response of XG has been extensively characterized by frequency sweep tests with oscillatory rheometry, reporting values in the same order of magnitude as our re-

sults. For concentrations lower than 0.5%, frequencies higher than 2 Hz have not normally been used, resulting in a G' between 5 and 10 Pa, and a G'' between 1 and 4 Pa.[27–31] For concentrations of 1%, excitations of about 15 Hz have been reached with G' between 30 and 35 Pa, and G'' between 10 and 15 Pa.[10,32] Although we have obtained values consistent with other studies, there are difficulties in making direct comparisons between shear wave methods and rheometry.[33] Rheometry is primarily sensitive to the intrinsic viscosity of the constituents of the medium and the frictional interactions between them. For its part, shear wave methods are also sensitive to the microstructure. When the wave propagates, there is wave scattering as a result of its interaction with the microstructure. Then another limitation is the addition of acoustic scatterers that can influence the attenuation and the frequency dependence of the propagation velocity.[3] In some rheometry studies using aqueous XG solution, the low frequency crossover point in the complex shear modulus has been detected at very low frequencies, on the order of a few microhertz.[10,24,29,30,32,34] The high frequency crossover point has not been observed since the system presented very sensitive phase angles at high frequencies, leading to significant errors,[2] however, it seems that G" would tend to intercept G'[27,32,34] as predicted by the Jeffreys model.

The studied XG media have shown a bandpass filter behavior, where the solid-to-liquid phase transition at high frequency has also been identified. This has been possible through the broad frequency spectrum in which shear wave methods can work, in contrast to the limitations of rotational rheometry. Shear wave cutoff frequencies have also been studied to better understand wave propagation in viscoelastic liquids. The study of shear waves within biological viscoelastic liquids is a promising tool to evaluate their mechanical properties. It could be used to differentiate pathological states, such as blood hyperviscosity syndrome, or sputum viscosity to diagnose chronic respiratory diseases.

Acknowledgements

This research was partly funded by RHU-V3 2016, Perfuse Project and R3-FLI 2022 « ViscOptic » project. MCIN/AEI 10.13039/501100011033 grant number PRE2018-086085 570 (Co-funded by European Social Fund "Investing in your future"). Ministerio de Educación, Cultura y Deporte grant numbers DPI2017-83859-R, and EQC2018-004508-P. Consejería de economía, conocimiento, empresas y universidad and European Regional Development Fund (ERDF) SOMM17/6109/UGR, B-TEP-026- IE2017-5537 and P18-RT-1653.

Author contributions statement

Jorge Torres: Data curation (equal); Formal analysis (equal); Writing – original draft (equal). Gabrielle Laloy-Borgna: Conceptualization (equal); Methodology (equal); Writing – original draft (equal); Writing – review & editing (equal). Guillermo Rus: Funding acquisition (equal); Supervision (equal); Writing – review & editing (equal). Stefan Catheline: Conceptualization (equal); Funding acquisition (equal); Writing – review & editing (equal).

Additional information

The data that support the findings of this study are available from the corresponding author upon reasonable request.

See supplementary material for the derivation of the mechanical parameters for each proposed rheological model.

References

[1] R. B. Bird, R. C. Armstrong, and O. Hassager. Dynamics of polymeric liquids. Vol. 1, 2nd Ed. : Fluid mechanics. John Wiley and Sons Inc.,New York, NY, January 1987.

[2] Anne Kowalczyk, Bernhard Hochstein, P Stähle, and Norbert Willenbacher. Characterization of complex fluids at very low frequency: Experimental verification of the strain rate-frequency superposition (srfs) method. *Applied Rheology*, 20(5), 2010.

[3] Carolina Amador, Bruno L. Otilio, Randall R. Kinnick, and Matthew W. Urban. Ultrasonic method to characterize shear wave propagation in micellar fluids. *The Journal of the Acoustical Society of America*, 140(3):1719–1726, September 2016.

[4] J. R. Gladden, A. M. Gamble, C. E. Skelton, and J. Mobley. Shear waves in viscoelastic wormlike micellar fluids over a broad concentration range. *The Journal of the Acoustical Society of America*, 131(3):2063–2067, March 2012.

[5] Hsiao-Chuan Liu, Piotr Kijanka, and Matthew W. Urban. Acoustic radiation force optical coherence elastography for evaluating mechanical properties of soft condensed matters and its biological applications. *Journal of Biophotonics*, 13(3), March 2020.

[6] Jean-Luc Gennisson, Sophie Lerouge, and Guy Cloutier. Assessment by transient elastography of the viscoelastic properties of blood during clotting. *Ultrasound in Medicine & Biology*, 32(10):1529–1537, October 2006.

[7] Cédric Schmitt, Anis Hadj Henni, and Guy Cloutier. Characterization of blood clot viscoelasticity by dynamic ultrasound elastography and modeling of the rheological behavior. *Journal of Biomechanics*, 44(4):622–629, February 2011.

[8] Ali Abdallah, Erwin K. Reichel, Thomas Voglhuber-Brunnmaier, and Bernhard Jakoby. Characterization of Viscous and Viscoelastic Fluids Using Parallel Plate Shear-Wave Transducers. *IEEE Sensors Journal*, 16(9):2950–2957, May 2016.

[9] Lynn M Walker. Rheology and structure of worm-like micelles. *Current Opinion in Colloid & Interface Science*, 6(5):451–456, November 2001.

[10] Necla Mine Eren, Paulo H.S. Santos, and Osvaldo Campanella. Mechanically modified xanthan gum: Rheology and polydispersity aspects. *Carbohydrate Polymers*, 134:475–484, December 2015.

[11] Anuj Kumar, Kummara Madhusudana Rao, and Sung Soo Han. Application of xanthan gum as polysaccharide in tissue engineering: A review. *Carbohydrate Polymers*, 180:128–144, January 2018.

[12] Armen Sarvazyan, Timothy J. Hall, Matthew W. Urban, Mostafa Fatemi, Salavat R. Aglyamov, and Brian S. Garra. An Overview of Elastography-An Emerging Branch of Medical Imaging. *Current Medical Imaging Reviews*, 7(4):255–282, November 2011.

[13] Nicolas Benech, Stefan Catheline, Javier Brum, Thomas Gallot, and Carlos A Negreira. 1-d elasticity assessment in soft solids from shear wave correlation: The time-reversal approach. *IEEE transactions on ultrasonics, ferroelectrics, and frequency control*, 56(11):2400–2410, 2009.

[14] Ivan Z. Nenadic, Bo Qiang, Matthew W. Urban, Heng Zhao, William Sanchez, James F. Greenleaf, and Shigao Chen. Attenuation measuring ultrasound shearwave elastography and in vivo application in post-transplant liver patients. *Physics in Medicine & Biology*, 62(2):484, December 2016.

[15] Heng Zhao, Pengfei Song, Duane D. Meixner, Randall R. Kinnick, Matthew R. Callstrom, William Sanchez, Matthew W. Urban, Armando Manduca, James F. Greenleaf, and Shigao Chen. External Vibration Multi-Directional Ultrasound Shearwave Elastography (EVMUSE): Application in Liver Fibrosis Staging. *IEEE Transactions on Medical Imaging*, 33(11):2140–2148, November 2014.

[16] G. Laloy-Borgna, A. Zorgani, and S. Catheline. Microelastography: Toward ultrasonic shear waves in soft solids. *Applied Physics Letters*, 118(11):113701, March 2021.

[17] S. Catheline, J.-L. Gennisson, G. Delon, M. Fink, R. Sinkus, S. Abouelkaram, and J. Culioli. Measurement of viscoelastic properties of homogeneous soft solid using transient elastography: An inverse problem approach. *The Journal of the Acoustical Society of America*, 116(6):3734–3741, December 2004.

[18] Bo Zhang, Sherif Makram-Ebeid, Raphael Prevost, and Guillaume Pizaine. Fast solver for some computational imaging problems: A regularized weighted least-squares approach. *Digital signal processing*, 27:107–118, 2014.

[19] Sverre Holm. *Waves with Power-Law Attenuation*. Springer International Publishing, 2019.

[20] Sunhyung Kim, Jan Mewis, Christian Clasen, and Jan Vermant. Superposition rheometry of a wormlike micellar fluid. *Rheologica Acta*, 52(8-9):727–740, August 2013.

[21] Jeffreys Sir, Harold. *The earth: its origin, history and physical constitution*. Cambridge University Press, Cambridge, 2nd ed. edition, 1929.

[22] AR Rzhanitsyn. Some problems of the mechanics of systems that are deformed in time. *Gostekhizdat, Moscow*, 1949.

[23] C Zemzemi, A Zorgani, L Daunizeau, S Belabhar, R Souchon, and S Catheline. Super-resolution limit of shear-wave elastography. *Europhysics Letters*, 129(3):34002, 2020.

[24] Willie E. Rochefort and Stanley Middleman. Rheology of Xanthan Gum: Salt, Temperature, and Strain Effects in Oscillatory and Steady Shear Experiments. *Journal of Rheology*, 31(4):337–369, May 1987.

[25] Kathryn R Nightingale, Mark L Palmeri, Roger W Nightingale, and Gregg E Trahey. On the feasibility of remote palpation using acoustic radiation force. *The Journal of the Acoustical Society of America*, 110(1):625–634, 2001.

[26] B. Veltkamp, K.P. Velikov, and D. Bonn. High velocity impact on a thin (non-Newtonian) fluid layer. *Journal of Fluid Mechanics*, 951:A40, November 2022.

[27] Guler Bengusu Tezel. A Study on Tunable Viscoelastic Properties of Xhantan Gum and Sodium Alginate Hyrogelling System. *Theoretical Foundations of Chemical Engineering*, 55(3):464–471, May 2021.

[28] GP Mota and RG Pereira. A comparison of the rheological behavior of xanthan gum and diutan gum aqueous solutions. *Journal of the Brazilian Society of Mechanical Sciences and Engineering*, 44(4):117, 2022.

[29] Xinxin Li, Stephen E. Harding, Bettina Wolf, and Gleb E. Yakubov. Instrumental characterization of xanthan gum and scleroglucan solutions: Comparison of rotational rheometry, capillary breakup extensional rheometry and soft-contact tribology. *Food Hydrocolloids*, 130:107681, September 2022.

[30] G. Cuvelier and B. Launay. Concentration regimes in xanthan gum solutions deduced from flow and viscoelastic properties. *Carbohydrate Polymers*, 6(5):321–333, January 1986.

[31] Lujiao Shi, Yi Wei, Nan Luo, Tianwei Tan, and Hui Cao. The rheological and thickening properties of cationic xanthan gum. *Journal of Dispersion Science and Technology*, 39(1):55–61, 2018.

[32] Timothy Lim, Jonathan T. Uhl, and Robert K. Prud'homme. Rheology of Self-Associating Concentrated Xanthan Solutions. *Journal of Rheology*, 28(4):367–379, August 1984.

[33] Lynne E Bilston. Soft tissue rheology and its implications for elastography: Challenges and opportunities. *NMR in Biomedicine*, 31(10):e3832, 2018.

[34] D. Y. Song and Ti Qian Jiang. Study on the constitutive equation with fractional derivative for the viscoelastic fluids - Modified Jeffreys model and its application. *Rheologica Acta*, 37(5):512–517, November 1998.

-
https://doi.org/10.1063/5.0150219

Supplementary material: A phase transition approach to elucidate the propagation of shear waves in viscoelastic materials

Jorge Torres[1,2], Gabrielle Laloy-Borgna[3]*, Guillermo Rus[1,2,4], Stefan Catheline[3]

Hereafter we present the equations used to fit the experimental results and to plot various curves for all the rheological models mentioned in the manuscript. First, using the rheological scheme, the relationship between shear stress $\boldsymbol{\tau}$ and strain γ is established. It is based on the fundamental expressions for a spring $\boldsymbol{\tau} = \mu\gamma$ and for a Newtonian damper $\boldsymbol{\tau} = \eta\frac{d\gamma}{dt}$. Then, by writing this expression in the frequency domain, the real and imaginary parts of the ratio $\frac{\boldsymbol{\tau}}{\gamma}$ give the expressions for G' and G". Next, using the fundamental principle of dynamics, which states that $\rho\frac{\partial^2\gamma}{dt^2} = \frac{\partial^2\boldsymbol{\tau}}{\partial x^2}$ (ρ being the density of the material), the expression of the wave vector is obtained as a function of the frequency and the rheological parameters. Finally, from the real and imaginary wave vector parts the wave velocity and attenuation for shear waves are obtained, respectively. The main steps of this derivation are described below.

1. Kelvin-Voigt model

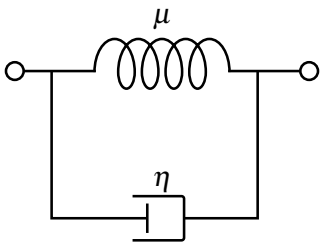

Stress-strain relationship in the time-domain:

$$\boldsymbol{\tau} = \mu_{kv}\gamma + \eta_{kv}\frac{d\gamma}{dt} \tag{1}$$

Stress-strain relationship in the frequency-domain:

$$\boldsymbol{\tau} = \mu_{kv}\gamma + \eta_{kv} j\omega\gamma \tag{2}$$

G^* expression:

$$G' = Re\left(\frac{\boldsymbol{\tau}}{\gamma}\right) = \mu_{kv} \text{ and } G'' = Im\left(\frac{\boldsymbol{\tau}}{\gamma}\right) = \omega\eta_{kv} \tag{3}$$

Wave vector expression:

$$k^2 = \frac{\rho\omega^2}{\mu_{kv} + j\omega\eta_{kv}} \tag{4}$$

Wave velocity:

$$c = \frac{\omega}{Re(k)} = \sqrt{\frac{2(\mu_{kv}^2 + \omega^2\eta_{kv}^2)}{\rho(\mu_{kv} + \sqrt{\mu_{kv}^2 + \omega^2\eta_{kv}^2})}} \tag{5}$$

Attenuation:

$$\alpha = Im(k) = \sqrt{\frac{\rho\omega^2(\sqrt{\mu_{kv}^2 + \omega^2\eta_{kv}^2} - \mu_{kv})}{2(\mu_{kv}^2 + \omega^2\eta_{kv}^2)}} \tag{6}$$

Attenuation per wavelength:

$$A(\omega) = \lambda\alpha = 2\pi Re(k)\alpha = 2\pi\sqrt{\frac{\sqrt{x^2+\omega^2} - x}{\sqrt{x^2+\omega^2} + x}} \text{ with } x = \frac{\mu_{kv}}{\eta_{kv}} \tag{7}$$

2. Maxwell model

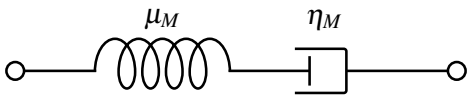

Stress-strain relationship in the time-domain:

$$\boldsymbol{\tau} + \frac{\eta_M}{\mu_M}\frac{d\boldsymbol{\tau}}{dt} = \eta_M \frac{d\gamma}{dt} \tag{8}$$

Stress-strain relationship in the frequency-domain:

$$\boldsymbol{\tau} + \frac{\eta_M}{\mu_M} j\omega\boldsymbol{\tau} = \eta_M j\omega\gamma \tag{9}$$

G^* expression:

$$G' = \frac{\mu_M \eta_M^2 \omega^2}{\mu_M^2 + \omega^2\eta_M^2} \quad \text{and} \quad G'' = \frac{\mu_M \eta_M^2 \omega^2}{\mu_M^2 + \omega^2\eta_M^2} \tag{10}$$

Wave vector expression:

$$k^2 = \frac{\rho\omega^2}{\mu_M} - j\frac{\rho\omega}{\eta_M} \tag{11}$$

Wave velocity:

$$c = \frac{\omega}{Re(k)} = \sqrt{\frac{2\mu_M}{\rho\left(1+\sqrt{1+\left(\frac{\mu_M}{\omega\eta_M}\right)^2}\right)}} \tag{12}$$

Attenuation:

$$\alpha = Im(k) = \sqrt{\frac{\rho\omega^2}{2\mu_M}\left(-1+\sqrt{1+\left(\frac{\mu_M}{\eta_M\omega}\right)^2}\right)} \tag{13}$$

Attenuation per wavelength:

$$A = 2\pi\sqrt{\frac{\sqrt{x^2+\omega^2}-\omega}{\sqrt{x^2+\omega^2}+\omega}} \quad \text{with} \quad x = \frac{\mu_M}{\eta_M} \tag{14}$$

3. Jeffreys model

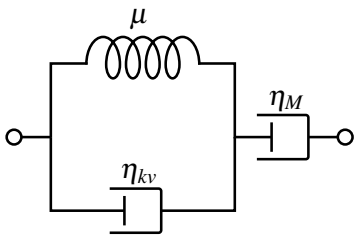

with $\eta_M \gg \eta_{kv}$

Stress-strain relationship in the time-domain:

$$\left(1+\frac{\eta_{kv}}{\eta_M}\right)\frac{d\boldsymbol{\tau}}{dt}+\frac{\mu}{\eta_M}\boldsymbol{\tau}=\mu\frac{d\gamma}{dt}+\eta_{kv}\frac{d^2\gamma}{dt^2} \tag{15}$$

Stress-strain relationship in the frequency-domain:

$$\left(1+\frac{\eta_{kv}}{\eta_M}\right)j\omega\boldsymbol{\tau}+\frac{\mu}{\eta_M}\boldsymbol{\tau}=\mu\, j\omega\gamma-\eta_{kv}\omega^2\gamma \tag{16}$$

G^* expression:

$$G'=\frac{\mu\omega^2\eta_M^2}{\mu^2+\omega^2(\eta_{kv}+\eta_M)^2} \quad \text{and} \quad G''=\eta_M\omega-\frac{\eta_M^2\omega^3(\eta_{kv}+\eta_M)}{\mu^2+\omega^2(\eta_{kv}+\eta_M)^2} \tag{17}$$

Wave vector expression:

$$k^2=\frac{\rho\omega^2(\mu+j\omega(\eta_{kv}+\eta_M))}{j\omega\mu\eta_M-\eta_{kv}\eta_M\omega^2} \tag{18}$$

Wave velocity:

$$c=\sqrt{\frac{2}{\rho}\times\frac{(\eta_{kv}\eta_M\omega^2)^2+(\mu\eta_M\omega)^2}{\mu\eta_M^2\omega^2+\sqrt{(\mu\eta_M^2\omega^2)^2+(\mu^2\eta_M\omega+\eta_{kv}^2\eta_M\omega^3+\eta_{kv}\omega^3\eta_M^2)^2}}} \tag{19}$$

Attenuation:

$$\alpha=\sqrt{\frac{\rho\omega^2}{2}\times\frac{-\mu\eta_M^2\omega^2+\sqrt{(\mu\eta_M^2\omega^2)^2+(\mu^2\eta_M\omega+\eta_{kv}^2\eta_M\omega^3+\eta_{kv}\eta_M^2\omega^3)^2}}{(\eta_{kv}\eta_M\omega^2)^2+(\mu\eta_M\omega)^2}} \tag{20}$$

Attenuation per wavelength:

$$A=2\pi\sqrt{\frac{-\mu\eta_M^2\omega^2+\sqrt{(\mu\eta_M^2\omega^2)^2+(\mu^2\eta_M\omega+\eta_{kv}^2\eta_M\omega^3+\eta_{kv}\eta_M^2\omega^3)^2}}{\mu\eta_M^2\omega^2+\sqrt{(\mu\eta_M^2\omega^2)^2+(\mu^2\eta_M\omega+\eta_{kv}^2\eta_M\omega^3+\eta_{kv}\eta_M^2\omega^3)^2}}} \tag{21}$$

4. Extended Maxwell model

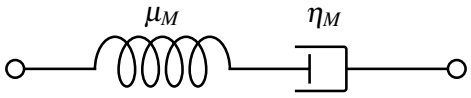

Stress-strain relationship in the time-domain:

$$\boldsymbol{\tau} + \frac{\eta_M}{\mu}\frac{d\boldsymbol{\tau}}{dt} = (\eta_M + \eta_{kv})\frac{d\gamma}{dt} + \frac{\eta_M \eta_{kv}}{\mu}\frac{d^2\gamma}{dt^2} \tag{22}$$

Stress-strain relationship in the frequency-domain:

$$\boldsymbol{\tau} + \frac{\eta_M}{\mu} j\omega\boldsymbol{\tau} = (\eta_M + \eta_{kv}) j\omega\gamma - \frac{\eta_M \eta_{kv}}{\mu}\omega^2\gamma \tag{23}$$

G^* expression:

$$G' = \frac{\mu\eta_M^2\omega^2}{\mu^2 + \eta_M^2\omega^2} \quad \text{and} \quad G'' = \frac{(\eta_{kv} + \eta_M)\omega - \eta_M\omega}{1 + \omega^2(\eta_{kv}/\mu)^2} + \eta_M\omega \tag{24}$$

Wave vector expression:

$$k^2 = \frac{\rho\omega^2(\mu + j\omega\eta_M)}{\mu(\eta_M + \eta_{kv})j\omega - \eta_M\eta_{kv}\omega^2} \tag{25}$$

Wave velocity:

$$c = \sqrt{\frac{2}{\rho} \times \frac{(\eta_{kv}\eta_M\omega^2)^2 + (\mu(\eta_M + \eta_{kv})\omega)^2}{\mu\eta_M^2\omega^2 + \sqrt{(\mu\eta_M^2\omega^2)^2 + \omega^2(\mu^2(\eta_M + \eta_{kv}) + \eta_M^2\eta_{kv}\omega^2)^2}}} \tag{26}$$

Attenuation:

$$\alpha = \sqrt{\frac{\rho\omega^2}{2} \times \frac{-\mu\eta_M^2\omega^2 + \sqrt{(\mu\eta_M^2\omega^2)^2 + \omega^2(\mu^2(\eta_M + \eta_{kv}) + \eta_{kv}\eta_M^2\omega^2)^2}}{(\eta_{kv}\eta_M\omega^2)^2 + (\mu(\eta_M + \eta_{kv})\omega)^2}} \tag{27}$$

Attenuation per wavelength:

$$A = 2\pi\sqrt{\frac{-\mu\eta_M^2\omega^2 + \sqrt{(\mu\eta_M^2\omega^2)^2 + \omega^2(\mu^2(\eta_M + \eta_{kv}) + \eta_M^2\eta_{kv}\omega^2)^2}}{\mu\eta_M^2\omega^2 + \sqrt{(\mu\eta_M^2\omega^2)^2 + \omega^2(\mu^2(\eta_M + \eta_{kv}) + \eta_M^2\eta_{kv}\omega^2)^2}}} \tag{28}$$

5. Three-element liquid models constitutive equation

The Extended Maxwell and Jeffreys model follow the same constitutive equation but with different coefficients. This means they will have different rheological parameters, but the same response curve will be obtained. The constitutive equation in general tensor form:

$$\boldsymbol{\tau} + \lambda_1 \frac{\partial \boldsymbol{\tau}}{\partial t} = \eta_0 \left(\frac{\partial \boldsymbol{\gamma}}{\partial t} + \lambda_2 \frac{\partial^2 \boldsymbol{\gamma}}{\partial t^2} \right) \tag{29}$$

where λ_1 and λ_2 are the relaxation and retardation times, and η_0 is the relaxed or zero shear viscosity, representing the viscosity of the material when at rest (or under low shear rates), respectively. Equation 30a represents the coefficients of the Jeffreys model, with $\eta_0 = \eta_M$. Equation 30b represents the coefficients of the Extended Maxwell model, with $\eta_0 = \eta_{kv} + \eta_M$. The rheological parameter η_{kv} is associated with the KV shear viscosity, while η_M is associated with the Maxwell shear viscosity.

$$\lambda_1 = \frac{\eta_{kv} + \eta_0}{\mu} \qquad \lambda_2 = \frac{\eta_{kv}}{\mu} \tag{30a}$$

$$\lambda_1 = \frac{\eta_M}{\mu} \qquad \lambda_2 = \frac{\eta_{kv}\eta_M}{\mu\eta_0} \tag{30b}$$

Part II

Appendices

Magnetic excitation

In Paper B, a magnetic excitation method is used to efficiently generate SWs at high frequencies. An important distinction is made between magnetic excitation and acoustic excitation, particularly the use of ARF. A significant advantage of using a magnetic force is its minimal impact on the medium, which is considered diamagnetic (soft tissue). Unlike acoustic waves, which would necessitate propagating throughout the entire medium, magnetic excitation enables the creation of SWs at a precise location without potentially causing disturbance.

The proposed excitation method involves placing a magnet inside the magnetic field of a coil, utilizing the principle of the Lorentz force. The Lorentz force is an electromagnetic force experienced by a charged particle in the presence of a magnetic field. In order to express this force in terms of magnetic flux density B, Ampère's law in its vector form can be employed.[207] Focusing on the effect along the z-axis and considering C as a constant dependent on magnetic parameters and the magnet's volume, it is determined that the force is proportional to the spatial gradient of B.

$$F(z,t) = C\left(B(z,t)\cdot\frac{\partial B(z,t)}{\partial z}\right) \tag{1}$$

Therefore, by controlling B(z,t), one can manipulate the Lorentz force to achieve desired effects. This field is experimentally characterized at various frequencies by employing Faraday's law of induction $\varepsilon = -NS\,(\partial B_z/\partial t)$, being ε the electromotive force (V) measured, N the number of turns, S the cross-section area of the measuring coil, and $(\partial B_z/\partial t)$ the time gradient of B_z. This is accomplished by utilizing a pickup coil consisting of 10 turns with a diameter of 10 mm. The pickup coil is positioned at different locations along the Z axis of the main coil, allowing for the measurement of ε. The curves in the figure show the three characterized coils with 0.03 mH, 0.1 mH, and 0.2 mH. B_z is higher in the center of the coil (z=0mm), but $\partial_z B_z$ is higher around 6 mm, which corresponds to the edges of the coil. The 0.1 mH is selected for reporting the highest F_z.

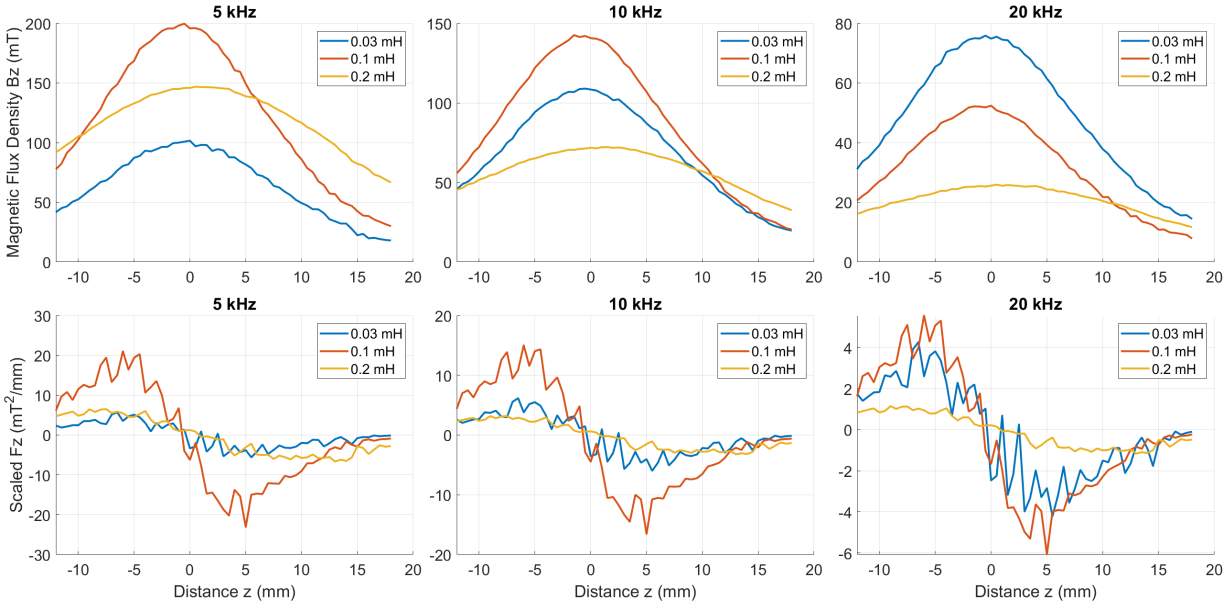

Experimental measurement of B_z (top) and scaled F_z (bottom) for coils with different inductances and at different frequencies.

Resumen Extendido

Introducción

En el campo biomédico, la elasticidad se ha utilizado para informar sobre el estado de un tejido blando y determinar condiciones anormales. Una de las aplicaciones más notables es la estadificación de la fibrosis, donde una mayor elasticidad (medio más rígido) en el hígado se relaciona con un estadio más avanzado de la enfermedad. Por otro lado, cuando se detecta una zona con diferente elasticidad dentro de un tejido blando, a menudo se debe a la presencia de un tumor, que en el caso de ser más rígido puede ser canceroso. Así pues, el sondeo de las propiedades mecánicas, y especialmente de la elasticidad, tiene el potencial de convertirse en una herramienta de diagnóstico. Tradicionalmente, los médicos han realizado una estimación aproximada de la elasticidad de los tejidos mediante palpación manual. El diagnóstico sólo puede realizarse en tejidos superficiales y con un carácter subjetivo y cualitativo.

La imagen médica engloba un conjunto de técnicas que tratan de crear imágenes del cuerpo humano con fines de diagnóstico o seguimiento de enfermedades. La elastografía dinámica es una de estas técnicas que permite medir la elasticidad de diferentes tejidos blandos, como órganos, tendones o músculos. El procedimiento se realiza de forma no invasiva y también es aplicable a tejidos que no necesariamente tienen que estar en la superficie. Además, al ser independiente del operador, la medición es objetiva y cuantitativa. La elastografía dinámica se basa en la generación, detección y seguimiento de ondas de cizalla (SWs). Se trata de un tipo de onda elástica cuya velocidad está relacionada con las propiedades mecánicas del medio en el que se propagan. Dependiendo de las características del medio, puede existir una relación directa con la elasticidad o puede depender también de la viscosidad y la geometría.

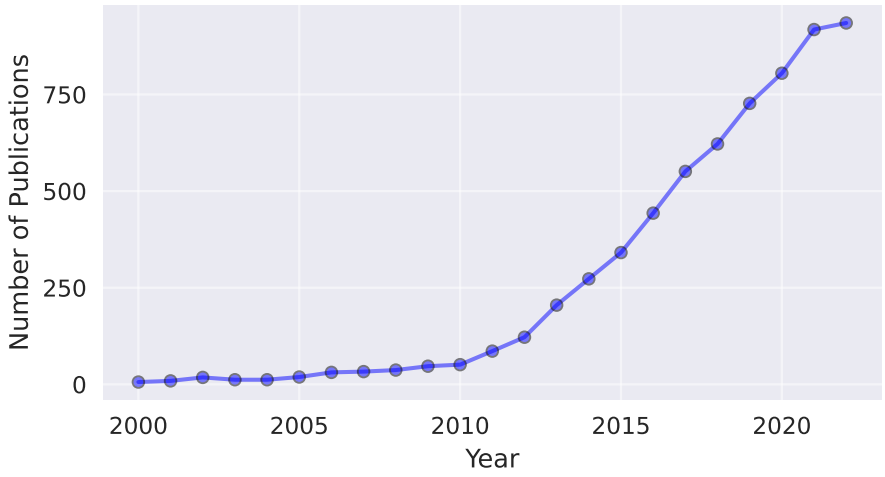

Número de publicaciones en Web Of Science (2022) que presentan el término "Shear Wave Elastography".

Este campo ha seguido aumentando su interés desde su concepción, y en los últimos años el impacto de los métodos de SWs ha sido más que notable. La figura muestra los registros de publicaciones en Web Of Science con el término ”Shear Wave Elastography” en su resumen. Como podemos ver, el número de publicaciones se ha multiplicado por diez en la última década, con más de 6000 publicaciones. A principios de la década de 2000, se realizaron las primeras pruebas de concepto para la detección de SWs. Se utilizó la ecografía rápida, una técnica de imagen basada en ondas de compresión, y se obtuvieron valores globales de la elasticidad tisular medida. Así nació la elastografía por ultrasonidos (USE). No fue hasta alrededor de 2005 cuando se produjeron los primeros mapas 2D de elasticidad y, en consecuencia, esta tecnología se expandió con sus primeras implementaciones clínicas.[1] Desde entonces, se han

desarrollado diferentes modalidades de imagen. Entre ellas podemos mencionar la Elastografía por Resonancia Magnética (MRE), técnicas ópticas como la Elastografía por Coherencia Óptica (OCE), y cámaras de alta velocidad. El punto en común de todas las técnicas es el uso de SWs para sondear las propiedades mecánicas del medio a analizar.

Ámbito de la tesis

Una de las razones para utilizar la elastografía dinámica es que no se puede confiar únicamente en la elasticidad, ya que los tejidos presentan diversos grados de comportamiento viscoelástico.[2] En un tejido viscoelástico, la respuesta mecánica depende del tiempo y, por tanto, de la frecuencia de excitación. La extracción de este tipo de propiedades dinámicas permite afinar el diagnóstico al conocer mejor la funcionalidad y la estructura del tejido. Esta situación puede plantear varias preguntas.

- ¿Podemos combinar diferentes modos de excitación con diferentes modalidades de imagen y obtener resultados adaptados al medio?
- ¿Se pueden generar SWs de forma que no se capten modos de propagación complejos, como las ondas guiadas, en medios finos como la córnea o los medios de cultivo? Apesar de las limitaciones de los modelos reológicos simples, ¿pueden proporcionar información suficiente para distinguir los estados mecánicos?
- ¿Es factible aplicar la elastografía dinámica a microescala y cuantificar los parámetros viscoelásticos?
- ¿Es posible estudiar la frecuencia a la que los SWs se atenúan fuertemente (cutoff) y por tanto dejan de ser observables con las técnicas actuales?
- ¿Pueden los SWs propagarse en líquidos viscoelásticos?

La medición de las propiedades mecánicas en medios biológicos reviste gran importancia para diversas aplicaciones. En concreto, el diagnóstico precoz de ciertas patologías es crucial para desarrollar tratamientos clínicos adaptados. En la actualidad, más allá del estándar de la elasticidad lineal, la viscoelasticidad está ganando impulso como resultado de los desarrollos teóricos y tecnológicos en el campo biomédico.[2],[3] Al mismo tiempo, está empezando a madurar la viabilidad de cuantificar las propiedades viscoelásticas a escala microscópica.[4],[5] Sin embargo, la relación entre las propiedades mecánicas a microescala y las propiedades a macroescala derivadas de ellas sigue siendo poco conocida, lo que dificulta nuestra capacidad para predecir el comportamiento mecánico basándonos únicamente en la microestructura. En consecuencia, resulta intrigante proponer técnicas que permitan una mejor comprensión de propiedades mecánicas que han sido ampliamente estudiadas a macroescala pero escasamente exploradas a microescala. Además, estas propiedades dilucidan la capacidad de los medios de cultivo para facilitar la migración celular e inducir la diferenciación celular.[6] Del mismo modo, los métodos de propagación de SW pueden superar las limitaciones técnicas de la reometría tradicional y explorar frecuencias más altas, raramente investigadas en materiales viscoelásticos, como los fluidos complejos. La elastografía dinámica podría desempeñar un papel fundamental en el perfeccionamiento de los diagnósticos tradicionales, en la optimización de la eficacia de los sistemas de cultivo para la medicina regenerativa y en una mejor comprensión de la propagación de SWs en diversos medios biológicos.

Objetivos

A lo largo de esta tesis se emplearon diversas modalidades de imagen y se propusieron nuevos métodos de generación de SWs. El objetivo era identificar la forma más óptima de propagación de SWs. Por ejemplo, al evitar modos de propagación complejos como las ondas guiadas, se simplificó el análisis y se facilitó la interpretación de los resultados. Cada montaje experimental se adaptó a las especificidades y geometría del medio biológico investigado, lo que permitió estudiar distintos tipos de ondas que interrogaban el medio. Entre ellos se incluyen SWs torsionales en la córnea, SWs longitudinales en hidrogeles utilizados para el cultivo celular y SW transversales en líquidos viscoelásticos. Los objetivos de esta tesis abarcan técnicas alternativas en elastografía dinámica, logradas a través de montajes experimentales innovadores o los enfoques para extraer información sobre las ondas que se propagan.

Objective 1

Desarrollar una técnica de elastografía basada en SWs torsionales (TWE) adaptada a las especificidades de la córnea y determinar su capacidad para diferenciar entre distintos estados mecánicos.

❶ Diseñar un disco emisor capaz de generar SWs torsionales y un sensor piezoeléctrico adecuado para recibir las ondas propagadas, considerando la curvatura de la córnea.

❷ Investigar desplazamientos de cizalla en el plano (el plano perpendicular al eje del emisor) para eliminar la influencia de las ondas guiadas.

❸ Evaluar la viabilidad de la técnica para detectar cambios en las propiedades reológicas introduciendo modificaciones estructurales mediante tratamiento químico.

Objective 2

Desarrollar una técnica de micro-elastografía óptica (OME) capaz de generar y rastrear SWs de alta frecuencia con suficiente resolución espacial y temporal, permitiendo el análisis viscoelástico de medios blandos a través de un rango de frecuencia ultra-ancho.

❶ Idear un nuevo método de generación de ondas utilizando la fuerza magnética transitoria para lograr SWs de alta frecuencia.

❷ Fabricar un medio viscoelástico transparente con un elemento magnético incrustado para observar desplazamientos de alta frecuencia utilizando una cámara de alta velocidad.

❸ Investigar el potencial del modelo reológico Kelvin-Voigt para explicar las altas frecuencias de corte (donde ya no se observan SWs) y determinar los errores en los parámetros mecánicos basados en el rango de frecuencia ajustado.

Objective 3

Utilizar un método basado en SWs transversales para examinar los rangos de frecuencia en los que un medio se comporta como un sólido clásico (el SW se propaga) o como un líquido (el SW no se propaga) en líquidos viscoelásticos.

❶ Emplear un enfoque independiente del modelo reológico para calcular el módulo de cizalla de almacenamiento y pérdida mediante el análisis de la velocidad de fase y la atenuación.

❷ Identificar la región de atenuación mínima para la amplitud de onda y determinar las frecuencias de corte.

❸ Desarrollar expresiones matemáticas para varios modelos reológicos para ajustar los parámetros de atenuación.

Contribuciones

Como compendio de tres publicaciones, el ámbito de esta tesis se sitúa dentro del campo de la elastografía dinámica. Las publicaciones examinan las propiedades viscoelásticas de diversos medios mediante la utilización de diferentes fuentes de generación de SWs y modalidades de obtención de imágenes. Se centran en el análisis de las curvas de dispersión e intentan proporcionar una interpretación exhaustiva de los parámetros reológicos obtenidos mediante procedimientos de ajuste.

En la siguiente figura se muestra una ilustración gráfica de las técnicas de elatografía dinámica aplicadas, así como las contribuciones de cada publicación.

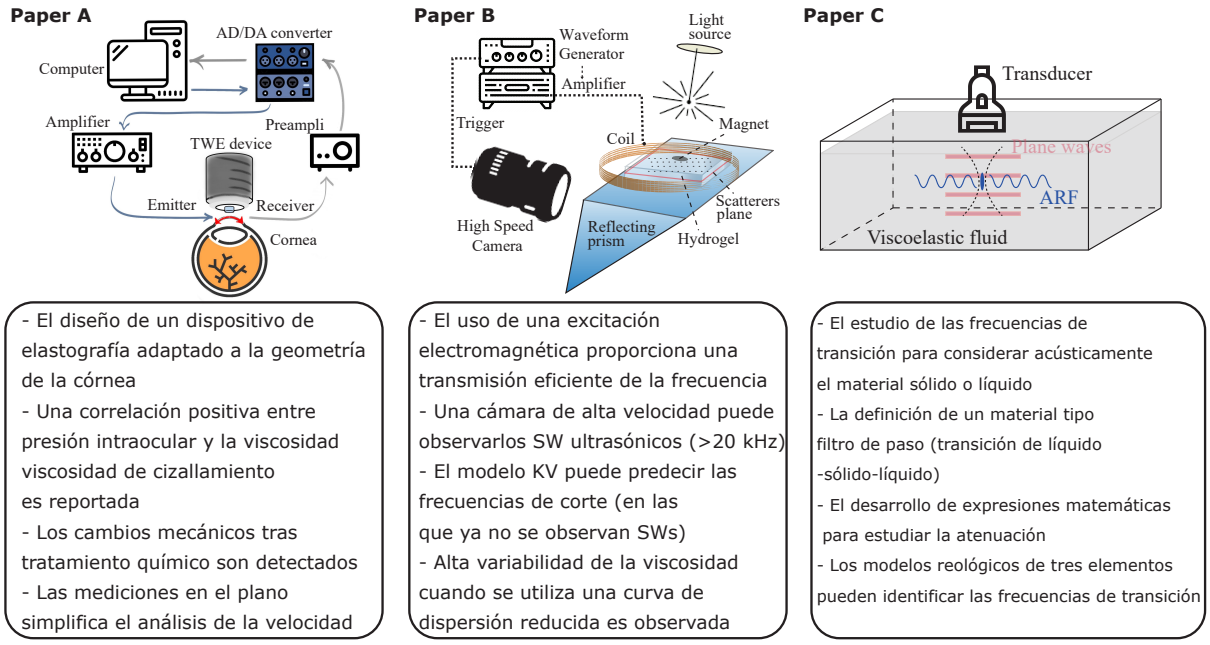

Ilustración gráfica de las técnicas de elastografía dinámica aplicadas con sus respectivos montajes experimentales, y las principales contribuciones de cada artículo.

En Paper A: *Torsional wave elastography to assess the mechanical properties of the cornea*, los cambios mecánicos de la córnea que preceden a las alteraciones estructurales visibles han sido de interés en la evaluación clínica. Este estudio propone una técnica de elastografía adaptada, la elastografía de ondas de torsión (TWE), para la córnea. Se realizan experimentos ex vivo en muestras de córnea porcina, incluyendo grupos de control y de tratamiento de quemaduras con álcalis, y se estima su viscoelasticidad utilizando un modelo Kelvin-Voigt (KV). Los resultados se compararon entre los grupos de control y de tratamiento, y se señaló la importancia de estudiar la propagación en el plano. Se diseñó un transductor de ondas de torsión adaptado a la geometría de la córnea.

En Paper B: *Optical micro-elastography with magnetic excitation for high frequency rheological characterization of soft media*, se aborda la limitada investigación sobre la propagación de SWs en elastografía a altas frecuencias (>3 kHz) debido a la atenuación y las limitaciones técnicas. Se generan SWs longitudinales a altas frecuencias (alcanzando SWs ultrasónicas) y se explora el límite de alta frecuencia, donde ya no se observan SWs (frecuencia de corte). Se demuestra que, para inferir parámetros viscoelásticos precisos, el modelo KV requiere el rango completo de frecuencias de la curva de dispersión. Para esta aplicación, la generación de ondas se realiza mediante excitación magnética e imágenes con una cámara de alta velocidad.

En Paper C: *A phase transition approach to elucidate the propagation of SWs in viscoelastic materials*, el estudio se centra en líquidos viscoelásticos donde la definición tradicional de líquido se vuelve ambigua. El estudio consiste en la dispersión y atenuación de SWs transversales utilizando un enfoque independiente del modelo reológico para explorar también frecuencias de corte bajas y altas. Se requieren modelos reológicos de tres elementos para ajustar con precisión los resultados experimentales. Se siguió una metodología estándar de elastografía por ultrasonidos.

Discusión y Conclusiones

En esta parte final se presentan las principales conclusiones derivadas de cada artículo, junto con un breve debate en el que se destacan sus respectivas aportaciones. Se revisa el cumplimiento de los objetivos propuestos (junto con las tareas propuestas) y se abordan las preguntas de investigación planteadas en

la introducción.

En el Paper A, se demostró la capacidad diagnóstica de la técnica TWE para evaluar las propiedades mecánicas de la córnea. El diseño del sensor piezoeléctrico y la generación de ondas de torsión mediante un actuador electromecánico permitieron trabajar con un dispositivo adaptado a la curvatura de la córnea (*Tarea 1*). Al medir los desplazamientos en el plano de propagación perpendicular al eje del emisor, se eliminó eficazmente la influencia de las ondas guiadas en el espesor corneal (*Tarea 2*). La técnica TWE proporcionó una evaluación directa y precisa de la viscoelasticidad corneal, reduciendo la necesidad de complejos modelos de ondas y proporcionó un método de reconstrucción rápido con un postprocesado mínimo. Los resultados mostraron que, a medida que aumentaba la deformación, también aumentaba el módulo elástico de la córnea, lo que pone de relieve la capacidad de TWE para captar los cambios en las propiedades reológicas. Es importante destacar que el estudio reveló que las mediciones realizadas en los planos de las láminas de colágeno (in-plane) proporcionaban información valiosa sobre la viscoelasticidad de la córnea, a diferencia de las técnicas USE y OCE que medían la propagación fuera del plano. Los resultados coinciden con los de estudios anteriores, lo que demuestra el potencial de TWE para evaluar las propiedades mecánicas de la córnea. Además, el estudio investigó los efectos de la quemadura alcalina en la viscoelasticidad corneal y observó alteraciones en los parámetros de elasticidad de cizalla y viscosidad. Los resultados indicaron que TWE podía detectar cambios en la córnea resultantes del tratamiento químico, lo que sugiere su potencial para evaluar las condiciones de salud de la córnea (*Tarea 3*). El parámetro de viscosidad aumentó en el grupo tratado, lo que indica una mayor pérdida de energía y un aumento de la amortiguación viscosa. El grosor de la córnea también aumentó en respuesta al tratamiento químico. El estudio también exploró la correlación entre la velocidad del SW y la presión intraocular (IOP). Los resultados revelaron una correlación positiva entre la velocidad de onda y la IOP, lo que indica la influencia de una precarga en el tejido en las propiedades mecánicas. Además, la viscosidad de cizalla mostró una correlación positiva con la IOP, lo que sugiere alteraciones en los proteoglicanos viscosos y en las interacciones de cizalla con la matriz extracelular en condiciones de tensión variables.

Aunque el estudio presentó resultados prometedores, es importante reconocer ciertas limitaciones. El método puede haber pasado por alto anomalías focales debido a la ausencia de un componente de imagen 2D. Deben incorporarse consideraciones como la distribución de la tensión generada por la IOP y las condiciones fisiológicas para abordar posibles errores. Los estudios futuros podrían centrarse en la integración de TWE en los procedimientos de examen convencionales y en explorar la viabilidad de las mediciones sin contacto. Las investigaciones futuras también podrían incorporar la anisotropía y la no linealidad en el análisis, teniendo en cuenta la naturaleza anisotrópica de la córnea. El uso de la propagación axisimétrica y de anillos sectorizados podría proporcionar información en múltiples direcciones simultáneamente, permitiendo la evaluación de la heterogeneidad regional en las propiedades mecánicas de la córnea.

En el Paper B, se demostró la viabilidad del uso de la Micro-Elastografía Óptica (OME) para obtener análisis viscoelásticos fiables en un amplio rango de frecuencias. Se empleó una técnica de excitación de alta frecuencia para lograr resoluciones micrométricas y evitar la propagación de ondas guiadas. Se propuso un método de excitación de base magnética sin contacto mecánico directo, que permite una transmisión eficiente de la frecuencia de excitación al desplazamiento del medio (*Tarea 1*). A diferencia de estudios anteriores, se consiguieron frecuencias más altas (>3 kHz) haciendo vibrar un imán incrustado en el medio investigado, lo que permitió la generación de SWs. Una señal de tipo chirp para la excitación garantizó una curva de dispersión continua y una mayor relación señal-ruido. El estudio demostró que iniciando la excitación a 5 kHz se podía conseguir un equilibrio para evitar las ondas guiadas causadas por grandes longitudes de onda. Se obtuvo información suficiente para reconstruir la velocidad a frecuencias inferiores a la de excitación, comenzando a 3 kHz. Al sustituir el imán por una placa metálica (aluminio), se observó una reducción de la fuerza magnética, lo que indica que el campo magnético permanente proporcionaba la fuerza necesaria para observar desplazamientos en el medio. Se utilizó una cámara de alta velocidad para capturar pequeños desplazamientos en un hidrogel transparente de poliacrilamida (PAM) (*Tarea 2*).

Las pruebas realizadas en muestras bicapa revelaron que sólo la resolución del sistema de captura de imágenes limitaba la precisión de la reconstrucción del campo de desplazamiento. Se analizó el impacto del tamaño de la ventana y las distancias de propagación en las estimaciones de velocidad, que afectaban a la resolución final y daban lugar a transiciones borrosas e irregulares. Se confirmó que las ondas observadas eran SW longitudinales y se midió su velocidad de grupo. Factores como la elevada atenuación

y la distribución no homogénea de las partículas podían influir en la forma de la curva de dispersión. El estudio demostró que el comportamiento dispersivo de las ondas de corte medidas con OME no era sensible a las condiciones geométricas del medio. El análisis del espacio (f, k) indicó un único modo de propagación dominante, descartando la presencia de otros modos. Se proporcionaron varios argumentos para confirmar que las ondas de cizalla observadas eran ondas de cizalla de volumen y no ondas Rayleigh o efectos de guía de ondas.

Se comprobó que el modelo KV, un modelo reológico simple basado en un proceso de relajación único, describía con precisión los materiales de hidrogel estudiados, y que las frecuencias de corte obtenidas a partir de OME eran coherentes con los tiempos de relajación de los materiales. Sin embargo, el ajuste de la curva de dispersión reducida al modelo KV presentaba problemas, con una alta variabilidad en los parámetros reológicos estimados. Una curva de dispersión con un ancho de banda de frecuencias más amplio mejoró el modelado de la respuesta desde las frecuencias cuasiestáticas hasta las frecuencias de corte. Las frecuencias de corte calculadas dependían únicamente de los parámetros reológicos e indicaban el punto más allá del cual el material no tenía tiempo para relajarse y vibrar a la frecuencia de excitación (*Tarea 3*).

La técnica OME propuesta tiene aplicaciones potenciales en medicina regenerativa y en el estudio de las interacciones mecánicas célula-sustrato. Ofrece una amplia gama de propiedades viscoelásticas para medios como los hidrogeles PAM, facilitando la monitorización sin afectar a las células.

En Paper C, se han estudiado los líquidos viscoelásticos, que presentan un comportamiento reológico complejo, utilizando métodos de propagación de SWs. A diferencia de los fluidos newtonianos, los líquidos viscoelásticos pueden soportar la propagación de SWs debido a sus estructuras internas. La evaluación experimental de estos líquidos se ha limitado tradicionalmente a bajas frecuencias utilizando reómetros convencionales. Para superar estas limitaciones, se han empleado métodos de propagación de SWs para alcanzar frecuencias más altas. Diversos estudios han detectado con éxito SWs en líquidos viscoelásticos utilizando métodos ópticos, ultrasónicos o mecánicos. Estos estudios han proporcionado información sobre las propiedades mecánicas y los procesos de flujo de estos líquidos. Aquí se investigaron los rangos de frecuencia en los que un medio transita entre un estado sólido y líquido clásico utilizando elastografía dinámica. Se eligió como medio una solución acuosa de goma xantana (XG), un polisacárido con propiedades viscoelásticas. La velocidad de fase y la atenuación de las ondas de cizallamiento se obtuvieron mediante métodos de transformada de Fourier. El módulo de almacenamiento (G') y el módulo de pérdida (G") se reconstruyeron a partir de la velocidad de fase y la atenuación mediante un enfoque independiente del modelo reológico (*Tarea 1*). Los resultados experimentales mostraron que la propagación de las onda en la solución de XG exhibía un comportamiento dispersivo, similar al de otros fluidos viscoelásticos. Se identificaron frecuencias de corte, indicando los límites de frecuencia más allá de los cuales cesaba la propagación de la onda de cizalla. La solución de XG mostraba un comportamiento similar al de un líquido a bajas frecuencias, donde dominaba el término de disipación, y un comportamiento similar al de un sólido a frecuencias intermedias, donde dominaba el término de almacenamiento. A frecuencias más altas, las ondas de corte se atenuaron fuertemente, y la solución de XG se comportó como un líquido de nuevo, por lo tanto, se asemeja a un filtro de paso de banda (*Tarea 2*). La comparación entre α y λ ofreció un método ventajoso que es independiente de un modelo reológico específico o del tipo de propagación de ondas. Proporcionó información valiosa sobre el número de λ que pueden observarse antes de que se atenúen hasta el nivel de ruido.

Se propusieron cuatro modelos reológicos para explicar el comportamiento observado. Sus expresiones se derivaron para estudiar principalmente la propiedad de atenuación, y sus parámetros se estimaron utilizando un algoritmo de ajuste (*Tarea 3*). El modelo de Jeffreys de tres elementos fue capaz de ajustarse con precisión a todo el rango de frecuencias e identificar la región de atenuación mínima para la amplitud de onda. El estudio de SWs en líquidos viscoelásticos biológicos se presenta como una herramienta prometedora para evaluar sus propiedades mecánicas.

Esta tesis comenzó destacando el crecimiento del número de trabajos que abordan la "Shear Wave Elastography" en las dos últimas décadas. Varios de estos trabajos han presentado nuevas modalidades de imagen y montajes experimentales cuyo potencial puede tener un impacto significativo en la práctica

clínica, particularmente en el campo del diagnóstico. La elastografía, por ejemplo, va más allá de la morfología y la evaluación por observación directa, como se observa habitualmente en los ultrasonidos y las radiografías. Utiliza principalmente el módulo de cizalla o la velocidad de onda para proporcionar información valiosa. Estos parámetros resultan muy ventajosos para diagnosticar tumores o fibrosis, ya que sustituyen eficazmente a las técnicas de palpación subjetivas y limitadas empleadas por los médicos, además de mitigar las molestias y la imprevisibilidad asociadas a las biopsias. La exploración de nuevos parámetros y enfoques de análisis aumenta aún más la versatilidad de esta técnica, reforzando su atractivo y utilidad potencial.

Cada uno de los trabajos incluidos ha investigado un medio distinto, y todos ellos han examinado la propagación de SWs y derivan propiedades viscoelásticas utilizando modelos reológicos.

Los hallazgos presentados en Paper B sobre la importancia de disponer de una curva de dispersión amplia nos permiten revisar los resultados obtenidos en el contexto de la córnea (Paper A). Cabe señalar que con la técnica TWE, el modelo reológico sólo se ajustó a un número limitado de puntos de datos en una curva de dispersión reducida. En consecuencia, existe la posibilidad de sobreestimar el parámetro de viscosidad de cizalla, lo que podría explicar en parte las disparidades observadas en comparación con otros métodos documentados en la bibliografía existente. La generación de un campo de desplazamiento de ancho de banda amplio ofrece numerosas oportunidades para una caracterización robusta y un diagnóstico refinado.

Como es evidente a lo largo de Paper B y Paper C, se observa que la elastografía dinámica se puede utilizar a varias escalas. En consecuencia, pueden emplearse diversas frecuencias de excitación, lo que obliga a explorar la dispersión de ondas para cada aplicación específica. En situaciones en las que el medio presenta características que no son puramente elásticas ni homogéneas y, además, en las que la propagación de las ondas puede ser guiada, la velocidad de las ondas pasa a depender de la frecuencia. Resulta interesante comprender la naturaleza de la onda propagada, establecer su correlación con la velocidad y la viscoelasticidad, y tener en cuenta y corregir cualquier efecto geométrico significativo que pueda estar presente. Uno de los objetivos comunes de estos estudios era evitar depender de las ondas guiadas, ya fuera induciendo una deformación en el plano o aumentando la frecuencia. Sin embargo, este último enfoque planteaba el reto de la atenuación, ya que las ondas se propagaban a distancias más cortas. Estableciendo una relación entre λ y las dimensiones del medio, así como analizando las curvas de dispersión, resulta posible discernir el tipo de propagación de ondas que se produce en un rango de frecuencias determinado. Esto puede ayudar a diferenciar entre la propagación de volumen y la propagación de ondas guiadas. La selección de una frecuencia adecuada para la elastografía debe atenerse a ciertos criterios que dependen del medio específico y de la aplicación de que se trate. En el contexto de la formación de imágenes, el criterio de Nyquist sirve de guía para determinar la frecuencia máxima capturable, mientras que la frecuencia mínima capturable viene determinada por el tiempo de formación de imágenes. En lo que respecta a la excitación, trabajar con SWs de volumen simplifica la estimación de su relación con las propiedades mecánicas.

La utilización de la micro-elastografía requiere la aplicación de SWs de muy alta frecuencia, que han sido objeto de una investigación limitada en el ámbito de la elastografía. Obtener un conocimiento exhaustivo de sus características y limitaciones utilizando la tecnología existente es un área de investigación de gran interés, especialmente en medios controlados. El estudio de características como la dispersión y la atenuación de SWs a altas frecuencias permite predecir y/o determinar el rango de trabajo óptimo. La determinación de una frecuencia de corte, más allá de la cual ya no se observan SWs, no sólo caracteriza las capacidades de la configuración experimental, sino que también define el rango de frecuencias adecuado para la micro-elastografía. La utilización de SWs ultrasónicas demuestra ser un enfoque prometedor para aplicaciones que implican medios relativamente rígidos, como la córnea, las capas de la piel o los medios de cultivo celular, entre otros. Sin embargo, es importante tener en cuenta que existe una frecuencia de corte a partir de la cual la λ se vuelve limitada, impidiendo un aumento indefinido de la frecuencia. En Paper B, se investigó experimentalmente la frecuencia máxima de propagación de SWs en un medio diseñado para cultivo celular. Además, se exploró la relación entre estas frecuencias y la utilidad de modelos reológicos simples, como el KV, demostrando la viabilidad de realizar una aproximación razonable a este límite de propagación. Asimismo, se aplicó este concepto a medios poco estudiados en elastografía, como los líquidos viscoelásticos, lo que permitió revisitar la reología en estos medios. Profundizar en este tipo de estudios permite comprender mejor la relación físico-química con los parámetros mecánicos. La relación entre λ y los constituyentes del medio es crucial para lograr una caracterización

adecuada. Explorar la evolución de los parámetros viscoelásticos en relación con la concentración y los tratamientos aplicados a los medios investigados es un área importante para futuras investigaciones. A pesar de los intentos por abordar esta cuestión, separar los efectos de cada componente o estructura y proporcionar una interpretación física para cada uno de ellos sigue siendo un reto.

Contributions

The outcomes, transversal applications, and collaborations in other projects, are reflected in the peer-reviewed journal publications, national and international conferences, and books enumerated below.

1. Articles in peer-reviewed journals:
   - Rus, G., Faris, I. H., Torres, J., Callejas, A., & Melchor, J. (2020). Why Are Viscosity and Nonlinearity Bound to Make an Impact in Clinical Elastographic Diagnosis? Sensors, 20(8), Article 8. https://doi.org/10.3390/s20082379
   - Ashofteh Yazdi, A., Melchor, J., Torres, J., Faris, I., Callejas, A., Gonzalez-Andrades, M., & Rus, G. (2020). Characterization of non-linear mechanical behavior of the cornea. Scientific Reports, 10(1), Article 1. https://doi.org/10.1038/s41598-020-68391-7
   - Faris, I. H., Melchor, J., Callejas, A., Torres, J., & Rus, G. (2020). Viscoelastic Biomarkers of Ex Vivo Liver Samples via Torsional Wave Elastography. Diagnostics, 10(2), Article 2. https://doi.org/10.3390/diagnostics10020111
   - Gomez, A., Hurtado, M., Callejas, A., Torres, J., Saffari, N., & Rus, G. (2021). Experimental Evidence of Generation and Reception by a Transluminal Axisymmetric Shear Wave Elastography Prototype. Diagnostics, 11(4), Article 4. https://doi.org/10.3390/diagnostics11040645
   - Torres, J., H. Faris, I., Callejas, A., Reyes-Ortega, F., Melchor, J., Gonzalez-Andrades, M., & Rus, G. (2022). Torsional wave elastography to assess the mechanical properties of the cornea. Scientific Reports, 12(1), Article 1. https://doi.org/10.1038/s41598-022-12151-2
   - Torres, J., Muñoz, M., Porcel, M. D. C., Contreras, S., Molina, F. S., Rus, G., Ocón-Hernández, O., & Melchor, J. (2022). Preliminary Results on the Preinduction Cervix Status by Shear Wave Elastography. Mathematics, 10(17), Article 17. https://doi.org/10.3390/math10173164
   - Torres, J., Callejas, A., Gomez, A., & Rus, G. (2023). Optical micro-elastography with magnetic excitation for high frequency rheological characterization of soft media. Ultrasonics, 132, 107021. https://doi.org/10.1016/j.ultras.2023.107021
   - Torres, J., Laloy-Borgna, G., Rus, G., & Catheline, S. (2023). A phase transition approach to elucidate the propagation of shear waves in viscoelastic materials. Applied Physics Letters, 122(22), 223702. https://doi.org/10.1063/5.0150219

2. Conferences:
   - Torres, J.; Rus, G.; Muñoz, R.; Cortes, J.; Molina, R.; Gomez, A.; Riveiro, M.; Melchor, J.; Callejas, A. "A prognostic framework for evolutive biomechanical properties". 23 Congress of the European Society of Biomechanics (2017).
   - Torres, J.; Callejas, A.; Faris, I.; Melchor, J.; Rus, G. "Contact hypothesis of a torsional wave probe on the human cervix". 31st Congress of the EFSUMB (EUROSON 2019).
   - Torres, J.; Callejas, A.; Faris, I.; Melchor, J.; Rus, G. "Impact of different contact conditions on the human cervix using a torsional elastographic probe." International Congress on Ultrasonics (2019).
   - Torres, J.; Callejas, A.; Rus, G. "Feasibility of Using Optical Elastography with Remote Magnetic Excitation". X Reunión del Capítulo Español de la Sociedad Europea de Biomecánica (ESB, 2021).

- Torres, J.; Callejas, A.; Gomez, A.; Rus, G. "High Frequency Propagation in Viscoelastic Media Using Optical Micro-Elastography". ISTU (2023).

3. Books:

- Melchor, J.; Torres, J.; Callejas, A.; Rus, G. Resistencia de Materiales para Ingeniería Electrónica. 4 edición., Godel Impresiones Digitales S. L. - Departamento de Mecánica de Estructuras, Universidad de Granada.. 09/2020. ISBN 978-84-17970-36-9.

References

[1] A. Sarvazyan and M. W. Urban, "Historical growth of ultrasound elastography and directions for the future," in *Ultrasound Elastography for Biomedical Applications and Medicine*, John Wiley & Sons, Ltd, 2018, ch. 37, pp. 567–579. DOI: 10.1002/9781119021520.ch37.

[2] G. Rus, I. H. Faris, J. Torres, A. Callejas, and J. Melchor, "Why are viscosity and nonlinearity bound to make an impact in clinical elastographic diagnosis?" *Sensors*, vol. 20, no. 8, p. 2379, 2020. DOI: 10.3390/s20082379.

[3] K. Zhang, M. Zhu, E. Thomas, S. Hopyan, and Y. Sun, "Existing and potential applications of elastography for measuring the viscoelasticity of biological tissues in vivo," *Frontiers in Physics*, vol. 9, p. 670 571, 2021. DOI: 10.3389/fphy.2021.670571.

[4] H. Li, G. Flé, M. Bhatt, *et al.*, "Viscoelasticity imaging of biological tissues and single cells using shear wave propagation," *Frontiers in Physics*, vol. 9, 2021.

[5] T. Akinyi, P. Grasland-Mongrain, M. Bhatt, S. Catheline, and G. Cloutier, "Recent advances in imaging of cell elasticity," in *Viscoelasticity and Collective Cell Migration*, Elsevier, 2021, pp. 257–296. DOI: 10.1016/B978-0-12-820310-1.00010-0.

[6] A. J. Engler, F. Rehfeldt, S. Sen, and D. E. Discher, "Microtissue elasticity: Measurements by atomic force microscopy and its influence on cell differentiation," in *Methods in Cell Biology*, ser. Cell Mechanics, vol. 83, Academic Press, 2007, pp. 521–545. DOI: 10.1016/S0091-679X(07)83022-6.

[7] K. F. Graff, *Wave Motion in Elastic Solids*. Dover Publications, 1991.

[8] A. P. Sarvazyan, A. R. Skovoroda, S. Y. Emelianov, *et al.*, "Biophysical bases of elasticity imaging," in *Acoustical Imaging*, ser. Acoustical Imaging, J. P. Jones, Ed., Boston, MA: Springer US, 1995, pp. 223–240. DOI: 10.1007/978-1-4615-1943-0_23.

[9] A. P. Sarvazyan, O. V. Rudenko, S. D. Swanson, J. B. Fowlkes, and S. Y. Emelianov, "Shear wave elasticity imaging: A new ultrasonic technology of medical diagnostics," *Ultrasound in Medicine & Biology*, vol. 24, no. 9, pp. 1419–1435, 1998. DOI: 10.1016/S0301-5629(98)00110-0.

[10] S. Holm, *Waves with Power-Law Attenuation*. Cham: Springer International Publishing, 2019. DOI: 10.1007/978-3-030-14927-7.

[11] S. Catheline and N. Benech, "Longitudinal shear wave and transverse dilatational wave in solids," *The Journal of the Acoustical Society of America*, vol. 137, no. 2, EL200–EL205, 2015. DOI: 10.1121/1.4907742.

[12] E. L. Carstensen and K. J. Parker, "Oestreicher and elastography," *The Journal of the Acoustical Society of America*, vol. 138, no. 4, pp. 2317–2325, 2015. DOI: 10.1121/1.4930953.

[13] E. Reissner and H. F. Sagoci, "Forced torsional oscillations of an elastic half-space. i," *Journal of Applied Physics*, vol. 15, no. 9, pp. 652–654, 1944. DOI: 10.1063/1.1707489.

[14] A. Ouared, E. Montagnon, and G. Cloutier, "Generation of remote adaptive torsional shear waves with an octagonal phased array to enhance displacements and reduce variability of shear wave speeds: Comparison with quasi-plane shear wavefronts," *Physics in Medicine & Biology*, vol. 60, no. 20, p. 8161, 2015. DOI: 10.1088/0031-9155/60/20/8161.

[15] D. Valtorta and E. Mazza, "Dynamic measurement of soft tissue viscoelastic properties with a torsional resonator device," *Medical Image Analysis*, Medical Image Computing and Computer-Assisted Intervention - MICCAI 2004, vol. 9, no. 5, pp. 481–490, 2005. DOI: 10.1016/j.media.2005.05.002.

[16] A. Callejas, A. Gomez, J. Melchor, *et al.*, "Performance study of a torsional wave sensor and cervical tissue characterization," *Sensors*, vol. 17, no. 9, p. 2078, 2017. DOI: 10.3390/s17092078.

[17] I. H. Faris, J. Melchor, A. Callejas, J. Torres, and G. Rus, "Viscoelastic biomarkers of ex vivo liver samples via torsional wave elastography," *Diagnostics*, vol. 10, no. 2, p. 111, 2020. DOI: 10.3390/diagnostics10020111.

[18] J. Melchor and G. Rus, "Torsional ultrasonic transducer computational design optimization," *Ultrasonics*, vol. 54, no. 7, pp. 1950–1962, 2014. DOI: 10.1016/j.ultras.2014.05.001.

[19] J. Zhao and D. Pedroso, "Strain gradient theory in orthogonal curvilinear coordinates," *International Journal of Solids and Structures*, vol. 45, no. 11, pp. 3507–3520, 2008. DOI: 10.1016/j.ijsolstr.2008.02.011.

[20] K. J. Parker, M. M. Doyley, and D. J. Rubens, "Imaging the elastic properties of tissue: The 20 year perspective," *Physics in Medicine & Biology*, vol. 56, no. 1, R1, 2010. DOI: 10.1088/0031-9155/56/1/R01.

[21] M. M. Doyley, "Model-based elastography: A survey of approaches to the inverse elasticity problem," *Physics in Medicine & Biology*, vol. 57, no. 3, R35, 2012. DOI: 10.1088/0031-9155/57/3/R35.

[22] K. J. Glaser, A. Manduca, and R. L. Ehman, "Review of mr elastography applications and recent developments," *Journal of Magnetic Resonance Imaging*, vol. 36, no. 4, pp. 757–774, 2012. DOI: 10.1002/jmri.23597.

[23] A. Sarvazyan and C. R. Hill, "Physical chemistry of the ultrasound–tissue interaction," in *Physical Principles of Medical Ultrasonics*, John Wiley & Sons, Ltd, 2004, ch. 7, pp. 223–235. DOI: 10.1002/0470093978.ch7.

[24] Z. Han, J. Li, M. Singh, *et al.*, "Optical coherence elastography assessment of corneal viscoelasticity with a modified rayleigh-lamb wave model," *Journal of the Mechanical Behavior of Biomedical Materials*, vol. 66, pp. 87–94, 2017. DOI: 10.1016/j.jmbbm.2016.11.004.

[25] V. Kumar, M. Denis, A. Gregory, *et al.*, "Viscoelastic parameters as discriminators of breast masses: Initial human study results," *PLOS ONE*, vol. 13, no. 10, e0205717, 2018. DOI: 10.1371/journal.pone.0205717.

[26] P. Garteiser, S. Doblas, J.-L. Daire, *et al.*, "Mr elastography of liver tumours: Value of viscoelastic properties for tumour characterisation," *European Radiology*, vol. 22, no. 10, pp. 2169–2177, 2012. DOI: 10.1007/s00330-012-2474-6.

[27] M. A. Meyers and K. K. Chawla, *Mechanical Behavior of Materials*. Cambridge University Press, 2008.

[28] J. Vappou, C. Maleke, and E. E. Konofagou, "Quantitative viscoelastic parameters measured by harmonic motion imaging," *Physics in Medicine & Biology*, vol. 54, no. 11, p. 3579, 2009. DOI: 10.1088/0031-9155/54/11/020.

[29] K. J. Parker, T. Szabo, and S. Holm, "Towards a consensus on rheological models for elastography in soft tissues," *Physics in Medicine & Biology*, vol. 64, no. 21, p. 215 012, 2019. DOI: 10.1088/1361-6560/ab453d.

[30] J. F. Greenleaf, M. Fatemi, and M. Insana, "Selected methods for imaging elastic properties of biological tissues," *Annual Review of Biomedical Engineering*, vol. 5, no. 1, pp. 57–78, 2003. DOI: 10.1146/annurev.bioeng.5.040202.121623.

[31] S. Chen, M. Fatemi, and J. F. Greenleaf, "Quantifying elasticity and viscosity from measurement of shear wave speed dispersion," *The Journal of the Acoustical Society of America*, vol. 115, no. 6, pp. 2781–2785, 2004. DOI: 10.1121/1.1739480.

[32] L. Cardoso and S. C. Cowin, "Role of structural anisotropy of biological tissues in poroelastic wave propagation," *Mechanics of Materials*, Microstructures and Anisotropies, vol. 44, pp. 174–188, 2012. DOI: 10.1016/j.mechmat.2011.08.007.

[33] T. Deffieux, G. Montaldo, M. Tanter, and M. Fink, "Shear wave spectroscopy for in vivo quantification of human soft tissues visco-elasticity," *IEEE Transactions on Medical Imaging*, vol. 28, no. 3, pp. 313–322, 2009. DOI: 10.1109/TMI.2008.925077.

[34] M. W. Urban, C. Pislaru, I. Z. Nenadic, R. R. Kinnick, and J. F. Greenleaf, "Measurement of viscoelastic properties of in vivo swine myocardium using lamb wave dispersion ultrasound vibrometry (lduv)," *IEEE Transactions on Medical Imaging*, vol. 32, no. 2, pp. 247–261, 2013. DOI: 10.1109/TMI.2012.2222656.

[35] C. Helfenstein-Didier, R. J. Andrade, J. Brum, *et al.*, "In vivo quantification of the shear modulus of the human achilles tendon during passive loading using shear wave dispersion analysis," *Physics in Medicine & Biology*, vol. 61, no. 6, p. 2485, 2016. DOI: 10.1088/0031-9155/61/6/2485.

[36] L. Ambrozinski, P. Packo, L. Pieczonka, T. Stepinski, T. Uhl, and W. J. Staszewski, "Identification of material properties – efficient modelling approach based on guided wave propagation and spatial multiple signal classification," *Structural Control and Health Monitoring*, vol. 22, no. 7, pp. 969–983, 2015. DOI: 10.1002/stc.1728.

[37] C. Amador, B. L. Otilio, R. R. Kinnick, and M. W. Urban, "Ultrasonic method to characterize shear wave propagation in micellar fluids," *The Journal of the Acoustical Society of America*, vol. 140, no. 3, pp. 1719–1726, 2016. DOI: 10.1121/1.4962531.

[38] R. G. Barr, K. Nakashima, D. Amy, *et al.*, "Wfumb guidelines and recommendations for clinical use of ultrasound elastography: Part 2: Breast," *Ultrasound in Medicine & Biology*, vol. 41, no. 5, pp. 1148–1160, 2015. DOI: 10.1016/j.ultrasmedbio.2015.03.008.

[39] R. G. Barr, "Shear wave liver elastography," *Abdominal Radiology*, vol. 43, no. 4, pp. 800–807, 2018. DOI: 10.1007/s00261-017-1375-1.

[40] J. Ormachea, K. J. Parker, and R. G. Barr, "An initial study of complete 2d shear wave dispersion images using a reverberant shear wave field," *Physics in Medicine & Biology*, vol. 64, no. 14, p. 145 009, 2019. DOI: 10.1088/1361-6560/ab2778.

[41] M. Tanter, J. Bercoff, A. Athanasiou, *et al.*, "Quantitative assessment of breast lesion viscoelasticity: Initial clinical results using supersonic shear imaging," *Ultrasound in Medicine & Biology*, vol. 34, no. 9, pp. 1373–1386, 2008. DOI: 10.1016/j.ultrasmedbio.2008.02.002.

[42] I. Z. Nenadic, B. Qiang, M. W. Urban, *et al.*, "Attenuation measuring ultrasound shearwave elastography and in vivo application in post-transplant liver patients," *Physics in Medicine & Biology*, vol. 62, no. 2, p. 484, 2016. DOI: 10.1088/1361-6560/aa4f6f.

[43] A. K. Sharma, J. Reis, D. C. Oppenheimer, *et al.*, "Attenuation of shear waves in normal and steatotic livers," *Ultrasound in Medicine & Biology*, vol. 45, no. 4, pp. 895–901, 2019. DOI: 10.1016/j.ultrasmedbio.2018.12.002.

[44] J. C. Bamber, "Attenuation and absorption," in *Physical Principles of Medical Ultrasonics*, John Wiley & Sons, Ltd, 2004, ch. 4, pp. 93–166. DOI: 10.1002/0470093978.ch4.

[45] S. Kazemirad, S. Bernard, S. Hybois, A. Tang, and G. Cloutier, "Ultrasound shear wave viscoelastography: Model-independent quantification of the complex shear modulus," *IEEE Transactions on Ultrasonics, Ferroelectrics, and Frequency Control*, vol. 63, no. 9, pp. 1399–1408, 2016. DOI: 10.1109/TUFFC.2016.2583785.

[46] M. Bhatt, M. A. C. Moussu, B. Chayer, *et al.*, "Reconstruction of viscosity maps in ultrasound shear wave elastography," *IEEE Transactions on Ultrasonics, Ferroelectrics, and Frequency Control*, vol. 66, no. 6, pp. 1065–1078, 2019. DOI: 10.1109/TUFFC.2019.2908550.

[47] D. Cosgrove, F. Piscaglia, J. Bamber, *et al.*, "Efsumb guidelines and recommendations on the clinical use of ultrasound elastography.part 2: Clinical applications," *Ultraschall in der Medizin - European Journal of Ultrasound*, vol. 34, no. 3, pp. 238–253, 2013. DOI: 10.1055/s-0033-1335375.

[48] R. M. Sigrist, J. Liau, A. E. Kaffas, M. C. Chammas, and J. K. Willmann, "Ultrasound elastography: Review of techniques and clinical applications," *Theranostics*, vol. 7, no. 5, pp. 1303–1329, 2017. DOI: 10.7150/thno.18650.

[49] Y. C. Fung, *Biomechanics: Mechanical Properties of Living Tissues*. Springer Science & Business Media, 2013.

[50] S. Aristizabal, "Anisotropic shear wave elastography," in *Ultrasound Elastography for Biomedical Applications and Medicine*, John Wiley & Sons, Ltd, 2018, ch. 26, pp. 399–421. DOI: 10.1002/9781119021520.ch26.

[51] J.-L. Gennisson, S. Catheline, S. Chaffaï, and M. Fink, "Transient elastography in anisotropic medium: Application to the measurement of slow and fast shear wave speeds in muscles," *The Journal of the Acoustical Society of America*, vol. 114, no. 1, pp. 536–541, 2003. DOI: 10.1121/1.1579008.

[52] J. Brum, M. Bernal, J. L. Gennisson, and M. Tanter, "In vivo evaluation of the elastic anisotropy of the human achilles tendon using shear wave dispersion analysis," *Physics in Medicine & Biology*, vol. 59, no. 3, p. 505, 2014. DOI: 10.1088/0031-9155/59/3/505.

[53] M. S. Spach, P. C. Dolber, and J. F. Heidlage, "Influence of the passive anisotropic properties on directional differences in propagation following modification of the sodium conductance in human atrial muscle. a model of reentry based on anisotropic discontinuous propagation," *Circulation Research*, vol. 62, no. 4, pp. 811–832, 1988. DOI: 10.1161/01.res.62.4.811.

[54] A. Samani and D. Plewes, "A method to measure the hyperelastic parameters of ex vivo breast tissue samples," *Physics in Medicine & Biology*, vol. 49, no. 18, p. 4395, 2004. DOI: 10.1088/0031-9155/49/18/014.

[55] J. J. O'Hagan and A. Samani, "Measurement of the hyperelastic properties of 44 pathological ex vivo breast tissue samples," *Physics in Medicine & Biology*, vol. 54, no. 8, p. 2557, 2009. DOI: 10.1088/0031-9155/54/8/020.

[56] Y. Lanir, "On the structural origin of the quasilinear viscoelastic behavior of tissues," in *Frontiers in Biomechanics*, G. W. Schmid-Schönbein, S. L.-Y. Woo, and B. W. Zweifach, Eds., New York, NY: Springer New York, 1986, pp. 130–136. DOI: 10.1007/978-1-4612-4866-8_10.

[57] M. Bernal, F. Chamming's, M. Couade, J. Bercoff, M. Tanter, and J.-L. Gennisson, "In vivo quantification of the nonlinear shear modulus in breast lesions: Feasibility study," *IEEE Transactions on Ultrasonics, Ferroelectrics, and Frequency Control*, vol. 63, no. 1, pp. 101–109, 2016. DOI: 10.1109/TUFFC.2015.2503601.

[58] S. Catheline, J.-L. Gennisson, and M. Fink, "Measurement of elastic nonlinearity of soft solid with transient elastography," *The Journal of the Acoustical Society of America*, vol. 114, no. 6, pp. 3087–3091, 2003. DOI: 10.1121/1.1610457.

[59] J. Melchor, W. J. Parnell, N. Bochud, L. Peralta, and G. Rus, "Damage prediction via nonlinear ultrasound: A micro-mechanical approach," *Ultrasonics*, vol. 93, pp. 145–155, 2019. DOI: 10.1016/j.ultras.2018.10.009.

[60] I. Sack, C. K. Mcgowan, A. Samani, C. Luginbuhl, W. Oakden, and D. B. Plewes, "Observation of nonlinear shear wave propagation using magnetic resonance elastography," *Magnetic Resonance in Medicine*, vol. 52, no. 4, pp. 842–850, 2004. DOI: 10.1002/mrm.20238.

[61] M. D. J. McGarry, C. L. Johnson, B. P. Sutton, *et al.*, "Suitability of poroelastic and viscoelastic mechanical models for high and low frequency mr elastography," *Medical Physics*, vol. 42, no. 2, pp. 947–957, 2015. DOI: 10.1118/1.4905048.

[62] M. A. Biot, "Theory of propagation of elastic waves in a fluid-saturated porous solid. ii. higher frequency range," *The Journal of the Acoustical Society of America*, vol. 28, no. 2, pp. 179–191, 1956. DOI: 10.1121/1.1908241.

[63] P. Vena and T. J. Royston, "Dilatational and shear waves in poro-viscoelastic media," *Journal of the Mechanical Behavior of Biomedical Materials*, vol. 97, pp. 99–107, 2019. DOI: 10.1016/j.jmbbm.2019.04.039.

[64] J. Aichele, B. Giammarinaro, M. Reinwald, G. Le Moign, and S. Catheline, "Capturing the shear and secondary compression waves: High-frame-rate ultrasound imaging in saturated foams," *Physical Review Letters*, vol. 123, no. 14, p. 148 001, 2019. DOI: 10.1103/PhysRevLett.123.148001.

[65] D. Royer and Valier-Brasier, Tony, *Elastic Waves in Solids, Volume 1: Propagation*. John Wiley \& Sons, 2022.

[66] S. J. Kirkpatrick, D. D. Duncan, and L. Fang, "Low-frequency surface wave propagation and the viscoelastic behavior of porcine skin," *Journal of Biomedical Optics*, vol. 9, no. 6, pp. 1311–1319, 2004. DOI: 10.1117/1.1803843.

[67] M. Tanter, D. Touboul, J.-L. Gennisson, J. Bercoff, and M. Fink, "High-resolution quantitative imaging of cornea elasticity using supersonic shear imaging," *IEEE Transactions on Medical Imaging*, vol. 28, no. 12, pp. 1881–1893, 2009. DOI: 10.1109/TMI.2009.2021471.

[68] J. J. Pitre, M. A. Kirby, D. S. Li, *et al.*, "Nearly-incompressible transverse isotropy (niti) of cornea elasticity: Model and experiments with acoustic micro-tapping oce," *Scientific Reports*, vol. 10, no. 1, p. 12 983, 2020. DOI: 10.1038/s41598-020-69909-9.

[69] M. Bernal, I. Nenadic, M. W. Urban, and J. F. Greenleaf, "Material property estimation for tubes and arteries using ultrasound radiation force and analysis of propagating modes," *The Journal of the Acoustical Society of America*, vol. 129, no. 3, pp. 1344–1354, 2011. DOI: 10.1121/1.3533735.

[70] M. W. Urban, I. Z. Nenadic, B. Qiang, M. Bernal, S. Chen, and J. F. Greenleaf, "Characterization of material properties of soft solid thin layers with acoustic radiation force and wave propagation," *The Journal of the Acoustical Society of America*, vol. 138, no. 4, pp. 2499–2507, 2015. DOI: 10.1121/1.4932170.

[71] E. E. Drakonaki, G. M. Allen, and D. J. Wilson, "Real-time ultrasound elastography of the normal achilles tendon: Reproducibility and pattern description," *Clinical Radiology*, vol. 64, no. 12, pp. 1196–1202, 2009. DOI: 10.1016/j.crad.2009.08.006.

[72] I. Z. Nenadic, M. W. Urban, S. A. Mitchell, and J. F. Greenleaf, "Lamb wave dispersion ultrasound vibrometry (lduv) method for quantifying mechanical properties of viscoelastic solids," *Physics in Medicine & Biology*, vol. 56, no. 7, p. 2245, 2011. DOI: 10.1088/0031-9155/56/7/021.

[73] H. Kanai, "Propagation of spontaneously actuated pulsive vibration in human heart wall and in vivo viscoelasticity estimation," *IEEE Transactions on Ultrasonics, Ferroelectrics, and Frequency Control*, vol. 52, no. 11, pp. 1931–1942, 2005. DOI: 10.1109/TUFFC.2005.1561662.

[74] C. A. Agten, F. M. Buck, L. Dyer, M. Flück, C. W. A. Pfirrmann, and A. B. Rosskopf, "Delayed-onset muscle soreness: Temporal assessment with quantitative mri and shear-wave ultrasound elastography," *American Journal of Roentgenology*, vol. 208, no. 2, pp. 402–412, 2017. DOI: 10.2214/AJR.16.16617.

[75] J. Blitz and G. Simpson, *Ultrasonic Methods of Non-Destructive Testing*. Springer Science & Business Media, 1995.

[76] G. Cloutier, F. Destrempes, F. Yu, and A. Tang, "Quantitative ultrasound imaging of soft biological tissues: A primer for radiologists and medical physicists," *Insights into Imaging*, vol. 12, no. 1, p. 127, 2021. DOI: 10.1186/s13244-021-01071-w.

[77] U. L. Mathiesen, L. E. Franzen, H. Åselius, *et al.*, "Increased liver echogenicity at ultrasound examination reflects degree of steatosis but not of fibrosis in asymptomatic patients with mild/moderate abnormalities of liver transaminases," *Digestive and Liver Disease*, vol. 34, no. 7, pp. 516–522, 2002. DOI: 10.1016/S1590-8658(02)80111-6.

[78] M. Tanter and M. Fink, "Ultrafast imaging in biomedical ultrasound," *IEEE Transactions on Ultrasonics, Ferroelectrics, and Frequency Control*, vol. 61, no. 1, pp. 102–119, 2014. DOI: 10.1109/TUFFC.2014.2882.

[79] G. Montaldo, M. Tanter, J. Bercoff, N. Benech, and M. Fink, "Coherent plane-wave compounding for very high frame rate ultrasonography and transient elastography," *IEEE Transactions on Ultrasonics, Ferroelectrics, and Frequency Control*, vol. 56, no. 3, pp. 489–506, 2009. DOI: 10.1109/TUFFC.2009.1067.

[80] J. .-. Gennisson, T. Deffieux, M. Fink, and M. Tanter, "Ultrasound elastography: Principles and techniques," *Diagnostic and Interventional Imaging*, Ultrasound Elastography, vol. 94, no. 5, pp. 487–495, 2013. DOI: 10.1016/j.diii.2013.01.022.

[81] T. Shiina, K. R. Nightingale, M. L. Palmeri, *et al.*, "Wfumb guidelines and recommendations for clinical use of ultrasound elastography: Part 1: Basic principles and terminology," *Ultrasound in Medicine & Biology*, vol. 41, no. 5, pp. 1126–1147, 2015. DOI: 10.1016/j.ultrasmedbio.2015.03.009.

[82] R. G. Barr, "Breast elastography: How to perform and integrate into a "best-practice" patient treatment algorithm," *Journal of Ultrasound in Medicine*, vol. 39, no. 1, pp. 7–17, 2020. DOI: 10.1002/jum.15137.

[83] H. E. von Gierke, H. L. Oestreicher, E. K. Franke, H. O. Parrack, and W. W. von Wittern, "Physics of vibrations in living tissues," *Journal of Applied Physiology*, vol. 4, no. 12, pp. 886–900, 1952. DOI: 10.1152/jappl.1952.4.12.886.

[84] T. A. Krouskop, D. R. Dougherty, and F. S. Vinson, "A pulsed doppler ultrasonic system for making noninvasive measurements of the mechanical properties of soft tissue," *Journal of Rehabilitation Research and Development*, vol. 24, no. 2, pp. 1–8, 1987.

[85] K. J. Parker, S. R. Huang, R. A. Musulin, and R. M. Lerner, "Tissue response to mechanical vibrations for "sonoelasticity imaging"," *Ultrasound in Medicine & Biology*, vol. 16, no. 3, pp. 241–246, 1990. DOI: 10.1016/0301-5629(90)90003-U.

[86] S. Catheline, F. Wu, and M. Fink, "A solution to diffraction biases in sonoelasticity: The acoustic impulse technique," *The Journal of the Acoustical Society of America*, vol. 105, no. 5, pp. 2941–2950, 1999. DOI: 10.1121/1.426907.

[87] L. Sandrin, S. Catheline, M. Tanter, X. Hennequin, and M. Fink, "Time-resolved pulsed elastography with ultrafast ultrasonic imaging," *Ultrasonic Imaging*, vol. 21, no. 4, pp. 259–272, 1999. DOI: 10.1177/016173469902100402.

[88] K. R. Nightingale, M. L. Palmeri, R. W. Nightingale, and G. E. Trahey, "On the feasibility of remote palpation using acoustic radiation force," *The Journal of the Acoustical Society of America*, vol. 110, no. 1, pp. 625–634, 2001. DOI: 10.1121/1.1378344.

[89] M. Fink and M. Tanter, "Multiwave imaging and super resolution," *Physics Today*, vol. 63, no. 2, pp. 28–33, 2010. DOI: 10.1063/1.3326986.

[90] L. Sandrin, B. Fourquet, J.-M. Hasquenoph, *et al.*, "Transient elastography: A new noninvasive method for assessment of hepatic fibrosis," *Ultrasound in Medicine & Biology*, vol. 29, no. 12, pp. 1705–1713, 2003. DOI: 10.1016/j.ultrasmedbio.2003.07.001.

[91] N. Frulio and H. Trillaud, "Ultrasound elastography in liver," *Diagnostic and Interventional Imaging*, Ultrasound Elastography, vol. 94, no. 5, pp. 515–534, 2013. DOI: 10.1016/j.diii.2013.02.005.

[92] L. Gerber, D. Kasper, D. Fitting, *et al.*, "Assessment of liver fibrosis with 2-d shear wave elastography in comparison to transient elastography and acoustic radiation force impulse imaging in patients with chronic liver disease," *Ultrasound in Medicine & Biology*, vol. 41, no. 9, pp. 2350–2359, 2015. DOI: 10.1016/j.ultrasmedbio.2015.04.014.

[93] J. Bercoff, M. Tanter, and M. Fink, "Supersonic shear imaging: A new technique for soft tissue elasticity mapping," *IEEE Transactions on Ultrasonics, Ferroelectrics, and Frequency Control*, vol. 51, no. 4, pp. 396–409, 2004. DOI: 10.1109/TUFFC.2004.1295425.

[94] T. Deffieux, J.-l. Gennisson, M. Tanter, and M. Fink, "Assessment of the mechanical properties of the musculoskeletal system using 2-d and 3-d very high frame rate ultrasound," *IEEE Transactions on Ultrasonics, Ferroelectrics, and Frequency Control*, vol. 55, no. 10, pp. 2177–2190, 2008. DOI: 10.1109/TUFFC.917.

[95] M. Muller, J.-L. Gennisson, T. Deffieux, M. Tanter, and M. Fink, "Quantitative viscoelasticity mapping of human liver using supersonic shear imaging: Preliminary in vivo feasability study," *Ultra-*

sound in Medicine & Biology, vol. 35, no. 2, pp. 219–229, 2009. DOI: 10.1016/j.ultrasmedbio.2008.08.018.

[96] J. Ormachea and K. J. Parker, "Elastography imaging: The 30 year perspective," *Physics in Medicine & Biology*, vol. 65, no. 24, 24TR06, 2020. DOI: 10.1088/1361-6560/abca00.

[97] F. Lb, H. T, and T. K, "Can ultrasound elastography substitute tissue biopsy in the diagnosis of malignancy?" *Mathews Journal of Cancer Science*, vol. 1, no. 1, pp. 1–4, 2016.

[98] T. J. Hall, A. Milkowski, B. Garra, *et al.*, "Rsna/qiba: Shear wave speed as a biomarker for liver fibrosis staging," in *2013 IEEE International Ultrasonics Symposium (IUS)*, 2013, pp. 397–400. DOI: 10.1109/ULTSYM.2013.0103.

[99] M. Palmeri, K. Nightingale, S. Fielding, *et al.*, "Rsna qiba ultrasound shear wave speed phase ii phantom study in viscoelastic media," in *2015 IEEE International Ultrasonics Symposium (IUS)*, 2015, pp. 1–4. DOI: 10.1109/ULTSYM.2015.0283.

[100] R. Muthupillai, D. J. Lomas, P. J. Rossman, J. F. Greenleaf, A. Manduca, and R. L. Ehman, "Magnetic resonance elastography by direct visualization of propagating acoustic strain waves," *Science*, vol. 269, no. 5232, pp. 1854–1857, 1995. DOI: 10.1126/science.7569924.

[101] S. K. Venkatesh, M. Yin, and R. L. Ehman, "Magnetic resonance elastography of liver: Technique, analysis, and clinical applications," *Journal of Magnetic Resonance Imaging*, vol. 37, no. 3, pp. 544–555, 2013. DOI: 10.1002/jmri.23731.

[102] S. J. Backhaus, G. Metschies, M. Billing, *et al.*, "Defining the optimal temporal and spatial resolution for cardiovascular magnetic resonance imaging feature tracking," *Journal of Cardiovascular Magnetic Resonance*, vol. 23, no. 1, p. 60, 2021. DOI: 10.1186/s12968-021-00740-5.

[103] G. Low, S. A. Kruse, and D. J. Lomas, "General review of magnetic resonance elastography," *World Journal of Radiology*, vol. 8, no. 1, pp. 59–72, 2016. DOI: 10.4329/wjr.v8.i1.59.

[104] Y. K. Mariappan, K. J. Glaser, and R. L. Ehman, "Magnetic resonance elastography: A review," *Clinical Anatomy*, vol. 23, no. 5, pp. 497–511, 2010. DOI: 10.1002/ca.21006.

[105] J. M. Schmitt, "Oct elastography: Imaging microscopic deformation and strain of tissue," *Optics Express*, vol. 3, no. 6, pp. 199–211, 1998. DOI: 10.1364/OE.3.000199.

[106] V. X. D. Yang, N. Munce, J. Pekar, *et al.*, "Micromachined array tip for multifocus fiber-based optical coherence tomography," *Optics Letters*, vol. 29, no. 15, pp. 1754–1756, 2004. DOI: 10.1364/OL.29.001754.

[107] F. Zvietcovich and K. V. Larin, "Wave-based optical coherence elastography: The 10-year perspective," *Progress in Biomedical Engineering*, vol. 4, no. 1, p. 012 007, 2022. DOI: 10.1088/2516-1091/ac4512.

[108] K. M. Kennedy, C. Ford, B. F. Kennedy, M. B. Bush, and D. D. Sampson, "Analysis of mechanical contrast in optical coherence elastography," *Journal of Biomedical Optics*, vol. 18, no. 12, p. 121 508, 2013. DOI: 10.1117/1.JBO.18.12.121508.

[109] B. F. Kennedy, K. M. Kennedy, and D. D. Sampson, "A review of optical coherence elastography: Fundamentals, techniques and prospects," *IEEE Journal of Selected Topics in Quantum Electronics*, vol. 20, no. 2, pp. 272–288, 2014. DOI: 10.1109/JSTQE.2013.2291445.

[110] F. Zvietcovich, G. R. Ge, H. Mestre, *et al.*, "Longitudinal shear waves for elastic characterization of tissues in optical coherence elastography," *Biomedical Optics Express*, vol. 10, no. 7, p. 3699, 2019. DOI: 10.1364/BOE.10.003699.

[111] A. Ramier, B. Tavakol, and S.-H. Yun, "Measuring mechanical wave speed, dispersion, and viscoelastic modulus of the cornea using optical coherence elastography," *Optics Express*, vol. 27, no. 12, p. 16 635, 2019. DOI: 10.1364/OE.27.016635.

[112] F. Zvietcovich, P. Pongchalee, P. Meemon, J. P. Rolland, and K. J. Parker, "Reverberant 3d optical coherence elastography maps the elasticity of individual corneal layers," *Nature Communications*, vol. 10, no. 1, p. 4895, 2019. DOI: 10.1038/s41467-019-12803-4.

[113] A. Ramier, A. M. Eltony, Y. Chen, *et al.*, "In vivo measurement of shear modulus of the human cornea using optical coherence elastography," *Scientific Reports*, vol. 10, no. 1, p. 17 366, 2020. DOI: 10.1038/s41598-020-74383-4.

[114] F. Zvietcovich, A. Nair, M. Singh, S. R. Aglyamov, M. D. Twa, and K. V. Larin, "Dynamic optical coherence elastography of the anterior eye: Understanding the biomechanics of the limbus," *Investigative Ophthalmology & Visual Science*, vol. 61, no. 13, p. 7, 2020. DOI: 10.1167/iovs.61.13.7.

[115] B. Giammarinaro, A. Zorgani, and S. Catheline, "Shear-wave sources for soft tissues in ultrasound elastography," *IRBM*, vol. 39, no. 4, pp. 236–242, 2018. DOI: 10.1016/j.irbm.2018.01.002.

[116] T.-M. Nguyen, S. Song, B. Arnal, *et al.*, "Shear wave pulse compression for dynamic elastography using phase-sensitive optical coherence tomography," *Journal of Biomedical Optics*, vol. 19, no. 1, p. 016 013, 2014. DOI: 10.1117/1.JBO.19.1.016013.

[117] S. P. Kearney, A. Khan, Z. Dai, and T. J. Royston, "Dynamic viscoelastic models of human skin using optical elastography," *Physics in Medicine & Biology*, vol. 60, no. 17, p. 6975, 2015. DOI: 10.1088/0031-9155/60/17/6975.

[118] Z. Jin, Y. Zhou, M. Shen, Y. Wang, F. Lu, and D. Zhu, "Assessment of corneal viscoelasticity using elastic wave optical coherence elastography," *Journal of Biophotonics*, vol. 13, no. 1, e201960074, 2020. DOI: 10.1002/jbio.201960074.

[119] T. Sugimoto, S. Ueha, and K. Itoh, "Tissue hardness measurement using the radiation force of focused ultrasound," in *IEEE Symposium on Ultrasonics*, 1990, 1377–1380 vol.3. DOI: 10.1109/ULTSYM.1990.171591.

[120] M. W. Urban, "Production of acoustic radiation force using ultrasound: Methods and applications," *Expert Review of Medical Devices*, vol. 15, no. 11, pp. 819–834, 2018. DOI: 10.1080/17434440.2018.1538782.

[121] G. Rus, "Nature of acoustic nonlinear radiation stress," *Applied Physics Letters*, vol. 105, no. 12, p. 121 904, 2014. DOI: 10.1063/1.4894827.

[122] Q. Wang, Y. Shi, F. Yang, and S. Yang, "Quantitative photoacoustic elasticity and viscosity imaging for cirrhosis detection," *Applied Physics Letters*, vol. 112, no. 21, p. 211 902, 2018. DOI: 10.1063/1.5021675.

[123] P. Grasland-Mongrain, R. Souchon, F. Cartellier, *et al.*, "Imaging of shear waves induced by lorentz force in soft tissues," *Physical Review Letters*, vol. 113, no. 3, p. 038 101, 2014. DOI: 10.1103/PhysRevLett.113.038101.

[124] P. Grasland-Mongrain, E. Miller-Jolicoeur, A. Tang, S. Catheline, and G. Cloutier, "Contactless remote induction of shear waves in soft tissues using a transcranial magnetic stimulation device," *Physics in Medicine & Biology*, vol. 61, no. 6, p. 2582, 2016. DOI: 10.1088/0031-9155/61/6/2582.

[125] Z. Sun, B. Giammarinaro, A. Birer, G. Liu, and S. Catheline, "Shear wave generation by remotely stimulating aluminum patches with a transient magnetic field and its preliminary application in elastography," *IEEE Transactions on Biomedical Engineering*, vol. 68, no. 7, pp. 2129–2139, 2021. DOI: 10.1109/TBME.2020.3028098.

[126] T. W. J. Almeida, D. R. T. Sampaio, A. C. Bruno, T. Z. Pavan, and A. A. O. Carneiro, "Comparison between shear wave dispersion magneto motive ultrasound and transient elastography for measuring tissue-mimicking phantom viscoelasticity," *IEEE Transactions on Ultrasonics, Ferroelectrics, and Frequency Control*, vol. 62, no. 12, pp. 2138–2145, 2015. DOI: 10.1109/TUFFC.2015.007353.

[127] T. Ersepke, T. C. Kranemann, and G. Schmitz, "Frequency response of soft tissue displacements induced by the force on magnetic nanoparticles," in *2017 IEEE International Ultrasonics Symposium (IUS)*, 2017, pp. 1–4. DOI: 10.1109/ULTSYM.2017.8092731.

[128] T. Z. Pavan, D. R. T. Sampaio, A. A. O. Carneiro, and D. T. Covas, "Ultrasound-based transient elastography using a magnetic excitation," in *2012 IEEE International Ultrasonics Symposium*, 2012, pp. 1846–1849. DOI: 10.1109/ULTSYM.2012.0463.

[129] E. Moeendarbary and A. R. Harris, "Cell mechanics: Principles, practices, and prospects," *WIREs Systems Biology and Medicine*, vol. 6, no. 5, pp. 371–388, 2014. DOI: 10.1002/wsbm.1275.

[130] X. Qian, T. Ma, M. Yu, X. Chen, K. K. Shung, and Q. Zhou, "Multi-functional ultrasonic micro-elastography imaging system," *Scientific Reports*, vol. 7, no. 1, p. 1230, 2017. DOI: 10.1038/s41598-017-01210-8.

[131] M. Bigot, F. Chauveau, O. Beuf, and S. A. Lambert, "Magnetic resonance elastography of rodent brain," *Frontiers in Neurology*, vol. 9, 2018.

[132] C. Alibert, B. Goud, and J.-B. Manneville, "Are cancer cells really softer than normal cells?" *Biology of the Cell*, vol. 109, no. 5, pp. 167–189, 2017. DOI: 10.1111/boc.201600078.

[133] D. Baruffaldi, G. Palmara, C. Pirri, and F. Frascella, "3d cell culture: Recent development in materials with tunable stiffness," *ACS Applied Bio Materials*, vol. 4, no. 3, pp. 2233–2250, 2021. DOI: 10.1021/acsabm.0c01472.

[134] D. Huang and S. Kidoaki, "Stiffness-optimized drug-loaded matrix for selective capture and elimination of cancer cells," *Journal of Drug Delivery Science and Technology*, vol. 55, p. 101 414, 2020. DOI: 10.1016/j.jddst.2019.101414.

[135] A. J. Engler, S. Sen, H. L. Sweeney, and D. E. Discher, "Matrix elasticity directs stem cell lineage specification," *Cell*, vol. 126, no. 4, pp. 677–689, 2006. DOI: 10.1016/j.cell.2006.06.044.

[136] V. Vogel and M. Sheetz, "Local force and geometry sensing regulate cell functions," *Nature Reviews Molecular Cell Biology*, vol. 7, no. 4, pp. 265–275, 2006. DOI: 10.1038/nrm1890.

[137] C. Guillot and T. Lecuit, "Mechanics of epithelial tissue homeostasis and morphogenesis," *Science*, vol. 340, no. 6137, pp. 1185–1189, 2013. DOI: 10.1126/science.1235249.

[138] W. H. Goldmann, "Chapter four - mechanosensation: A basic cellular process," in *Progress in Molecular Biology and Translational Science*, ser. Mechanotransduction, A. J. Engler and S. Kumar, Eds., vol. 126, Academic Press, 2014, pp. 75–102. DOI: 10.1016/B978-0-12-394624-9.00004-X.

[139] J. Z. Kechagia, J. Ivaska, and P. Roca-Cusachs, "Integrins as biomechanical sensors of the microenvironment," *Nature Reviews Molecular Cell Biology*, vol. 20, no. 8, pp. 457–473, 2019. DOI: 10.1038/s41580-019-0134-2.

[140] Z. Zhao, C. Vizetto-Duarte, Z. K. Moay, *et al.*, "Composite hydrogels in three-dimensional in vitro models," *Frontiers in Bioengineering and Biotechnology*, vol. 8, 2020.

[141] P.-H. Wu, D. R.-B. Aroush, A. Asnacios, *et al.*, "A comparison of methods to assess cell mechanical properties," *Nature Methods*, vol. 15, no. 7, pp. 491–498, 2018. DOI: 10.1038/s41592-018-0015-1.

[142] B. F. Kennedy, R. A. McLaughlin, K. M. Kennedy, *et al.*, "Optical coherence micro-elastography: Mechanical-contrast imaging of tissue microstructure," *Biomedical Optics Express*, vol. 5, no. 7, pp. 2113–2124, 2014. DOI: 10.1364/BOE.5.002113.

[143] R. Schäfer, "Labeling and imaging of stem cells – promises and concerns," *Transfusion Medicine and Hemotherapy*, vol. 37, no. 2, pp. 85–89, 2010. DOI: 10.1159/000287271.

[144] Y. Tseng, J. S. H. Lee, T. P. Kole, I. Jiang, and D. Wirtz, "Micro-organization and visco-elasticity of the interphase nucleus revealed by particle nanotracking," *Journal of Cell Science*, vol. 117, no. 10, pp. 2159–2167, 2004. DOI: 10.1242/jcs.01073.

[145] C. Guilluy, L. D. Osborne, L. Van Landeghem, *et al.*, "Isolated nuclei adapt to force and reveal a mechanotransduction pathway in the nucleus," *Nature Cell Biology*, vol. 16, no. 4, pp. 376–381, 2014. DOI: 10.1038/ncb2927.

[146] S. F. Othman, H. Xu, T. J. Royston, and R. L. Magin, "Microscopic magnetic resonance elastography (μmre)," *Magnetic Resonance in Medicine*, vol. 54, no. 3, pp. 605–615, 2005. DOI: 10.1002/mrm.20584.

[147] B. F. Kennedy, P. Wijesinghe, and D. D. Sampson, "The emergence of optical elastography in biomedicine," *Nature Photonics*, vol. 11, no. 4, pp. 215–221, 2017. DOI: 10.1038/nphoton.2017.6.

[148] P. Wijesinghe, B. F. Kennedy, and D. D. Sampson, "Chapter 9 - optical elastography on the microscale," in *Tissue Elasticity Imaging*, S. K. Alam and B. S. Garra, Eds., Amsterdam: Elsevier, 2020, pp. 185–229. DOI: 10.1016/B978-0-12-809661-1.00009-1.

[149] P. Grasland-Mongrain, A. Zorgani, S. Nakagawa, *et al.*, "Ultrafast imaging of cell elasticity with optical microelastography," *Proceedings of the National Academy of Sciences*, vol. 115, no. 5, pp. 861–866, 2018. DOI: 10.1073/pnas.1713395115.

[150] G. Laloy-Borgna, A. Zorgani, and S. Catheline, "Micro-elastography: Toward ultrasonic shear waves in soft solids," *Applied Physics Letters*, vol. 118, no. 11, p. 113 701, 2021. DOI: 10.1063/5.0039816.

[151] G. Scarcelli, R. Pineda, and S. H. Yun, "Brillouin optical microscopy for corneal biomechanics," *Investigative Ophthalmology & Visual Science*, vol. 53, no. 1, pp. 185–190, 2012. DOI: 10.1167/iovs.11-8281.

[152] R. Prevedel, A. Diz-Muñoz, G. Ruocco, and G. Antonacci, "Brillouin microscopy: An emerging tool for mechanobiology," *Nature Methods*, vol. 16, no. 10, pp. 969–977, 2019. DOI: 10.1038/s41592-019-0543-3.

[153] K. V. Larin and D. D. Sampson, "Optical coherence elastography – oct at work in tissue biomechanics [invited]," *Biomedical Optics Express*, vol. 8, no. 2, pp. 1172–1202, 2017. DOI: 10.1364/BOE.8.001172.

[154] L. Z. Yanez, J. Han, B. B. Behr, R. A. R. Pera, and D. B. Camarillo, "Human oocyte developmental potential is predicted by mechanical properties within hours after fertilization," *Nature Communications*, vol. 7, no. 1, p. 10 809, 2016. DOI: 10.1038/ncomms10809.

[155] A. J. Teo, A. Mishra, I. Park, Y.-J. Kim, W.-T. Park, and Y.-J. Yoon, "Polymeric biomaterials for medical implants and devices," *ACS Biomaterials Science & Engineering*, vol. 2, no. 4, pp. 454–472, 2016. DOI: 10.1021/acsbiomaterials.5b00429.

[156] Y. Deng, N. C. Rouze, M. L. Palmeri, and K. R. Nightingale, "Ultrasonic shear wave elasticity imaging sequencing and data processing using a verasonics research scanner," *IEEE Transactions on Ultrasonics, Ferroelectrics, and Frequency Control*, vol. 64, no. 1, pp. 164–176, 2017. DOI: 10.1109/TUFFC.2016.2614944.

[157] T. Loupas, J. Powers, and R. Gill, "An axial velocity estimator for ultrasound blood flow imaging, based on a full evaluation of the doppler equation by means of a two-dimensional autocorrelation approach," *IEEE Transactions on Ultrasonics, Ferroelectrics, and Frequency Control*, vol. 42, no. 4, pp. 672–688, 1995. DOI: 10.1109/58.393110.

[158] V. Delattre, S. Catheline, G. Laloy-Borgna, A. Zorgani, and S. Roman, "Passive elastography of the esophagus: From model to preliminary in-vivo experiments using diameter measurements," *Biomedical Physics & Engineering Express*, vol. 7, no. 6, p. 065 029, 2021. DOI: 10.1088/2057-1976/ac277d.

[159] N. Benech, S. Catheline, J. Brum, T. Gallot, and C. A. Negreira, "1-d elasticity assessment in soft solids from shear wave correlation: The time-reversal approach," *IEEE Transactions on Ultrasonics, Ferroelectrics, and Frequency Control*, vol. 56, no. 11, pp. 2400–2410, 2009. DOI: 10.1109/TUFFC.2009.1328.

[160] B. D. Lucas and T. Kanade, "An iterative image registration technique with an application to stereo vision," in *International Joint Conference on Artificial Intelligence*, 1981.

[161] G. Farnebäck, "Two-frame motion estimation based on polynomial expansion," in *Image Analysis*, J. Bigun and T. Gustavsson, Eds., ser. Lecture Notes in Computer Science, Berlin, Heidelberg: Springer, 2003, pp. 363–370. DOI: 10.1007/3-540-45103-X_50.

[162] T. Deffieux, J.-l. Gennisson, J. Bercoff, and M. Tanter, "On the effects of reflected waves in transient shear wave elastography," *IEEE Transactions on Ultrasonics, Ferroelectrics, and Frequency Control*, vol. 58, no. 10, pp. 2032–2035, 2011. DOI: 10.1109/TUFFC.2011.2052.

[163] H. Zhao, P. Song, D. D. Meixner, *et al.*, "External vibration multi-directional ultrasound shearwave elastography (evmuse): Application in liver fibrosis staging," *IEEE Transactions on Medical Imaging*, vol. 33, no. 11, pp. 2140–2148, 2014. DOI: 10.1109/TMI.2014.2332542.

[164] K. J. Parker, J. Ormachea, and Z. Hah, "Group versus phase velocity of shear waves in soft tissues," *Ultrasonic Imaging*, vol. 40, no. 6, pp. 343–356, 2018. DOI: 10.1177/0161734618796217.

[165] M. L. Palmeri, M. H. Wang, J. J. Dahl, K. D. Frinkley, and K. R. Nightingale, "Quantifying hepatic shear modulus in vivo using acoustic radiation force," *Ultrasound in Medicine & Biology*, vol. 34, no. 4, pp. 546–558, 2008. DOI: 10.1016/j.ultrasmedbio.2007.10.009.

[166] P. Song, A. Manduca, H. Zhao, M. W. Urban, J. F. Greenleaf, and S. Chen, "Fast shear compounding using robust 2-d shear wave speed calculation and multi-directional filtering," *Ultrasound in Medicine & Biology*, vol. 40, no. 6, pp. 1343–1355, 2014. DOI: 10.1016/j.ultrasmedbio.2013.12.026.

[167] H.-C. Liu, P. Kijanka, and M. W. Urban, "Four-dimensional (4d) phase velocity optical coherence elastography in heterogeneous materials and biological tissue," *Biomedical Optics Express*, vol. 11, no. 7, pp. 3795–3817, 2020. DOI: 10.1364/BOE.394835.

[168] B. R. Chintada, R. Rau, and O. Goksel, "Acoustoelasticity analysis of shear waves for nonlinear biomechanical characterization of oil-gelatin phantoms," in *2019 IEEE International Ultrasonics Symposium (IUS)*, 2019, pp. 423–426. DOI: 10.1109/ULTSYM.2019.8925670.

[169] T. Poynard, M. Munteanu, E. Luckina, *et al.*, "Liver fibrosis evaluation using real-time shear wave elastography: Applicability and diagnostic performance using methods without a gold standard," *Journal of Hepatology*, vol. 58, no. 5, pp. 928–935, 2013. DOI: 10.1016/j.jhep.2012.12.021.

[170] N. C. Rouze, M. H. Wang, M. L. Palmeri, and K. R. Nightingale, "Parameters affecting the resolution and accuracy of 2-d quantitative shear wave images," *IEEE Transactions on Ultrasonics, Ferroelectrics, and Frequency Control*, vol. 59, no. 8, pp. 1729–1740, 2012. DOI: 10.1109/TUFFC.2012.2377.

[171] C. Zemzemi, A. Zorgani, L. Daunizeau, S. Belabhar, R. Souchon, and S. Catheline, "Super-resolution limit of shear-wave elastography," *Europhysics Letters*, vol. 129, no. 3, p. 34 002, 2020. DOI: 10.1209/0295-5075/129/34002.

[172] S. Catheline, J.-L. Gennisson, G. Delon, *et al.*, "Measurement of viscoelastic properties of homogeneous soft solid using transient elastography: An inverse problem approach," *The Journal of the Acoustical Society of America*, vol. 116, no. 6, pp. 3734–3741, 2004. DOI: 10.1121/1.1815075.

[173] B. R. Chintada, R. Rau, and O. Goksel, "Nonlinear characterization of tissue viscoelasticity with acoustoelastic attenuation of shear waves," *IEEE Transactions on Ultrasonics, Ferroelectrics, and Frequency Control*, vol. 69, no. 1, pp. 38–53, 2022. DOI: 10.1109/TUFFC.2021.3105339.

[174] R. B. Bird, R. C. Armstrong, and O. Hassager, "Dynamics of polymeric liquids. vol. 1, 2nd ed. : Fluid mechanics," 1987.

[175] B. Qiang, J. C. Brigham, S. Aristizabal, J. F. Greenleaf, X. Zhang, and M. W. Urban, "Modeling transversely isotropic, viscoelastic, incompressible tissue-like materials with application in ultrasound shear wave elastography," *Physics in medicine and biology*, vol. 60, no. 3, pp. 1289–1306, 2015. DOI: 10.1088/0031-9155/60/3/1289.

[176] P. Kijanka and M. W. Urban, "Local phase velocity based imaging of viscoelastic phantoms and tissues," *IEEE Transactions on Ultrasonics, Ferroelectrics, and Frequency Control*, vol. 68, no. 3, pp. 389–405, 2021. DOI: 10.1109/TUFFC.2020.2968147.

[177] S. S. Poul, J. Ormachea, G. R. Ge, and K. J. Parker, "Comprehensive experimental assessments of rheological models' performance in elastography of soft tissues," *Acta Biomaterialia*, vol. 146, pp. 259–273, 2022. DOI: 10.1016/j.actbio.2022.04.047.

[178] D. Klatt, U. Hamhaber, P. Asbach, J. Braun, and I. Sack, "Noninvasive assessment of the rheological behavior of human organs using multifrequency mr elastography: A study of brain and liver viscoelasticity," *Physics in Medicine and Biology*, vol. 52, no. 24, pp. 7281–7294, 2007. DOI: 10.1088/0031-9155/52/24/006.

[179] P. Asbach, D. Klatt, B. Schlosser, *et al.*, "Viscoelasticity-based staging of hepatic fibrosis with multifrequency mr elastography," *Radiology*, vol. 257, no. 1, pp. 80–86, 2010. DOI: 10.1148/radiol.10092489.

[180] C. Schmitt, A. Hadj Henni, and G. Cloutier, "Characterization of blood clot viscoelasticity by dynamic ultrasound elastography and modeling of the rheological behavior," *Journal of Biomechanics*, vol. 44, no. 4, pp. 622–629, 2011. DOI: 10.1016/j.jbiomech.2010.11.015.

[181] J. Torres, G. Laloy-Borgna, G. Rus, and S. Catheline, "A phase transition approach to elucidate the propagation of shear waves in viscoelastic materials," *Applied Physics Letters*, vol. 122, no. 22, p. 223 702, 2023. DOI: 10.1063/5.0150219.

[182] J.-L. Gennisson, "Rheological model-based methods for estimating tissue viscoelasticity," in *Ultrasound Elastography for Biomedical Applications and Medicine*, John Wiley & Sons, Ltd, 2018, ch. 8, pp. 105–117. DOI: 10.1002/9781119021520.ch8.

[183] R. Sinkus, S. Lambert, K. Z. Abd-Elmoniem, *et al.*, "Rheological determinants for simultaneous staging of hepatic fibrosis and inflammation in patients with chronic liver disease," *NMR in Biomedicine*, vol. 31, no. 10, e3956, 2018. DOI: 10.1002/nbm.3956.

[184] L. A. Levin, S. F. E. Nilsson, J. V. Hoeve, S. Wu, P. L. Kaufman, and A. Alm, *Adler's Physiology of the Eye E-Book: Expert Consult - Online and Print*. Elsevier Health Sciences, 2011.

[185] Y. Ruan, S. Jiang, A. Musayeva, N. Pfeiffer, and A. Gericke, "Corneal epithelial stem cells–physiology, pathophysiology and therapeutic options," *Cells*, vol. 10, no. 9, p. 2302, 2021. DOI: 10.3390/cells10092302.

[186] B. J. Blackburn, M. W. Jenkins, A. M. Rollins, and W. J. Dupps, "A review of structural and biomechanical changes in the cornea in aging, disease, and photochemical crosslinking," *Frontiers in Bioengineering and Biotechnology*, vol. 7, 2019.

[187] A. Elsheikh, D. Wang, and D. Pye, "Determination of the modulus of elasticity of the human cornea," *Journal of Refractive Surgery*, vol. 23, no. 8, pp. 808–818, 2007. DOI: 10.3928/1081-597X-20071001-11.

[188] A. Ashofteh Yazdi, J. Melchor, J. Torres, *et al.*, "Characterization of non-linear mechanical behavior of the cornea," *Scientific Reports*, vol. 10, no. 1, p. 11 549, 2020. DOI: 10.1038/s41598-020-68391-7.

[189] S. R. Sloan Jr, Y. M. Khalifa, and M. R. Buckley, "The location- and depth-dependent mechanical response of the human cornea under shear loading," *Investigative Ophthalmology & Visual Science*, vol. 55, no. 12, pp. 7919–7924, 2014. DOI: 10.1167/iovs.14-14997.

[190] D. Xia, S. Zhang, J. Ø. Hjortdal, *et al.*, "Hydrated human corneal stroma revealed by quantitative dynamic atomic force microscopy at nanoscale," *ACS Nano*, vol. 8, no. 7, pp. 6873–6882, 2014. DOI: 10.1021/nn5015837.

[191] D. Ortiz, D. Piñero, M. H. Shabayek, F. Arnalich-Montiel, and J. L. Alió, "Corneal biomechanical properties in normal, post-laser in situ keratomileusis, and keratoconic eyes," *Journal of Cataract & Refractive Surgery*, vol. 33, no. 8, pp. 1371–1375, 2007. DOI: 10.1016/j.jcrs.2007.04.021.

[192] ó. R. Ambr, B. T. Lopes, .-. F. Faria, *et al.*, "Integration of scheimpflug-based corneal tomography and biomechanical assessments for enhancing ectasia detection," *Journal of Refractive Surgery*, vol. 33, no. 7, pp. 434–443, 2017. DOI: 10.3928/1081597X-20170426-02.

[193] B. J. Blackburn, S. Gu, M. R. Ford, *et al.*, "Noninvasive assessment of corneal crosslinking with phase-decorrelation optical coherence tomography," *Investigative Ophthalmology & Visual Science*, vol. 60, no. 1, pp. 41–51, 2019. DOI: 10.1167/iovs.18-25535.

[194] M. A. Kirby, I. Pelivanov, S. Song, *et al.*, "Optical coherence elastography in ophthalmology," *Journal of Biomedical Optics*, vol. 22, no. 12, p. 1, 2017. DOI: 10.1117/1.JBO.22.12.121720.

[195] T. Ling, Q. Jin, H. Yao, and H. Zheng, "Design and characterization of a tissue-mimicking phantom for ultrasonic elastography," in *2010 4th International Conference on Bioinformatics and Biomedical Engineering*, 2010, pp. 1–4. DOI: 10.1109/ICBBE.2010.5515427.

[196] A. F. Prokop, S. Vaezy, M. L. Noble, P. J. Kaczkowski, R. W. Martin, and L. A. Crum, "Polyacrylamide gel as an acoustic coupling medium for focused ultrasound therapy," *Ultrasound in Medicine & Biology*, vol. 29, no. 9, pp. 1351–1358, 2003. DOI: 10.1016/S0301-5629(03)00979-7.

[197] C. Lafon, V. Zderic, M. L. Noble, *et al.*, "Gel phantom for use in high-intensity focused ultrasound dosimetry," *Ultrasound in Medicine & Biology*, vol. 31, no. 10, pp. 1383–1389, 2005. DOI: 10.1016/j.ultrasmedbio.2005.06.004.

[198] M. J. Choi, S. R. Guntur, K. I. Lee, D. G. Paeng, and A. Coleman, "A tissue mimicking polyacrylamide hydrogel phantom for visualizing thermal lesions generated by high intensity focused ultrasound," *Ultrasound in Medicine & Biology*, vol. 39, no. 3, pp. 439–448, 2013. DOI: 10.1016/j.ultrasmedbio.2012.10.002.

[199] G. Ge, Y. Zhang, J. Shao, *et al.*, "Stretchable, transparent, and self-patterned hydrogel-based pressure sensor for human motions detection," *Advanced Functional Materials*, vol. 28, no. 32, p. 1 802 576, 2018. DOI: 10.1002/adfm.201802576.

[200] K. Kumar, M. E. Andrews, V. Jayashankar, A. K. Mishra, and S. Suresh, "Measurement of viscoelastic properties of polyacrylamide-based tissue-mimicking phantoms for ultrasound elastography applications," *IEEE Transactions on Instrumentation and Measurement*, vol. 59, no. 5, pp. 1224–1232, 2010. DOI: 10.1109/TIM.2009.2038002.

[201] E. Çetin, B. Karaböce, H. O. Durmuş, H. Gürbüz, and S. Altınay, "Determination of thermal lesions formed by hifu using polyacrylamide based phantom containing egg white," in *2019 IEEE International Symposium on Medical Measurements and Applications (MeMeA)*, 2019, pp. 1–6. DOI: 10.1109/MeMeA.2019.8802131.

[202] M.-S. Kim, J.-Y. Kim, D.-J. Moon, S.-C. Noh, and H.-H. Choi, "Evaluation of acoustic, thermal, and morphological properties in the egg white phantom," *Journal of Biomedical Engineering Research*, vol. 36, no. 1, pp. 7–15, 2015. DOI: 10.9718/JBER.2015.36.1.7.

[203] F. García-Ochoa, V. E. Santos, J. A. Casas, and E. Gómez, "Xanthan gum: Production, recovery, and properties," *Biotechnology Advances*, vol. 18, no. 7, pp. 549–579, 2000. DOI: 10.1016/S0734-9750(00)00050-1.

[204] H. Fang, K. Ni, J. Wu, J. Li, L. Huang, and D. Reible, "The effects of hydrogen bonding on the shear viscosity of liquid water," *International Journal of Sediment Research*, vol. 34, no. 1, pp. 8–13, 2019. DOI: 10.1016/j.ijsrc.2018.10.008.

[205] A. Kumar, K. M. Rao, and S. S. Han, "Application of xanthan gum as polysaccharide in tissue engineering: A review," *Carbohydrate Polymers*, vol. 180, pp. 128–144, 2018. DOI: 10.1016/j.carbpol.2017.10.009.

[206] N. M. Eren, P. H. Santos, and O. Campanella, "Mechanically modified xanthan gum: Rheology and polydispersity aspects," *Carbohydrate Polymers*, vol. 134, pp. 475–484, 2015. DOI: 10.1016/j.carbpol.2015.07.092.

[207] J. F. Schenck, "Safety of strong, static magnetic fields," *Journal of Magnetic Resonance Imaging*, vol. 12, no. 1, pp. 2–19, 2000. DOI: 10.1002/1522-2586(200007)12:1<2::AID-JMRI2>3.0.CO;2-V.